PHYSIK-DEPARTMENT

Cryogenic Silicon Detectors
and
Analysis of Primakoff Contributions to the Reaction $\pi^- \mathrm{Pb} \rightarrow \pi^- \pi^- \pi^+ \mathrm{Pb}$ at COMPASS

Dissertation von Stefanie Grabmüller

TECHNISCHE UNIVERSITÄT
MÜNCHEN

TECHNISCHE UNIVERSITÄT MÜNCHEN
Physik-Department E18

Cryogenic Silicon Detectors and Analysis of Primakoff Contributions to the Reaction $\pi^- \mathrm{Pb} \rightarrow \pi^- \pi^- \pi^+ \mathrm{Pb}$ at COMPASS

Stefanie Grabmüller

Vollständiger Abdruck der von der Fakultät für Physik der Technischen Universität München zur Erlangung des akademischen Grades eines

Doktors der Naturwissenschaften

genehmigten Dissertation.

Vorsitzender: Univ.-Prof. Dr. Andrzej J. Buras (i.R.)

Prüfer der Dissertation:

1. Univ.-Prof. Dr. Stephan Paul
2. Univ.-Prof. Dr. Laura Fabbietti

Die Dissertation wurde am 20.09.2012 bei der Technischen Universität München eingereicht und durch die Fakultät für Physik am 25.09.2012 angenommen.

Abstract

An important part of the physics programme of the COMPASS experiment at CERN is the measurement of reactions with hadron beam particles impinging on fixed targets at small momentum transfer.

These measurements require tracking of charged particles with high precision, which is only reachable employing silicon microstrip detectors placed around the target, both as a part of the beam telescope and in the first part of the spectrometer. These detectors have been operated at a sensor temperature of 200 K starting with the 2009 beam time. They are cooled with liquid nitrogen in thin capillaries attached to the silicon sensors. For stable long-term operation, various extensions around the previously existing setup were required. Particularly the mechanical stability of the cooled detector modules concerning thermal deformation, as well as the cooling stability, have been improved to the level where installation in the experiment became feasible. The detector performance profits significantly from the cryogenic operation, so that a time resolution in the range of $1.4 - 1.8\,\mathrm{ns}$ and a spatial resolution of $4 - 6\,\mu\mathrm{m}$ and $7 - 11\,\mu\mathrm{m}$ (for two and one strips hit, respectively) is reached. This corresponds to an improvement of $15 - 20\,\%$ with respect to the warm operation.

Meson spectroscopy using a high-energetic pion beam impinging on heavy nuclear targets features both diffractive and Primakoff, i.e. electro-magnetic, production of the final state, the latter becoming competitive particularly at lowest momentum transfer t'. Four million exclusive $\pi^-\pi^-\pi^+$ final state events, emerging from π^- beam scattering off a lead target, have been recorded during the COMPASS 2004 hadron run. About one million feature $t' < 10^{-3}\,\mathrm{GeV}^2/c^2$. Employing partial-wave analysis techniques, Primakoff-produced resonances, and the interference between Primakoff and diffractive production have been observed. Using the free decay of the kaon component of the beam as normalization, the absolute cross-section for the process $\pi^-\gamma \to \pi^-\pi^-\pi^+$ could be determined for the first time. It is in good agreement with the prediction of Chiral Perturbation Theory.

Kurzfassung

Als wichtigen Teil seines Physik-Programms untersucht das COMPASS Experiment am CERN Reaktionen, bei denen ein Hadronstrahl unter kleinen Impulsübertragen an ruhenden Targets streut.

Die Messung dieser Reaktionen erfordert die hochpräzise Spurrekonstruktionen geladener Teilchen, wie sie aktuell nur mit Silizium-Mikrostreifendetektoren erreicht werden kann. Sie sind bei COMPASS vor und nach dem Target eingesetzt und werden seit der Strahlzeit 2009 bei einer Sensor-Temperatur von 200 K betrieben. Dies wird durch Kühlung mit flüssigem Stickstoff erreicht, der durch dünne Kapillaren am Sensor entlang geführt wird. Für den stabilen Langzeitbetrieb waren mehrere Erweiterungen des bestehenden Aufbaus notwendig. Vor allem die mechanische Stabilität der Detektormodule hinsichtlich thermischer Verformung, sowie die Zuverlässigkeit der Kühlung, wurden verbessert, so dass der Einbau ins Experiment erfolgen konnte. Durch die Kühlung verbessern sich auch die Detektoreigenschaften, so dass eine Zeitauflösung von $1.4 - 1.8$ ns und eine Ortsauflösung von $4 - 6$ µm bzw. $7 - 11$ µm (für zwei bzw. einen getroffenen Streifen) erreicht wird, was eine Verbesserung von $15 - 20$ % gegenüber dem warmen Betrieb darstellt.

Bei Mesonspektroskopie mit einem hochenergetischen Pionstrahl und schweren Kernen als Targetmaterial treten sowohl diffraktive als auch Primakoff, d.h. elektromagnetische, Produktion der Endzustände auf, wobei letztere überwiegend bei sehr kleinen Impulsüberträgen t' beobachtet wird. Während der COMPASS Strahlzeit mit Hadronenstrahl im Jahr 2004 wurden vier Millionen exklusiver $\pi^-\pi^-\pi^+$ Endzustände aufgezeichnet, die von einem π^- Strahl an einem Bleitarget erzeugt wurden. Eine Million davon weist $t' < 10^{-3}\,\mathrm{GeV}^2/c^2$ auf. Durch eine Partialwellenanalyse wurden Primakoff-produzierte Resonanzen und die Inferenz zwischen diffraktiver und Primakoff-Produktion beobachtet. Mit Hilfe des freien Zerfalls des Kaonanteils im Strahl als Normierung wurde zum ersten Mal der absolute Wirkungsquerschnitt für den Prozes $\pi^-\gamma \to \pi^-\pi^-\pi^+$ bestimmt. Dieser befindet sich in guter Übereinstimmung mit der Voraussage der Chiralen Störungsrechnung.

Contents

Chapter 1

Introduction

The Standard Model of particle physics groups the constituents of matter into quarks, leptons, and gauge bosons. Quarks build up the strongly interacting particles, called hadrons, with gluons as exchange particles. As protons and neutrons they form the atomic nuclei and consequently more than 99 % of the matter experienced every day. The Higgs boson, expected to complete the theoretical foundation of the Standard Model, is one of the most prominent research topics in experimental particle physics.

Investigations of these elementary particles are carried out in high-energy collisions of highly accelerated particles with each other, or with stationary targets. The technological progress of particle acceleration makes collisions possible with highest luminosities and unprecedented energies, as in the Large Hadron Collider at CERN, where a particle consistent with the Higgs boson has recently been reported. The particles resulting from these collisions are detected in suitable experimental apparatuses, and are studied intensively to shed more light on the basic laws of nature.

Quantum ChromoDynamics (QCD) is the quantum field theory that describes the strong interaction, i.e. the force between the color charge of the quarks exchanged by gluons. As the gluons carry color charge themselves, they interact both with quarks and with each other. As consequence, the attracting force becomes stronger at larger distances between quarks (confinement). Thus only bound states of hadrons exist, like baryons and mesons with a constituent-quark content of three quarks or a quark-antiquark pair, respectively.

The present thesis is embedded in the field of meson spectroscopy. The properties of the short-lived mesonic states are reconstructed from their decay products. They can be analyzed within a wide kinematical range, giving access to the involved physics processes. The reconstruction of the produced charged or neutral particles from the experimental data is mandatory with highest precision to obtain conclusive results, particularly with reactions featuring small scattering or decay angles.

This work has been carried out within the framework of the COMPASS experiment at the Super Proton Synchrotron at CERN which has been designed to investigate different physics topics in the non-perturbative range of QCD. It is a fixed-target experiment with a two-stage magnetic spectrometer which is able to cope with high luminosities, can measure particles within a large range of momenta and scattering angles, and provides a uniform acceptance. Chapter 2 gives a short general overview of this experiment and summarizes the topics and components relevant for this thesis. The spectrometer is described on the basis of the 2004 hadron setup, which was used to record the data presented in chapter 9.

One important ingredient to precision measurements of charged particle trajectories are silicon detectors in the target region due to their excellent spatial and time resolution. Chapter 3 summarizes the general aspects of the specific silicon microstrip detectors used in the COMPASS experiment.

Due to the high beam fluxes at COMPASS, a significant deterioration of the silicon detector performance due to radiation damages was expected on short time scales. This triggered the development of silicon detectors operable at cryogenic temperatures, which had been contemporarily found by a CERN research and development group to increase the charge collection efficiency of irradiated detectors significantly. Chapter 4 describes the detector components developed and improved for the cooling by the evaporation of liquid nitrogen, which had its stable long-term operation established in the course of this thesis, and is now employed since the 2009 beam time.

Chapter 5 summarizes the radiation impact which the silicon detectors have been exposed to during the various COMPASS beam times, and shortly sketches the trend of two observables, noise behaviour and leakage currents, related to radiation damages.

The performance of both warm and cryogenic silicon detectors in COMPASS is discussed in chapter 6, emphasizing the profit for both time and spatial resolution from the cryogenic operation.

Chapter 7 introduces the basic concepts of meson spectroscopy at low momentum transfer, which are relevant for the data analysis presented in chapter 9. In the selected kinematic range, Primakoff reactions and diffractive dissociation dominate the observed spectra. The key technique for the analysis of spectroscopy data, based on angular distibutions of the decay particles, is the partial-wave analysis as described in chapter 8. The special features introduced for this analysis are described in detail.

The data analysis of $\pi^-\pi^-\pi^+$ final state events produced at smallest momentum transfer $t' < 10^{-3}\,\mathrm{GeV}^2/c^2$, recorded during the COMPASS 2004 hadron run, is presented in chapter 9. The analysis includes various Monte Carlo studies and partial-wave analyses executed in bins of both mass and momentum transfer. This leads to indications for Primakoff-produced resonances like the $a_2(1320)$. Thus the interference between Primakoff and diffractive production of these resonances can be studied. In the mass range just above threshold, the first measurement of the total cross-section of $\pi^-\gamma \to \pi^-\pi^-\pi^+$ is presented, and compared to a leading order calculation in the framework of Chiral Perturbation Theory.

Chapter 10 summarizes the main results and conclusions acquired in the course of this work.

Chapter 2

The COMPASS Experiment

The Common Muon Proton Apparatus for Structure and Spectroscopy (COMPASS) [COM] is a high-luminosity fixed-target experiment at the Super Proton Synchrotron (SPS) accelerator at CERN[1]. It uses high-luminosity polarized muon or unpolarized hadron beams to investigate various physics topics addressing open questions in the non-perturbative regime of Quantum ChromoDynamics (QCD), i.e. nucleon structure functions and the hadron spectrum itself. Those topics had originally been on the agenda of two different collaborations, CHEOPS[2] and HMC[3], but needed essentially the same experimental setup, which was finally merged as the COMPASS spectrometer.

The proposal for the COMPASS programme of the first decade [COM96] was approved by CERN in 1996. Physics data taking started in 2002 and continued until 2011 with various upgrades of the spectrometer in the course of this time. The proposal for the successor physics programme, named COMPASS-II, was approved in 2010, covering the first three years of data taking from 2012 on [COM10a].

An overview of the COMPASS physics programme is presented in section 2.1. Most topics are summarized only very briefly, while the hadron programme, relevant for this thesis, is discussed separately with more details. The general layout of the COMPASS spectrometer is roughly similar for all measurements. It is presented in section 2.2 exemplarily for the 2004 hadron setup which was used for the data analysis in chapter 9. A summary of the software tools employed at COMPASS for the reconstruction and analysis of the recorded data, as well as for simulations, is given in section 2.3.

2.1 Physics Programme

COMPASS investigates various topics related to hadron structure and spectroscopy. The main physics objectives of the hadron programme, concerning spectroscopy and the measurement of the pion polarizabilities, are presented in the following. In addition, the muon programme concentrating mainly on the determination of the gluon polarization, as well as the GPD and Drell-Yan parts of the COMPASS-II proposal, is briefly sketched.

---

[1] The Conseil Européenne pour la Recherche Nucleaire (European Organisation for Nuclear Research), located near Geneva, Switzerland, is the world's largest particle physics laboratory [CERN].

[2] CHarm Experiment with Omni-Purpose Setup [CHE95].

[3] Hadron Muon Collaboration [HMC95].

2.1.1 The Hadron Programme

The main topics of the COMPASS hadron programme are described in the following. Several weeks in the end of the 2004 beam time, the full 2008 and 2009 beam times, and the first half of the COMPASS 2012 beam time have been dedicated to the pion polarizabilities and hadron spectroscopy.

2.1.1.1 The Pion and Kaon Polarizabilities

Chiral Perturbation Theory (ChPT, see section 7.1.3) is an effective theory for QCD at low energies. Calculations for e.g. the pion-pion scattering length have been confirmed by measurements from kaon decay experiments. Other predictions, like the one for the pion polarizabilities, still need confirmation. The electric and magnetic polarizabilites of the pion, α_π and β_π, describe the behaviour of the quark-gluon structure in an electromagnetic field, which can be depicted as the deformation of the pion. Calculations within various theoretical models have been carried out, with different results of these parameters. The existing experimental results vary on even larger scales, so that a measurement with higher precision is desired.

At COMPASS, the pion polarizabilities are experimentally studied in Primakoff Compton scattering using a high-energetic pion beam impinging on heavy nuclear targets (lead or nickel[4]) as depicted in figure 2.1. As detailed in section 7.3, the electro-magnetic field surrounding a heavy nucleus provides quasi-real photons as interaction particles for high-energetic beam particles like pions (*Primakoff effect*). The deformation of the pion in the electro-magnetic field of the quasi-real photon leads eventually to the emission of another real photon. The leading deviation of the Compton cross-section, depending on both the scattering angle θ_{cm} in the $\pi\gamma$ system and its invariant mass $\sqrt{s}$, from the cross-section of the Compton scattering of a point-like spin-0 particle, gives access at leading and next-to-leading order to $\alpha_\pi + \beta_\pi$, $\alpha_\pi - \beta_\pi$, and the quadrupole polarizability combination $\alpha_2 - \beta_2$:

$$\frac{d\sigma_{\pi\gamma}}{d\Omega_{cm}} = \frac{\alpha^2(s^2 z_+^2 + m_\pi^4 z_-^2)}{s(sz_+ + m_\pi^2 z_-)^2} - \frac{\alpha\, m_\pi^3\,(s - m_\pi^2)^2}{4s^2(sz_+ + m_\pi^2 z_-)} \cdot \mathcal{P} \tag{2.1}$$

with

$$\mathcal{P} = z_-^2\,(\alpha_\pi - \beta_\pi) + \frac{s^2}{m_\pi^4} z_+^2\,(\alpha_\pi + \beta_\pi) - \frac{(s - m_\pi^2)^2}{24s} z_-^3\,(\alpha_2 - \beta_2) \tag{2.2}$$

where $z_\pm = 1 \pm \cos\theta_{cm}$, m_π the pion mass, and α the fine structure constant. The cross-section given by equation 2.1 is most strongly influenced by $\alpha_\pi + \beta_\pi$ in forward scattering, and by $\alpha_\pi - \beta_\pi$ in backward scattering in the center-of-mass system. The comparison to the cross-section of the Compton scattering of a point-like particle has to be carried out

---

[4] Despite featuring lower Z, nickel was found to be preferable to lead, as the radiative corrections to be applied are significantly less important for nickel.

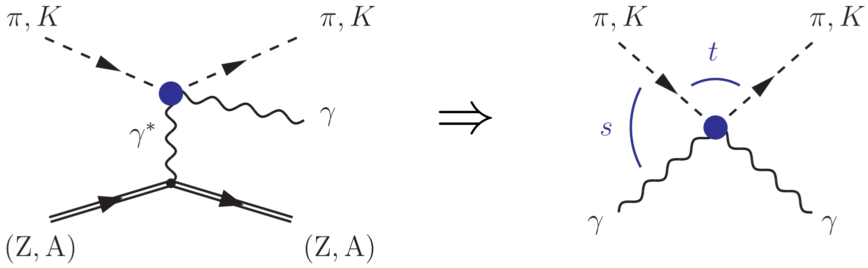

Figure 2.1: Primakoff scattering of pions at quasi-real photons with the emission of a real photon provides access to pion Compton scattering.

by the comparison of the experimental data to a dedicated Monte Carlo simulation of a point-like pion scattering off the nuclear target in the respective spectrometer. A control measurement with muon beam, featuring both a pure electro-magnetic interaction, and a point-like beam particle without any polarizability effects, is a unique advantage of the COMPASS setup. It provides a rigorous check of the spectrometer description in the simulation.

After explorative studies with the 2004 data [Din10], the pion polarizabilities have been measured with a pion beam on nickel target, and an improved calorimeter trigger, during two weeks of the COMPASS 2009 hadron beam time (*2009 Primakoff data*). A set of 23 000 exclusive $\pi^-\gamma \rightarrow \pi^-\gamma$ events fulfill the various kinematic cuts applied. This data set serves as the basis for the extraction of the polarizability difference $\alpha_\pi - \beta_\pi$ under the assumption $\alpha_\pi + \beta_\pi \approx 0$. The resulting value is $\alpha_\pi = 1.9 \pm 1.1 \times 10^{-4}\,\text{fm}^3$ [Nag12].

As a part of the COMPASS-II proposal, several months of the 2012 beam time are dedicated to the recording of high statistics polarizability data (*2012 Primakoff data*). The separation of α_π and β_π is expected to be possible with these data, as well as a first determination of the difference of the quadrupole polarizabilities, and a first value of the kaon[5] polarizabilities [COM10a].

2.1.1.2 Exotic States and Spectroscopy

QCD allows further color-neutral states in addition to the mesonic quark-antiquark ($q\bar{q}$) systems and the baryonic qqq or $\bar{q}\bar{q}\bar{q}$ systems allowed in the constituent-quark model. This concerns e.g. pentaquarks ($qqqq\bar{q}$) or tetraquarks ($qq\bar{q}\bar{q}$) with a higher number of valence quarks. Other systems contain excited gluons (g) contributing to or defining the quantum numbers of the system, i.e. hybrids ($q\bar{q}g$) or glueballs (gg). Many of those are difficult to identify in experimental data, as they mix with ordinary mesons or baryons of the same quantum numbers. Thus spectroscopy searches for so-called *spin-exotic* states with forbidden quantum numbers. Concerning mesons, these quantum numbers are e.g.

---

[5] The COMPASS negative pion beam features also a few percent of negative kaons, see section 2.2.1.

$J^{PC} = 0^{+-}, 1^{-+}, 2^{+-}, 3^{-+}, \dots$ (see also section 7.1.1). The unambiguous experimental observation of such spin-exotic mesons would provide a clear evidence of physics beyond the constituent-quark model and thus a fundamental confirmation of QCD.

Lattice QCD calculations have predicted the lightest glueballs to have the quantum numbers $J^{PC} = 0^{++}$ with a mass of about $1.7\,\mathrm{GeV}/c^2$, and $J^{PC} = 2^{++}$ with a mass of about $2.4\,\mathrm{GeV}/c^2$ [Che06]. A promising experimental candidate for the ground state scalar glue ball, the $f_0(1500)$, was observed [CB95, WA10200], but its interpretation is difficult due to potential mixing with ordinary isoscaler mesons. The lowest-lying hybrid instead is expected to feature the quantum numbers $J^{PC} = 1^{-+}$, so that mixing with ordinary mesons is not possible. Lattice QCD calculations [McN06] and flux-tube model calculations [Clo95, Isg85] predict a mass between 1.7 and $2.2\,\mathrm{GeV}/c^2$ for this hybrid, and a preferred decay into $b_1\pi$ and $f_1\pi$. Two experimental candidates have been observed, the $\pi_1(1400)$ and the $\pi_1(1600)$. The $\pi_1(1400)$ was mostly seen in $\eta\pi$ decays [E85297, VES93, CB98]. The $\pi_1(1600)$ was observed in various final states, i.e. $\rho\pi$ [E85298, VES00], $\eta'\pi$ [E85201, VES93], $f_1\pi$ [E85204, VES05] and $\omega\pi\pi$ [E85205, VES05], but also counter statements have been published [Dzi06]. Thus, the resonant nature of these hybrid candidates is heavily disputed, so that further high-statistics data covering the complete phase-space and several decay modes was necessary for a better clarification.

The COMPASS experiment contributes with the study of various decay channels of the exotic candidates, produced from proton, pion or kaon beam particles scattering off nuclear or hydrogen targets, and can also identify and analyze neutral or kaonic particles in the final states. Two physics processes are mainly exploited for this purpose, central and diffractive production. In *central production* a meson is produced in the fusion of two Reggeons that are exchanged between the beam and the target as depicted in figure 2.2 (left). This process features a rapidity gap between the fast scattered beam particle and the produced state, and is expected to be well-suited for the search for glueballs, as the dominant two-Pomeron exchange particles have no net quark content. *Diffractive production* is a one-Reggeon exchange between the beam and the target, in which the beam particle is excited (figure 2.2 (middle); see also section 7.2). This process features more forward kinematics, and is traditionally exploited for the search for hybrids. The scope of spectroscopy is nowadays extended by taking into account also Primakoff production, i.e. scattering off a quasi-real photon appearing at lowest momentum transfer (figure 2.2 (right); see section 7.3). This serves as another potential source for hybrids decaying into $\rho\pi$, and such provides an additional consistency check for the hybrid analysis, but it is also exploited for the experimental measurement of selected $\pi\gamma$ reaction cross-sections which have been calculated by ChPT [KF08]. The fundamental analysis technique for any precision spectroscopy studies is an amplitude analysis, usually called *partial-wave analysis*, which decomposes the observed spectrum into a set of angular eigenstates (see chapter 8).

At COMPASS, the first spectroscopy data were recorded during the 2004 hadron beam time with pion beam on lead target, i.e. in parallel to the polarizability data taking. The

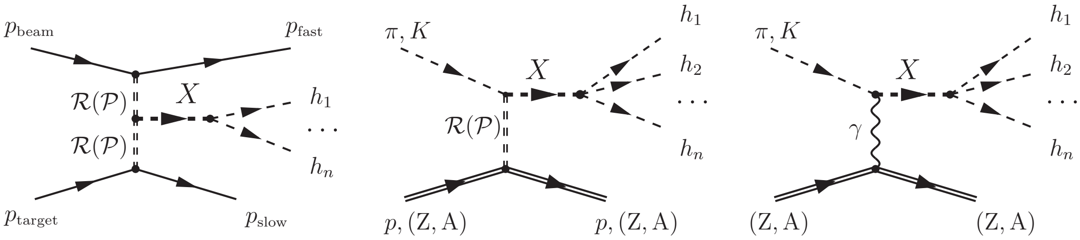

Figure 2.2: Exemplary graphs for central production (left), diffractive production (middle), and Primakoff production (right) of the intermediate state X, decaying into hadrons $h_1 \dots h_n$, at COMPASS.

analysis of the diffractively produced $\pi^-\pi^-\pi^+$ final state at comparatively high momentum transfer lead to the observation of a resonance with $J^{PC} = 1^{-+}$ decaying into $\rho\pi$, consistent with the $\pi_1(1600)$ [COM10c]. The same final state, but produced at lowest momentum transfer, represents the focus of the physics analysis part of this thesis (see chapter 9). The cross-section of $\pi^-\gamma \to \pi^-\pi^-\pi^+$ at $m_{3\pi} < 0.72\,\mathrm{GeV}/c^2$ was found to be in agreement with the leading-order calculations from ChPT, a published result obtained within the work of this thesis [COM12a]. In addition, the $\pi^-\pi^-\pi^-\pi^+\pi^+$ final state was subject to a partial-wave analysis, allowing to access also higher masses. It revealed well-known resonances and also the quasi-two-body decay of the hybrid candidate $\pi_2(1880)$ into ρa_1 and ρa_2 [Neu12].

The COMPASS 2008 and 2009 beam times were mainly dedicated to hadron spectroscopy. For the major part of the time, a liquid hydrogen target was employed, but also small data sets with lead and nickel targets were recorded for comparison issues. Most statistics was collected in three-pion final states. The diffractive $\pi^-\pi^-\pi^+$ final state events collected with the liquid hydrogen target and π^- beam at comparatively high momentum transfer exceed the previous world statistics of this channel significantly more than one order of magnitude, allowing for more detailed investigations of all aspects of this final state, including non-resonant contributions from the Deck effect [Haa12]. As the amplitudes featuring spin projection $M = 1$ were found to be comparatively less intensive than in the 2004 data, the measurements with lead and nickel target are supposed to shed light on the M-dependence of the target material [Haa12]. The analysis of the $\pi^-\pi^0\pi^0$ final state provides an important consistency check [Pfl11, Ner11]. Furthermore, the reactions $\pi^- p \to \eta\pi^- p$ and $\pi^- p \to \eta'\pi^- p$ reveal known resonances and further structures, which are in agreement between both channels, except for the spin-exotic amplitude, which is enhanced in the $\pi^-\eta'$ system [Sch12]. Diffractive dissociation of kaon beam allows for the measurement of $K^-\pi^-\pi^+$ events, which are expected to improve the knowledge of the light isospin-1/2 meson spectrum [Jas12]. The measurements with the nuclear targets are also supposed to complement the 2004 data featuring low momentum transfer with more statistics and the $\pi^-\pi^0\pi^0$ final state. -Central production of presumably gluon-rich mesons is studied with dedicated data with proton beam on the liquid hydrogen target.

2.1.1.3 Charmed Baryons

The measurements of the life times and decays widths of charmed and particularly doubly-charmed baryons are expected to contribute significantly to the knowledge of charm physics, which is still poor in many aspects. Double charmed baryons are presumably similar to heavy mesons consisting of a light and a heavy meson, if the *cc* pair is bound very tightly, and the third light quark surrounds them. Their life times can offer significant insights into decay dynamics. These measurements need on optimized setup with triggering on and high-precision reconstruction of secondary vertices, so that a segmented target with interleaved silicon counters is followed by additional sets of silicon detectors. This measurement has been on the agenda since the beginning [COM96], but has not been addressed yet.

2.1.2 Further Physics Topics

The main topics of the COMPASS physics programme which are not covered in section 2.1.1 are briefly listed in the following. More details, and, where available, results can be found in the references. From 2002–2004, and in 2006/2007 and 2010/2011 data have been recorded for the investigation of the spin-dependent structure of the nucleon with polarized muon beam on longitudinally or transversely polarized proton or deuteron targets. In the second half of the 2012 beam time and in 2015, first data for the GPD part of the COMPASS-II proposal will follow, and in 2014 the Drell-Yan measurement.

2.1.2.1 The Muon Programme of COMPASS-I

Gluon Polarization: The determination of the gluon spin contribution ΔG to the total spin of the nucleon has been an important topic since it was found that the sum of the spins of quarks accommodates only a part of the nucleon spin. The gluon polarization $\Delta G/G$ is experimentally accessed in semi-inclusive deep inelastic scattering (DIS) in photon-gluon fusion $\gamma^* g \rightarrow q\bar{q}$. This is a second order process, where the photon interacts with the gluon via a virtual quark line. It is studied in COMPASS in two processes. The *open charm* channel is based on the production of $c\bar{c}$ pairs which fragment into D mesons that decay into $K\pi$. The gluon polarization is extracted from the cross-section asymmetry for the different spin configurations of the COMPASS target [COM09c]. The second process involves events with hadron pairs or single hadrons with high transverse momentum. $\Delta G/G$ is calculated from the helicity asymmetry of quasi-real photo-production of these *high-*p_t hadron pairs [COM06] and the longitudinal double spin asymmetry for their production in the DIS regime [COM12b]. The high-p_t channel has the advantage of significantly more statistics compared to the open charm channel, but the result depends on the models used in the simulations of the background processes which have to be substracted.

Longitudinal Spin Structure Functions: Further important knowledge on the nucleon spin structure can be obtained in semi-inclusive DIS. The longitudinal spin asymmetry A_1^d and the spin-dependent structure function g_1^d of the deuteron are measured with significantly higher accuracy than in previous experiments [COM05b, COM07b, COM07d]. Additional contributions are measurements of polarized valence quark distributions [COM08] and a full flavour separation of the helicity distributions [COM09b, COM10d].

Transverse Spin Distributions: A more complete picture of the quarks inside the nucleon requires also the transverse spin distributions. The Collins and Sivers asymmetries can be measured via the cross-sections of hadrons produced in semi-inclusive DIS of polarized leptons on transversely polarized nucleons. These are measured on both deuteron and proton targets [COM05a, COM07c, COM09a, COM10b].

Lambda Polarization: Information from the sea quarks in the nucleon is accessible also from lambda polarization. The longitudinal polarization of Λ and $\bar{\Lambda}$ baryons can be measured in semi-inclusive DIS of muons on longitudinally polarized nucleons. The spin transfer from the target nucleon to the final state hyperon are studied [COM09d]. The transverse polarization, i.e. the polarization normal to the production plane, of the hyperons which are inclusively produced from unpolarized beam scattering off an unpolarized target, is related to the properties of the hadronization process [Gru06].

2.1.2.2 Generalized Parton Distributions

Generalized Parton Distributions (GPDs) are a generalized description for the structure of the nucleon regarded as an extended three-dimensional object. They describe both the longitudinal momentum fraction of the quark and its transverse position inside the nucleus. They include nucleon electromagnetic form factors and the parton distribution functions (PDFs). They are also supposed to shed light onto the orbital momenta of quarks and gluons. At COMPASS, the GPDs are experimentally accessed in Deeply Virtual Compton Scattering (DVCS). This implies muon scattering on a proton target, whereby a virtual photon kicks out a quark, which falls back into the proton under the emission of a real photon. The measurement requires exclusivity, which implies the reconstruction of the momentum of the recoil proton in a Recoil Proton Detector (RPD) that surrounds the new (unpolarized) liquid hydrogen target which is 2.5 m long, and the installation of an additional electromagnetic calorimeter (ECAL0) to increase the photon acceptance. The main background comes from a Bremsstrahlung process, called Bethe-Heitler (BH). In contrast to DVSC, the BH process is not spin-dependent, so that its contribution cannot only be substracted, but at COMPASS also cancels out in measurements with both positive and negative muon beams, which naturally feature opposite polarization [COM10a].

2.1.2.3 Drell-Yan

When the description of the three-dimensional structure of the nucleon takes into account the transverse momentum of partons in the nucleon, also Transverse Momentum Dependent Parton Distributions (TMDs) are required. They can be measured preferably in the Drell-Yan (DY) quark-antiquark annihilation process, which does not involve any fragmentation process. A quark and an antiquark from two different hadrons annihilate into a lepton pair. At COMPASS, the process $\pi^- p^\uparrow \to \mu^+ \mu^- X$ will be measured, with pion beam on transversely polarized NH_3 target. A hadron absorber will be installed downstream of the target, to reduce the high flux of secondary particles and to stop the non-interacting beam particles, to allow in return for a significant increase of the beam intensity [COM10a].

2.2 The Experimental Setup

The COMPASS experiment is located at the M2 beam line of the SPS, which can provide high-intensity hadron or muon beams. The setup in the experimental area consists of a two-stage magnetic spectrometer with various detectors for tracking, calorimetry, and particle identification in each stage. The spectrometer is presented very briefly in the following, with the focus on the 2004 hadron setup used to record the data presented in section 9. More details on the spectrometer components used up to 2004 can be found in [COM07e], and the upgrades for the COMPASS hadron runs 2008 and 2009 are given in [COM12c].

2.2.1 Beam from the M2 Beam Line

All COMPASS beams are derived from a primary proton beam delivered by the CERN SPS with $400\,\mathrm{GeV}/c$ momentum and a nominal intensity of approximately $1 \cdot 10^{13}$ protons per spill[6]. The primary proton beam impinges on a production target ("T6") made from beryllium, where various thicknesses of up to 500 mm are possible. A thinner production target results in lower beam intensity that is guided subsequently to the experiment. The M2 beam lime can be tuned to transport either secondary hadron beam or tertiary muon beam[7] in certain momentum ranges. At its beginning, a system of six quadrupoles and three dipoles selects a high pion flux with a nominal momentum[8] of up to $225\,\mathrm{GeV}/c$, which is transported about 1 km through a system of collimators, dipoles and quadrupoles. As part of the pions decays along this way into a muon and a neutrino, the muon beam can be selected by moving hadron absorbers of a total length of about 10 m beryllium into the beam line. As the pion decay violates parity conservation,

---

[6] A spill is the extraction phase of the beam from the SPS. In 2004, it lasted 4.8 s within the 16.8 s long SPS cycle.

[7] The beamline can also be used to deliver electron beam of up to $40\,\mathrm{GeV}/c$ for calibration purposes. This is not explained in the following, see [COM07e] instead.

[8] If the acceptance optics is modified, a maximum momentum of $280\,\mathrm{GeV}/c$ can be reached.

Particle	π^+	K^+	p	π^-	K^-	$\bar{p}$
Fraction at 0 m	0.255	0.029	0.715	0.947	0.046	0.007
Fraction at 1100 m	0.240	0.014	0.746	0.968	0.024	0.008

Table 2.1: Beam composition of the positive and negative 190 GeV/c hadron beams (numbers taken from [Jas12]).

the muon beam is naturally polarized. The momentum of the muon beam, featuring a spread of up to 5 %, can be measured by a system of six Beam Momentum Stations (BMS) placed around three consecutive dipole magnets at the end of the beam line. Due to the high interaction length of the detectors this system is not used with hadron beams, so that for hadron beams only the direction of the beam particle is measured by the beam telescope.

The hadron beams consist of a momentum dependent mixture of protons, pions and kaons. The beam composition of the positive and negative hadron beams at 190 GeV/c is stated at the positions of both right behind the production target and at the COMPASS target in table 2.1. To distinguish between the nature of single beam particles, two ChErenkov Differential counters with Achromatic Ring focus (CEDARs) are installed 30 m upstream of the COMPASS target. Their detector volumes are filled with pressurized helium, so that particles with different masses, i.e. different velocity at the same momentum, emit Cherenkov Light with different cones when passing the radiator volume. The Cherenkov photons are focused on different rings, which are distinguished by a diaphragm in the focal plane, so that only photon created by the desired particle type are detected by photo multipliers. The CEDARs were not operated stably in 2004 so that their information could not be used in the analysis yet, but improved significantly for the 2008 and 2009 beam times [Jas12].

The typical spot size of the beam at the COMPASS target was $\sigma_x \times \sigma_y = 3 \times 3\,\text{mm}^2$ for the hadron beam in 2004, and $\sigma_x \times \sigma_y = 15 \times 10\,\text{mm}^2$ for the hadron beam in 2008 and 2009 [COM12c]. The maximum allowed hadron flux of $1 \cdot 10^8$ particles per spill is limited by radiation protection rules.

The maximum allowed muon flux is $2 \cdot 10^8$ muons per spill. This value can be reached with positive muons of 160 GeV/c and below. For higher momenta or negative muons, the maximum intensities are lower. The typical spot size at the COMPASS target is $\sigma_x \times \sigma_y = 8 \times 8\,\text{mm}^2$. The muon beam is accompagnied by a large halo, i.e. that about 23 % of the nominal muon beam intensity pass the nominal beam axis at a distance of more than 2 cm.

2.2.2 The Spectrometer

The physics programme of the COMPASS experiment requires a spectrometer that provides large and uniform angular and momentum acceptance for fixed targets. This in-

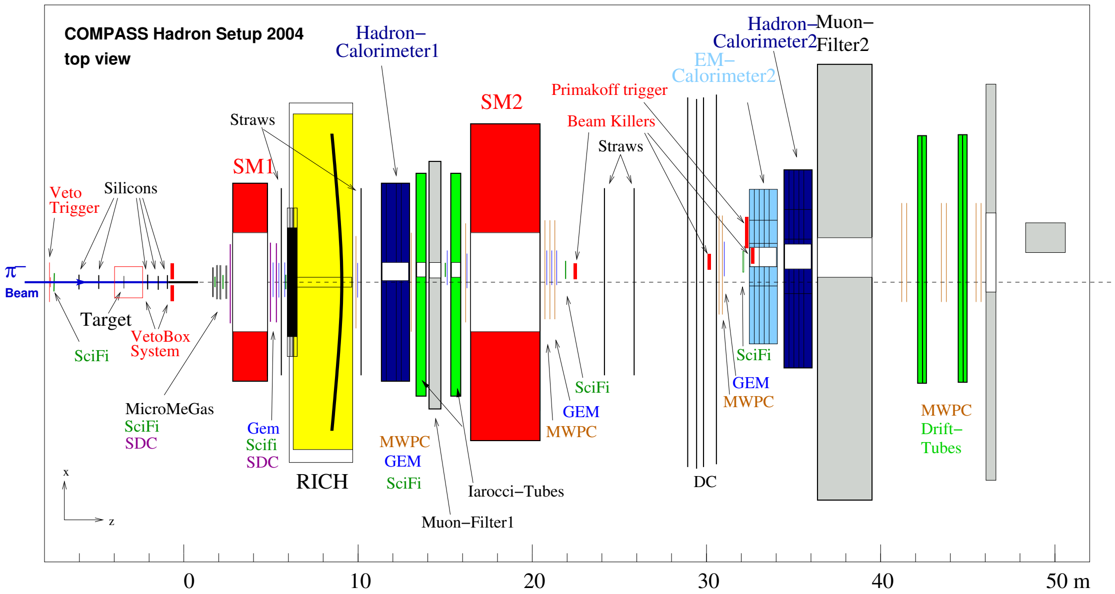

Figure 2.3: Sketch of the COMPASS spectrometer setup as used during the 2004 hadron run, from [COM].

cludes a reliable reconstruction of both charged and neutral particles in the final state over a wide kinematical range, a precise measurement of extremely small scattering angles, and a reliable particle identification. It needs high statistics and thus must be able to handle high luminosities, involving beam rates of up to $2 \cdot 10^8$ particles per spill and a design value for the trigger rates of up to 100 kHz.

A schematic overview of the spectrometer used during the 2004 hadron run is depicted in figure 2.3. That beam time was mainly dedicated to the measurement of the pion polarizability via the Primakoff effect, and partly to diffractive production. These goals are reflected in the specific setup of the target region and the triggers, while the rest of the spectrometer was basically the same for all beam times up to now.

2.2.2.1 The Spectrometer Regions

The COMPASS spectrometer is composed of three regions. The target region differs most between the various measurement, and is described here for the 2004 hadron setup. The additional two stages, marked by two large dipole magnets, are designed for detecting particles in forward direction featuring small or large momenta, respectively. Thus optimal tracking capabilities are provided. The three regions of the setup are explained here, and the employed detector components in the following subsections.

Target Region of the 2004 Hadron Run: In general the target region is covered by fast and high-resolution tracking detectors in the beam telescope upstream of the target, and, for hadron data taking, also downstream of the physics target. A veto system is employed to distinguish between beam particles crossing the target and halo particles.

The center of the 2004 hadron target region consisted of thin disks of nuclear targets, with a diameter of 3 cm, that were centered on the axis of the incoming beam, and placed at about 3 m upstream of the origin of the COMPASS coordinate system[9]. These targets were mainly lead disks with a total thickness of 3 mm, corresponding to 0.54 radiation lengths. Some data were also taken with copper or carbons disks, to study the dependence of the Primakoff cross-section on the charge of the nucleus ($\propto Z^2$) of the target material. The target was placed inside a barrel-shaped veto detector to measure low energy target fragments. Two stations of silicon detectors, each measuring four projections, were placed upstream of the target for beam definition together with a scintillating fiber detector. Three silicon stations were additionally installed downstream of the target, see also figure 3.6, to ensure optimal vertexing for the very small scattering angles coming along with Primakoff scattering. Two additional veto detectors, i.e. sandwiches of scintillating counters and lead foils, were installed upstream and downstream of the spectrometer silicon telescope. Their purpose was to veto events with photons or charged particles emitted at large angles. Another important part of the trigger, the multiplicity counter, was also installed between the target and the first downstream silicon station.

Large Angle Spectrometer (LAS): The first spectrometer stage following the target is built around the first spectrometer magnet *SM1* which provides a field integral of 1.0 Tm and covers a polar acceptance of ±180 mrad. The magnet is surrounded by sets of tracking detectors. The LAS features a Ring Imaging CHerenkov detector (RICH) to identify hadrons[10]. A hadronic calorimeter and a muon filter complete the LAS. Both have central holes which cover the acceptance of the subsequent small angle spectrometer,

Small Angle Spectrometer (SAS): The second spectrometer stage is located around the second spectrometer magnet *SM2* with a field integral of 4.4 Tm, which is also sandwiched between tracking detectors. The SAS covers a polar acceptance of ±30 mrad and detects particles with momenta larger than 5 GeV/c. The electromagnetic calorimeter ECAL2 is located just before the second hadronic calorimeter and the second muon filter.

2.2.2.2 Charged Particle Tracking

Different types of tracking detectors are employed at COMPASS to accomodate different conditions and cover the whole spectrometer acceptance. In the regions along the beam and close to the target, detectors have to stand high particle rates and provide excellent spatial resolution, but feature a minimum material budget. Far away from the beam

---

[9] The origin of the coordinate system is at the center of the polarized target used during muon data taking.

[10] The RICH was filled with N_2 during the 2004 hadron run, so that its information could not be used, as explained later.

larger areas have to be covered. The tracking detectors used in 2004 can be classified into three groups dependent on their place of installation.

Very Small Area Trackers (VSAT) cover the area in and around the beam to reconstruct the beam particles. Thus they need to feature excellent time and spatial resolution. They are fully sensitive, and consequently have to stand the full beam rate. Silicon detectors provide a spatial resolution[11] of $5 - 14\,\mu\mathrm{m}$ and time resolution of $2 - 3\,\mathrm{ns}$. They are installed only in the target region where their excellent spatial resolution is mandatory (for more details on this detector see chapters 3 and 6). Scintillating Fiber (SciFi) detectors feature spatial resolutions of $130 - 180\,\mu\mathrm{m}$, but time resolutions of 400 ps. They are installed at several places along the spectrometer, where their covered area increases from $3.9 \times 3.9\,\mathrm{cm}^2$ to $12 \times 12\,\mathrm{cm}^2$, related to the increasing beam divergence along the spectrometer. As they feature a significant material budget, only a limited number of them is used with hadron beam, i.e. in 2004 four of eight SciFi stations were removed.

Small Area Trackers (SAT) detect particles with distances larger than 2.5 cm from the beam axis, where still high rates are observed and good spatial resolution and low material budget are required. Two types of high-rate capable gaseous detectors are employed at COMPASS. Three stations of Micromesh Gaseous Structure detectors (MicroMegas) with an active area of $40 \times 40\,\mathrm{cm}^2$ are installed upstream of SM1, and eleven stations of Gas Electron Multipliers (GEMs) with an active area of $31 \times 31\,\mathrm{cm}^2$ along the spectrometer downstream of SM1. Both detector types have insensitive zones of 5 cm diameter in their centers[12]. The centers of some of the GEMs were switched on during the 2004 hadron run to substitute the removed SciFi detectors. Both detector types feature spatial resolutions in the order of $70 - 90\,\mu\mathrm{m}$ and time resolutions of $9 - 12\,\mathrm{ns}$.

Large Area Trackers (LAT) cover the areas at large angle acceptance of the setup. In the LAS, one Drift Chamber (DC) is located upstream and two immediately downstream of SM1, with active areas of $1.8 \times 1.3\,\mathrm{m}^2$ and dead zones of 30 cm diameter. Furthermore, 15 straw tube chambers (Straws), eleven Multi Wire Proportional Chambers (MWPCs) and six large area drift chambers, with dimensions between $3.2 \times 2.8\,\mathrm{m}^2$ and $5.0 \times 2.5\,\mathrm{m}^2$, and dead zone between $20 \times 20\,\mathrm{cm}^2$ to $1 \times 1\,\mathrm{m}^2$, depending on position and detector type. These detectors reach spatial resolutions between $200\,\mu\mathrm{m}$ and 2 mm. The dead zones of several LATs are covered by GEM detectors.

The tracking performance reached for charged particles in the COMPASS experiment, based on a Monte Carlo simulation, is summarized in figure 2.4. The fraction of reconstructible hadron tracks, dependent on the simulated momentum, is between 60 % and

---

[11] Here the silicon performance achieved for the 2004 hadron data is stated. With cryogenic detectors, even $4 - 11\,\mu\mathrm{m}$ and $1.4 - 1.8\,\mathrm{ns}$ can be reached, see section 6.3.

[12] Since 2008, also detectors with a pixel readout structure in the central region that can stand the beam are employed.

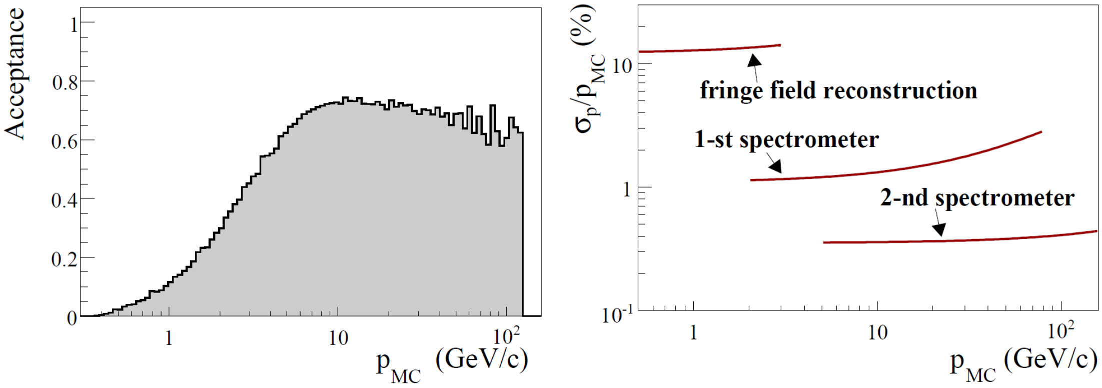

Figure 2.4: Reconstruction performance for charged tracks at COMPASS. Dependent on the particle momentum, the acceptance of the apparatus (left) and the momentum resolution for tracks reconstructed in the different spectrometer regions (right) are shown, from [COM07e].

80 % for most of the kinematic range and drops significantly only for particles with less than 10 GeV/*c*. The resolution of the momentum reconstruction is depicted dependent on the track momentum, but also distinguishing between the contributions of the different spectrometer parts. Slow particles that do not pass SM1 can still be reconstructed from their trajectory in the fringe field upstream of SM1. Tracks that are reconstructed using only information from the LAS have an accuracy of about 1 %, while a reconstruction from information of both spectrometer stages reaches a momentum resolution of 0.4 %. This performance allows for exclusive measurements of multi-particle final states over a wide kinematic range.

2.2.2.3 Particle Identification and Calorimetry

Particle identification in the spectrometer is provided by two types of detectors. The **RICH**[13] installed in the LAS has the task to distinguish between the nature of charged hadrons in the kinematic range[14] between 5 GeV/*c* and 43 GeV/*c*. For this purpose it is filled with C_4F_{10} as radiator gas. During the hadron run 2004 it was filled with nitrogen gas to reduce the radiation length, so that its information was not used in the data analysis. The RICH covers the whole angular acceptance of the LAS, except a dead zone of 10 cm diameter, which is separated from the radiator gas by a stainless steel tube and filled with helium to prevent interactions of unscattered beam particles (beam pipe). Two **muon filters** at the end of the two spectrometer stages consist of tracking detectors upstream and downstream of a massive absorber (60 cm of iron for the Muon Filter 1 in the LAS and 2.4 m of concrete for the Muon Filter 2, both with holes for the unscattered beam particles). Scattered particles can such be assumed to be muons if they are still detected downstream of this material, as hadrons would be stopped inside.

---

[13] Ring Imaging CHerenkov Detector

[14] With the new readout electronics in charge since 2006, the kinematic range was extended up to 60 GeV/*c*.

The energies of particles were measured in 2004 by two hadronic and one electromagnetic calorimeter[15]. The hadronic calorimeters **HCAL1** in the LAS and **HCAL2** in the SAS are installed in front of the muon filters. They consist of scintillator slices sandwiched between plates of iron or steel. The deposited energy is converted to light and transferred to photo multipliers. Their information can be used in the trigger system. The electromagnetic calorimeter **ECAL2** is placed in front of HCAL2. Electrons and photons create electromagnetic showers in the lead glass modules, and their Cherenkov light is collected by photo multipliers and proportional to the energy deposit. The ECAL2 is the most important detector in the Primakoff trigger for the polarizability measurement.

2.2.2.4 The 2004 Hadron Triggers and the Online Filter

Two types of physics triggers, aiming at the detection of Primakoff or diffractive events, were implemented for the 2004 hadron run. They have in common the beam trigger, the veto system and the beam killers. The beam trigger is activated, if a particle crosses two scintillator disks of 5 cm diameter which are placed several meters upstream of the target. The veto system rejects beam particles that do not pass the 4 cm hole of the veto dector centered at the beam axis, and consequently do not cross the target. Also the veto box surrounding the target and the sandwich detectors downstream of the target participated in the veto system. In addition, three plastic scintillators are placed along the spectrometer between SM2 and ECAL2, that are supposed to be hit by beam particles that did not interact in the target, and thus need to be rejected.

The conditions for the **Primakoff triggers** are fulfilled by a scattered pion in coincidence with a high-energetic photon detected in ECAL2. The *PRIM1* trigger required a hit in a hodoscope placed in front of ECAL2, by a pion with a momentum between $20\,\mathrm{GeV}/c$ and $110\,\mathrm{GeV}/c$, an energy deposit in ECAL2 of at least 50 GeV, and an energy deposit of at least 18 GeV in HCAL2 from the pion. This topology is sketched in figure 2.5, with the scattered pion in red, the high energetic photon in green, and a non-interacting beam particle hitting the beam killers drawn in black. The *PRIM2* trigger was sensitive to events with pion energies of less than 20 GeV. Thus the summed energy deposit in ECAL2 had to exceed 90 GeV. The overall Primakoff trigger rate was about $7 \cdot 10^4/\mathrm{spill}$ in 2004.

The **diffractive trigger** was aimed at events with several charged hadrons in the final state. Its main element was a multiplicity counter placed directly downstream of the target veto box. The scintillator disk featured a thickness of 3 mm and a diameter of 5 cm. The signal induced by traversing charged particles had to feature an energy deposit of at least 1.5 MIP, so that it could be assumed that at least two charged particles had crossed it. In addition, an energy deposit of several GeV in HCAL2 was required. Figure 2.5 depicts an event with three charged pions in the final state fulfilling the trigger condition (in green), and in addition a non-interacting beam particle in read. The diffractive trigger reached a typical rate of $2 \cdot 10^4/\mathrm{spill}$ in 2004.

---

[15] The second electromagnetic calorimeter in the LAS, ECAL1, was only operational from 2006 on.

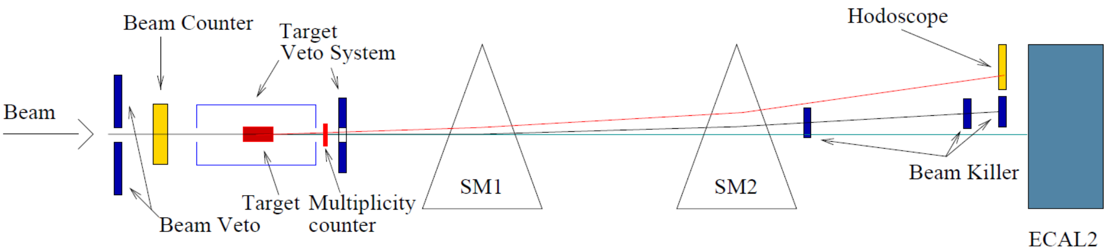

Figure 2.5: Schematic view of the 2004 Primakoff trigger elements, from [COM07e].

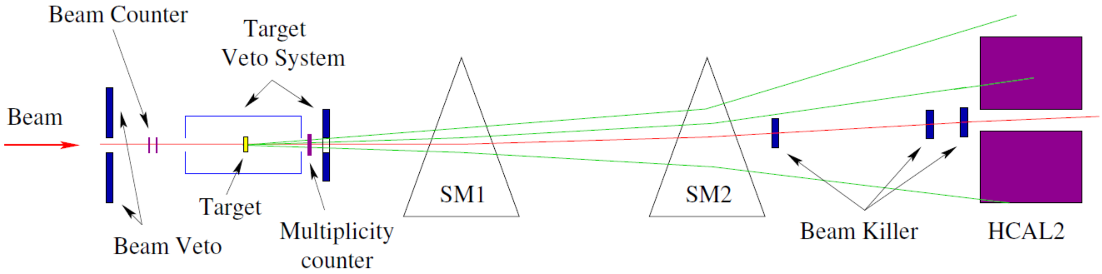

Figure 2.6: Schematic view of the 2004 diffractive trigger elements, from [Wei08a].

The **Online Filter** acted as a second level trigger in software for the diffractive trigger in 2004. It checked the data stream online for a minimum number of hits in the spectrometer silicon detectors before the data was written to disk. The number of hits in every single one of the twelve silicon planes was determined. To be insensitive to inefficiencies or noise, the four planes with the highest and the four planes with the lowest numbers of hits were discarded. The number of hits in the remaining four planes had to be larger than five so that the event was accepted by the filter. This procedure increased the probability of having more than one outgoing track reconstructed, so that the trigger selectivity was improved.

2.3 Reconstruction and Analysis Software

The software tools that are used in COMPASS for online monitoring, data reconstruction, the physics analysis and, last but not least, the simulation of the apparatus, are shortly introduced in this section.

2.3.1 The ROOT Framework

The object-oriented framework ROOT [Bru97, ROOT, ROOT09], written in C++ and developed at CERN, provides basic utilities and features particularly suited for the analysis of high-energy physics data. ROOT is able to handle huge amounts of data, with optimized procedures for input and output. Data storage is organized in objects called

`TTrees` which reduce the required disk space and allow the acces to the data on an event-by-event basis. Data is visualized and analyzed using ROOT's histogramming packages and its fitting routines, based on the MINUIT package. The COMPASS reconstruction and analysis software tools are linked to ROOT.

2.3.2 Online Monitoring with COOOL

The online monitoring program at COMPASS, COOOL, can be used to study basic detector performance already during data aquisition. It uses ROOT for the graphical user interface and histogramming of the detectors' properties. COOOL can produce `TTrees` containing histograms and/or data for a subsequent detector analysis. It provides also a simple tracking package, that is useful for detector studies if straight tracks can be assumed.

2.3.3 Data Reconstruction with CORAL

The event reconstruction software CORAL[16] [CORAL] performs all steps to get from the raw data to the full event information, i.e. particle tracks, vertices, calorimeter clusters and RICH probabilities. During the *decoding* of the raw data, the digitized signals from each detector channel are extracted. The *clustering* step groups neighbouring detector channels, and calculates the positions of the cluster in the main reference system of the apparatus. The found clusters are combined to particle trajectories within three steps. First, track segments are reconstructed in five different regions of the spectrometer (*pattern recognition*). These are connected to full tracks during the *bridging* step. Then the best track parameters and their corresponding error matrices are calculated by a *Kalman filter*. The *vertexing* algorithm performs the calculations of the primary interaction point of the beam particle and the decay point of neutral particles. In addition, CORAL performs the reconstruction of the energy deposit and cluster position of particles in the *calorimeters*. It also calculates probabilites for particles crossing the radiator gas of the *RICH* to be a proton, a kaon or a pion.

The reconstructed events are stored as `TTrees`. These mini Data Summary Trees (mDSTs) serve as the basis for all physics analyses. For detector analyses also special DST files containing the raw information of the detector type under investigation can be produced.

2.3.4 Physics Analysis with PHAST

PHAST[17] [PHA] provides the access to all important information contained in the mDSTs. This concerns both static information like magnetic field or detector geometric information, and the reconstructed tracks, particles, vertices, and calorimeter clusters for

---

[16] **CO**MPASS **R**econstruction and **A**na**L**ysis project

[17] **Ph**ysics **A**nalysis **S**oftware **T**ools

each event. The analysis is performed by user specific functions, which can output ROOT histograms, `TTrees` for the final analysis, or a filtered µDST file for further processing.

2.3.5 Simulations with COMGEANT

COMGEANT is used to simulate the performance of the COMPASS spectrometer. It is based on GEANT 3.21 [GEANT]. Generators for photon, lepton or hadron interactions can be linked to COMGEANT, but it can also handle files written separately by external generators. COMGEANT simulates the materials of the detectors, magnets, calorimeters, absorbers ect. in the experimental area. The interaction of the produced or scattered particles in the material are generated, the particles are tracked through the spectrometer, and the hit points of particles at the detectors are determined. The output files contain for each event a list of hits in detectors, i.e. positions and energy deposit. Those have to be modified by CORAL to look like or similar to the information coming from the detectors' readout electronics, before the data can be reconstructed.

Chapter 3

Silicon Detectors at COMPASS

Silicon detectors are widely used in modern high-energy physics experiments for the detection of charged particles[1]. Due to their excellent spatial resolution, achieved by microstrip or pixel readout structures on their surface, they are placed around the main interaction region, i.e. the collision region of collider experiments or the target region of fixed-target experiments, respectively.

The COMPASS experiment uses silicon microstrip detectors for beam definition, and, in the hadron setup, for optimized vertex reconstruction of smallest scattering angles. Their basic description concerning the hardware is given in this chapter. All enhancements related to the liquid nitrogen cooling, which had its long-term operation established in the course of this thesis, are described in chapter 4. A basic insight into the radiation impact to the COMPASS silicon detectors is presented in chapter 5. The performance of both warm and cold detectors is summarized in chapter 6.

The basic properties of silicon as a material for particle detection are introduced in section 3.1, including a short statement on the impact of radiation damages. The main requirements of silicon detectors in the COMPASS experiment are specified in section 3.2. Section 3.3 describes the detector module, which, apart from the sensor itself, also includes parts of the mechanical support structure, the readout electronics and cooling facilities. The integration of these modules into the COMPASS experiment, from both the logistic and the readout point of view, are given in section 3.4.

3.1 Basic Operation Principles

Silicon detectors used for particle detection usually consist of a p-n junction, which works as a diode. This is built by the passage of n-type material (with implanted donors, e.g. phospor) and p-type material (with implanted acceptors, e.g. boron). Typically, a bulk of several 100 µm of moderately doped material is combined with a thin layer in the order of 1 µm of highly, but contrarily, doped material, forming a, e.g., p^+-n junction. The free charge carriers, i.e. electrons and holes, are attracted to the respective opposite sides of the junction and recombine there, so that a region without any free charge carriers,

---

[1] Silicon detectors can also be used to detect low-energy photons, e.g. in avalanche photo diodes or silicon photo-multipliers, e.g for positron emission tomography. This aspect is not discussed here at all.

the *depletion zone* with an electric field inside, is created. This zone is asymmetric and extends deep into the bulk, due to the different concentrations of doping atoms. It can be enlarged up to the full thickness, i.e. the bulk can be fully depleted, by applying a *reverse bias voltage*.

The depletion zone is the region sensitive for particle detection. A charged particle crossing a semiconductor deposites energy[2], i.e. it creates pairs of electrons and holes[3], along its trajectory. Inside the depleted bulk, the electrons and holes are attracted to the correspondent electrodes by the bias voltage, and induce signals there which can be analyzed. To obtain the particle's position, the electrodes have to be structured in small pads or strips which are read out.

With high beam intensities the impact of *radiation damage* to the detector material becomes apparent[4]. Simply stated, the signal-to-noise ratio achievable with a detector becomes worse, until it does not deliver reliable signals any more. The cause is *Non-Ionizing Energy Loss* (NIEL), which means that lattice nuclei are displaced by incident particles and leave vacancies. Both, these nuclei and the vacancies, can generate additional lattice defects. As a result, the effective doping concentration changes, so that the detector can only be fully depleted with higher bias voltage. Defects can also form traps for the created charge carriers, so that those are lost before being transferred to the readout. This means the charge collection efficiency, i.e. the ratio between collected charge and generated charge, decreases. In addition, the resistivity of the silicon bulk decreases, causing higher leakage currents[5] and therefore higher noise.

Several concepts have been developed to operate silicon detectors in high radiation environment. The sensor geometry can be optimized to be less sensitive to radiation induced changes (see section 3.3.1 for an example). Suitable introduction of impurities (oxygen) into the detector material, called defect engineering, can also increase the radiation hardness. This goal is persued e.g. by the RD48 and RD50 collaborations [ROSE, RD50]. As a different ansatz, the operation of silicon detectors at cryogenic temperatures is supposed to recover the charge collection efficiency (see e.g. [Pal98]).

A more exhaustive overview of the principles and properties of silicon detectors, and radiation damages, can be found in [Wie04], for more details see the reference therein (especially [Pei92]), and [Spi05].

---

[2] In thin materials like silicon wafers of 300 μm thickness, the deposited energy of minimum ionizing particles (MIPs) follows a Landau distribution.

[3] For silicon, an energy of 3.6 eV is necessary to create one electron-hole pair.

[4] The number typically cited, for problems with particle detection in silicon detectors to appear, is 10^{14} neutron equivalents per cm^2. All damages are traditionally scaled to the impact of 1 MeV neutrons, often called *NIEL* as the underlying physics process causing the damages (see section 5.1 for estimations of the radiation exposure of the COMPASS detectors).

[5] Despite the diode being operated in reverse bias, a small leakage current is caused by thermal excitations of electron-hole pairs. This current increases with the applied bias voltage, and saturates when the detector is fully depleted.

3.2 Requirements for Silicon Detectors in COMPASS

The COMPASS experiment uses silicon microstrip detectors for beam definition in the beam telescope, and, in the hadron setup, for the reconstruction of particles scattered at comparatively small angles. Especially for spectroscopy and polarizability data, scattering angles in the order of 50 µrad have to be measured properly, requiring excellent spatial resolution in the order of 10 µm [COM12c]. Due to the high beam flux as stated in section 2.2.1, the detectors have to be able to stand a radiation impact in the order of $10^{14}\ NIEL/\mathrm{cm}^2$, making a radiation hard design desirable. In addition, measuring up to $2 \cdot 10^7$ beam particles per second on-spill[6], makes a time resolution in the order of a few nanoseconds necessary. The active area of the detectors needs to cover at least the beam size, which is typically $8 \times 8\,\mathrm{mm}^2$ for muon beam [COM07e] and $15 \times 10\,\mathrm{mm}^2$ for the wide hadron beams of 2008/9 and 2012 [COM12c]. During these hadron beam times, the detectors in the spectrometer have to cover the small-angle scattering area, where most of the detectors further downstream in the spectrometer have dead zones. For high-precision measurements, the material budget which is traversed by the relevant particles needs to be minimized to avoid multiple scattering as far as possible. This is not only true for the silicon sensors themselves, but also for the necessary infrastructure surrounding the sensor. This is traversed by beam halo particles, and in case of the spectrometer stations inside the conical cryostat (see sections 3.4 and 4.4), also by particles which pass outside of the active area of the silicons, but are still inside of the acceptance of larger trackers more downstream in the spectrometer.

3.3 Detector Modules

A silicon *detector module* denotes the assembly of the silicon *wafer*, i.e. the sensor, with its supporting infrastructure for parts of the readout electronics and cooling facilities. With this composition the fragile parts can be reasonably handled. First, the wafer design is summarized in the beginning of this section. Up to now, two slightly different types of detector modules have been used in the COMPASS experiment. The basic idea, i.e. the common design, is given here as well, while the special features of the enhanced type, being used since 2008, are described in section 4.1.

3.3.1 The Silicon Wafer

The silicon wafers used in COMPASS were originally designed for the HERA-B experiment by the Semiconductor Laboratory (HLL) of the Max-Planck-Institutes in Munich [Abt00]. A part of the wafers available was also produced at the HLL, while the others

---

[6] A SPS cyle consists of a period of a few seconds, during which beam is extracted for the T6 target ("on-spill"), with a following longer period, during which beam is extracted for other experiments ("off-spill"). Before 2007, a spill at COMPASS lasted 4.8 s during the 16.8 s of the SPS cycle, which changed to 9.8 s and ≈ 40 s, respectively, in 2007.

were produced at SINTEF [Sin] with a slightly different technology. The wafers feature double-sided readout, which reduces the material budget by a factor of two compared to single-sided designs. Furthermore, the correlations between the signals of the two readout sides, induced by the same traversing particle, can be exploited for improved data reconstruction [Lee11].

The wafer, with a total thickness of 300 µm, features an active area of $50 \times 70\,\mathrm{mm}^2$, with 1280 readout strips on the n-side, read out along the longer edge, with 54.6 µm pitch. Those are perpendicular to the 1024 readout strips on the p-side with 51.7 µm pitch, so that two-dimensional information (by two *projections*, i.e. coordinates) is provided by each sensor. The pitches have been found to be slightly different with the original HLL design, see table 3.1. The strips are tilted by 2.5 degrees with respect to the sensor edge, which was optimized for the geometry of the HERA-B vertex detector [Bau00], and delivers in total four projections if two equivalent detector modules are mounted back-to-back (see section 3.4.1). The charges collected on the respective strips can be accessed via bond pads, arranged in staggered groups of four pads, at one edge for each projection[7].

	Sensors from HLL		Sensors from SINTEF	
	n-side	p-side	n-side	p-side
pitch at 300 K [µm]	54.342	51.555	54.574	51.687
pitch at 200 K [µm]	54.316	51.530	54.548	51.662

Table 3.1: List of pitches for wafers from HLL and SINTEF design, as measured exemplarily at 300 K, and thereof calculated for 200 K, by [Fri11].

The wafer was designed to stand high particle fluxes (up to $3 \cdot 10^{14}$ minimum ionising particles (MIP) per cm^2), and proven to cope with the induced radiation damages [Bau02]. Depletion voltages of up to[8] 250 V are applicable. This is achieved by a multi-guard ring structure of p$^+$ implanted rings around the wafer, which allows for gradual drops of the bias voltage to the bulk level. The bias voltage is applied via a bias ring, connected to the strips via 1 MΩ polysilicon resistors. Typical bias voltages at COMPASS are in the order of $40 - 200$ V.

The wafer is based on 280 µm of n-type silicon crystal, with a resistivity of $2 - 3$ kΩcm. On n-side and p-side, n$^+$ and p$^+$ implanted strips, respectively, form the p-n junction. These strips are covered with an insulating layer of silicon oxide, and with silicon nitride, and have the aluminum readout strips on top, see figure 3.1. This means, the readout is achieved via capacitive coupling, which is preferable when leakage currents caused by radiation damages occur. The n$^+$ strips have to be insulated from each other to avoid shorts with the n-type bulk. This can be either achieved by p-stop technology (as done at SINTEF and shown in figure 3.1), or p-spray technology (as originally foreseen by, and

---

[7] At the p-side, the shorter tilted channels, which do not reach the "main readout edge", can be accessed by bond pads on the opposing edge. Those strips are not connected and read out at COMPASS.

[8] For wafers produced at SINTEF up to 500 V.

produced at, HLL). The p-spray technology is more difficult, but allows to have intermediate strips, which improve the spatial resolution by charge sharing with the neigboring strips via capacitive coupling. The p-sides feature intermediate strips at both wafer designs.

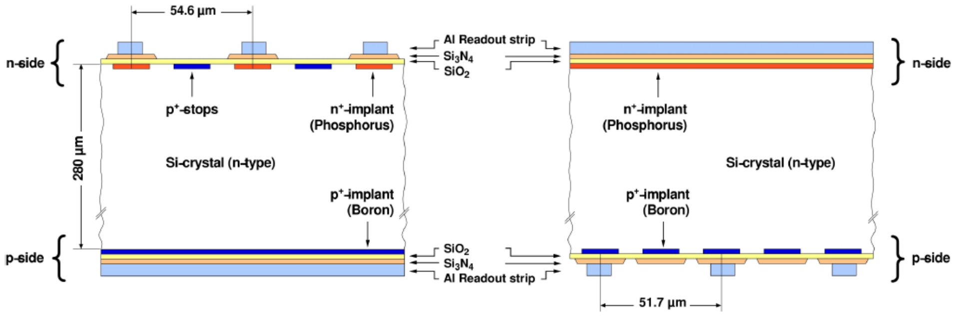

Figure 3.1: Cross-section through a silicon wafer of the SINTEF design, from [Lee11].

3.3.2 Basic Layout of the Modules

The silicon sensor is sandwiched between two L-shaped 6-layer Printed Circuit Boards (PCBs), called *L-Boards*, which keep the sensor reliably in place. As the modules were planned from the beginning on to be operated at cryogenic temperatures, the sensor is attached with the silicone glue NEE001 [NEE], which features a very small electrical conductance [Abt98], and is supposed to be comparatively elastic when it becomes cold. The L-Boards house the APV readout chips with all necessary infrastructure (see section 3.4.2.1). As each APV chip is able to handle 128 readout channels, 10 chips are connected to the n-side and 8 chips to the p-side of the sensor, respectively, alongside the bonding pads of the sensor. Also the *pitch adapter* is glued to it, which translates the pitch of the sensor readout strips to the pitch of the APV input. It consists of thin aluminum wires on glass or ceramic substrate. The connections from the readout strips at the wafer to the pitch adapter, as well as from the pitch adapter to the APV input, and the APV to the respective pads at the L-Boards, are made by bonds, i.e. thin aluminum wires. Thus[9] the electronics ground of each L-Board, and also the ground of the subsequent electronics, is given by the potential of the bias voltage of the wafer side whose data it processes. This makes floating power supplies, i.e. without external grounding, necessary. A HV capacitor, soldered directly on the L-Boards between the two bias potentials, decreases the common-mode noise picked up by the floating power lines of the readout electronics.

Along the two sides of the wafer, where the readout is connected, a capillary is soldered on the backside of the PCB (see figure 3.2), which directs the nitrogen for cooling. In case of warm operation with gaseous nitrogen at room temperature, just the APV chips are

---

[9] As the readout strips at the wafer couple capacitively to the n^+ or p^+ implants which make the p-n junction, they could be on any potential, and such also the readout electronics. In order to avoid potential problems with breakthroughs, the readout strips were still put on the same potential as the implants they couple to.

cooled by a constant gas flow such that the temperatures close to the APVs do usually not exceed 60 °C. With liquid nitrogen for cryogenic operation, both the silicon wafer and the APVs are cooled in a controlled way, and the nitrogen fulfills its task of thermally decoupling the wafer from the power dissipated by the APVs. Each detector module is cooled by one cooling line only, which means, the capillaries of the two detector sides are connected via a custom built *epoxy connector*. This connector insulates the capillaries from each other electrically, which is important as those can accidentally be connected to the electronics ground of the respective L-Board.

A detector module contains also four Pt100 temperature sensors, of which one is glued to the wafer, and three are glued to various places at the L-Boards. With cryogenic operation, the values read out by these temperature sensors are elementary for the flow adjustment by the temperature regulation system, and an important input to the safety system (see section 4.5).

The detector modules operated in the warm mode during the first years (i.e. from 2001 to 2007, partly still in 2008) have been described and analyzed in detail mainly by [Wie04, Din10]. They are uniquely named like `SIL xx`, with `xx` sequential numbers. These modules were all equipped with SINTEF sensors. An example is pictured in figure 3.3, showing also the white ERNI connectors in which the cables transporting all electric signals are plugged. The extended detector modules (see section 4.1) operated partly in 2008, and exclusively from 2009 on in the cryogenic mode, are instead named like `SI 1.xx` (2008 production, with HLL sensors) and `SI 2.xx` (2009 production, with SINTEF sensors). They have been built at `HighTec` [HiT].

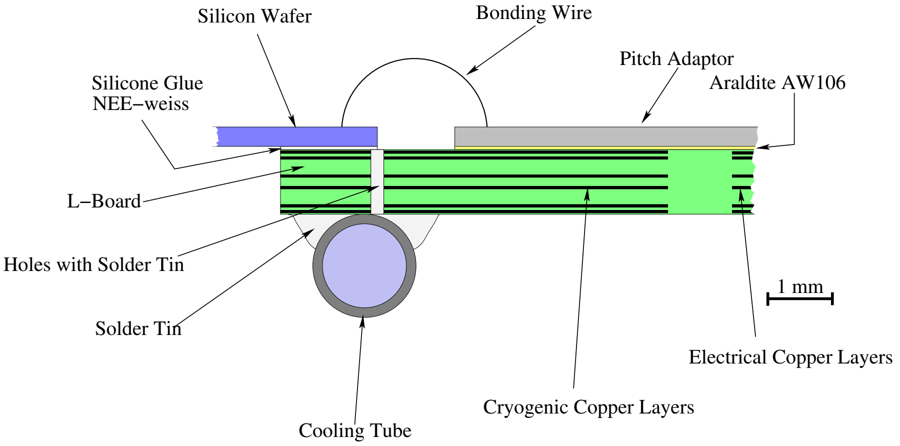

Figure 3.2: Schematic cross-section through a L-Board with silicon wafer and capillary attached, from [Wie04].

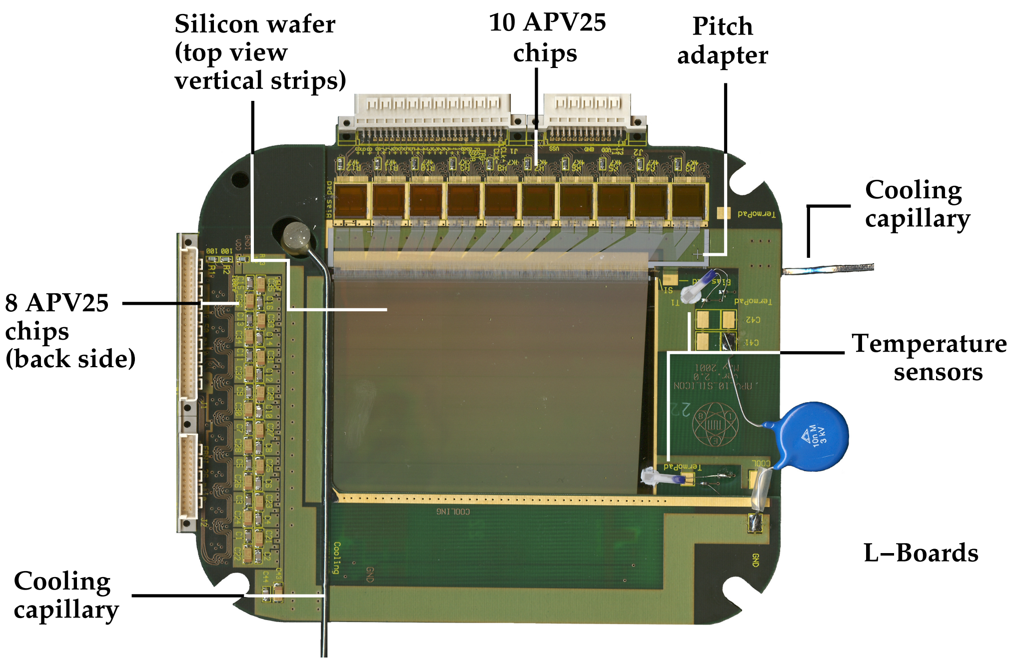

Figure 3.3: A COMPASS silicon detector module, as used in warm operation, from [Din10].

3.4 Integration into the COMPASS environment

The silicon detector modules described in the previous section have to be integrated in the COMPASS experiment. The logistic integration is achieved by arranging two detector modules into a *silicon station* and placing this station in the experimental area, as summarized in section 3.4.1. The information from particles traversing the silicon sensors is processed by the frontend electronics and the readout chain, as summarized in section 3.4.2, before it reaches the COMPASS DAQ system and participates in the formed events.

3.4.1 The Silicon Detector Stations

Each silicon station contains two detector modules, which are mounted back-to-back with a distance of 1 cm. As the readout strips on the sensors have an angle of 2.5 degrees with respect to the sensor edges, each station delivers information from four projections of a traversing particle. The right-handed COMPASS main reference system has its z axis in beam direction, the x axis pointing from the Jura to the Saleve side in the experimental hall, and the y axis from the ground to the ceiling. The two silicon modules are mounted with an additional overall angle of 2.5 degrees, and are arranged such, that they measure the X coordinate with n-side readout along the x axis, i.e. at 0 degrees w.r.t. it. Y is measured with p-side readout along the y axis, i.e. at 90 degrees, U with n-side readout at 5 degrees, and V with p-side readout at -85 degrees (see figure 3.4 for a scheme of the detector geometry). Thereby the XY detector module is placed downstream of the UV module, so that in z direction, the order of measured projections is U, V, Y, and X.

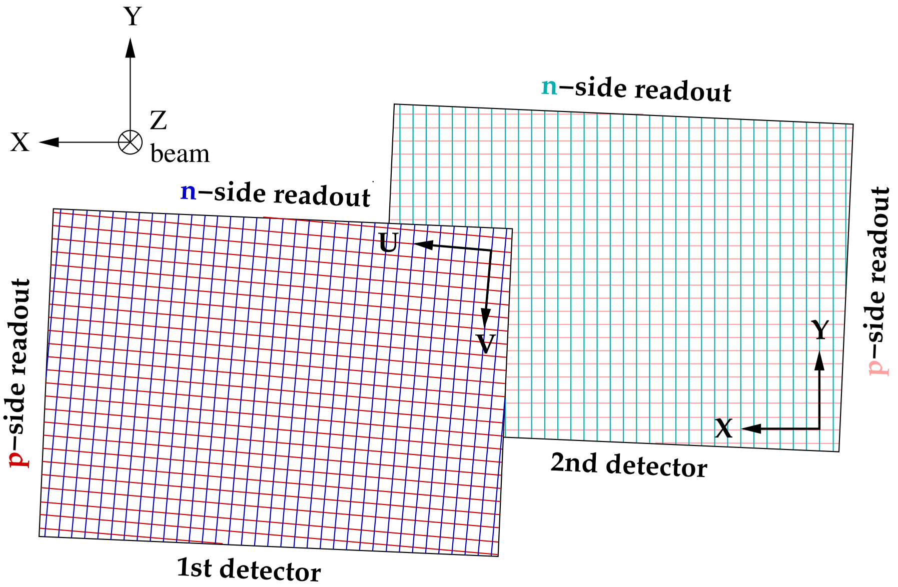

Figure 3.4: Scheme of the geometry of two silicon detector modules forming one silicon station, adapted from [Din10].

Each silicon station placed in the experimental area is identified by a name like `SI01`, `SI02`, ... Its projections are named like `SI01U` and modules like `SI01UV`. Up to and including 2012, the COMPASS experiment has been using typically three silicon stations during muon data taking and five silicon stations during hadron data taking. The modules mounted at the respective places may change from one beam time to another. For detailed lists which modules were installed when and where, see [Din10] up to and including 2006, and tables A.1 and A.2 for the COMPASS beam times 2007 – 2012.

During operation, the silicon detectors have to be placed inside light-tight and electrically shielded boxes, which provide the necessary cooling infrastructure as well as electrical feedthroughs for power lines and readout. The area traversed by the beam (or scattered) particles has to feature low material budget, so that windows with aluminized mylar foils are mounted here. The modules have to be mounted with respect to each other and inside these boxes with high precision, which is achieved by suitable support structures[10] made from glass-fiber or carbon-fiber. The boxes are placed on suitable mounting structures in the experimental area. As cryogenic operation of the silicons was intended from the beginning, already the first warm detectors were placed inside so-called cryostats made from stainless steel and prepared for evacuation (see [Din10] and references therein for details on that kind of setup). The two types of cryostats used from 2008 on are described in more detail in sections 4.3 and 4.4.

The arrangements of silicon stations inside the COMPASS experiment depend on the

---

[10] These support structures themselves are attached to precision mounting points inside the boxes.

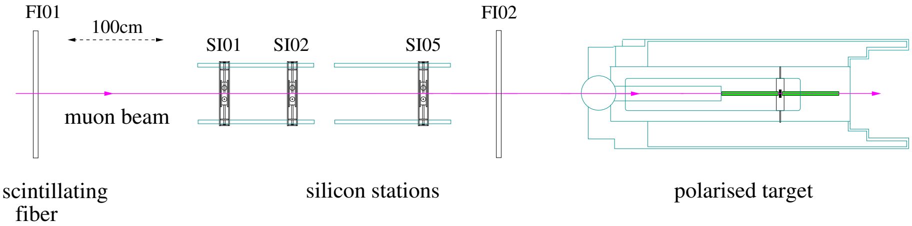

Figure 3.5: Silicon stations in the muon setup, with the specific names used in the 2004 muon setup, from [Din10]

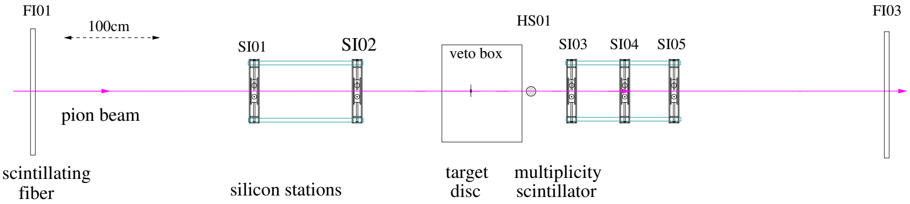

Figure 3.6: Silicon stations in the 2004 hadron setup, from [Din10]

investigated physics programme:

- During muon runs, just three stations in the beam telescope are used as sketched in figure 3.5. They are placed inside independent cryostats, the so-called *beam station cryostats*. These are placed on top of optical benches, which allow for precision placement of the cryostats in all three dimensions better than 0.5 mm, i.e. in the order of the surveying precision. The benches are placed on top of concrete blocks, to reach the beam position[11].

- During the hadron run 2004, only two beam stations were used, but three spectrometer stations downstream of the target were installed. Also the latter were placed in the same kind of independent crysostat on an optical bench as the beam stations, as shown in figure 3.6.

- In the hadron runs 2008, 2009, and 2012, three beam stations were installed as depicted in figure 3.7. The target area was governed by the recoil proton detector (RPD) surrounding the liquid hydroden target, or solid-state nuclear targets mounted accordingly, see figure 3.8. This setup left only limited space, inside the acceptance of other detectors further downstream, for silicon spectrometer stations. A dedicated *conical cryostat* (see section 4.4) was constructed to adapt to these conditions. It housed the silicon stations `SI04` and `SI05`.

---

[11] The nominal COMPASS beam position is 3152 mm above the nominal floor height. The floor just upstream of the place of the silicon beam station, where this height can be measured, is 7 mm below its nominal level.

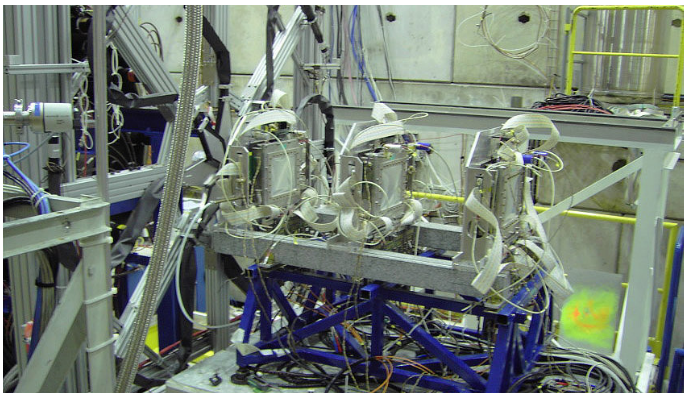

Figure 3.7: Warm beam stations in the COMPASS area in 2008. The beam comes from the right.

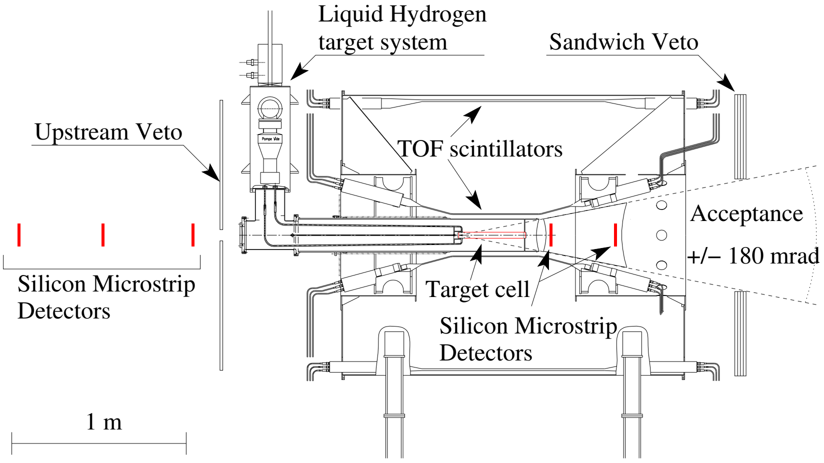

Figure 3.8: Scheme of the target region for 2008/9 and 2012 data taking, from [COM07a]. The beam enters from the left side. The silicon stations are indicated by vertical red lines; each line refers to the two modules of one station.

3.4.2 Electronics and Readout Chain

When a particle traverses a biased silicon sensor, the created charges are transferred via the adjacent readout strip(s) of both sensor sides to the analog input of the AVP25 readout chips. There these signals are shaped, preamplified, buffered and sent out via the repeater card, the ADC card, and the GeSiCA to the DAQ system, upon request by the trigger system. The most relevant points of the electronics and the readout chain are given in the following. For more details see e.g. [Wie04] and references therein.

3.4.2.1 The Frontend Chip APV25 and the *L-Board*

The APV25 is an analog pipeline ASIC[12] originally developed for the readout of the silicon detectors used in the CMS experiment [APV01]. Its main features are comparatively low noise, low power consumption, high circuit density, and high radiation hardness, which make it well suitable for the COMPASS silicon detectors.

One chip provides 128 input channels[13]. Each of those provides a low-noise CR-RC type shaping amplifier, which integrates the arriving analog signals and forms well defined voltage pulses from them. The APV chip samples the signals persistently with 38.88 MHz, which is the frequency of the reference clock of the Trigger Control System (TCS) at COMPASS. For each input channel, the samples are stored inside successive cells of an analogue ring buffer. The pipeline depth of 192 cells allows for a trigger latency of up to 4 µs. 32 cells are reserved for buffering events awaiting readout. On request of an external trigger, a pre-determined column (referring to all input channels) in this pipeline is marked and not overwritten until their readout of FIFO[14] type is completed. Then the data are internally multiplexed and sent out as one differential output line for each trigger.

The configurable settings of the APV25 are controlled via digital registers which are set via an I^2C compatible protocol. Each chip can be addressed individually by a 5 bit address[15]. The most important settings to be adjusted are the latency, the baseline (zero line), the mode, the polarity of the expected signal, and settings managing the shaper and the preamplifier, i.e. the signal shape.

The APV25 chips used in COMPASS are operated in *Multi Mode*. This means that for each trigger three consecutive pipeline columns are read out. These three samples contain information on the pulse shape, from which precise time information can be extracted as explained in section 6.1.

At the COMPASS silicon detectors, the APV25 chips are glued and bonded to the respective *L-Boards*. These are 6-layer PCBs[16] which provide all necessary infrastructure for the operation of the APVs, like power distribution, configuration bus, clock, trigger, and analog data transmission. The APVs are glued with a conductive glue to big power pads on the negative APV bias level. This grounding, as well as capacitors mounted between the power lines on the backside of the boards just below the chips, are substantial, as the APVs are very sensitive to noise on the power lines. In addition, the boards also serve the pads for the silicon bias voltage, the temperature readout of the detector modules, and the soldering lines for the cooling capillaries.

---

[12] Application Specific Integrated Circuit

[13] of which each is connected to one detector readout channel, i.e. one readout strip in case of the COMPASS silicon detectors

[14] First In - First Out: Data are processed in the order of their arrival.

[15] 5 address pads are provided on each chip, whose bits can be set by pulling the respective pad to the negative supply voltage.

[16] Printed Circuit Boards with 6 layers of conductive material between insulating material, e.g. copper between glass fiber.

3.4.2.2 The Repeater Card

Each L-Board is connected via cable and electrical feedthrough to a *Repeater Card* which is directly plugged into the feedthrough outside of the cryostat. This card forwards and refreshes all signals going to the APVs (trigger, clock, I^2C) and provides the necessary APV power of ±1.3 V, formed by voltage regulators from ±3.3 V applied. The analog differential output signals of the APVs are amplified by high-speed operational amplifiers before being transferred to the ADC via a flat cable. In addition, the two wires of each temperature sensor are splitted to allow four-wire measurements, and then guided out to the temperature monitoring and control system via a separate cable.

3.4.2.3 The ADC

The digitization of the analog signals is performed by `sg_ADC`s[17] with 10 bit precision. Two programmable FPGA[18] chips process the data online. During physics data taking, they operate in *sparse mode*[19]. Here the *zero suppression* algorithm filters the data to transfer only signals from channels featuring amplitudes significantly above a certain predefined noise level, compared to the *pedestal* value of each channel, to reduce the amount of data transferred to the DAQ. It corrects also for *common mode noise*, which means simultaneous fluctations of all channels of one APV. A detailed description of these algorithms can be found in [Gru01].

3.4.2.4 The GeSiCA

The GeSiCA[20] receives the data from the four ADCs of one silicon station via optical fibers, which electrically decouple the GeSiCA from the readout electronics potentials. Here the data is multiplexed into one serial data stream for each silicon station, with event headers added, before being sent via an optical S-Link to the DAQ system. The GeSiCA also distributes the TCS clock and trigger and reset signals to its connected ADCs, and provides an interface for the configuration of ADCs and APVs via I^2C.

---

[17] Silicon and GEM Analog to Digital Converters, a common development for both detector types. As one card is able to handle a maximum of 12 APVs, each silicon projection is connected to a dedicated ADC card.

[18] Field Programmable Gate Array

[19] In the other mode, called *latchall mode*, all three samples from all 128 channels of each APV are transferred to the DAQ. This kind of data is useful for commissioning and calibration issues, e.g. for the creating the *pedestals*, containing the baseline (often called pedestals itself) and the common-mode corrected noise for each channel. Those are needed by the zero suppression algorithm.

[20] GEM and Silicon Control and Acquisition

Chapter 4

Cryogenic Operation of Silicon Detectors

Historically, the idea to operate the COMPASS silicon detectors at cryogenic temperatures, was triggered by the discovery of the *Lazarus effect*. It was claimed, that the charge collection efficiency of severely irradiated (up to $5 \cdot 10^{14}\ NIEL/\mathrm{cm}^2$) silicon detectors could be recovered with cryogenic operation, with a recovery maximum at a sensor temperature of 130 K [Bor00b, Bor00a]. A comparable amount of radiation impact was forseen to be collected for a silicon detector within one COMPASS hadron beam time (see section 5.1). Thus, the lifetime of the detectors was a crucial topic, and was planned to be significantly increased by cryogenic operation.

The COMPASS silicon detectors were foreseen for cryogenic operation with wafer temperatures of 130 K from the beginning on. As the amount of material close to the beam, i.e. also close to the detectors, needs to be kept low, the implementation of cold heads or similar was not an option. The cryogenic temperatures were planned to be achieved by the evaporation of liquid nitrogen, which is guided through capillaries arranged next to the sensor, in a way, that also the power dissipated by the APV chips (up to 8 watts per detector module) is absorbed. The liquid nitrogen is provided by a central dewar at CERN, and guided via distribution boxes, transfer lines, and then the capillaries to the detectors, where it evaporates. The properties of the APV25 readout chips at cryogenic temperatures have been determined, and the suitability of the components (especially the glues) used for the assembly of the detector modules have been tested [dMa04]. The cryostats for the beam stations have been introduced [Wie04], with improved vacuum-tight windows [Fuc03]. A liquid nitrogen distribution system has been developed [dMa04, Bec04, See04]. A first silicon station could be operated at 130 K in the COMPASS area, still with the laboratory setup for the liquid nitrogen cooling, for a couple of days already in 2003 [Fuc03].

Still, several bottlenecks in the complete setup prevented an established long-term operation of the cryogenic silicon detectors. The different thermal expansion coefficients of the components of the detector module caused significant mechanical stress when the modules where cooled down, so that several silicon sensors cracked [Bec04]. For about half of the data collected in 2003, a high noise level was visible, which suggested that the APVs reached their limit of smooth operation and started to oscillate [Fuc03]. Problems with the vacuum inside the cryostat and the long-term temperature stability (corresponding to problems with the supply of liquid nitrogen) complete this list. Thus, several modifications of various parts of the setup had to be carried out, before the all five silicon stations in COMPASS could be operated continuously with liquid nitrogen cooling, still at 200 K, in 2009.

The current cryogenic[1] silicon setup, as being used in the COMPASS experiment since 2009, is summarized in this chapter. The implemented modifications with respect to previous setups are given in more detail. The changes to the detector modules, mainly supposed to relax the impact of the different thermal expansion coefficients, are explained in section 4.1. An important piece which improves the cooling stability is the phase separator, as depicted in section 4.2. The features of the cryostats are exemplarily given for the beam station cryostats in section 4.3, and the peculiarities of the conical cryostat in section 4.4. The cooling regulation and safety system has been completely revised, see section 4.5. Some relevant features of the operation of cold APVs are summarized in section 4.6.

4.1 New Adaptions for Detector Modules

The basic layout of the silicon detector modules has been described in section 3.3.2. The dominating components have significantly different thermal expansion coefficients. While silicon features $3 \cdot 10^{-6}/\mathrm{K}$, PCB has $20 \cdot 10^{-6}/\mathrm{K}$, the capillary about $15 \cdot 10^{-6}/\mathrm{K}$, glass about $3.3 \cdot 10^{-6}/\mathrm{K}$, and ceramics (aluminumoxide) $6.5 \cdot 10^{-6}/\mathrm{K}$. The latter two are candidates for the material of pitch adapters. Obviously, the thermal expansion coefficient of glass matches better the one of silicon, while the one of ceramics instead matches better the one of PCB. Ceramics also has a higher thermal conductivity, and is less stiff than glass[2]. The pitch adapters of the new modules were made of ceramics nevertheless, as the aluminum wires can be applied to the ceramics subtrate in a more reliable way, so that also bonding becomes more reliable.

As mentioned already in section 3.3.2, the silicone glue NEE001 is expected to stay flexible also at low temperatures. Still, e.g. the long side of the PCB housing the 10 APVs, which is 13 cm long, shrinks about 0.3 mm, which imposes significant mechanical stress to the silicon sensor glued to it, having caused several ones of them to crack. Due to time constraints, the development of a substitution of the current L-Boards, by a more suitable material like ceramics or carbon-fiber reinforced plastic, was not possible for the detector modules currently used.

As a first measure, the silicon wafer is glued only on its two readout sides to the PCBs,

---

[1] The full system is designed for the operation at 130 K. For this reason, the denotation “cryogenic” is kept throughout this thesis, despite the present operation temperature of 200 K would be denoted more correctly with “cold” or “quasi-cryogenic”.

[2] A test sample of PCB with a pitch adapter of ceramics bent more than a sample with a pitch adapter of glass, when put into a liquid nitrogen bath, though one expects the opposite behaviour from the differences in thermal expansion coefficients.

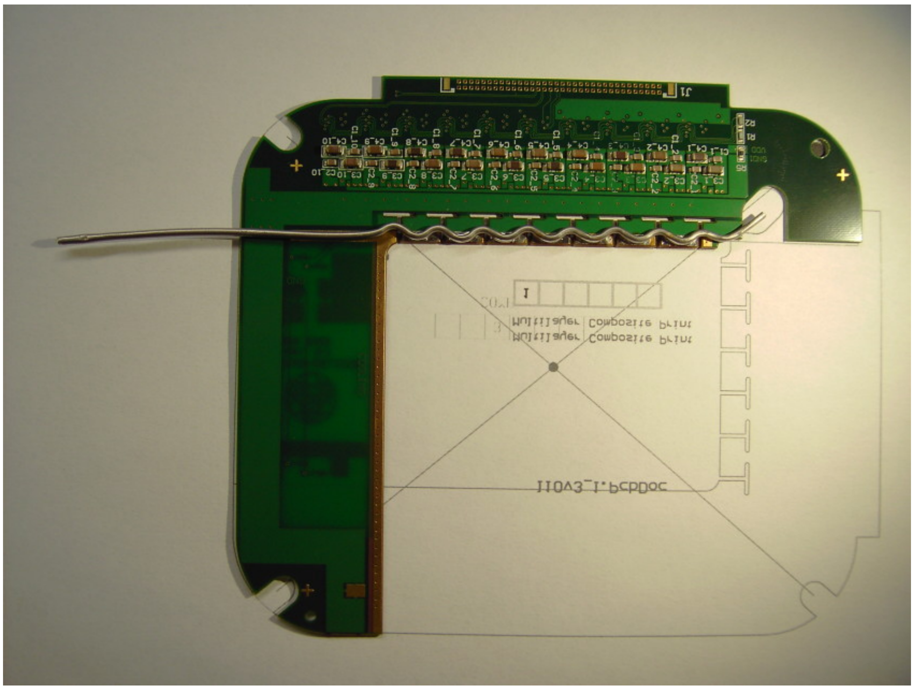

Figure 4.1: L-Board of the 10-side readout, with T-cuts milled and the curled capillary soldered.

instead of all four edges. Furthermore, the PCBs are locally cut such, that pads of about $9 \times 6\,\mathrm{mm}^2$, which are still connected to the main piece, result along the edge, where the silicon wafer is glued (see figure 4.1). These T-shaped cuts allow the PCB to shrink most locally at the place, where it becomes coldest, so that the most severe mechanical stress is distributed to several places and cannot accumulate any more. The cuts have to be milled carefully, as they are applied in a region of the board, which has both a cooling copper layer and a copper layer of the electronics ground underneath, which must not be connected electrically[3].

As a consequence of these cuts, the capillary supplying the liquid nitrogen cannot be directly soldered along the edge any more. It features an outer diameter of 1.6 mm, with a wall thickness of only 0.15 mm. The material, a copper-nickel alloy called *Monel400*, is stable but extremely flexible. Thus, the capillary can be bent to a wavy structure with radii below 5 mm without breaking. It also does not close inside, if the bending procedure is carried out in a liquid nitrogen environment. The curled capillary is soldered to the PCB with every second curve onto the cooling rail at the matching pad, as depicted in figure 4.1. The bendings turned out to have also a positive impact on the cooling stability, as the more turbulent nitrogen flow improves the heat transfer between the wall and the gas-fluid nitrogen mixture.

---

[3] For every milled board, it has been checked, that there are no breakthroughs between the APV ground and the cooling ground (tested at the cooling rails of each pad), when 900 V are applied, which exceeds the worst-case scenario by a factor of 2.

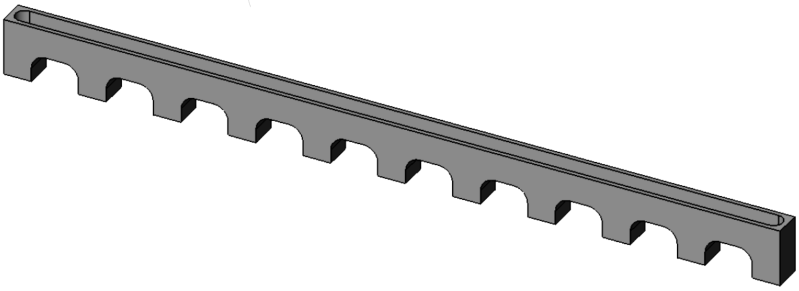

Figure 4.2: Model of the stabilization bridge.

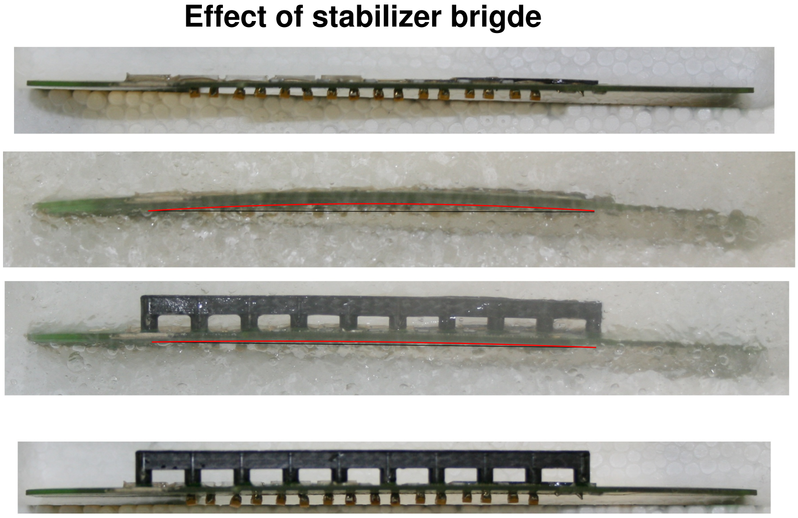

Figure 4.3: Impact of a stabilization bridge to the stability of a PCB in liquid nitrogen bath (present at the two central photos; see text for explanations).

The temperature sensors, of the type[4] Pt100, are glued to the silicon sensor or the PCB, respectively, with the silicone glue instead of standard heat conductive paste, which was found to perish when it becomes cold. For the same reason, the previously used two-component conductive glue for gluing the APVs was replaced by a version suggested by `HighTec`.

As some of the detector modules are installed in the conical cryostat, and such all their material is placed inside the acceptance of detectors further downstream in the spectrometer, the material budget had to be reduced wherever possible. The 10 µF tantal capacitors below the APV chips have been replaced by equal ceramic capacitors. Another huge amount of material was present with the ERNI connectors (see figure 3.3), in which the cables transferring the electric signals were plugged. The pins of these connectors were even covered with a gold surface. These connectors were abolished, and flexible cables were directly soldered to the respective connection holes in the PCBs, with a minimized amount of solder tin.

---

[4] Platin sensors with a resitivity of 100 Ω at 0 °, which change their resistance reliably with temperature.

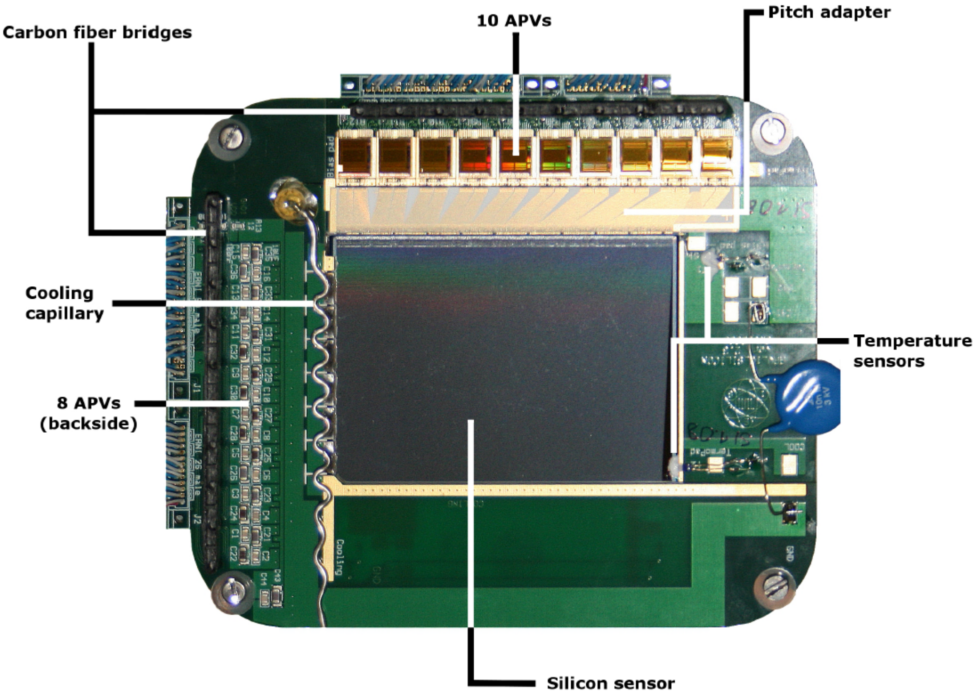

Figure 4.4: A silicon detector module as used for the operation at 200 K, from [Bic11]. The soldered cables of the electronic signals are cut from the picture for a clearer arrangement.

Still, the rigid ERNI connectors had had a mechanical stabilizing effect to the cold PCBs. In other words, despite the T-cuts, the PCBs became still cold enough to bend, which caused a silicon wafer to crack[5]. This triggered the development of a custom-made *stabilization bridge* made from a carbon-fiber reinforced polymer, which provides maximum stability with a minimum of material involved. A model of this brigde-like structure is depicted in figure 4.2. Its stabilizing effect to a PCB, which has been put into a liquid nitrogen bath for a worst-case stress test, is demonstrated in figure 4.3: The two upper photos show a piece of PCB, before and inside the nitrogen bath. The red line on the second picture illustrates the surface of the PCB, while the black line is drawn straight. The same piece of PCB, now with a stabilization bridge glued to it, is again shown in the lower two photos, inside and outside the nitrogen bath. The red line, i.e. the surface of the PCB, is significantly less bent now. The bridges are glued to the PCBs, just next to the place where the connectors had been before, as shown in figure 4.4, which depicts an example of the actually used modules.

4.2 The Phase Separator

As the nitrogen flow through the transfer lines to the stations is comparatively low, the nitrogen stays inside there for some time and collects heat input, so that a part of the

---

[5] This incident with `SI 1.03` (see section A.1.2) contributed also to the decision to operate the silicon detectors only at 200 K.

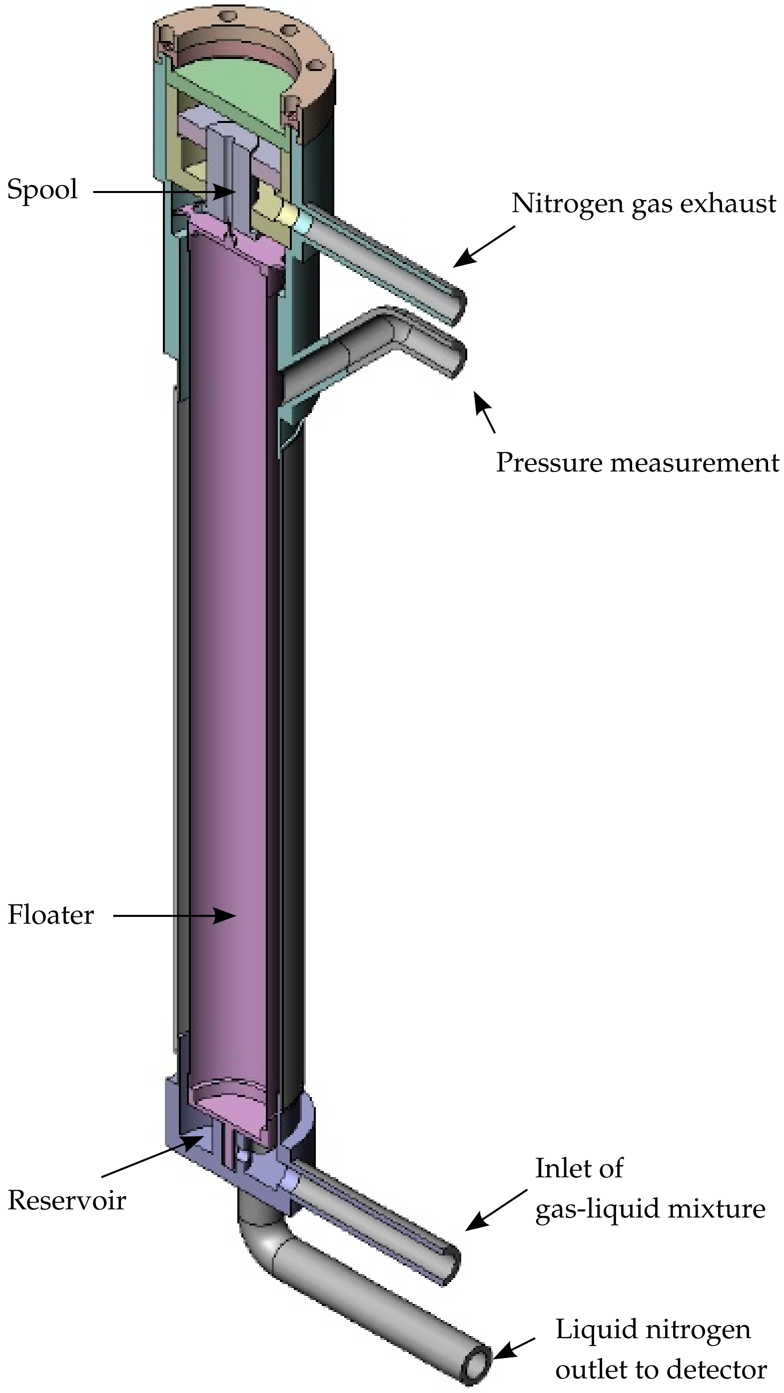

Figure 4.5: Cutaway view drawing of the phase separator.

nitrogen evaporates already inside the transfer line. This gaseous part of the nitrogen, arriving at the cooling capillary, was found to make the cooling instable (or even unfeasible) on a timescale longer than a couple of hours. Thus, the gaseous part has to be separated from the pure liquid nitrogen just before that enters the capillary at the detector module. This process is carried out by a device called *phase separator*.

A model of the version currently used in the COMPASS experiment is shown as cutaway view in figure 4.5. It is a cylindric device, made from stainless steel, with an inlet for the nitrogen supplied, two outlets which connect to the detectors, one outlet which connects to the gas exhaust, and one outlet forseen for a pressure measurement. Its main feature is a mechanical valve that releases accumulated nitrogen gas through the exhaust in a controlled way. The valve consists of a spool made from brass, which can move up and down, has a cylindrical hole in the middle, grooves along the outer wall, and a flange with larger diameter on top. A spring applies an upward force to the spool in static conditions. Most of the volume is taken by a light floater, a cylinder with a thin wall of stainless steel which is welded up, and is stably guided inside the main volume by a small rod at its bottom, a thin rim with holes surrounding the top level, and a needle-like rod on top, that matches the hole in the spool when the floater is lifted up. Due to manufacturing contraints, the full device is closed on top by a plate and a fixation rim which is screwed, and glue is applied to make the device tight.

When the first nitrogen arrives through the inlet, the floater is in the bottom position as drawn. The hole in the spool is open, so that nitrogen gas goes through, and equal pressure in the top and bottom parts of the phase separator develops. As the gas pressure on top effects the larger flange of the spool, a net force arises which presses the spool downwards, so that the gas can flow through the grooves and leave the system at the exhaust. When liquid gathers in the bottom of the phase separator, its rising level lifts the floater upwards, until the hole in the spool is closed. The gas pressure in the top part decreases, as the gas still exhausts, until the pressure in the bottom part is sufficient to lift the spool and such close the valve. The system is designed to work with a pressure difference of 200 mbar between the nitrogen inlet (at 1800 mbar absolute pressure) and the gas exhaust (to be kept at 1600 mbar).

This type of the phase separator made a successful long-term cooling operation in the COMPASS experiment possible at all. Still, during both the commissioning and the operation, several constraints of this system were found. The pressure at the gas outlet is supposed to be kept at its design value of 1600 mbar with the help of a flowmeter, which reacts on the pressure currently measured inside the outlet tube. But the pressure inside the phase separator was found to change quite rapidly and with higher oscillation values than those arriving at the distant pressure sensor, so that the regulation parameters of the control system (see section 4.5) are delicate to obtain and individual for each single device. It happened e.g that a measured pressure at the outlet went such low, that the floater got stuck in the spool and the valve closed, so that the detectors finally warmed up. A special algorithm in the control program was finally introduced to cope with such a scenario. The phase separator of `SI03` is even operated most stably with a constant gas flow. Also leak tightness became an issue for some phase separators after some time of operation. Especially the seals on top, which are achieved with the help of glue, are prone to leaks and especially cold leaks, which are hard to identify and repair.

A revised version of the phase separator has been developed [Bic11], which abolishes the floater and the valve. It consists of a reservoir and several Pt100 sensors at different heights, which measure the filling level of the reservoir, so that the filling can be steered by opening the gas exhaust flowmeter dependent on this level. The first phase separator of this type has been installed in the cryostat of `SI02`, replacing a leaky predecessor, before the 2011 beam time and works highly satisfactorily.

4.3 The Beam Station Cryostat

For the operation with liquid nitrogen, the silicon detectors have to be placed inside a suitable cryostat. First of all, this cryostat must provide an insulation vacuum to prevent icing on the cold surfaces which could potentially destroy the detector, and for the thermal shielding of the cold equipment. Typical operation values for this vacuum are in the order of $10^{-5} - 10^{-4}$ mbar for a fully equipped cryostat, so that an empty cryostat has to reach about 10^{-6} mbar. Furthermore, the cryostat has to be light-tight and provide electric shielding.

A model of the beam station cryostat, without connected cables and pipes, but including the plates for the fixation to the optical bench, is shown in figure 4.6. The body of a beam station cryostat, made from stainless steel, faces the beam with an inner surface of 240 mm × 240 mm, with a depth of 82 mm. This facing surface is completely covered by a beam window on both the upstream and the downstream end of the cryostat. This window needs to feature as low material budget as possible in the inner area, while fulfilling all contraints of stable operation. Glued to a frame of stainless steel, carbon fiber mesh serves as support for an aluminized mylar foil, such being able to cope with the forces applied by the athmospheric pressure with respect to the vacuum inside. The window is screwed to the cryostat body and sealed by an o-ring, as is also the case for all other screwed connections of attachments to the body.

At the bottom of the cryostat, three ports for the vacuum equipment, i.e. the vacuum pump, the gauge and the ventilation valve, are provided. At the two sides and at the top, two ports in each case are foreseen for the installation of nitrogen inlet and outlets, as well as the feedthroughs. The nitrogen inlet, in which the end tube of the transferline is plugged, consists of two concentrical tubes soldered such, that the insulation vacuum of the cryostat extends between them. The nitrogen outlet consists of a large pipe of 190 mm length with a comparatively large diameter, inside which 4 tubes can be plugged and fixed with Swagelok fitting from the outside at the outer edge. Inside the cryostat, these tubes are connected to the capillaries from the detectors, or the gas outlets of the phase separator, respectively. The feedthrough connections of these inner tubes, which become quite cold, had to be arranged at that outer edge at quite far distance from the

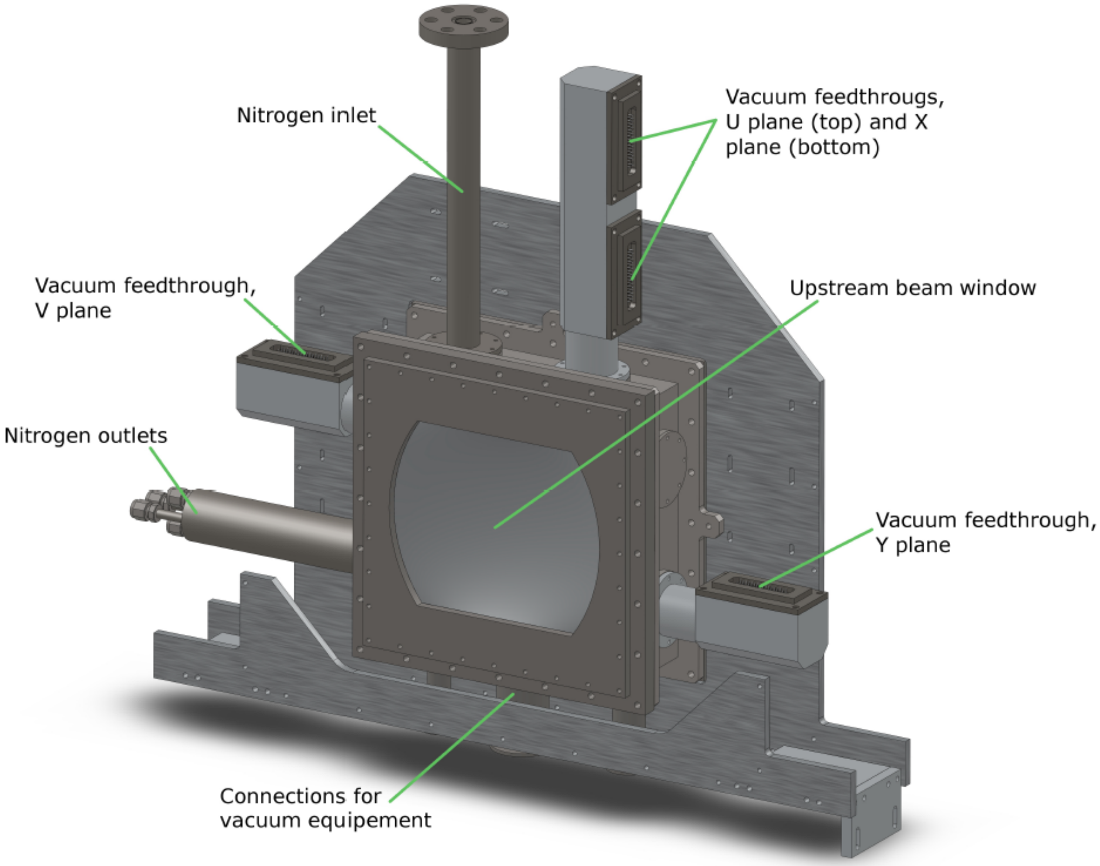

Figure 4.6: 3D model of a beam station cryostat, view from upstream, from [Bic11].

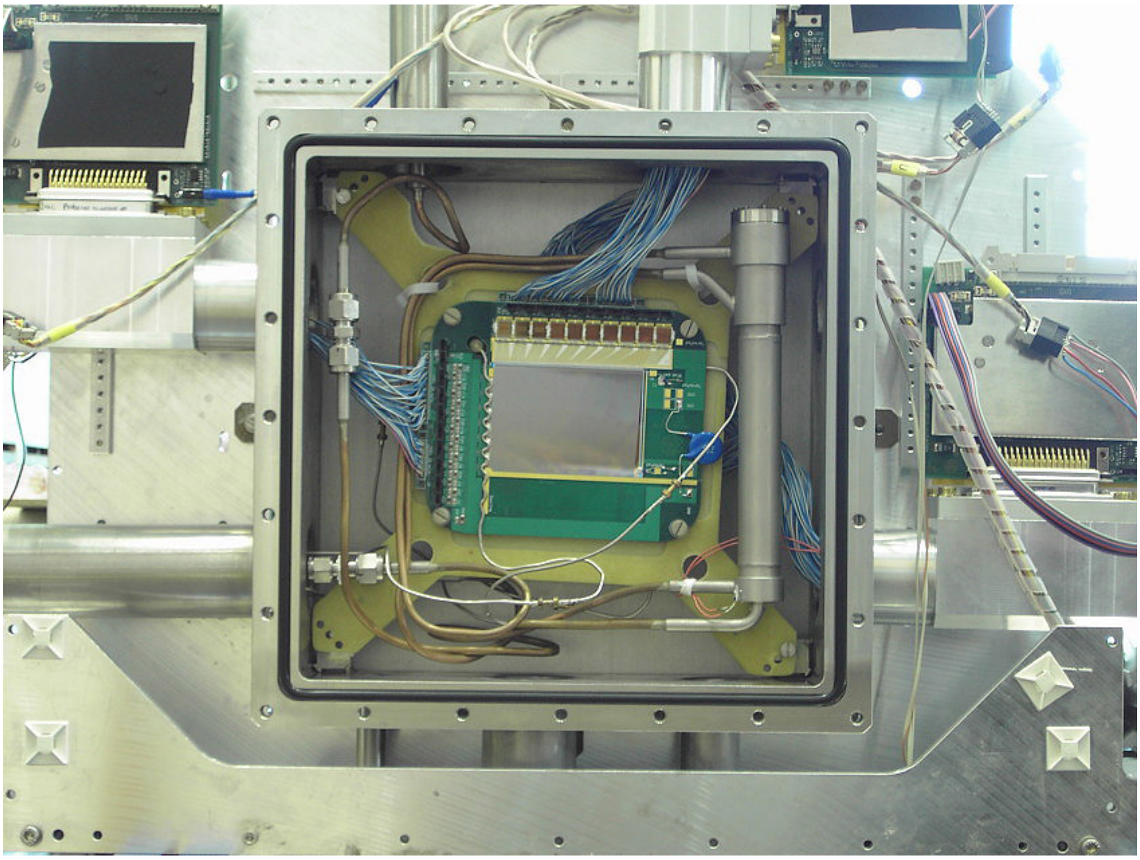

Figure 4.7: The first beam station cryostat, that was finally installed in the COMPASS area, in the lab. The UV detector module is visible, the XY module is mounted on the back side of the shuriken. The back window is substituted by a massive plate, which is exchanged with a beam window in the experimental area.

cryostat body, to prevent the o-ring sealing between the outlet and the cryostat body to become too cold and break. At the outlet, the port originally foreseen for the pressure measurement of the phase separator, is not used and capped, as this pressure is now measured at the gas exhaust line directly. The vacuum feedthroughs of the electrical connections consist of vacuum-tight Sub-D connectors with 50 pins, which are able to stand 500 V. These connectors are too large for the original ports in the cryostat body, so that they are screwed to plates which are screwed to little boxes which match the round ports at the cryostat body at one of their sides. The boxes have the positive second effect, that they offer some space for the storage of the 25 cm long cables of the detector modules. There are four electrical feedthrough connections, one for each detector plane, at each station, into which the respective repeater cards (see section 3.4.2.2) are plugged.

The arrangement of the detector modules and the other equipment inside a beam station cryostat is depicted in figure 4.7, from the same perspective as the model in figure 4.6. The two modules are screwed back-to-back onto their support structure, called shuriken, made from stesalit. One can see that the shuriken is tilted by an overall angle of 2.5 ° as already mentioned in section 3.4.1. Also the phase separator, visible in the right, is fixed to the shuriken. This turned out to be the most reliable way of fixation without being in danger of touching the stainless steel part of the front window or the wall, and such creating a heat bridge to the room temperatures outside of the cryostat. The liquid nitrogen circuit starts with the copper pipe from the nitrogen inlet in the left upper corner, and proceeds via the phase separator and the capillaries at the detectors, to the outlet. This circuit, as well as the fixation of the phase separator, have been arranged more neatly in later assemblies of the cryostats.

4.4 The Conical Cryostat

The cryostat housing the two spectrometer stations has to fulfill the same requirements for the operation of the silicon detectors as the beam station cryostats, but needs to cope with further restrictions on the available space and requirements for low material budget inside it. Inside the RPD almost all space, which is not in the acceptance of other detectors further downstream in the spectrometer, is already taken by photo multipliers of the inner scintillator ring of the RPD. Still, the first spectrometer station has to be placed as close as possible to the target. Also downstream of the RPD no space is available, as the Sandwich Veto detector follows immediately (see also figure 3.8). Thus, the two silicon stations were placed into one common cryostat, which was built with a conical shape to adapt optimally to the available space. This cryostat consists of three conical pieces, which are screwed together, to make the assembly easier. The most upstream one is the smallest and houses the two detector modules of `SI04`. Like the central part, to which the electrical vacuum feedthroughs are attached, it consists of aluminum. The most downstream part, made from stainless steel, houses `SI05`, and provides the flanges for the fixation to the RPD, as well as eight ports for connections to the vacuum volume.

As already mentioned before, everything inside this cryostat is situated inside the acceptance of other detectors in the spectrometer. As a first consequence, the full area of both windows is covered by a carbon-fiber reinforced plastic mesh, which is glued to rings from stainless steel, which are screwed to the cryostat body. Secondly, the two support structures of the detector modules are custom-made from carbon-fiber reinforced plastic, which is lighter than stesalit. The arrangement of the two support structures, with detector modules attached, inside the conical cryostat is shown in figure 4.8. The XY detectors modules of both stations are visible, the UV modules are mounted to the back side of the respective support (view from downstream, where the big window is still to be attached). The plastic tubes visible in this photo were installed for the nitrogen gas cooling the conical cryostat was operated with in 2008, as a tough schedule and an incident with a broken vacuum window during the commissioning phase prevented a cryogenic operation in that year.

The conical cryostat is fixed to rails at the downstream side of the RPD, so that it can be easily moved in and out during the (de-)installation. Once inside the RPD at the operating position, the conical cryostat is directly screwed to the massive back plate of the RPD, called marguerite due to its shape. Figure 4.9 gives an impression of the environment of the concial cryostat, when it is not yet moved into the RPD completely, and the big

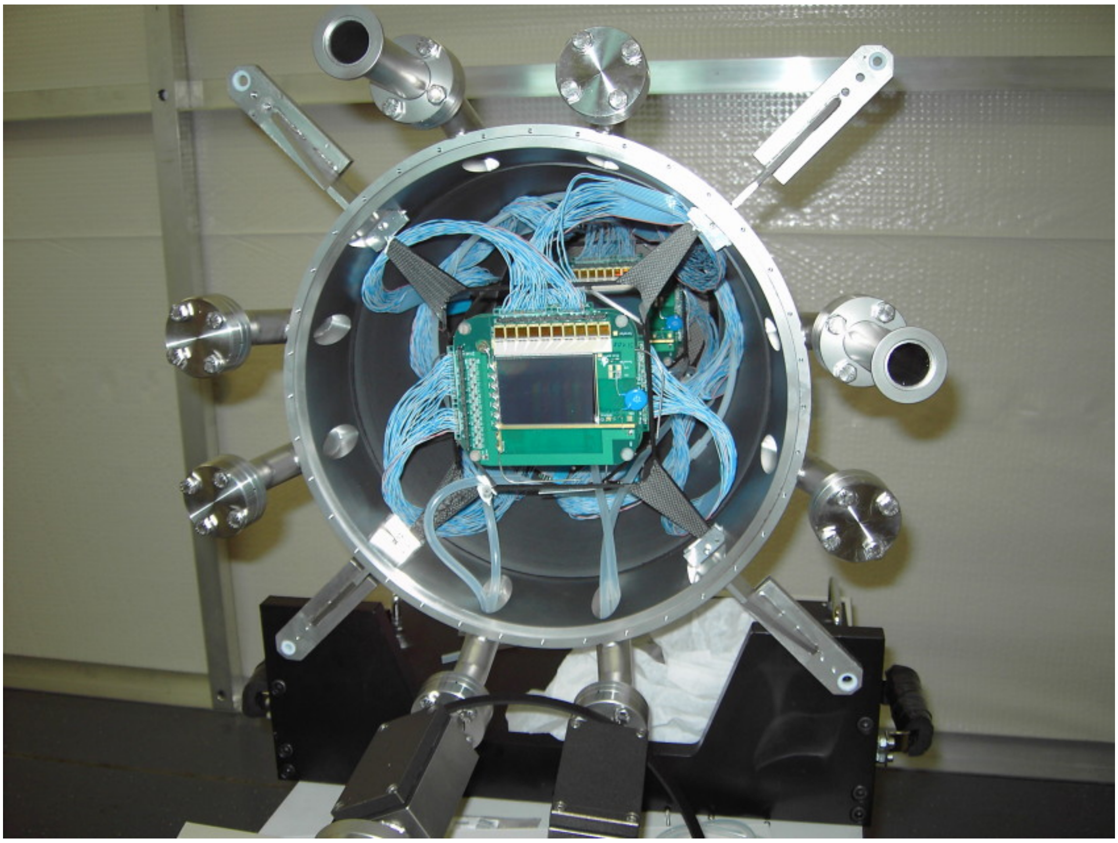

Figure 4.8: The conical cryostat, open view from downstream. The plastic tubes are related to the nitrogen gas cooling, installed only in 2008.

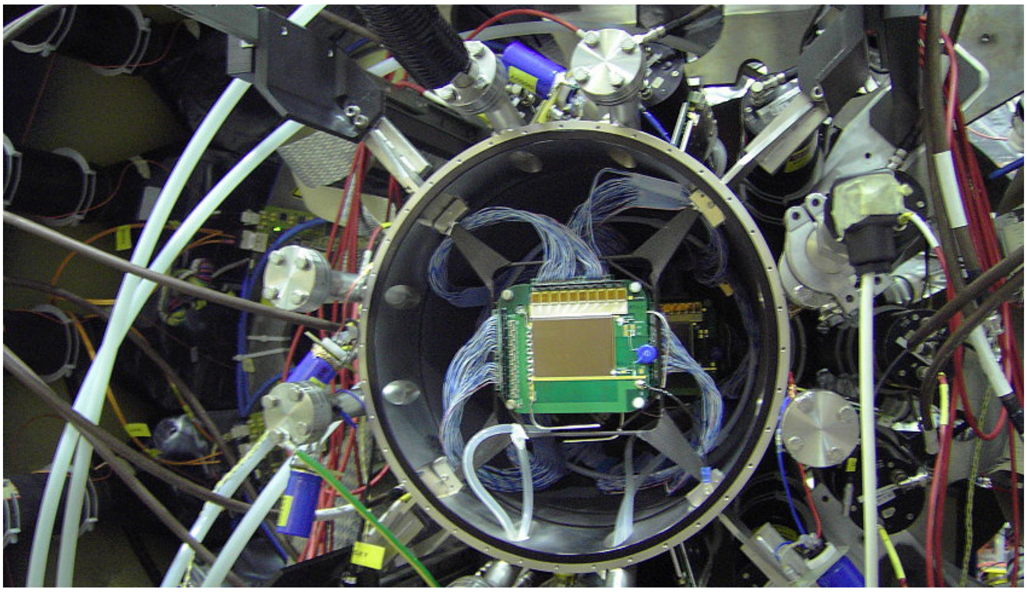

Figure 4.9: The conical cryostat and its crowded environment at the RPD. The cryostat is not moved into its final position yet, and the downstream window is still missing.

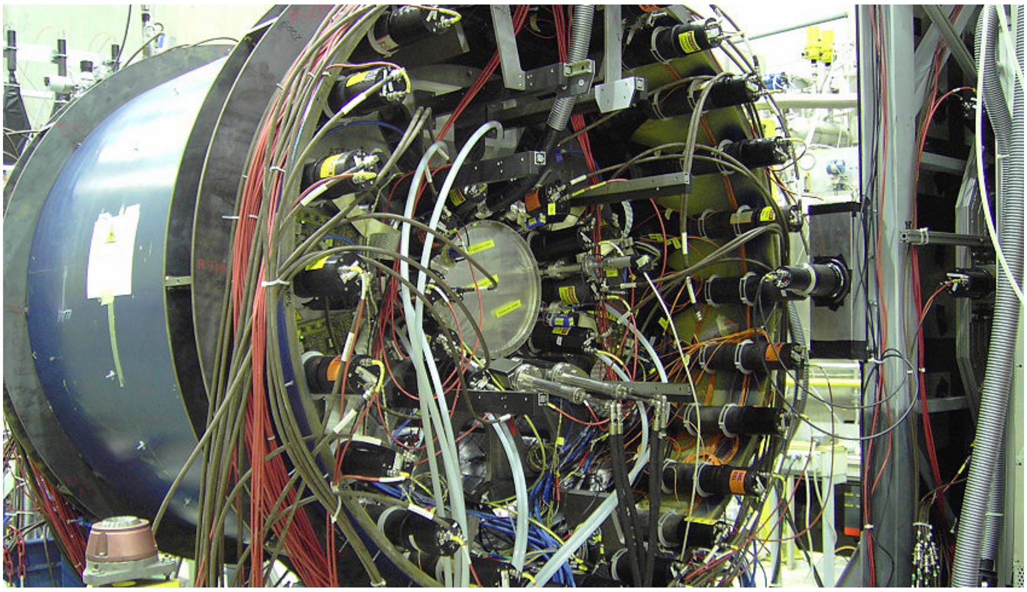

Figure 4.10: The conical cryostat at its final position inside the RPD.

window is again not attached yet, so that the detectors are visible. Figure 4.10 gives a wider overview of this crowded region, with the conical cryostat moved to its operating position (the big window is now mounted, but still covered by a plastic cover with three yellow labels), where it perfectly fits the available space inside the RPD[6].

Concerning the liquid nitrogen cooling, the most massive device, the phase separator, is placed inside a special box. This box is attached further outside at the RPD, i.e. outside of the acceptance of the spectrometer, but still shares a common vacuum with the cryostat. This ensemble is depicted in figure 4.11, taken during a commissioning step of the phase separator box outside of the RPD in 2008. In this picture, also the positions of the repeater cards are visible[7]. The functions of the vacuum ports are also indicated: One upper port is connected to the phase separator box, the two bottom ports are used for the nitrogen outlets (closed here, but indicated similarly in figure 4.8). The other ports are used for the connections to vacuum pumps or gauges. The liquid nitrogen circuit works in the same way as explained in section 4.3 for the beam station cryostats. The phase separator is of the same type, but its outlet is splitted into four pipes (instead of two), which deliver the liquid nitrogen to the detectors. Also the same kind of nitrogen inlet is used as for the beam station cryostats, attached here to the phase separator box.

For accessing connections at places hard to access, as inside the tube between the phase

---

[6] Here, the RPD is still in its parking position, so that the conical cryostat is visible and accessible at all. That means, with respect to the beam position, the RPD is moved roughly 2.5 meters to the Saleve side, which is on the left side of this picture.

[7] The repeater cards are positioned at the upstream end of the central part, as this position features most space between the photomultipliers of the inner ring of the RPD when the conical cryostat is at its operation position. Similar as for the beam station cryostats, the electrical feedthrough connectors are fixed to aluminum plates, which are then screwed to dedicated sealing surfaces at the cryostat body. Unlike with the beam stations, the connectors are glued to the plates instead of screwed, which was expected to be more vacuum tight.

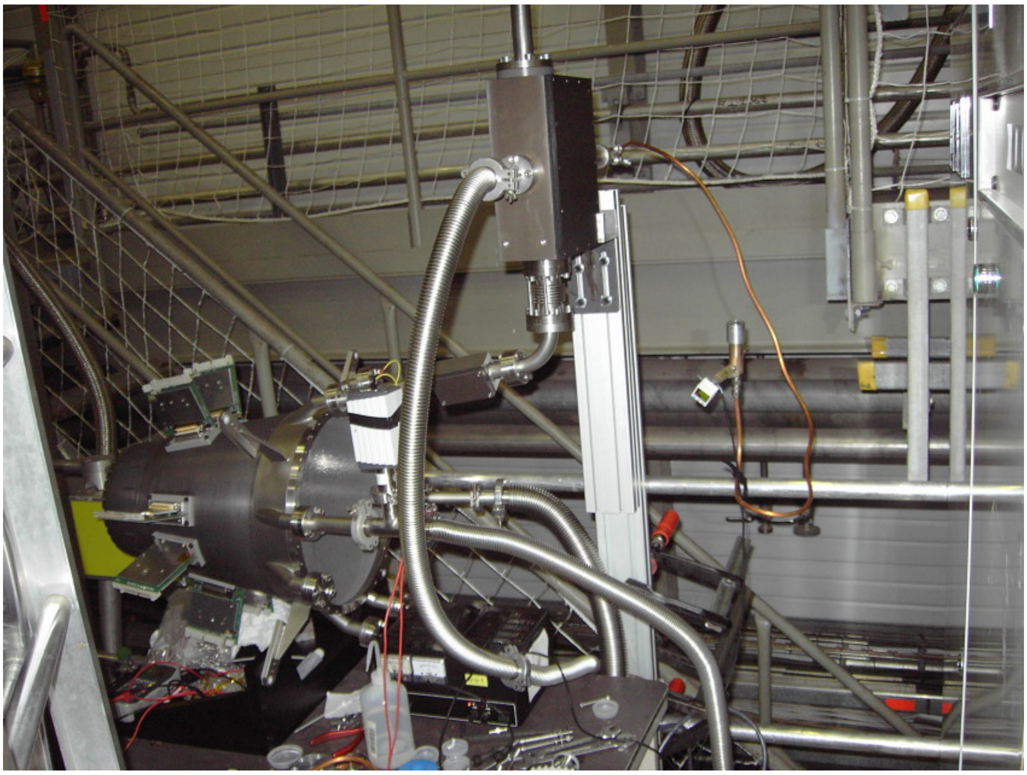

Figure 4.11: The conical cryostat and its phase separator box.

separator box and the cryostat body, several little boxes, which can be opened at one side, are integrated. The connections between cooling capillaries are made by epoxy connectors instead of Swagelok fittings, especially inside the cryostat body.

4.5 The Liquid Nitrogen Cooling and Control System

The functional schematics of the liquid nitrogen cooling system of the COMPASS silicon detectors is depicted in figure 4.12. The liquid nitrogen is provided by a central dewar next to the COMPASS experimental hall. A distribution box, called *valve box*, is filled automatically, so that a constant pressure of 1.8 bar and a fill level between two setpoints around 50 % are reached and kept inside its buffer volume of 50 l. The stainless steel vessel is placed inside an insulation vacuum and shielded by passive cooling of exhausting gaseous nitrogen. The valve box allows to continuously supply the silicon detector stations with liquid nitrogen. The nitrogen flow to each station can be roughly regulated by dedicated valves on top of the valve box, which allow or stop the transport of nitrogen to the stations via dedicated vacuum-insulated transfer lines. Inside the stations, already evaporated nitrogen gas is separated from the liquid by the phase separator, as explained in section 4.2. Thus, only liquid nitrogen is guided through the capillaries along the detector modules, where it provides cooling power by its evaporation. The detector temperatures are regulated by controlling the nitrogen flow through the exhaust lines after

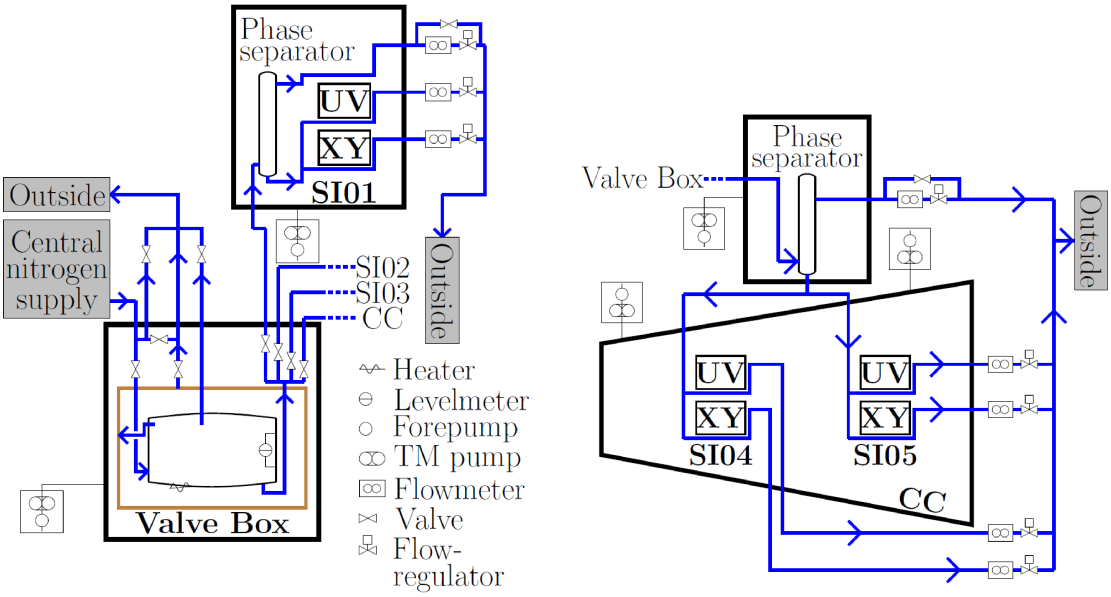

Figure 4.12: Functional schematics of the liquid nitrogen cooling system: The valve box with an exemplary beam station (left), and the conical cryostat (right), from [COM12c].

the detector modules.

The complete system is controlled by a SIEMENS PLC[8]. It reads all available temperature, pressure and level sensors, and regulates various parameters dependent on these readings. It takes care of the automatic filling procedure for the valve box. It controls both the pressure in the phase separator and the nitrogen flows through the detectors by adapting setpoints of the flow controllers in the connected flow meters, until predefined values are reached. This is achieved both during continuous operation with a constant temperature setpoint, and also in cooling-down or warm-up phases, during which the temperature setpoint changes regularly in a defined way. The PLC works also as a safety system, that provides pre-defined emergency procedures to react properly on conditions which are potentially dangerous for the detectors. In case of vacuum problems or failing pumps, it initiates the warm-up of the cryostat concerned. In case of cooling problems, i.e. detector temperatures near the APV chips above a certain limit in the continuous operation mode, it restarts the cool-down of the module concerned, and interrupts the low voltage of the APVs, i.e. the crucial heat input to the respective module. The data collected by the PLC can be monitored by the *Anibus* software, which allows also manual interventions to the regulation procedures and parameters, with different levels of authorization necessary. Both the hardware design and the software development of the PLC system have been provided by the CEA/Saclay group of COMPASS, and have already been described extensively in [Bic11].

---

[8] Programmable Logic Controller

4.6 Operation of cold APV25 Chips

The design of the COMPASS silicon detector modules implies that also the APV25 readout chips become significantly colder, when the detectors are cooled with liquid nitrogen. Their temperatures are not measured directly at the APVs themselves, but can only be guessed from the temperatures read by the sensors placed next to the pitch adapters[9]. These sensors read typically about 60 °C with warm operation and $200\,\mathrm{K} = -73\,^\circ\mathrm{C}$ or $245\,\mathrm{K} = -28\,^\circ\mathrm{C}$ for sensor temperatures of 130 K and 200 K, respectively, when all APVs are powered and programmed.

When the operating temperatures of APVs are changed, the properties of the shaper and the preamplifier of the CR-RC circuit change. Generally, the changes can be compensated by adjusting the APV settings related to the shaper (ISHA, VFS) and the preamplifier (VFP). In practice, investigations on this have been carried out, originally triggered by high noise levels, with varying the mentioned settings. These tests, partly conducted with calibration signals, have been heavily overshadowed by more essential problems with the operation of cold APVs, as detailed in the following. Thus they were not ultimately successful, so that it was pragmatically decided to run also the cold APVs with the warm settings in the beginning of 2009. Like this, the signal shape changes such, that the signals of cold APVs are about 30 % faster for both the rising and the falling part, which results in an improved time resolution as presented in section 6.3.3. At the same time, the gain of the APVs drops and has to be readjusted by increasing the VPSP setting, to ensure working conditions inside the dynamic range.

During the winter 2007/2008, extensive tests of cold APVs took place in the laboratory. For logistic reasons, the biggest part of these tests has been carried out with the detector module `SI 1.02` (see table A.3), that still featured ERNI connectors and such the warm version of connecting cables, feedthroughs and repeater cards. The tests were carried out with wafer temperatures in the range of $115 - 135\,\mathrm{K}$, and were accompanied by serious problems related to instability: When recording latchall data (see section 3.4.2.3), the baseline of the APVs was found to jump by magnitudes the zero suppression algorithm cannot cope with, and readout errors occured frequently after a couple of hours. This could partly be cured by temporarily increasing a little bit the low voltage supplying the APVs. This suggested the interpretation, that the APVs became too cold after some time (a couple of hours) and such could not be read out any more, but the APVs could be warmed up again by the increased power consumption. Another issue was huge noise that occurred occassionally without correlation to anything in the near environment, being remindful of the suspicion of osciallating behaviour of the APVs as already reported in [Fuc03]. This behaviour can possibly also be explained by the ERNI connectors, which become also quite cold and such potentially loose, making the power supplied to the

---

[9] The temperature values typically recorded are the ones from the sensor equivalent to the "upper" temperature sensors shown in figures 3.3 and 4.4, but on the 8-side L-Board. This choice is purely traditional. The visible upper sensor on the mentioned two photos displays usually similar values, if the APVs of both sides are operated.

APVs unreliable. This theory needs confirmation by readout tests of modules with soldered cables.

In early 2008, the sensors of two of the first modules with soldered cables, i.e. `SI 1.03` and `SI 1.07`, broke during cooling tests due to well explicable reasons, see section A.1.2. Thus, the spare module situation became such critical, that it was then decided to operate the detectors only with a safety margin at sensor temperatures of 200 K. From that time on, no serious problems with the stability of the APV operation occured any more. Still, no long-term tests with modules with cables have been carried out at 130 K up to now, so that it is unclear, whether the problems mentioned before arose from the cold ERNI connectors, or from the APVs themselves at the corresponding lower temperature.

As a further aspect, cold APVs seem to be more sensitive to a proper grounding, which improves the noise level more obviously than it was the case for the warm detectors. The detector modules are now grounded directly inside their cryostat. The ground level of the APVs of the 8-side (which are connected to the p-side of the sensor) is now directly connected to the cryostat via a short cable. The APV ground of the 10-side is floating at the level of the bias voltage applied, see section 3.3.2. The cryostats are properly grounded to the electronics ground in the COMPASS experimental area, and insulated from their support structures[10], which themselves are grounded to the structure ground[11]. In addition, cold APVs seem to not properly reset in all cases[12], so that the current through the APVs is not a good indication for properly programmed APVs any more, as was the case for warm APVs.

---

[10] These support structures are the optical benches or the RPD, respectively.

[11] To the structure ground, noise-producing equipment like pumps or ventilating fans are connected, while the electronics ground is reserved for "quiet" equipment sensitive to noise.

[12] e.g. when the zero chip of the ADC is programmed

Chapter 5

Radiation Impact to the Silicon Detectors

The operation and performance of silicon detectors are sensitive to radiation damages, as already stated in section 3.1. Thus radiation hardness and the reduction of radiation damages to the detectors is a crucial point to consider in high energy physics experiments. According to this, for the COMPASS silicon detectors a radiation hard wafer design has been chosen (see section 3.3.1), and the operation at cryogenic temperatures (see chapter 4) was considered appropriate.

This chapter gives a basic insight into the relevance of radiation impact to the COMPASS silicon detectors. The radiation exposure of the detectors is estimated in section 5.1, where the originally foreseen exposure is opposed to the radiation input actually accumulated. In addition, two key observables of radiation damages, i.e. the development of noise and leakage currents, are exemplarily presented in section 5.2.

5.1 Estimations of Radiation Exposure of the COMPASS Detectors

For the comparison of the radiation damages induced by different types of particles, usually the NIEL[1] scaling hypothesis is used. The damages are scaled to the equivalent effects of 1 MeV neutrons, resulting in the unit $1\,\mathrm{n_{eq}}$ or $1\,NIEL$.

The decisive estimations of the radiation exposure of the COMPASS silicon detectors during hadron beam times were carried out in the planning phase [COM96], similarly as quantitatively sketched here. The pion flux Φ_π for a beam time of 100 days was estimated to be

$$\Phi_\pi = 100\,\mathrm{days} \times 4800\,\mathrm{spills/day} \times 2 \cdot 10^{8}\,\mathrm{pions/spill} = 9.6 \cdot 10^{13}\,\mathrm{pions/beam\ time}\ . \tag{5.1}$$

The damage estimations were based on a narrow 190 GeV pion beam with a beam dimension of $3 \times 3\,\mathrm{mm}^2$, from which one can estimate an irradiated area of approximately

---

[1] Non-Ionizing Energy Loss, describing the consequences to the semiconductor properties by displaced lattice atoms in the crystal, as shortly summarized in section 3.1.

$0.1\,\mathrm{cm}^2$, and an equivalent damage of $\approx 1\,\mathrm{n}_{\mathrm{eq}}$ for high-energetic pions (and $\approx 0.1\,\mathrm{n}_{\mathrm{eq}}$ for high-energetic muons), as taken from figure 5.1. As the beam has a gaussian shape, the irradiation in the center is higher than the average radiation, so that an additional factor of roughly 1.5 is introduced for the equivalent damages Φ_{eq} in the center:

$$\Phi_{\mathrm{eq}} = 9.6 \cdot 10^{13}\,\mathrm{pions}/0.1\,\mathrm{cm}^2 \times 1\,\mathrm{n}_{\mathrm{eq}}/\mathrm{pion} \times 1.5 = 1.44 \cdot 10^{15}\,\mathrm{n}_{\mathrm{eq}}/\mathrm{cm}^2\ . \tag{5.2}$$

This number made the challenge very attractive, to go for exploiting the Lazarus effect for increasing the lifetimes of the detectors.

In the mean time, the conditions have been changed: Before the hadron run 2008, it was decided to use a wide pion beam of $15 \times 10\mathrm{mm}^2$, so that the radiation impact per area to the silicon detectors could be significantly reduced. In addition, new approaches for the NIEL scaling parameters result in an equivalent damage of $\approx 0.3\,\mathrm{n}_{\mathrm{eq}}$ for high-energetic pions, see figure 5.2 and the respective references in [Mol99a].

Exact determination of the pion flux in the COMPASS area is difficult after the beam times, as for other purposes only the knowledge of "protons on T6" or "good spills on tape" is required and such noted down, while "beam in the area" is obviously given by a quantity in between. The ionization chambers at the entrance of the beam into the experimental hall are supposed to monitor the beam in the area, and deliver values which are written to a database. But they are delicate to use as they need rescaling factors which are unknown a priori and change from time to time. Thus, just rough estimations of the radiation impact to the silicon detectors have been carried out, to obtain an idea of the orders of magnitudes of the radiation the detectors had to stand. These estimations are based on the number of spills, as far as they were available in the weekly report or run reports, and guessed otherwise. The number of incident particles is first equally averaged over the area of the beam spot (estimated from figure 5.3). Impact to the central region is estimated to be about 1.5 times this average. The results for the COMPASS beam times since 2003 are given in table 5.1. It becomes obvious, that unlike propagated, with the current conditions, the pion beam does not harm the detectors more than the muon beam, which has a higher intensity. The warm beam station detectors, used until 2008, have been exposed to roughly $7.2 \cdot 10^{12}\,\mathrm{n}_{\mathrm{eq}}/\mathrm{cm}^2$. The cold beam station detectors, used since 2009, have been exposed to $3.2 \cdot 10^{12}\,\mathrm{n}_{\mathrm{eq}}/\mathrm{cm}^2$ up to and including the Primakoff 2012 beam time. For the spectrometer detectors in the conical cryostat, the situation is more complex. They see also the low-energetic scattering products, and especially low-energetic protons damage the silicon significantly, but can only be quantified in a detailed dedicated Monte Carlo study.

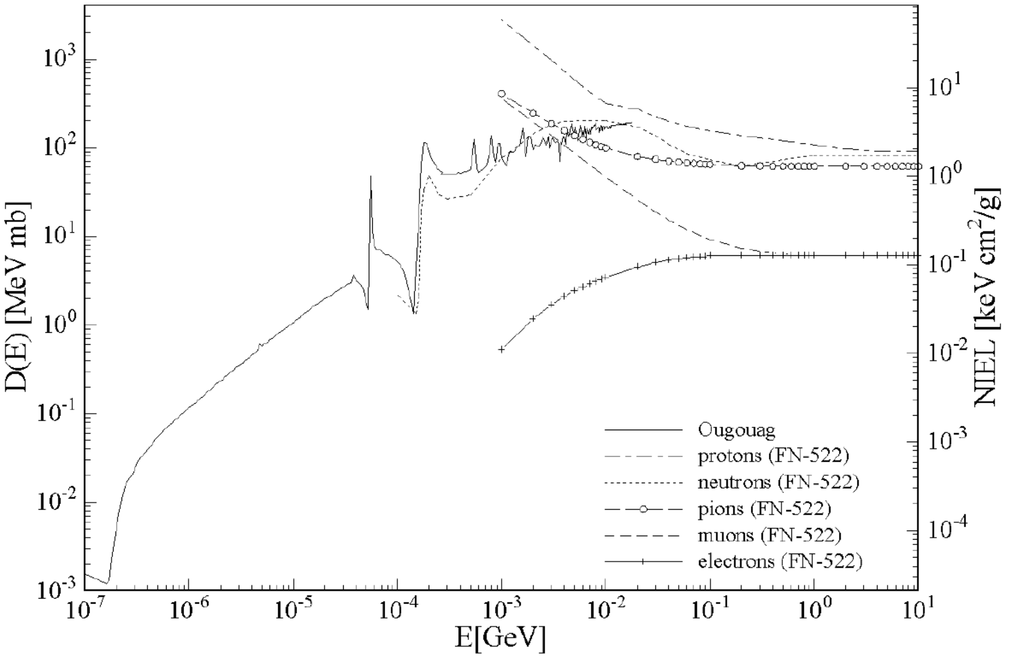

Figure 5.1: Damage functions in silicon for protons, pions, neutrons, muons, and electrons, from [ROSE97].

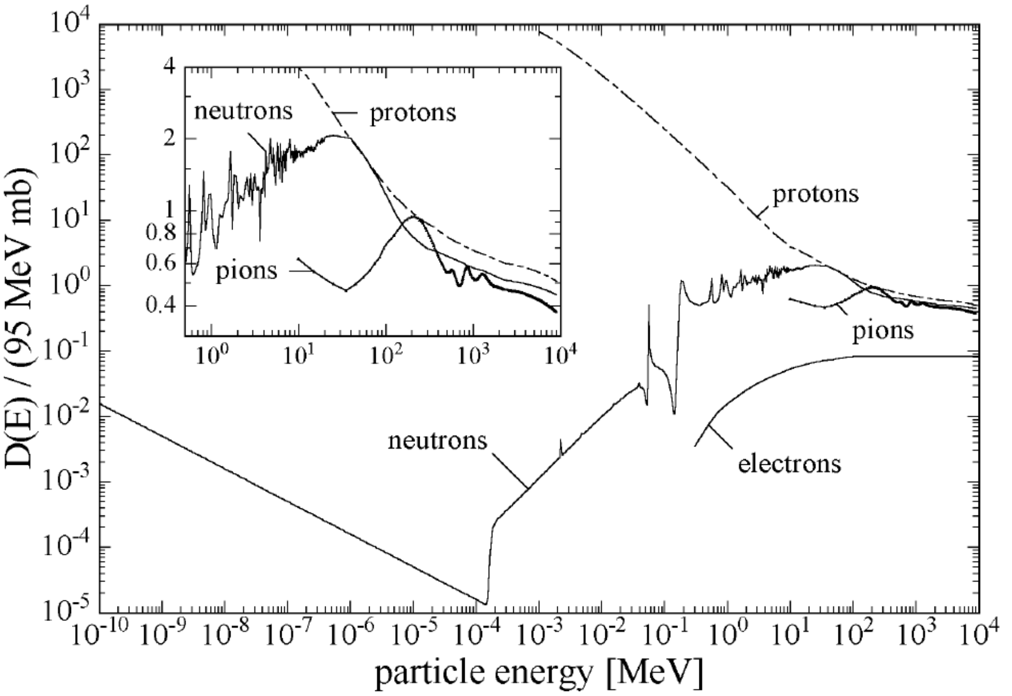

Figure 5.2: Displacement damage functions for protons, pions, neutrons, and electrons, from [Mol99a]. The ordinate is normalized such, that the scale directly provides the damage equivalent to 1 MeV neutrons.

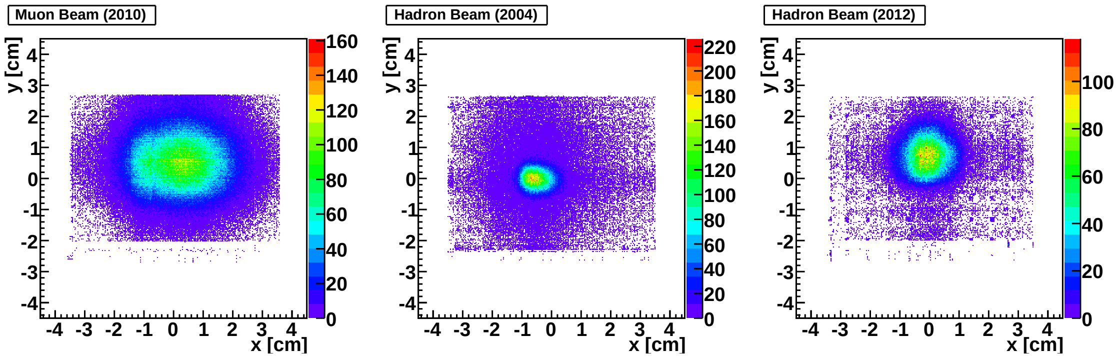

Figure 5.3: Beam spots seen by the silicon detectors, examplarily for muon beam (left), the narrow 2004 hadron beam (middle) and the wide hadron beam (right).

	particles/spill	particles/beam time	spot size	n_{eq}/cm^2 (central)
2003	$2 \cdot 10^8\ \mu$	$5 \cdot 10^{13}\ \mu$	$6\,cm^2$	$1.3 \cdot 10^{12}$
2004	$2 \cdot 10^8\ \mu$	$8 \cdot 10^{13}\ \mu$	$6\,cm^2$	$1.9 \cdot 10^{12}$
2004	$5 \cdot 10^6\ \pi$	$3 \cdot 10^{11}\ \pi$	$1\,cm^2$	$1.5 \cdot 10^{11}$
2006	$2 \cdot 10^8\ \mu$	$7 \cdot 10^{13}\ \mu$	$6\,cm^2$	$1.8 \cdot 10^{12}$
2007	$2 \cdot 10^8\ \mu$	$9 \cdot 10^{13}\ \mu$	$6\,cm^2$	$2.0 \cdot 10^{12}$
2008	$2 \cdot 10^7\ \pi$	$1.5 \cdot 10^{12}\ \pi$	$4\,cm^2$	$0.2 \cdot 10^{12}$
2009	$5 \cdot 10^7\ \pi$	$1 \cdot 10^{13}\ \pi$	$4\,cm^2$	$1.2 \cdot 10^{12}$
2010	$2 \cdot 10^8\ \mu$	$6.3 \cdot 10^{13}\ \mu$	$6\,cm^2$	$1.5 \cdot 10^{12}$
2011	$1 \cdot 10^8\ \mu$	$1.3 \cdot 10^{13}\ \mu$	$6\,cm^2$	$3.3 \cdot 10^{11}$
2012	$2 \cdot 10^7\ \pi$	$1.4 \cdot 10^{12}\ \pi$	$4\,cm^2$	$1.7 \cdot 10^{11}$
2012	$4 \cdot 10^7\ \mu$	$1.0 \cdot 10^{12}\ \mu$	$6\,cm^2$	$2.5 \cdot 10^{10}$

Table 5.1: Estimation of the radiation exposure of the COMPASS silicon detectors up to and including the 2012 Primakoff beam time (i.e. including September 2012).

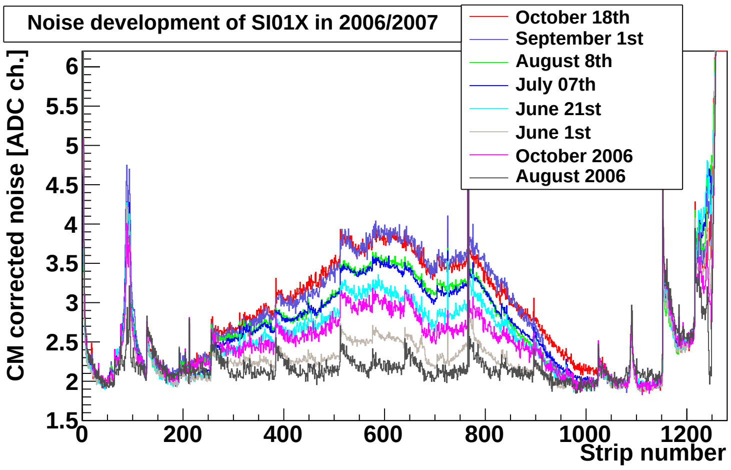

Figure 5.4: Noise development of the readout plane `SI01X` (from module `SIL10`) during 2007. For comparison also two curves obtained in 2006 are shown. The shadow of the beam profile is clearly visible as increased noise.

5.2 Impact of Radiation Damages

For the visualization of the damages induced by the radiation impact as estimated in section 5.1, two observables have been chosen. The warm detectors showed an increased noise level, obviously related to the beam, since the end of the beam time in 2006. The leakage currents of those detectors increased significantly over the years as well.

5.2.1 Signal-to-Noise Ratio

The ratio between signal amplitude and noise level decides about the usability of a silicon detector. For the detectors used in COMPASS the bias voltage is regularly adjusted such, that the full depletion of the silicon bulk can presumably be taken for granted. For the warm detectors used until 2008, the signal amplitude[2] did not decrease significantly. The observed amplitude heights fluctuate, and the average reduction amounts to less than 10 % over the years. The noise level and profile of the detectors, instead, changed significantly. Starting in autumn 2006, the noise level in the center of the readout planes, corresponding to the location where the beam particles traverse the detectors, rose. The profile of the common-mode corrected noise (see section 3.4.2.3) started to look more and more similar to the occupancy spectra, i.e. to show the beam profile in this projection. During the winter break 2006/2007, the sensor seemed to partially recover from the induced damages, so that at the beginning of the 2007 beam time, the noise level was reduced again. During this beam time, the noise level increased again significantly to about double the values as compared to the beginning of 2006 in the center of the plane. This development is shown exemplarily for the 10chip-side of the detector module `SIL10` in figure 5.4. This behaviour could not be cured with an increase of the bias voltage, so that

---

[2] The quantity usually stated for comparison is the *cluster amplitude*, see section 6.2.

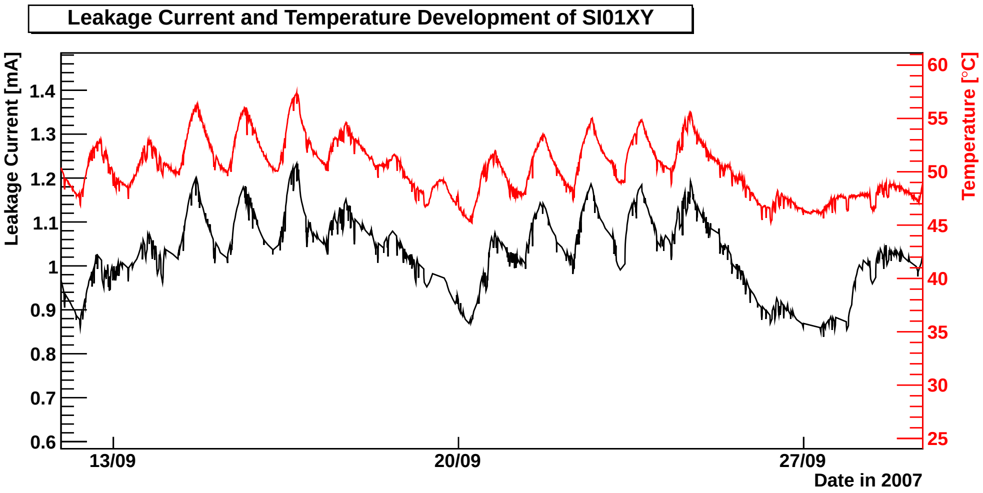

Figure 5.5: Measured leakage current and sensor temperature for `SI01XY` dependent on time for an exemplary period in 2007, showing the strong correlation between those two observables.

a reduction of the signal-to-noise ratio to half of the original value has to be stated for the detectors used in the warm beam stations. No negative effect to the tracking efficiency has been reported, but nevertheless the detectors have been replaced by new ones for the 2009 beam time[3]. For the new detectors operated at 200 K, no increase of the noise level could be observed including the 2012 Primakoff beam time. A correlation with the cooling cannot be stated here yet, as the detectors have not been exposed yet to comparable radiation impact as the warm detectors ($5.0 \cdot 10^{12}\,\mathrm{n_{eq}/cm^2}$ until 2006 or $7.2 \cdot 10^{12}\,\mathrm{n_{eq}/cm^2}$ in total in the central region, compared to $3.2 \cdot 10^{12}\,\mathrm{n_{eq}/cm^2}$ from 2009 until September 2012, see table 5.1).

5.2.2 Leakage Currents

As already introduced in section 3.1, radiation damages cause the leakage currents observed for fully depleted detectors to rise. The leakage currents of the COMPASS silicon detectors, as measured by the bias voltage power supply, have been recorded since the 2004 beam time, and are presented in the following.

Leakage currents of silicon sensors are strongly temperature dependent. The temperature in the COMPASS experimental hall changes significantly between day and night, and the average depends on the time of the year. These temperature changes are also visible in the temperatures of the silicon sensors of the warm stations[4]. The obvious correlation between sensor temperature and leakage current on a time scale of several days is shown exemplarily in figure 5.5.

---

[3] The replacement of the warm beam stations by cryogenic ones, including new detector modules, had already been scheduled for 2008, but had to be postponed to 2009 for organizational reasons.

[4] Unlike for cryogenic detectors, the temperatures of the warm silicon detectors have not been regulated to a defined value.

For a reasonable statement, the measured leakage currents $I(T)$ at the present temperature T need to be corrected to the leakage current $I(T_O)$ at a predefined reference temperature T_0. This can be done using [Mol99b, Sze84]:

$$I(T) = I(T_0) \cdot \frac{T^2}{T_0^2} \cdot \exp\left(-\frac{E_g}{2k_B} \cdot \frac{T_0 - T}{TT_0}\right) \tag{5.3}$$

with E_g the energy gap between the valence band and the conduction band of silicon and k_B the Boltzmann constant. The correlation between current and temperature given by equation (5.3) is exploited for single days, with $I(T_0)$ and E_g as independent fit parameters. This approach assumes that the radiation impact per single day is not significant compared to a full beam time, i.e. $I(T_0)$ does not change within one day. For each silicon detector, the temperature recorded by the sensor placed at or nearest the wafer was chosen for the evaluation. For the cases, where the wafer temperature was not measured[5], the temperature outside the experimental hall was found to be the best reference, but needed additional care due to offsets in time and absolute temperature with respect to the silicon wafers. The leakage currents depend also on the applied bias voltage. Changes, i.e. mostly increases, are carried out when full depletion seems to require it. The relevant quantity for this is the observed noise level. For the detectors involved in the leakage current analysis, the bias voltage was changed from 180 V to 200 V for the detectors of `SI01`, and varied between 130 V and 170 V for `SI02`, and between 150 V and 170 V for `SI03`, in 2007 and 2008. The fit of $I(T_0)$ did not improved when taking the changes into account. For previous years, the settings have not even been recorded, so that the dependence on the bias voltage is completely omitted in this analysis.

The results are presented in figure 5.6 for all detectors operated warm in COMPASS for a couple of years, with the naming of 2007. Between 2004 and 2008, the measured leakage currents, corrected to a defined reference temperature, increased from below 100 µA to 1 400 µA for `SI01` and 1 000 µA for `SI02` and `SI03`. In all cases, the leakage currents were observed to increase approximately linearly during one beam time. After each winter break, the current is observed to start at a lower level than the last value from the previous year. This points to the assumption that the detectors recover during the break, which is indicated by equivalent observations in the noise level, as suggested in section 5.2.1. Still, in the subsequent beam time, the leakage current rises with a steeper slope. This faster rise is not seen for 2008, which is presumably related to the very low radiation impact to the detectors in that year. A closer look shows also several drops at the same times for all detectors, e.g. in september[6] 2006. These drops can be correlated to times, when there was no beam inside the experimental area for several days. A clear correlation between the leakage currents and the beam intensity that hits the detectors is observed here, with a delay of about one day.

For the cryogenic detectors, the leakage currents are expected to be significantly lower. They are recorded with values in the range of 20 µA to 40 µA. These currents have been

---

[5] For `SI02` and `SI03` in 2004, and all detectors in 2008, the temperatures were not recorded.

[6] September 2006 refers to the middle of the 2006 beam time.

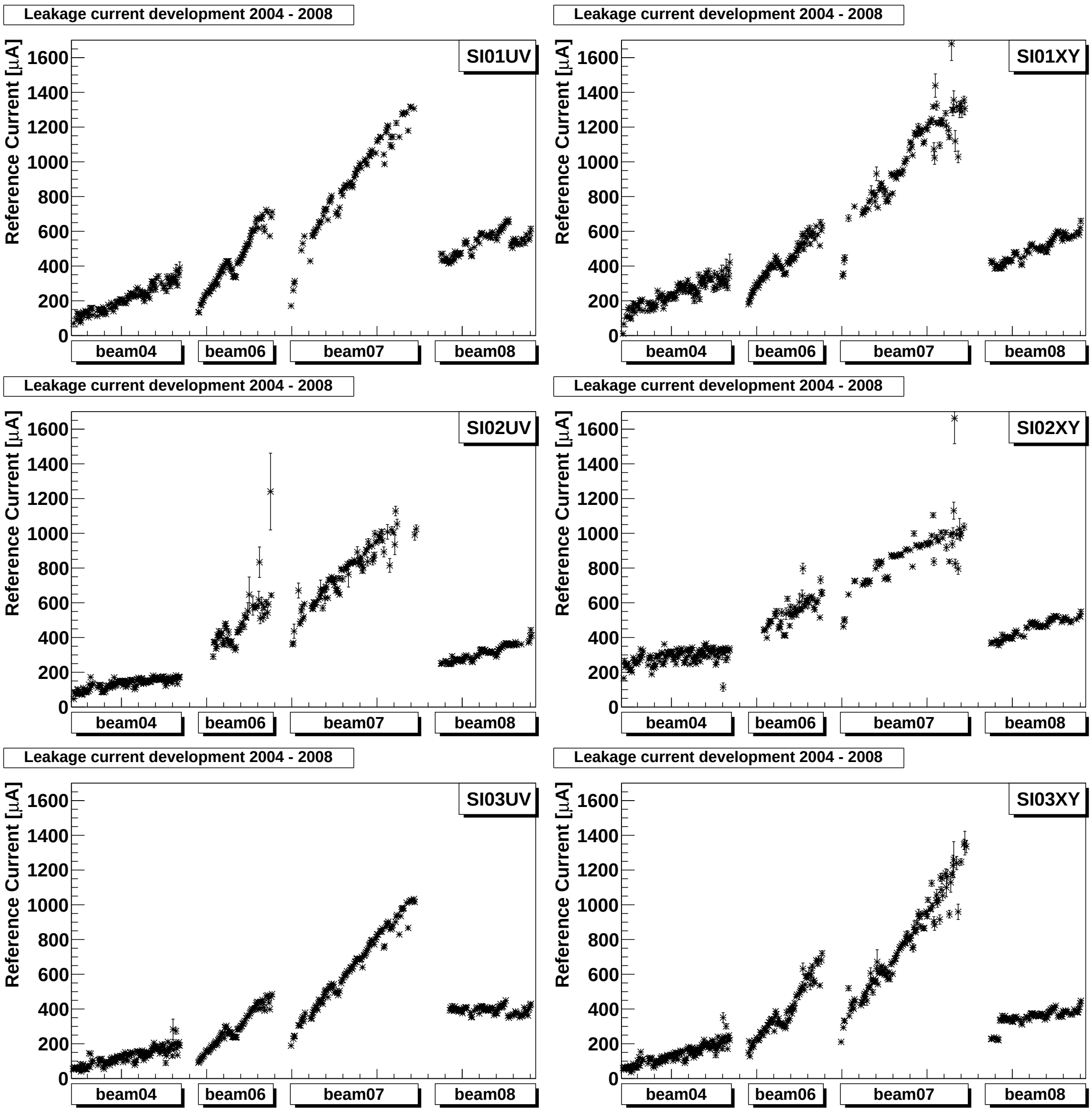

Figure 5.6: Development of the leakage currents of the warm beam station detectors during the beam times 2004 to 2008.

found to be drawn exclusively from the Deutronics modules[7]. Thus, the leakage currents attributed to the silicon sensors themselves are negligible for cryogenic detectors, at least up to and including the 2012 Primakoff beam time.

---

[7] The low voltage power supplies of the ADC cards were designed to be floating. Still they feature a finite resistance, which was found to be responsible for the full leakage current measured for the cryogenic detectors during the comissioning phase in 2012.

Chapter 6

Performance of Warm and Cryogenic Silicon Detectors

The COMPASS silicon detectors are installed in places, where the best possible resolution for the reconstruction of charged particles has to be achieved and only comparatively small areas need to be covered, i.e. in the region around the fixed target. Especially the analysis of physics processes featuring very small scattering angles, as it is the case for Primakoff reactions (see section 7.3) requires excellent spatial resolution and reliable track reconstruction.

The performance of the silicon detectors is evaluated by their time resolution and spatial resolution. In this chapter, the basic concepts of the silicon data reconstruction and the obtained results are summarized. More details and extensive descriptions of the analyses that have been carried out are already given in [Din10, Zim11, Lee11].

Section 6.1 summarizes how the time information of particles crossing the active detector are reconstructed from their signal shape. The corresponding position of these particles at the location of the detector is obtained during the clustering process, as explained in section 6.2. Different signal shapes for warm and cryogenic detectors also imply different performances. Those are compared in section 6.3. This comparison covers the time and spatial resolution, and summarizes the impact of cryogenic operation.

6.1 Signal Shape and Time Reconstruction

When a charged particle hits the silicon detector volume and induces an electric signal at the respective readout strip, the APV25 readout chip's circuit shapes a defined signal from it, which is sampled and buffered for clock cycle. The APV chips of the COMPASS detectors are operated in Multi Mode. When requested by a trigger, they deliver three consecutive samples of amplitudes A related to a predefined time t, for each input channel. The samples are taken with a time difference Δ between them:

$$a_0 = A(t-2\Delta) \quad a_1 = A(t-\Delta) \quad a_2 = A(t) \quad \text{with} \quad \Delta = 25.8\,\text{ns}\,. \tag{6.1}$$

When the *latency* is set correctly, the values read out from the ring buffer of the APV (see section 3.4.2.1) are such, that the three samples are taken from the rising edge of the signals whose origins are related to the event having caused the trigger. This allows for the most reliable time reconstruction. The observed signal factorizes into the signal amplitude (which is proportional to the energy deposit and the charge collected at the readout strips) and the intrinsic signal shape. Thus, the following two ratios between two amplitudes are related to the signal shape only, and the time information can be extracted from them:

$$r_0 = \frac{a_0}{a_2} \quad \text{and} \quad r_1 = \frac{a_1}{a_2} \,. \tag{6.2}$$

An empirical parametrization, depending on the signal time t with respect to the TCS phase[1], which is valid for both of these ratios, is given by

$$\begin{aligned} r(t) &= r_m \cdot \exp[-\exp[-s(t')]] \\ \text{with} \quad s(t') &= \frac{a+c}{2} \cdot t' + \frac{a-c}{2}\left(\sqrt{t'^2+b^2} - |b|\right) + d \\ \text{and} \quad t' &= t - t_0 \,. \end{aligned} \tag{6.3}$$

The parameter t_0 is the inflection point, and r_m the maximum ratio at which the function converges due to the exponential decay of the signal. d states the value of the ratio at the inflection point. The sum and the difference of a and c describe the gradients of both parts of $s(t')$, and b the transition width between these parts (see [Din10] for an illustration). These parameters need to be determined for each detector plane individually from dedicated data, which is recorded with different latency settings, with a special time calibration procedure for each beam time [Din10, Zim11].

The signal parametrization is given by equation (6.3) in an analytical form. Thus, the signal time can be directly reconstructed from its inverted form [Lee11]

$$\begin{aligned} t(r) &= t_0 + s^{-1}\left(-\log\left[-\log\left(\frac{r}{r_m}\right)\right]\right) \\ \text{with} \quad s^{-1} &= \frac{1}{2ac}\left[(a+c)\cdot f(x) - (a-c)\cdot\sqrt{f(x)^2 + acb^2}\right] \\ \text{and} \quad f(x) &= x - d + \frac{|b|}{2}\cdot(a-c) \,. \end{aligned} \tag{6.4}$$

From the two ratios r_0 and r_1, for each hit strip two times are calculated. Their errors depend on the uncertainties in the amplitude measurement, and are asymmetric due to the strong curvature of the signal shape. The two time values are merged to one strip time, weighted by the single errors, with a common error obtained by proper propagation, as explained e.g. in [Nag05]. When clusters are built from adjacent strips (see section 6.2), the times of their contributing strips are combined to a common cluster time in the same way.

---

[1] The TCS phase is the difference between the rising edge of the TCS clock and the trigger time. Taking it into account increases the precision of the time information.

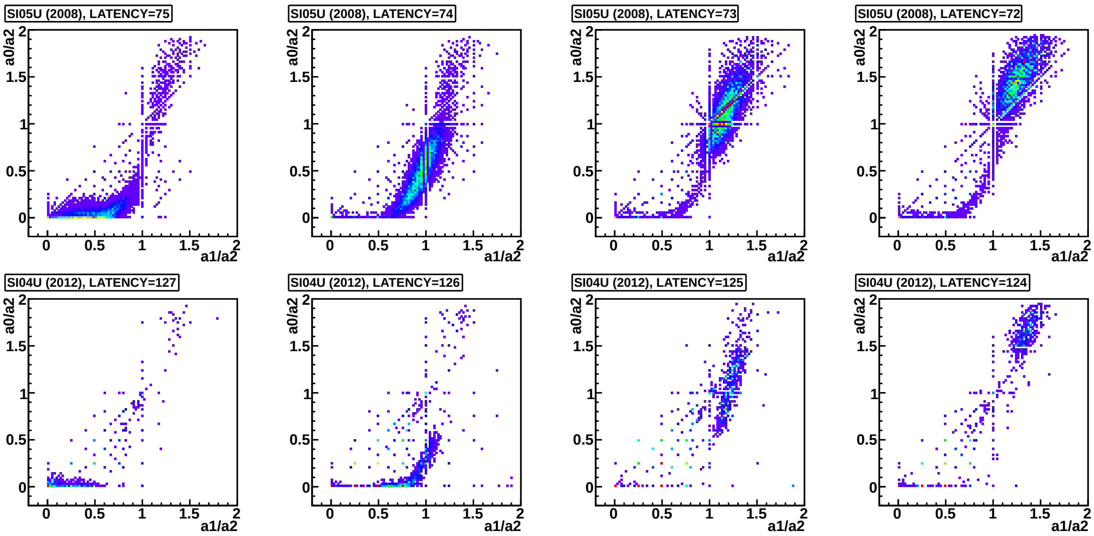

Figure 6.1: Ratio plots of r_0 vs. r_1 for warm (top) and cryogenic (bottom row) detectors (exemplarily for module `SI 1.11` 10-side) during a latency scan. The typical curve (see text) is passed ≈ 30 % faster with cold APVs. As these plots are taken from the online monitoring, the artefact lines stemming from the division of amplitudes featuring small integer values are still visible.

The intrinsic signal shape depends mainly on the shaping circuit parameters of the APV chip, but also on its temperature. Thus, the signal shape differs noticably between warm and cold AVP chips, even if the settings for the preamplifier and shaper are kept the same, which is the case for the COMPASS silicon detectors[2].

The differences in the signal shapes are, on the online level, already apparent during the latency scan[3]. The changes of both r_0 and r_1, plotted against each other for different latency settings (one unit difference is equivalent to 25.8 ns) is depicted exemplarily in figure 6.1. The detector plane shown is the 10chip-side of module `SI 1.11`, which was installed as `SI05U` in 2008 and `SI04U` in 2009 and 2012 (see table A.2). The top row depicts four different latency settings during the scan from 2008, when this detector was operated warm, and the bottom row four different settings from 2012 with cold operation[4]. In both cases, with the highest depicted value of latency in the most left plot, the three samples a_0, a_1 and a_2 are taken at a very early time, so that $a_0 \approx 0$. With lower latencies, later sample points of the signal are read out, resulting in both r_0 and r_1 rising, and finally becoming larger than 1, when a_2 lies on the falling edge of the signal (see also figure 6.2). The latency values chosen for data taking have been a setting between the first and the second one in the top row for 2008, and the setting of the second plot on the bottom row for 2012.

For APV chips used at cryogenic silicon detectors operated at 200 K, the typical curve is

---

[2] The settings for VFS, VFP, and ISHA have been kept up to and including 2012. They might potentially change in the future, if dedicated work on the cold signal shape can be accomplished successfully.

[3] Latency scans are carried out to confirm or adjust the proper latency setting.

[4] The absolute scale of the latency settings differ significantly between 2008 and 2012, as the digital calorimeter trigger used in 2012 needs additional delays.

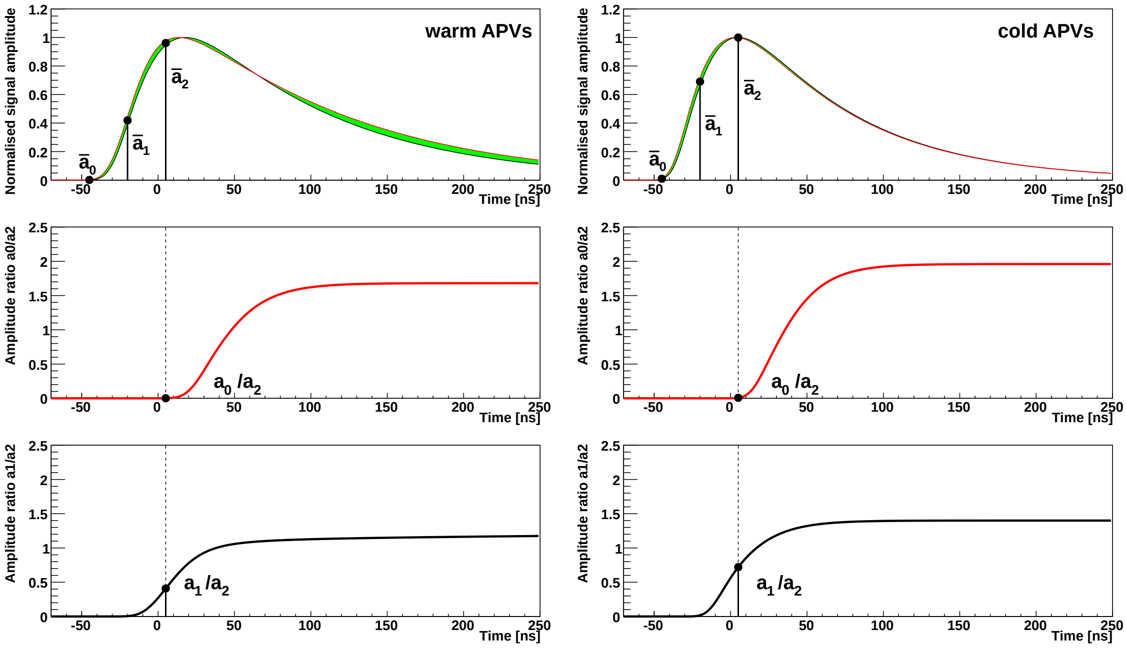

Figure 6.2: Comparison of the APV signals for warm (left) and cold (right) detectors, adapted from [Zim11]. The mean postion of the samples is marked. For signal shapes as well as the single ratios, the red curve is constructed from the r_0 and the black curve from the r_1 time calibration parameters.

passed ≈ 30 % faster than with detectors at approximately 60 °C. The maximum ratios $r_{m,i}$ of both ratios r_i (see before) change from $r_{m,0} \approx 1.5$ and $r_{m,1} \approx 1.22$ to $r_{m,0} \approx 2$ and $r_{m,1} \approx 1.43$ (slightly depending on the detector plane). These values are directly related to the decay time τ of the signal, which decreases from $\tau \approx 127$ ns to $\tau \approx 74$ ns [Zim11]. The full curves $r_0(t)$ and $r_1(t)$, from which the signal shape can be obtained independently but with differences of only a few percent, are depicted in figure 6.2. They can be reconstructed from the parameters introduced with equation (6.3), which are obtained from the time calibration of exemplary detector planes. The differences between the signal shapes of warm and cold APVs are also visible here as stated before.

6.2 Clustering and Position Reconstruction

A single particle crossing the detector volume produces a charge cloud of typically 5 − 10 µm width. Thus, this charge is expected to induce a signal to one, or if the charge is shared, at maximum two readout strips. Two particles traversing the detector very close to each other, may cause signals on up to three or four adjacent strips, while hits accompanied by high-energetic δ-electrons can even affect more than five readout strips.

The determination ot the hit position of a particle is done during the *clustering* process of the data reconstruction. The applied algorithm combines adjacent strips with signals above noise level to *regions*. The time information of the single strips (see section 6.1) is used to distinguish between accidental contributions, e.g. from neighbouring noisy

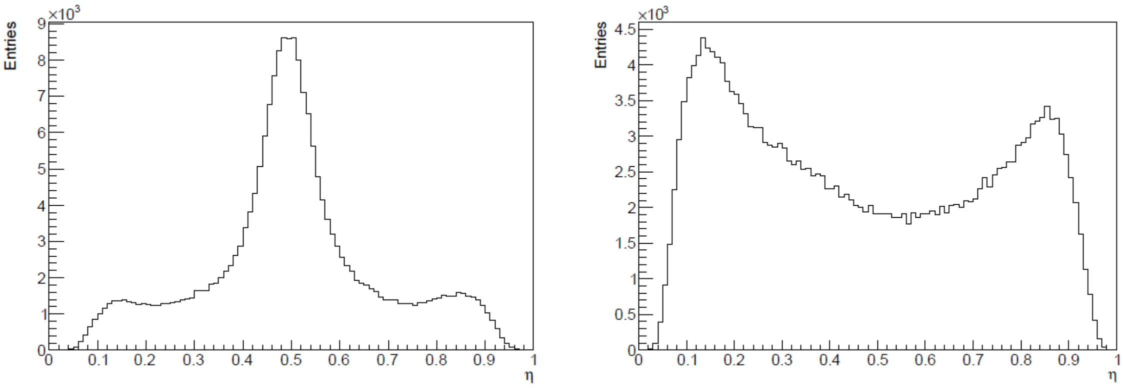

Figure 6.3: Charge distribution η for a readout plane with (left) and without (right) intermediate strips, from [Lee11].

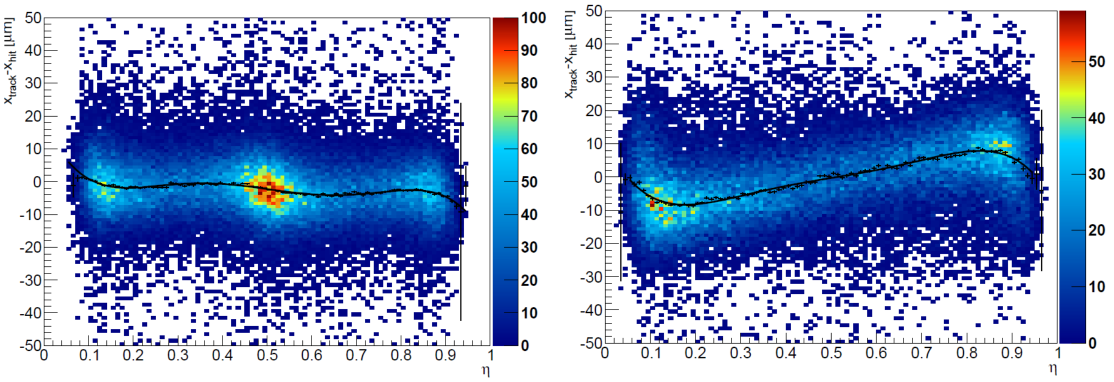

Figure 6.4: Residual distribution vs. charge sharing factor η for a readout plane with (left) and without (right) intermediate strips, from [Lee11].

channels, and real clusters, where contributing neighbouring strips need to provide a time consistent with each other. This method, including some extensions, is called *Cinderella clustering*, as it was first implemented in the online filter [Nag05].

For a cluster consisting of one strip only, the hit position is assigned to the center of this strip, providing a precision of $1/\sqrt{12}$ times the pitch in first order. For clusters with more strips, usually a center-of-gravity method, that weights the strips' positions with their recorded amplitudes, is applied to calculate the effective cluster position.

The charge sharing between adjacent strips is observed to be a non-linear process. For two-strip clusters, it can be characterized by the charge distribution η, which describes the fraction of the amplitude of one strip related to the sum of both contributing amplitudes. η is found to differ significantly between detector planes with and without intermediate strips (see section 3.3.1): The capacitive coupling those provide, clearly enhances $\eta \approx 0.5$, i.e. equal charges are collected on both readout strips, while without them, the main part of the charge is seen by one strip only, as depicted exemplarily in figure 6.3.

The distributions of the residuals, i.e. the differences of the hit positions from a simple center-of-gravity approach to the track positions, can be fitted by 4th- or 6th-order polynomials for sensor sides without and with intermediate strips, respectively, see figure 6.4. This information is used to correct the position of two-strip clusters during the clustering step.

For three-strip (or even more-strip) clusters, the situation is more complex. These originate either from misidentified two-strip clusters, that picked up an additional low-amplitude strip caused by noise, or from overlapping clusters or δ-electrons. In all cases, the spatial resolution, and thus the detector performance, becomes significantly worse the more three-strip clusters are observed and treated with a simple center-of-gravity approach. Their improved treatment is discussed in great detail in [Lee11] and only summarized in the following.

Concerning the identification of misidentified two-strip clusters, three- (and four-) strip clusters are checked if their border strips feature amplitudes lower than a certain threshold (15 ADC channels), and, if present, those low-amplitude strips are removed, so that a two-strip cluster remains. Stricter general cuts on the time information have also been investigated, but found to be inefficient for this purpose, as low amplitudes have higher relative uncertainties in time, so that also regular two-strip clusters are more often split.

Due to the double-sided readout, both readout sides see the same amount of charge induced in the active volume by a traversing particle. Thus the observed signal amplitudes of both sides are expected to agree within the noise uncertainties. This knowledge of the *amplitude correlation* can be exploited to identify clusters that overlap in one of the two projections only, or δ-electrons. Thus, all clusters with a size of more than 3 strips after the Cinderella clustering explained above, are selected for an additional step, called *mate clustering*. The sums of cluster amplitudes of two single-strip or two-strip clusters in one projection are compared to the cluster amplitudes of clusters consisting of more than two strips in the mate plane[5] (*amplitude matching*). Three different cases are treated here. For *real mates*, where the amplitude matching is successful within the consistency criteria, two clusters are created from the large cluster. Its amplitude is split proportional to the two amplitudes of the two clusters of the mate plane. If the amplitudes do not match, three-strip clusters are separated into two clusters statically. Thereby the amplitude of the central strip is divided equally between the two new neighbouring clusters (*factor 0.5*). If one of these is a fake cluster, it is likely to be discarded during the tracking, so that is does not harm. δ-electrons can pass distances in the order of several 100 µm in the silicon, resulting in large *δ-clusters*. In this case, only one border corresponds to the hit of the traversing particle. Thus, for clusters consisting of at least four strips, the two strips at each border are used to create two new clusters, of which one is supposed to refer to the original hit.

---

[5] The mate plane of a U plane is the V plane of the same detector, etc.

6.3 Comparison of Warm and Cryogenic Detectors

The performance of warm and cryogenic silicon detectors operated in the COMPASS experiment is listed in the following. The results available refer to selected data sets, for which optimizations have been applied during the respective analyses described in [Din10, Zim11, Lee11]. This means, in most cases, the performance of the warm detectors used during the 2004 Primakoff beam time is compared to the performance of the cold detectors from the 2009 Primakoff beam time. Direct comparisons between those might not be 100 % conclusive, as simply the modules were different and operated with different readout electronics, and the warm 2004 modules might have suffered already from radiation damages resulting in higher noise. The time resolutions and spatial resolutions achieved for the respective cases are presented, accompanied by the temperature stabilities, the observed signal-to-noise ratios, and some words on the impact on the tracking.

6.3.1 Temperature Stability

The temperature stability of the silicon detectors, in particular of the APV chips, is important for reliable signal output from the APVs.

For the warm silicon detectors with gaseous nitrogen cooling, no regulation system was employed, and the temperature of the detectors and the APVs was varying typically by up to 10 °C within a beam time.

The temperatures of the cryogenic detectors are controlled by a PLC (see section 4.5), which is able to keep the temperature fluctuations on the wafer below 1 K, resulting in comparable values for the APV temperature. Nevertheless, the system is quite sensitive to distortions. In July 2009, the cooling of `SI05XY` became instable as an after-effect of a thunderstorm. The nitrogen flow necessary for a reliable cooling could not be reached any more, so that the regulation system did not succeed to keep the detector at 200 K, and finally a regulation to 220 K for this sensor had to be chosen. The suspected reason was a partial blocking in the capillary circuit, i.e. at one of its epoxy connectors (see section 4.4). This problem was solved only before 2012, the next beam time involving `SI05`. For the 2012 beam time, the temperatures in the conical cryostat could be regulated to 200 K with temperature oscillations of up to $+10$ K only[6]. The situation was improved (i.e. the frequency of large fluctuations was reduced) by adapting the PID parameters, but could not be solved satisfactory on the software side. The origin of the problem seems to be related to hardware problems, i.e. concerns presumably the transferline and/or the phase separator, which could not be convincingly identified and solved during the beam time.

---

[6] The temperature rises from time to time. When 210 K are reached, a cooling down of the detector concerned is carried out, so that 210 K are never exceeded unless more serious problems appear

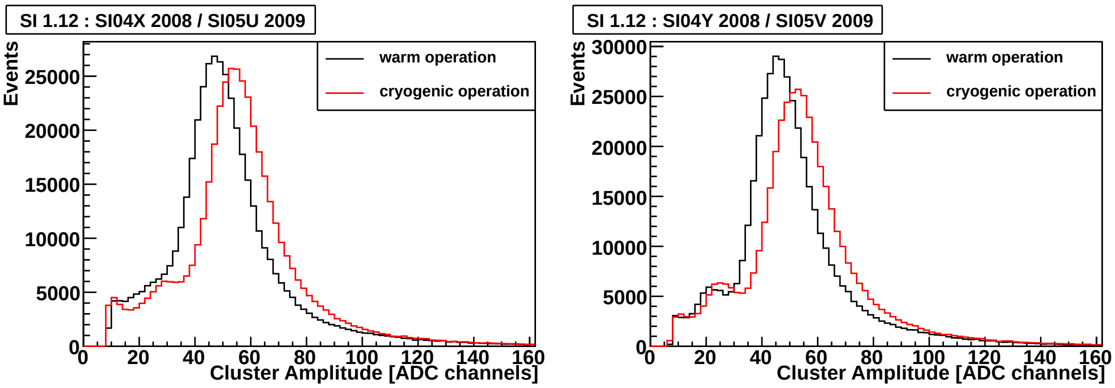

Figure 6.5: Cluster amplitudes for `SI 1.12` for n-side (left) and p-side (right) for non-cryogenic (2008, black lines) and cryogenic (2009, red lines) operation. This detector module changed its place from `SI04XY` in 2008 to `SI05UV` in 2009.

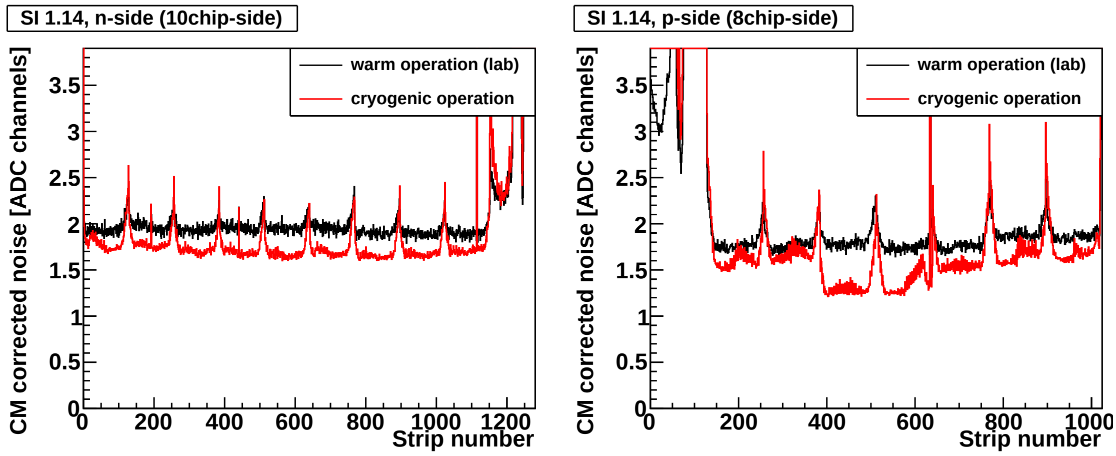

Figure 6.6: Common-mode corrected noise for the n-side (left) and p-side (right) of the detector module `SI 1.14` during warm operation in the lab (black lines) and cryogenic operation in the experimental area (red, `SI02XY` in 2012). The high noise at the chip 10 at the 10-side and chip 1 at the 8-side is a feature of all COMPASS silicon detectors, see also figure A.1.

6.3.2 Signal-to-Noise Ratio

The important quantity to judge the usability of a particle detector is its signal-to-noise ratio, i.e. whether signals can be reliably identified and extracted. For the COMPASS silicon detectors, both the signal amplitude and the noise of a readout plane in working conditions depend on the electronics employed[7] and the radiation impact this detector has collected already. Thus, for pure comparisons of the impact of cryogenic temperatures, the detector modules in the conical cryostat, which have been operated warm in 2008 and cold in 2009, need to be addressed.

---

[7] Two different versions of the APV25 readout chips are employed. The S0 version, used only for the very first detector modules, i.e. those assembled in the warm setup in `SI01` and `SI02`, delivers both lower noise and lower amplitudes than the S1 version used for all subsequently built modules. In addition, both quantities were reduced again with the new repater cards used with the new detector modules.

Figure 6.5 compares the cluster amplitudes for an exemplary detector module (`SI 1.12`) in 2008 and 2009. The most probable value increased from 47 ADC channels for the n-side and 45 ADC channels for the p-side to 54 and 53 ADC channels, respectively, for cryogenic operation. At the same time, the noise level was kept at the same average value of $\approx$ 2.1 ADC channels[8], which allows for more relatively low amplitudes to be recorded, and more two-strip clusters potentially to be reconstructed.

This is not apparent from a comparion of the η distributions of the detectors in the conical cryostat in 2008 and 2009. The detectors installed there feature intermediate strips which enhance charge sharing in any case, and they showed locally higher noise due to a bad capacitor configuration (see section A.1.2 and figure A.1) which disturbed the overall distribution. Nevertheless, comparing the warm detectors from 2004 to the cryogenic detectors from 2009[9], the improved signal-to-noise ratio results in enhancements of the η distribution at high and low values for 2009 (figure 6.3 compared to the corresponding figure 4.17 from [Din10], which shows the η distribution of warm detectors from 2004). This means, small amplitudes are more likely to exceed the noise level and thus to be recorded. Like this, the spatial resolution of the gained two-strip clusters is obviously improved with respect to the previous single-strip clusters.

The comparison of the noise level during warm and cryogenic operation of a detector, is exemplarily shown for the detector module `SI 1.14` in figure 6.6. The warm noise level was recorded during the test in the lab after the removal of the unnecessary capacitors (see section A.1.2) and amounts in average to 1.95 and 1.83 ADC channels, respectively, for the n-side and the p-side. The noise level during cryogenic operation was recorded in the experimental area in 2012, where 1.74 and 1.57 ADC channels were obtained. When these values are combined with the increased cluster amplitudes in cryogenic operation, the signal-to-noise ratio is found to be drastically improved. The typically specified ratio of the cluster amplitude divided by the averaged common-mode corrected noise, increases from $S_{\text{clus}}/N_{\text{cor}} \approx 24$ with warm operation to $S_{\text{clus}}/N_{\text{cor}} \approx 32$ with cryogenic operation, an improvement by 33 %.

6.3.3 Time Resolution for Warm and Cold Detectors

The numbers for time resolutions given in the following refer to the time of clusters, which is the relevant quantity for the further treatment of detector information in the tracking process.

For the warm silicon detectors used in 2004, time resolutions (gaussian sigmas) of 3.0 ns for readout sides with intermediate strips (i.e. the p-side of all detectors concerned) or 2.0 ns for sides without intermediate strip (i.e. the n-side) have been reached for the

---

[8] Slight changes of less than ±10 % have been observed between 2008 and 2009. As the noise level was observed to also depend on the specific place inside the conical cryostat, which changed for all modules as well, no change due to the cryogenic operation can be claimed from this specific comparison.

[9] I.e. comparing to detectors from the 2009 production (see section A.1.2), which did not feature the bad capacitor configuration and such show an overall satisfactorily low noise level.

hadron run, and 4.0 ns or 2.8 ns, respectively, for the muon run. A systematic offset between the time of a single strip and the combined time of two strips to a cluster time was observed, which accounts for 1 ns (for the n-side) and 2.5 ns (for the p-side), respectively, which caused the worse time resolution of the planes with intermediate strips (and hence more two-strip clusters). For tracks that are reconstructed with the information of at least 10 silicon projections contributing, a most probable track time error of 530 ps is achieved, and all track time errors are distributed within 1 ns (from [Din10]).

A preliminary comparison of a detector module used in both warm and cryogenic operation in 2008 and 2009, respectively, was carried out in [Zim11]. Cryogenic operation, which features a steeper signal shape, was found to lead to an improved time resolution of 1.4 ns in the best case for both muon[10] and hadron beam, and 2.2 ns for hadron beam and 2.5 ns muon beam in the worst case. For non-cryogenic operation in the hadron beam 2008, a best time resolution of 1.8 ns (for a plane without intermediate strips), and 3.0 ns in the worst case (for a plane with intermediate strips), were obtained. Concerning non-cryogenic operation in muon beam, the above stated 2.8 ns or 4.0 ns, are the only comparison values available[11]. If the difference of 2 ns of the mean timing for different cluster sizes, mentioned in the previous paragraph, is corrected for in addition, an improvement of up to 10 % is observed. Particularly, all detectors planes show time resolutions better than 2.0 ns for hadron beam.

A subsequent analysis focussed particularly on the cryogenic silicon performance during parts of the the 2009 Primakoff data taking [Lee11]. For this data, an average intrinsic RMS, i.e. with the track time error unfolded, of 1.84 ns was obtained. The corresponding average gaussian sigma, ignoring the outliers of the time distribution, is 1.68 ns. All planes reached a time resolution better than 2.5 ns RMS for both muon and hadron beam. A worse performance in the muon data, as observed for the warm 2004 detectors [Din10], is not seen here. This is explained by the absence of significantly more pileup usually observed with the muon beam, as the cryogenic signal is faster, and for the Primakoff data 2009, the muon beam featured only 1.3 times the intensity of the hadron beam. If the time information of the two planes of one sensor is combined to one time information by exploiting the amplitude correlation, time resolutions between 1.08 ns and 1.46 ns are reachable.

6.3.4 Spatial Resolution

The spatial resolution of a detector plane is evaluated by its *residual* distribution. This describes the distance of a track reconstructed without information from the plane under investigation to the position of the nearest reconstructed cluster in the coordinate system the plane provides.

---

[10] In this specific case, the muon beam refers to the muon beam used during the 2009 Primakoff beam time for comparison issues in the polarizability analysis.

[11] A few days of muon beam for a DVCS test were also taken in 2008, but this data have not been analyzed from the silicon performance point of view.

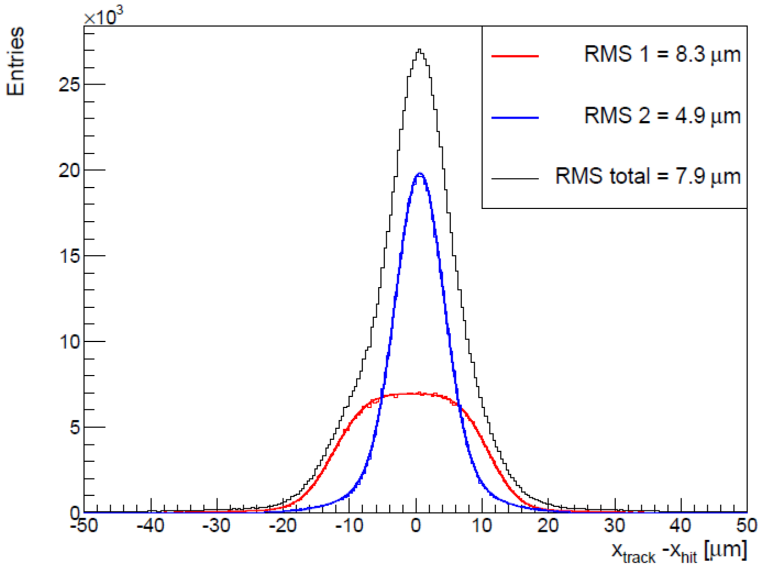

Figure 6.7: Exemplary residual distribution from the Primakoff 2009 muon data, from [Lee11].

For the warm silicon detectors used in the 2004 hadron run, spatial resolutions for single-strip clusters of 14 μm or 9 μm, for readout sides without and with intermediate strips, respectively, were obtained. For the corresponding two-strip clusters, spatial resolutions of 6 μm or 5 μm, respectively, were achieved [Din10].

In first comparisons of spatial resolutions in hadron beams for warm and cryogenic operation, detectors in the conical cryostat from 2008 and 2009 were investigated. For these overall spatial resolutions of around 13 μm were obtained. Two-strip clusters reached resolutions between $5 - 12$ μm, and single-strip clusters between $11 - 15$ μm for both cryogenic and non-cryogenic operation [Zim11]. The detectors under investigation featured intermediate strips on both readout sides. As the comparing analysis was based on a preliminary alignment, the full potential of the silicon detectors could not be exploited at the time of this analysis.

A more detailed analysis of the Primakoff 2009 data using cryogenic detectors, based on the muon beam part, was carried out with a preselected data set and used a sophisticated run-by-run alignment. For single-strip clusters a reachable standard deviation of $\sigma = 6.4$ μm is exemplarily stated, which corresponds to an effective pitch[12] of 22 μm. The overall spatial resolution depends drastically on the fraction of two-strip clusters, which is between 33% and 67%. This value depends dominantly on the presence of intermediate strips, so that in average 34% without and 57% with them, respectively, are observed. For the average intrinsic spatial resolution of the whole plane, i.e. with the uncertainty of the track unfolded, 6.8 μm with and 8.5 μm without intermediate strips are obtained.

---

[12] The fact that a single-strip cluster occurs, provides already some spatial information. It means, that the particle crossed the sensor near the center of a strip, and not in the middle between two strips, because in the latter case the charge would be shared between two strips.

The smallest value achieved is 5.0 µm, and all planes are found to be better than 10 µm. As the best result for two-strip clusters a spatial resolution of 3.3 µm was reached (all numbers are taken from [Lee11]). Figure 6.7 shows an exemplary distribution of the distance of cluster positions to the reconstructed tracks, with the distributions of single-strip and two-strip clusters plotted separately, while bigger cluster sizes are contained in the overall distribution only.

With the 2009 Primakoff data with hadron beam, the optimization of the treatment of three-strip clusters was studied in detail [Lee11]. For the case of presumably misidentified two-strip clusters, the RMS of the spatial resolution could be reduced from 21.7 µm to 7.8 µm. For this case, also the number of clusters within a range of ±25 µm increased by 40 %. This approach affects approximately 70 % of all previous three- or four-strip clusters. It prevails especially for the detectors in the conical cryostat, where a bad capacitor configuration (see section A.1.2 and figure A.1) and a worse overall grounding caused a slightly increased noise level. The detector module `SI05XY` also suffered from a worse cooling stability, which also increased the noise.

Also the performance of the mate clustering was examined for the Primakoff 2009 hadron data [Lee11]. For the clusters concerned, the RMS of the spatial resolution is reduced to less than half of the original value (i.e. the uncertainties are reduced from values of in the range of $38 - 43$ µm to $13.5 - 18.6$ µm). In 50 % to 75 % of all these cases, the factor 0.5 method is applied, while the splitting due to real mates is performed in average for 12 % of all cases (varying from 5 % to 22 %, depending on the detector plane involved).

6.3.5 A Glimpse to Efficiencies and Tracking Issues

Efficiency is defined as the ratio of the number of observed hits in a plane by the number of expected hits, which is defined by the reconstructed tracks. For the cold detectors, an average efficiency of all silicon planes of 99.1 % for muon beam and 99.3 % for hadron beam is obtained for the Primakoff 2009 data [Lee11].

The amplitudes read by the APV chips depend strongly on the TCS phase (see section 6.1). Consequently, also the time and spatial resolution, which are worse for lower amplitudes, are affected. As the signal of cold APVs is significantly faster, the latency is set such, that the major part of the recorded signals features significant amplitudes. Events triggered at the very beginning or end of the TCS phase may thus feature worse resolutions. An effect of a few percent of the mean number of reconstructed tracks in the downstream silicon detectors, dependent on the TCS phase, for the Primakoff 2009 data has been reported [Gus12].

The impact to tracking resulting from the improved treatment of three-strip clusters was investigated in a first analysis [Lee11]. Depending on the reconstruction option and the specific physics channels studied, a gain of up to 2.3 % of reconstructed events is found. The clearest impact occurs for small decay angles of charged particles, where the tracks are more likely to be very close to each other and can be distinguished significantly better with the improved algorithm.

6.3.6 Summary

The cryogenic operation of the silicon detectors obviously demands higher efforts compared to the warm operation. This concerns the necessary time budget and manpower for the commissioning and operation of the cooling system and the cryostat infrastucture, as well as investment costs for additional hardware. Also highest caution during handling of the complete system has to be assured, as any cooling incidents or vacuum problems may lead to losses of beam time or even destroyed detectors in the worst case. This has to be compared to the obvious benefits of the cryogenic operation.

The control of the cooling delivers more stable temperature conditions for the operation of the APVs with lower uncertainties. Better time resolutions of the cryogenic detectors stem from the faster APV signals. The improved spatial resolutions are attributed to lower noise and negligible leakage currents of cold detectors. The fact that several detectors, especially in the conical cryostat, suffered from increased noise at the central channels of the APVs, affected both the warm 2008 and the cold 2009 data, and is not related to cooling.

Concerning the time resolution of the detectors, the best achievement for warm detectors from 2004 hadron data states 3.0 ns and 2.0 ns gaussian sigma depending on the presence of intermediate strips. This compares to 2.0 ns and 1.4 ns resolution that were achieved for the cryogenic 2009 Primakoff data as presented in table 6.1. Further optimizations exploiting the amplitude correlations suggest that the cryogenic detectors can potentially reach time resolutions between 1.08 ns and 1.46 ns.

The overall spatial resolutions depend on the presence of intermediate strips as well. For the warm operation, resolutions of 8 µm (with) and 11 µm (without them) are reached, compared to 6.8 µm and 8.5 µm with cryogenic operation. This is correlated to the fraction of double-strip clusters, that concern 50% and 30% for the warm, and 57% and 34% for the cryogenic case, as given in table 6.2. Thus, the improved spatial resolutions can be traced back to charge sharing, as more double-strip clusters with very high or low values of η could be reconstructed with the cryogenic detectors, due to their higher signal-to-noise ratio. Nevertheless, for the comparison of the numbers from above, it has to be stated that for the data with cryogenic detectors a more sophisticated run-by-run alignment has been applied. This is also necessary to achieve the best resolutions, but its effects have not been disentangled from the improvements caused by the cryogenic operation itself.

A major step towards exploiting the full potential of the spatial resolution is the improved treatment of clusters consisting of more than two strips. The effects were only studied for cryogenic detectors, but show nevertheless the importance of this implementation for physics channels with particle tracks close to each other.

Detector Type	Warm	Cryogenic
Intermediate Strips	3.0 ns	1.8 ns
No Intermediate Strips	2.0 ns	1.4 ns
Potentially		1.08 – 1.46 ns

Table 6.1: Comparison of the average time resolutions obtained from Gaussian fits for warm and cryogenic silicon detectors [Din10, Lee11]. The resolution achievable with further optimizations exploiting amplitude correlations is also given.

Detector Type		Warm	Cryogenic
Intermediate Strips	Average	8 µm	6.8 µm
	- Single-strip cluster	9 µm	(7.4 µm)
	- Two-strip cluster	5 µm	(4.1 µm)
	Nb. of Two-strip clusters	50 %	57 %
No Intermediate Strips	Average	11 µm	8.5 µm
	- Single-strip cluster	14 µm	(11.1 µm)
	- Two-strip cluster	6 µm	(5.5 µm)
	Nb. of Two-strip clusters	30 %	34 %
Best Plane	Average		5.0 µm
	- Two-strip cluster		3.3 µm

Table 6.2: Comparison of spatial resolution as average numbers and for cluster sizes one and two for warm and cryogenic silicon detectors. Numbers are taken from [Din10] for warm detectors and from [Lee11] for cryogenic detectors. Values given in brackets are averaged from the values provided in table 5.5 in [Lee11]. All numbers have been achieved still without the improved treatment of clusters consisting of more than two strips.

Chapter 7

Meson Spectroscopy at Low Momentum Transfer

The goal of spectroscopy is the identification of all resonances and non-resonant short-lived states in experimental data and the determination of their quantities, i.e. the masses and widths of resonances and their quantum numbers, and the strength of the contribution and properties of non-resonant states. These intermediate states can be produced by scattering of high-energetic particles (e.g. pion, kaons or protons) off nuclear or hydrogen targets, so that a wide range of kinematics and physics processes is available. The short-lived intermediate states are usually reconstructed from their decay products, i.e. a specific combination of final state particles like charged pions.

This chapter deals with the basic concepts of meson spectroscopy at low momentum transfer from the beam to the target, such providing the basic knowledge for the analyis of $\pi^-\pi^-\pi^+$ events presented in chapter 9. Section 7.1 starts with the introduction of the basic features of meson spectroscopy. This includes also non-resonant dynamics that can be calculated in the framework of Chiral Perturbation Theory (ChPT). Scattering processes of mesons at low momentum transfer feature two production processes. The main contribution results from diffractive production by Pomeron exchange, as summarized in section 7.2. At lowest momentum transfer, Primakoff (or Coulomb) production featuring photon exchange (section 7.3) becomes also significant and is of high interest: At low masses, down to the threshold of the investigated final state, calculations of ChPT are supposed to be applicable, while at higher masses, i.e. in the range of resonances, radiative coupling of the $a_2(1320)$ [SELEX01], and potentially also of heavier resonances, can be extracted. Also the interference of diffractive and Coulomb production of these resonances can be studied.

7.1 Meson Spectroscopy and Non-Resonant Dynamics

This section summarizes the basic features of meson spectroscopy including non-resonant contributions to the meson spectrum. It covers the properties of ordinary and spin-exotic mesons, including their basic quantum numbers and their description by Breit-Wigner functions in case of resonances. The kinematical variables important in the experimentally observed scattering processes are also introduced. In addition, the basic idea of Chiral Perturbation Theory (ChPT), describing non-resonant scattering at threshold, is presented and illustrated with the results for non-resonant $\pi\gamma \to 3\pi$ scattering, which are an important input to the analysis presented in section 9.4.

7.1.1 Meson Resonances

In the naive constituent-quark model, mesons are described as color-neutral quark-antiquark ($q\bar{q}$) objects and characterized by their quantum numbers J^{PC}, with the total angular momentum J, parity P and charge conjugation C, which is only properly established for neutral mesons. The meson's total spin J is composed from the total intrinsic spin S and the relative orbital angular momentum L of the $q\bar{q}$ pair, $J = L \oplus S$. The quantum numbers are extended by the isospin I and the G-parity G, defined as a charge conjugation operation followed by a rotation in isospin space around the y axis. I^G are both conserved in strong interaction. For $q\bar{q}$ pairs, these quantum numbers fulfill the following relations:

$$P = (-1)^{L+1} \qquad C = (-1)^{L+S} \qquad G = C \cdot \mathrm{e}^{i\pi I_2} = (-1)^I C = (-1)^{L+S+I} \tag{7.1}$$

Quantum numbers violating these rules, e.g. $J^{PC} = 0^{+-}, 1^{-+}, 2^{+-}, 3^{-+}, \ldots$, are thus not possible for $q\bar{q}$ pairs. If states with these *spin-exotic* quantum numbers can still be established, they are interpreted as states beyond the constituent-quark model, featuring gluonic excitations (g) or more than two quarks, like glueballs (gg), hybrids ($q\bar{q}g$) or tetraquarks ($qq\bar{q}\bar{q}$). These are still allowed by Quantum ChromoDynamics (QCD), but difficult to identify if they feature the same quantum numbers as $q\bar{q}$ pairs and mix with those. Thus they are only clearly observed in terms of mesons with spin-exotic quantum numbers. Such spin-exotic states have been reported, also at COMPASS, but need further clarification and are such still subject of current interest (see section 2.1.1.2 and [Wei08a, Neu12, Haa12] for comprehensive information).

Resonances occur as peaks in the production cross-section dependent on the mass of the system under investigation. As a prominent example, a clear enhancement of the cross-section of electron-positron scattering in the mass region around $0.8\,\mathrm{GeV}/c^2$ with a width of $150\,\mathrm{MeV}/c^2$ is interpreted dominantly by the $\rho(770)$ resonance which decays into two pions. Resonances are short-lived states, that decouple their production method from their decay mode. They can be regarded as quasi-stable intermediate states, that come along with a relative phase between the waves of the incoming and the outgoing particles of the scattering process.

Mathematically, resonances can be described by a pole of the scattering amplitude similar to stable particles. While the pole for a stable particle is a real value of the center-of-mass energy s, the pole of a resonance lies in the analytic continuation into the complex s-plane below the real axis. Thus the mass dependence is usually parametrized by a relativistic Breit-Wigner function $\Delta(m)$ with mass-dependent width $\Gamma_T(m)$, with m_0 the nominal

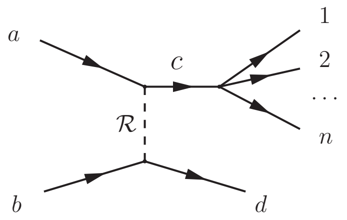

Figure 7.1: General sketch of the scattering process of a high-energetic beam particle a impinging on a target b that recoils as d, whereby a is excited to the intermediate state c which subsequently decays. The interaction is arranged by the exchange particle $\mathcal{R}$.

mass and Γ_0 the nominal width of the resonance:

$$\Delta(m) = \frac{m_0\,\Gamma_0}{m_0^2 - m^2 - i\,m_0\,\Gamma_T(m)} \tag{7.2}$$

The mass-dependent total width is given by

$$\Gamma_T(m) = \sum_n \Gamma_{0\,n} \frac{m_0}{m} \frac{p_n}{p_{0\,n}} \frac{F_{L\,n}^2(p_n)}{F_{L\,n}^2(p_{0\,n})} \quad \text{with} \quad \Gamma_{0\,n} = \Gamma_n(m_0) \tag{7.3}$$

which contains a sum over all the partial widths $\Gamma_{0\,n}$ of all n possible decay channels of this resonance. p_n states the breakup momentum of a particular decay, and $F_{L\,n}$ the angular momentum barrier factors given in detail in section 8.2.1.3. For unknown branching ratios, a Breit-Wigner function with constant width Γ_0 is usually chosen as best approximation.

The parametrization of resonances by a Breit-Wigner function has the practical feature, that for the establishment of a (new) resonance, not only its intensity parameters (mass and width), but also its relative phase, especially with respect to another resonance, are required.

7.1.2 Scattering Processes

The analysis following in chapter 9 will deal with exclusive scattering processes of high-energetic beam impinging on a fixed target at relatively low momentum transfer. The basic observations are based on diffractive scattering (see section 7.2), but the properties summarized here apply for Primakoff scattering (see section 7.3) as well. Such processes are very generally written as

$$a + b \to c + d \quad \text{with} \quad c \to 1 + 2 + \ldots + n \tag{7.4}$$

with a the beam particle that just grazes the target particle b, which recoils at small momentum transfer as d. a is excited to the intermediate state c that subsequently decays into n particles (see figure 7.1). c is often referred to be a resonance in the simple picture, but of course also non-resonant states can be created here. The target supplies the exchange particle[1] $\mathcal{R}$, but stays itself intact[2] during the reaction. The quantum numbers I^G and the electric charge of the beam particle a are conserved for the excited particle c. Momentum and angular momentum L are transferred from the target to the beam particle, but only negligible energy is transferred, so that the process can be regarded as *exclusive*. The beam energy E_a is such in a good approximation equal to the energy of the excited particle E_c, which is reconstructed from the energies of its decay products

$$E_a \approx E_c = E_1 + E_2 + \ldots + E_n \,. \tag{7.5}$$

The scattering process can be described by two kinematic variables composed of the four-momenta p_a, p_b, and p_c of the participating particles. The squared center-of-mass energy s and the square of the four-momentum transfer t' are given by

$$s = (p_a + p_b)^2 \quad \text{and} \tag{7.6}$$

$$t' = |t| - |t|_{\text{min}} \quad \text{with} \quad t = (p_a - p_c)^2 \tag{7.7}$$

and $|t|_{\text{min}}$ the minimum longitudinal momentum transfer that is needed to excite a to c, i.e. to create the higher mass $m_c > m_a$ (i.e. $|t|_{\text{min}} = 0$ in case of elastic scattering). For high beam energies, $|t|_{\text{min}}$ can be approximated quite accurately in the laboratory system by [Wei08a]

$$|t|_{\text{min}} = \frac{(m_c^2 - m_a^2)^2}{4|\vec{p}_a|^2_{\text{lab}}} \,. \tag{7.8}$$

The reaction features a t-channel exchange, so that factorization of the beam-resonance and the target-recoil vertices can be assumed. This means, that neither the intermediate state c nor its decay particles interact again with the recoil particle d.

7.1.3 Chiral Perturbation Theory

Quantum ChromoDynamics (QCD) has already been introduced before as the gauge theory that describes the strong interaction based on the $\text{SU}(3)_{\text{color}}$ symmetry. It describes the interactions of quarks with the field quanta of the color field, the gluons. The gluons carry a color charge themselves and thus also interact with each other. The key parameter of QCD is the strong coupling constant $\alpha_s(Q^2)$ which varies significantly with the momentum scale (i.e. for Q^2 between $1 - 100\,\text{GeV}^2/c^2$). For processes at high energies (i.e. short distances) $\alpha_s(Q^2)$ is small, which is related to the *asymptotic freedom* of the quarks inside hadrons, so that perturbative calculations in $\alpha_s(Q^2)$ can be carried out and are confirmed experimentally. At low energies (long distances), it becomes instead obvious that quarks and gluons can only exist in bound states of finite size due to the color charge of the gluons (*confinement*). Thus $\alpha_s(Q^2)$ becomes very large, so that such processes cannot

---

[1] In figure 7.1, the labeling $\mathcal{R}$ for the exchange particle is chosen already in anticipation of having reggeons exchanged in diffractive scattering, but includes here also the quasi-real photon of Primakoff interaction.

[2] The following analysis considers momentum transfers which are such small, that nuclear excitations play a minor role.

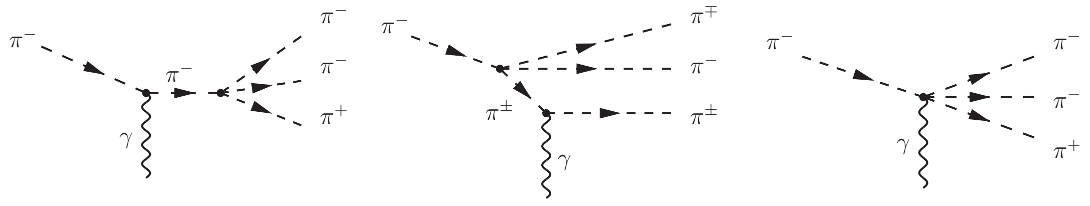

Figure 7.2: Leading order processes in ChPT [KF08] for the reaction $\pi^-\gamma \rightarrow \pi^-\pi^-\pi^+$.

be treated perturbatively in $\alpha_s(Q^2)$. An effective theory is needed that exhibits pions and nucleons as degrees of freedom.

This effective theory can be deduced as sketched in the following. Chiral symmetry is valid for the quark condensate in the vacuum, but it is spontaneously broken. According to the Goldstone theorem massless pseudoscalar $J^P = 0^-$ Goldstone bosons occur, which are quark-antiquark pairs. Here the $\mathrm{SU}(2)_L \times \mathrm{SU}(2)_R$ symmetry is broken down to the vector part of the $\mathrm{SU}(2)$ isospin symmetry. With the explicit symmetry breaking small masses are assigned to the light quarks[3] (u, d) and consequently also to the Goldstone bosons. Chiral Perturbation Theory (ChPT) identifies the experimentally observed π^+, π^0, and π^- mesons with the Goldstone bosons. This theory is perturbative in the symmetry breaking parameters, which is formulated as series expansions in the particle momenta. All inner quark-gluon dynamics are condensed to low-energy constants (LECs). For leading order calculations (tree diagrams) these LECs are the pion mass m_π and the pion decay constant f_π which are known accurately. For the next-to-leading order calculations (loop diagrams) six additional LECs ($\ell_1 \ldots \ell_6$) are needed, which are known with varying precision and can potentially be improved by input from experimental data.

The LECs are used in calculations that finally have to be tested experimentally to establish ChPT as the correct low-energy description of QCD. The most prominent example, the pion-pion scattering length, has been confirmed in kaon decay experiments. Other predictions still wait for experimental confirmation. In addition to the scattering of strongly interacting particles, also electromagnetic processes, i.e. $\pi\gamma$ scattering, can be calculated in the framework of ChPT. Results are available for the radiative pion decay, which is related to the pion polarizabilities [Bur96, Gas06] accessible in the process $\pi\gamma \rightarrow \pi\gamma$ (also studied at COMPASS, see section 2.1.1.1), and for the chiral axial anomaly [Ame01] apparant in $\gamma\pi^\pm \rightarrow \pi^0\pi^\pm$. Also the cross-sections of the processes $\pi\gamma \rightarrow 3\pi$ have been calculated [KF08, Kai10] and are discussed in more detail in the following, as they are relevant for the analysis presented in chapter 9.

The tree diagrams that enter the ChPT calculations at leading order for $\pi^-\gamma \rightarrow \pi^-\pi^-\pi^+$ are depicted in figure 7.2. For their evaluation the *σ-gauge* can be chosen, in which the $\gamma - 4\pi$ coupling vanishes, so that the contribution from the contact graph, i.e. the photon couples to both incoming and outgoing poins as given in the right diagram, van-

---

[3] ChPT covers also strange mesons with s quarks, but those are not needed for the following discussions and thus omitted here.

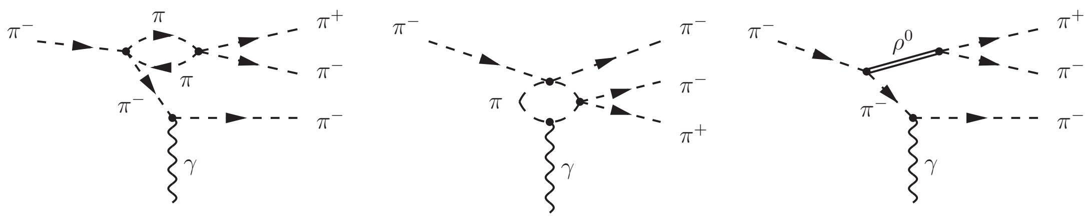

Figure 7.3: Examples for higher order processes in ChPT containing loops (left, middle) and explicit ρ (right) [Kai10, Kai11] for the reaction $\pi^-\gamma \to \pi^-\pi^-\pi^+$.

ishes. Choosing in addition the *radiation gauge* for the photon in the center-of-mass system, also the graph that represents the photon coupling to the incoming beam particle in the left diagram, vanishes. The contribution of the middle diagram, which is exemplary for the three graphs, in which the photon couples to one of the outgoing pions, remains to be written down explicitely [Kai11]. The cross-section depends on the four-momenta k of the photon, p of the beam π^-, $q_{1,2}$ of the two final state π^- and q_3 of the final state π^+. In the following expressions, $\vec{k}$ indicates the corresponding three-momentum vector of the photon ($\vec{q}_i$, $i \in 1,2,3$ accordingly), $\hat{k} = (0,0,-1)$ the corresponding unit vector, and $(\vec{q}_i)_j, j \in x,y,z$, the x, y or z component of the three-momentum vector $\vec{q}_i$, respectively. The unpolarized cross-section for the scattering of a real photon in $\pi^-(p)\gamma(k) \to \pi^-(q_1)\pi^-(q_2)\pi^+(q_3)$ is calculated in the chosen frame as [KF08]

$$\begin{aligned} d\sigma_\gamma(s) = {} & \frac{8\pi\alpha \cdot s}{(s-m_\pi^2)^3 f_\pi^4} \cdot d\Phi_3(p+k, q_1, q_2, q_3) \\ & \cdot \left[\frac{\vec{q}_1 \times \hat{k}}{\omega_1 - \vec{q}_1 \cdot \hat{k}} \left(p_0(\sqrt{s} - \omega_2) - \sqrt{s}\omega_1 - \vec{k} \cdot \vec{q}_2 \right) \right. \\ & + \frac{\vec{q}_2 \times \hat{k}}{\omega_2 - \vec{q}_2 \cdot \hat{k}} \left(p_0(\sqrt{s} - \omega_1) - \sqrt{s}\omega_2 - \vec{k} \cdot \vec{q}_1 \right) \\ & \left. + \frac{\vec{q}_3 \times \hat{k}}{\omega_3 - \vec{q}_3 \cdot \hat{k}} \left(\sqrt{s}k_0 - p_0\omega_3 - \vec{k} \cdot \vec{q}_3 \right) \right]^2 \end{aligned} \tag{7.9}$$

with $d\Phi_3$ the phase space element as given in [PDG10], equation 39.11, $\omega_i = \sqrt{\vec{q}_i^{\,2} + m_\pi^2}$, $k_0 = (s - m_\pi^2)/2\sqrt{s}$, $p_0 = (s + m_\pi^2)/2\sqrt{s}$, and the pion decay constant $f_\pi = 92.4\,\mathrm{GeV}$. This non-resonant pion-gamma scattering is experimentally observed in pion-lead collisions via the Primakoff effect (see section 7.3). As the cross-section is worked out depending on the particle momenta, its fully differential form can be introduced as a special amplitude to a partial-wave analysis as explained in section 8.2.2.1. Thus the contribution of the processes depicted in figure 7.2 can be extracted from the experimental data.

Also higher order processes in ChPT, taking into account loop contributions to $\pi^-\gamma \to \pi^-\pi^-\pi^+$, as exemplarily depicted in figure 7.3 (left), have been calculated including the necessary counter-terms [Kai10]. The cross-section does not change noticeably with the additional diagrams up to center-of-mass energies $m_{3\pi} \approx 5\,m_\pi$ as indicated in fig-

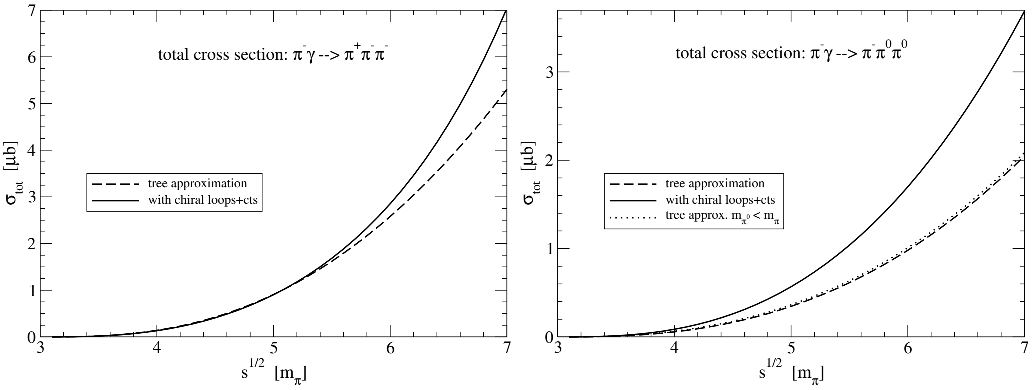

Figure 7.4: Total cross-sections for the processes $\pi^-\gamma \to \pi^-\pi^-\pi^+$ (left) and $\pi^-\gamma \to \pi^-\pi^0\pi^0$ (right) as a function of the center-of-mass energy $\sqrt{s} = m_{3\pi}$ with only trees (dashed line) and including loops (solid line), from [Kai10].

ure 7.4, so that is seems justified to perform the first measurement with the leading order calculation only in this mass range. This is substantially different for the reaction $\pi^-\gamma \to \pi^-\pi^0\pi^0$, where the cross-section changes significantly already at lower masses when the loop contributions are taken into account. Starting at $m_{3\pi} \geq 5\,m_\pi$, the tail of the ρ^0 resonance can develop from 2 pion loops as depicted in figure 7.3 (left), leading to processes with an explicit ρ contribution as depicted in figure 7.3 (right) [Kai11]. These higher order processes can be introduced as amplitudes to a partial-wave analysis as well.

7.2 Diffractive Dissociation

Diffractive dissociation describes a strong interaction scattering process as depicted in section 7.1.2. It is a isospin $I = 0$ t-channel exchange which is traced back to the exchange of a special Reggeon, called *Pomeron*. The Pomeron was historically introduced to describe features in hadronic scattering that could not be explained by the exchange of mesons or baryons, like the slowly rising cross-section of hadronic interaction with rising energy. The Pomeron is a manifestation of gluon exchange, however, its nature is still unclear. It features the quantum numbers of the vacuum $J^{PC} = 0^{++}$ and $J^{PC} = 2^{++}$, and is associated with natural parity exchange $P_{exchange} = (-1)^{J_{exchange}}$, i.e. the naturality $\eta = P(-1)^J = +1$.

The cross-section for diffractively produced states with spin-projection M, dependent on t', is given by

$$\sigma \propto t'^{|M|} \mathrm{e}^{-bt'} \; . \tag{7.10}$$

This means, that in the present analysis of events at lowest momentum transfer $t' < 10^{-3}\,\mathrm{GeV}^2/c^2$, only intermediate states with $M = 0$ are produced diffractively, while diffractive $M = 1$ states are negligible here and become only important for larger values of t'.

Many features of the diffraction of hadronic waves can be described by optical concepts [AJM76]. In particular, the slope parameter b stated in equation 7.10 is related to the radius R of the target particle (the diffracting object) via $R \approx 0.3\sqrt{b\,[\mathrm{GeV}^2/c^2]}\mathrm{fm}$ for diffractive scattering close to forward direction, i.e at very small t'.

7.3 Primakoff Production

$\pi\gamma$ scattering processes are difficult to access experimentally, as neither pion nor photon targets are directly available. Nevertheless, they can be seen in Primakoff reactions, when a ultra-relativistic (i.e. quasi-stable) pion beam scatters off the field quanta of the electromagnetic field surrounding a heavy nucleus, i.e quasi-real photons. This can be understood in the inverse kinematics in the rest frame of the high-energetic pion, where a relativistic heavy nucleus passes by rapidly with the velocity v. Due to Lorentz contraction, with increasing $\beta = v/c$, the electromagnetic field lines of the nucleus are deformed such, that the field becomes larger by a factor $\gamma = 1/\sqrt{1 - v^2/c^2}$ in the direction transversely to the movement and are contracted longitudinally (i.e. the strength is down by γ^{-2}). For $v \approx c$, the transverse strength of the electrical and the magnetic field becomes equal. Thus, the pion is exposed to a high electromagnetic field for a short time. A closer investigation of the field geometry shows that this is equivalent to the interaction with a quasi-real photon [Jac99]. This is called the equivalent-photon method, and results in the cross-section dependence of t' as

$$\frac{d\sigma}{dt'} \propto \frac{t'}{(t' + |t|_{\mathrm{min}})^2} \tag{7.11}$$

The presence of quasi-real photons is obviously also influenced by the charge Z of the nucleus and the center-of-mass energy s. These are taken into account in the Weizsäcker-Williams equivalent-photon approximation [EPA61], which relates the experimentally observed cross-section $\sigma_{\mathrm{nucleus}}$ to the cross-section of real photon scattering σ_γ as

$$\frac{d\sigma_{\pi-\mathrm{nucleus}}}{ds\,dt'\,d\Phi} = \frac{\alpha \cdot Z^2}{\pi(s - m_\pi^2)} \cdot F^2_{\mathrm{eff}}(t') \cdot \frac{t'}{(t' + t_{\mathrm{min}})^2} \cdot \frac{d\sigma_{\pi-\gamma}(s)}{d\Phi} \tag{7.12}$$

with $t_{\mathrm{min}} = [(s - m_\pi^2)/2E_{\mathrm{beam}}]^2$ providing the scale on which the cross-section is peaked on small values of momentum transfer t' to the nucleus. For a lead target, the elastic form factor, which is applicable in the limit of very small t', is given by the equivalent sharp radius approximation

$$F^2_{\mathrm{eff,\,lead}}(t') = \left[\frac{3}{(qr)^3}\left(\sin(qr) - qr\cos(qr)\right)\right]^2 \qquad \text{with } q = \sqrt{t'} \quad \text{and} \quad r = 6.39\,\mathrm{fm}\,. \tag{7.13}$$

Photons feature total spin and parity $J^P = 1^-$, i.e. a natural parity exchange, which leads to a positive reflectivity as introduced in section 8.1. As the helicities of quasi-real photons are $\lambda_\gamma = \pm 1$, intermediate states presumably produced from pions by photon exchange have to exhibit $|M| = 1$. The spin projection $M = 0$ is suppressed for quasi-real photons due to smallness of their mass.

Chapter 8

The Partial-Wave Analysis Technique

Partial-wave analysis (PWA) is a crucial technique for analyzing spectroscopy data (see section 7.1) in particle physics. Its traditional goal is to find and characterize all resonances present in a defined data set consisting of the decay particles detected in a particular final state. Thereby the main focus is typically placed on the discovery of unknown or the confirmation of disputed resonances. The contributing resonances' properties (i.e. mass, width, and quantum numbers J^{PC}) are determined by fitting the angular distributions of the decay particles to pre-defined angular correlations, in addition to the calculation of kinematic quantities like the invariant mass of the mother state. Interference effects between those resonances are taken into account as well. This approach may be extended by considering also non-resonant contributions to the final state, if their angular relations are established.

The PWA technique applied for the analysis of $\pi^-\pi^-\pi^+$ final states emerging at very low momentum transfer t' from the beam particle to the target (see chapter 9) is explained in this chapter, with a clear focus on the special features introduced for this specific analysis. While the basic principles are presented in the most general way, all details and examples are explicitely described for the $\pi^-\pi^-\pi^+$ case.

A full PWA is performed in two steps, the *mass-independent PWA* and the subsequent *mass-dependent* χ^2 *fit*. The essential idea of the mass-independent PWA[1] is depicted in section 8.1. It is based on several physics and technical ingredients described in the following sections. The parametrization of the decay amplitudes is specified in section 8.2: For candidates of resonances the *isobar model* is assumed to be valid, and several non-isobaric amplitudes are introduced in addition. The applied t' dependences are summarized here as well. Another important aspect deals with the normalization integrals used in the fit and describes several special implementations of them in section 8.3. Furthermore the selection of the proper *rank* of the fit is extended by introducing the technique of partial coherence presented in section 8.4. All these ingredients enter the extended log-likelihood fit applied to the data as depicted in section 8.5. The results of this fit are then interpreted using several quantities derived from the fit parameters, as intensities and relative phases between amplitudes, as described in section 8.6. Section 8.7 shows how the quality of the fit result can be jugded. All these steps of the mass-independent

---

[1] "Mass-independent PWA" has been an established expression during the recent years. As such it is still used in this thesis, and not yet replaced everywhere by the more correct expression "PWA in mass bins" which is currently being established in the community.

PWA have been carried out for the analysis presented in section 9.4. The remaining step towards a full PWA, i.e. the mass-dependent χ^2 fit to the result of the mass-independent fit, has not been applied yet, but is still described in section 8.8 for completeness.

8.1 Mass-Independent PWA

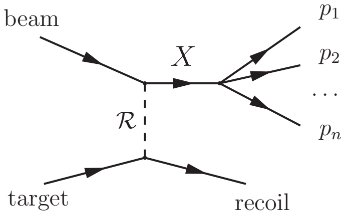

Figure 8.1: Sketch of the scattering process the PWA technique is based on.

In general, all particles in the final state have to be properly reconstructed for a reliable calculation of angles, which is necessary for a reliable PWA. This includes also the recoil particle, which is often poorly measured experimentally. The following description of the analysis procedure is based on scattering processes as the one depicted in figure 8.1, featuring t-channel Reggeon ($\mathcal{R}$) exchange between the beam and the target. This means, the interaction between beam and target is supposed to take place such fast[2] that the thereby produced particles do not interact with each other. In other words, all calculations of such processes can be factorized into the beam-resonance vertex and the target-recoil vertex. In this case the quantum numbers of the intermediate state X are completely deduced from the angular correlations between its daughter particles p_1, p_2, $\ldots$, p_n, which are consequently the only relevant final state particles.

The experimentally observed intensity for the production of a particular state X depends on its invariant mass m_X and on the momentum transfer t', which would both have to be taken into account in a one-level *global fit*, with little correlation between these two quantities. In contrast, the PWA method described here is divided into the two steps mentioned before for technical simplicity. In the first step, the mass-independent PWA, the data is divided into reasonably narrow[3] bins of m_X and selected t' ranges, so that the production strength in a single bin can be assumed to constant within the mass bin[4]. This way, the angular distributions depend only on the phase space variables τ and can be fitted independently in each mass bin.

Assuming the decay of each state X can be completely decoupled from its production, the total experimentally observed intensity $\mathcal{I}_m$ in a certain mass bin is generally written

---

[2] Which is reasonable as strong interaction takes place on timescales in the order of 10^{-15} seconds.

[3] On the one hand, the narrower a mass bin, the better the condition "constant with mass" inside it is fulfilled. On the other hand, the fit becomes more reliable with more statistics inside the single bins. So the choice of bin width depends strongly on the statistics available. Typical values for $\pi^-\pi^-\pi^+$ analyses are $20 - 40\,\mathrm{MeV}/c^2$ mass bins.

[4] The traditional PWA concentrates on the analysis of a specific range of t'.

as

$$\mathcal{I}_m(\tau, t') = \sum_{\epsilon=\pm1} \sum_{r=1}^{N_r} \left| \sum_i T_{ir}^{\epsilon}(m)\, \overline{f}_i^{\epsilon}(t', m)\, \overline{\psi}_i^{\epsilon}(\tau, m) \right|^2 . \tag{8.1}$$

Here $\overline{\psi}_i^{\epsilon}(\tau, m)$ denotes the normalized *decay amplitude* of a particular partial wave i, depending only on τ within a mass interval Δm around the mass m. It is multiplied with its corresponding normalized t' dependence $\overline{f}_i^{\epsilon}(t', m)$, depending only on t' within this interval. The decay amplitudes are usually used in their normalized mode, as the relative mass dependences between different decay amplitudes ψ_i^{ϵ} are preferably cancelled out. This is achieved by dividing the decay amplitude $\psi_i^{\epsilon}(\tau, m)$ (described in detail in section 8.2) by its phase-space integral[5] as denoted in equation (8.2) and explained in more details in section 8.3.1. The real functions $f_i^{\epsilon}(t', m)$ describe the $t'(m)$ dependence of the decay amplitudes, which are stated explicitely in section 8.2.3 for the following analysis, and are also normalized according to equation (8.2).

$$\overline{\psi}_i^{\epsilon}(\tau, m) = \frac{\psi_i^{\epsilon}(\tau, m)}{\sqrt{\int \left|\psi_i^{\epsilon}(\tau, m)\right|^2 \mathrm{d}\tau}} \qquad \overline{f}_i^{\epsilon}(t', m) = \frac{f_i^{\epsilon}(t', m)}{\sqrt{\int \left|f_i^{\epsilon}(t', m)\right|^2 \mathrm{d}t'}} \tag{8.2}$$

The complex numbers $T_{ir}^{\epsilon}(m)$ in equation (8.1) are the *transition amplitudes* which contain the information about the strengths of the individual amplitudes i and their mutual interferences. Since they are the only fitting parameters, they contain also unknown coupling constants belonging to the decay amplitudes[6]. They are obtained using an extended log-likelihood method as explained in section 8.5, respecting the acceptance of the spectrometer obtained from a dedicated Monte Carlo simulation (see section 9.2.2).

The *rank* N_r (of the fit) is usually chosen according to the (in)coherence of the scattering process. $N_r > 1$ introduces an additional incoherent sum over sets of coherent decay amplitudes, so that additional freedom is created by multiplication of the number of fitting parameters (see section 8.4 for details).

The *reflectivity* ϵ describes the symmetry of the decay under a reflection through the production plane. For bosons it can take the values $\epsilon = \pm 1$, while it limits the values for the spin projection to $M \geq 0$ as denoted in section 8.2.1.5. Parity conservation can be expressed in this manner as amplitudes with opposite ϵ not being allowed to interfere. This is very convenient from the technical point of view, as the final sum over ϵ in equation (8.1) is incoherent, so that the number of fitting parameters can be significantly reduced [CT75]. In addition, to a good extend the reflectivity corresponds to the naturality η exchanged in high-energy reactions, so that for exchange particles with $\eta = +1$ only partial waves with $\epsilon = +1$ are expected to contribute significantly to the cross-section [Chu97].

---

[5] These phase-space integrals are often called “diagonal integrals”.

[6] This means, that the naming “production amplitudes” which is often used for T_{ir}^{ϵ}, is not fully correct.

8.2 Parametrization of Decay Amplitudes and t' Dependences

An important input to the PWA is a proper description of the decay amplitudes $\psi_i^{\epsilon}(\tau, m)$, as these provide the angular and dynamical relations within the fit model. Resonances that originate during the scattering process can effectively be treated in the framework of the isobar model, that assumes subsequent two-body decays, which are the basis for the construction of the occuring spin states of these resonances from the decay particles. For this task various spin formalisms are available, e.g. the tensor formalism using Zemach tensors [Wei08a, Zem65] or the helicity formalism using rotation functions [Chu71] depicted in the following for the $\pi^-\pi^-\pi^+$ final state. Also non-resonating intermediate states that end up as the same final state particles have to be taken into account with the most possible correct description, as they are present in the data and interfere with resonances. For the data analysis described in section 9.4, especially pure pion scattering, that can be evaluated by ChPT, and the decay of negative kaons contained in the beam into the $\pi^-\pi^-\pi^+$ final state are important.

The t' dependences $f_i^{\epsilon}(t', m)$ depend on the assumed production process related to the corresponding decay amplitudes $\psi_i^{\epsilon}(\tau, m)$. In the following data analysis, diffractive dissociation, Primakoff production, and kaon decays have to be treated properly.

8.2.1 Isobaric Amplitudes for Resonances

A full description of the decay amplitudes of resonances, potentially excited from π^- beam and decaying into the $\pi^-\pi^-\pi^+$ final state, is given in the following. The applied model is derived from common observations in experimental data: When the invariant masses m_{sub} of the subsystems of the final state, i.e. here the $\pi^-\pi^+$ pairs, are evaluated for a certain region of invariant mass of the mother state X, structures in m_{sub} become apparent. These are more clearly depicted in *Dalitz plots*, that depict the squared invariant masses of two of these subsystems versus each other. These structures correspond to known resonances with the subsystem's particles as daughter particles, e.g. the $\rho(770)$ in the $\pi^-\pi^+$ subsystem (see figure 9.5 for examples from the following analysis). These observations suggest the use of the *isobar model*, a phenomenological model of sequential two-body decays of X via intermediate states, the *isobars*, that decay further into the particles finally measured in the experiment. Starting from this model, the angular description is based on rotation functions of two-body decays that are combined later for the construction of the complete decay amplitude. Furthermore, the parametrization of the isobar masses play an important role, as well as a dynamical contribution from angular momentum barrier factors.

8.2.1.1 The Isobar Model and Two-Body Decays

The isobar model is based on the assumption of sequential two-body decays of the produced resonance X with the invariant mass m_X. This means, X decays first into two par-

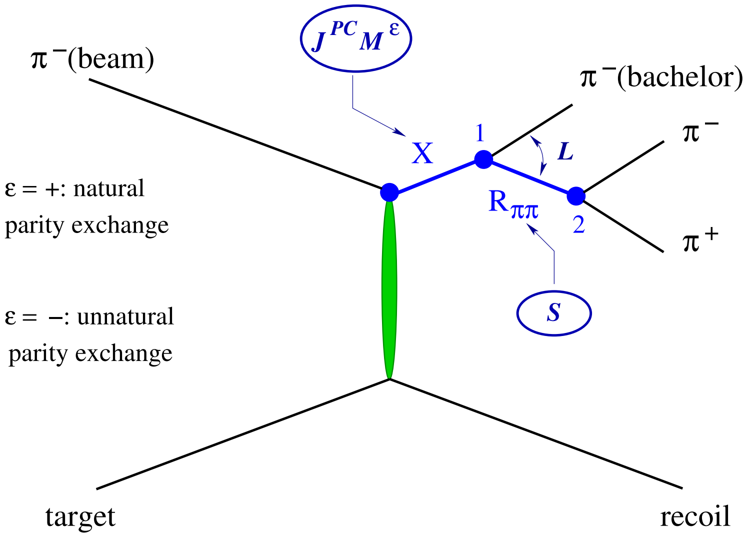

Figure 8.2: Schematic Drawing of the Isobar Model for a Resonance decaying into $\pi^-\pi^-\pi^+$ (taken from [Wei08a]).

ticles, and in case one or both of these two daughter states are not yet final state particles, they are subject of a subsequent two-body decay.

For each two-body decay in this chain the decay amplitude in the helicity formalism can be written as

$$A_{JM}(\tau) = \sum_{\lambda_1\lambda_2} D^J_{M,\lambda_R}(\theta,\phi,0) f_{\lambda_R}(m_R, m_1, m_2) \cdot A_1 \cdot A_2. \tag{8.3}$$

It is based on the rotation functions $D^J_{M,\lambda_R}(\theta,\phi,0)$ (see section 8.2.1.2), which describe the angular correlations of two decay angles θ and ϕ with the total spin J, its spin projection M and helicity λ_R of the supposed mother state R of the respective two decay particles 1 and 2. $f_{\lambda_R}(m_R, m_1, m_2)$ (with m_R the invariant mass of the mother state, and m_1 and m_2 the masses of the two daughter particles) takes into account all the other, especially the dynamic, contributions to this two-body decay amplitude (see section 8.2.1.3). This has to be multiplied with the respective decay amplitudes A_1 and A_2 of the daughter particles, if these are not stable[7]. The sum over the possible helicities $\lambda_{1,2}$ of the decay particles, with $\lambda_R = \lambda_1 - \lambda_2$, respects that these helicities are potentially not measured experimentally.

Three-body decays are fully specified by five kinematic variables. In the framework of the isobar model, these are chosen as two angles θ, ϕ describing the first decay in the rest frame of the resonance, the mass of the isobar, and two angles θ, ϕ describing the decay of the isobar in its rest frame.

The application of the isobar model for a $\pi^-\pi^-\pi^+$ final state emerging from a π^- beam

---

[7] "Stable" is meant here in the sense of providing a particle trajectory measured in the experiment, i.e. being a final state particle.

is depicted in figure 8.2, introducing also the relevant quantum numbers that define the full decay. The resonance X decays into a π^- and a neutral di-pion resonance, the *isobar*, that decays further into a $\pi^-\pi^+$ pair. A partial wave is fully defined by $J^{PC}M^{\epsilon}[isobar\ \pi]L$, giving the quantum numbers of the resonance J^{PC}, its spin projection M onto the beam axis, its reflectivity ϵ, the isobar $R_{\pi\pi}$ with spin S, and the angular momentum L between the isobar and the unpaired π^-.

8.2.1.2 Angular Part of Decay Amplitudes

The angular distributions related to the respective two-body decays have to be analyzed in the proper reference frames that are determined individually for each event. For the decay of the resonance, this is the *Gottfried-Jackson frame* (GJF) [Han74, GJ64], which is the rest frame of the resonance with the z_{GJ} axis in beam direction. The y_{GJ} axis is normal to the production plane (which is spanned up by the three-momentum vectors of target and recoil), and is defined by $\vec{p}_{\text{recoil}} \times \vec{z}_{GJ}$, and $x_{GJ} = y_{GJ} \times z_{GJ}$. The relevant angles are θ_{GJ}, the polar angle of the isobar, and ϕ_{TY}, the corresponding azimutal angle[8]. The decay of the isobar is described analogously in its own rest frame, the *Helicity frame*, with the z_{hel} axis parallel to the momentum direction of the isobar in the GJF and $y_{hel} = z_{GJ} \times z_{hel}$, providing θ_{hel} and ϕ_{hel} of one of the daughter particles [Chu71].

The rotation functions $D^J_{M,\lambda}(\phi,\theta,0)$ (as applied for each individual two-body decay according to equation (8.3)) are given by ([Chu71], following [Ros57])

$$D^J_{M,\lambda}(\phi,\theta,0) = e^{-iM\phi} d^J_{M\lambda}(\theta) \tag{8.4}$$

with the total spin J, its spin projection M and helicity λ of the mother state as stated already before, and

$$\begin{aligned} d^J_{M\lambda}(\theta) =& [(J+\lambda)!(J-\lambda)!(J+M)!(J-M)!]^{1/2} \\ & \cdot \sum_{\kappa} \frac{(-)^{\kappa}}{(J-M-\kappa)!(J+\lambda-\kappa)!(\kappa+M-\lambda)!\kappa!} \\ & \cdot \left(\cos\frac{\theta}{2}\right)^{2J+\lambda-M-2\kappa} \left(-\sin\frac{\theta}{2}\right)^{M-\lambda+2\kappa} \end{aligned} \tag{8.5}$$

where the sum takes into account all integer values of κ for which the factorial arguments are greater than or equal zero [Ros57].

For the special case $\lambda = 0$, that appears e.g. with decays into scalar mesons as in the case of $\pi^-\pi^+$ isobars, the rotation functions can be written in a simpler way. The $D^J_{M,0}(\phi,\theta,0)$ are now related to the spherical harmonics $Y^L_M(\theta,\phi)$ via [Chu71]

$$D^{L*}_{M,0}(\phi,\theta,0) = \sqrt{\frac{4\pi}{2L+1}} Y^L_M(\theta,\phi) \tag{8.6}$$

---

[8] ϕ_{TY} is named after S. B. Treiman and C.-N. Yang.

The spherical harmonics are given by

$$Y^L_M(\theta,\phi) \sim P_{LM}(\cos\theta)\mathrm{e}^{iM\phi} \tag{8.7}$$

with $P_{LM}(\cos\theta)$ the associated Legendre polynomials. Nevertheless, even for the $\pi^-\pi^+$ isobar decays in the following analysis the complete formula given in equation (8.4) is used, in order to avoid potential errors with the normalization of the complete decay amplitudes.

8.2.1.3 Normalizations and Dynamical Part of Decay Amplitudes

The non-angular part of the two-body decay amplitude (equation (8.3)) in the helicity formalism is given by [Han74, Chu71]

$$\begin{aligned} &f_{\lambda_R}(m_R, m_1, m_2) = \\ &\sqrt{2L+1}(I_1 I_{1z} I_2 I_{2z}|I_R I_{Rz})(L_R 0 s_R \lambda_R|J_R\lambda_R)(s_1\lambda_1 s_2 -\lambda_2|s_R\lambda_R)\cdot\Delta(m_R)\cdot F_L\,. \end{aligned} \tag{8.8}$$

This contains a normalization from angular momentum L, and the Clebsch-Gordan coefficients for the couplings of isospin I_i (with z-component I_{iz}) and spin s_i (where the z-component is the helicity λ_i) of the two daughter particles (indices $i = 1$ and $i = 2$) to the mother particle (index $i = R$). The L-S-coupling of the mother particle reveals $L_{Rz} = 0$, as the quantization axis in the helicity formalism is chosen to be in the direction of the breakup momentum p, which means $\vec{L} \perp \vec{p}$.

$\Delta(m_R)$ parametrizes the dependence on the mass m_R of the mother state, usually described by Breit-Wigner forms or based on fits to specific data (see section 8.2.1.4 for the descriptions of the isobars used in the following $\pi^-\pi^-\pi^+$ analysis).

F_L are connected to the angular momentum barrier factors as developped by C. Quigg and F. von Hippel [QuH72]. They have been introduced to match both, the amplitude behaviour with respect to the breakup momentum of the mother state at threshold by $F_L|_{p\to 0} \sim p^L$, and the finite intensity of the amplitude for high momenta p of one of the decay particles by $F_L|_{p\to\infty} \sim 1$. Using a classical angular momentum of magnitude $x = pR$, with R being the effective range[9], they are given as follows for $L \leq 3$:

---

[9] The following analysis uses $R = 4.94\,(\mathrm{GeV}/c)^{-1}$. This is approximately equal to $x = p/p_R$, $p_R = 0.1973\,\mathrm{GeV}/c$, both corresponding to 1 fm, which is the effective interaction range of gluons (i.e. of strong interaction).

$$
\begin{aligned}
F_0(x) &= 1 \\
F_1(x) &= \frac{p}{\sqrt{x^2+1}} \\
F_2(x) &= \frac{p^2}{\sqrt{(x^2-3)^2+9x^2}} \\
F_3(x) &= \frac{p^3}{\sqrt{(x^2+5)^3-30x^2-9x^4}}
\end{aligned}
\tag{8.9}
$$

8.2.1.4 Mass Dependence of Isobar Parametrization

The analysis of the $\pi^-\pi^-\pi^+$ final states which will be presented in section 9.4 uses as isobars $\rho(770)$, $f_2(1270)$, $f_0(980)$, $f_0(1500)$, and the $(\pi\pi)_S$ wave, all decaying into $\pi^-\pi^+$. Their parametrization is summarized here very shortly only, for more details see [Haa12].

The mass dependence of isobars that occur as resonances can be described by relativistic Breit-Wigner functions $\Delta(m)$ as given by equation (7.2), with the mass-dependent width $\Gamma(m)$ (see equation (7.3) for the typical form), and m_0 the nominal mass and Γ_0 the nominal width of the resonance. For the following analysis, the mass dependence of the resonant isobars is described according to table 8.1, using the breakup-momentum p, p_0 the breakup-momentum at the nominal mass m_0, $x = pR$, and $x_0 = p_0R$.

Isobar	$\Delta(m_{2\pi}) \cdot F_L$	$\Gamma(m)$	m_0 [GeV/c^2]	Γ_0 [GeV/c^2]
$\rho(770)$	$\frac{\sqrt{m_0\Gamma_0}}{m_0^2-m^2-im_0\Gamma(m)} \cdot F_1(x)$	$\Gamma_0 \frac{p}{p_0} \frac{F_1^2(x)}{F_1^2(x_0)}$	0.7685	0.1507
$f_2(1270)$	$\frac{\sqrt{m_0\Gamma_0}}{m_0^2-m^2-im_0\Gamma(m)} \cdot F_2(x)$	$\Gamma_0 \frac{p}{p_0} \frac{m_0}{m} \frac{F_2^2(x)}{F_2^2(x_0)}$	1.275	0.185
$f_0(980)$	$\frac{m_0\Gamma(m)\frac{m}{p}}{m_0^2-m^2-im_0\Gamma(m)}$	$\Gamma_0 \frac{p}{p_0}$	0.980	0.04
$f_0(1500)$	$\frac{\sqrt{m_0\Gamma_0}}{m_0^2-m^2-im_0\Gamma_0}$		1.507	0.109

Table 8.1: Isobar parametrizations using Breit-Wigner functions

The parametrization of the $(\pi\pi)_S$ wave is delicate and still subject of ongoing research, from both theorists' and experimentalists' sides. There are efforts to extract it from the COMPASS 2008 high-statistics high-t' $\pi^-\pi^-\pi^+$ data set [Haa12, Rya12]. For the following analysis the established parametrization given by the K_1 *solution* is used. This is a fit function based on coupled-channel analysis [AMP87] over the $\pi\pi$ mass spectrum for $2m_\pi < m_{2\pi} < 1.6\,\text{GeV}/c^2$. The narrow $f_0(980)$ resonance is subtracted from this, as it is introduced as independent isobar as given by table 8.1. Thus the $(\pi\pi)_S$ wave is given as

$$
\Delta_{(\pi\pi)_s}(m_{2\pi}) = \mathcal{T}_{11} - c \cdot BW_{f_0(980)}, \quad \text{with} \quad c = -0.3878 + i\,0.2991\,. \tag{8.10}
$$

$BW_{f_0(980)}$ denotes the Breit-Wigner form of the $f_0(980)$ with[10] $m_0 = 0.9855\,\text{GeV}/c^2$ and

---

[10] The parameters of the subtracted $f_0(980)$ are slightly different from the parameters of the independent

$\Gamma_0 = 0.0449\,\mathrm{GeV}/c^2$. While the complete K_1 solution consists of a full 2×2 matrix $\mathbb{T}$, considering both $\pi\pi$ and KK S-waves as initial and final states, for the following analysis only the element containing $\pi\pi$ in both initial and final state, i.e. $\mathcal{T}_{11}$, is used for the parametrization of the $(\pi\pi)_S$ wave. The matrix $\mathbb{T}$ is constituted as

$$\mathbb{T} = \mathbb{K}(\mathbb{1} - i\rho\mathbb{K})^{-1} = (\mathbb{M} - i\rho\mathbb{1})^{-1} \tag{8.11}$$

from the $\mathbb{K}$ matrix, which is real and symmetric, or its inverse $\mathbb{M}$. $\mathbb{K}$ is defined by its elements $\mathcal{K}_{ij}$ as

$$\mathcal{K}_{ij} = \frac{s - s_0}{4m_K^2}\left(\frac{f_i f_j}{(s_1 - s)(s_1 - s_0)} + \sum_{n=0}^{4} c_{n,ij}\left(\frac{s}{4m_K^2} - 1\right)^n\right) \tag{8.12}$$

with $s = m_{2\pi}^2$, and m_K the average[11] kaon mass introduced only as a convenient scaling factor. s_0 stands for the Adler zero of the $\mathbb{T}$ matrix, s_1 the pole, f_i, f_j, c_{ij} are real numbers determined in the fit (see table 1 in [AMP87]).

The diagonal matrix ρ contains the phase space factors ρ_1 of the $\pi\pi$ and ρ_2 of the KK final states. For the latter, the Flatté approach is used, appointing the phase space imaginary if s is below threshold of the final state:

$$\rho_1 = \sqrt{1 - \frac{4m_\pi^2}{s}} \tag{8.13}$$

$$\rho_2 = \begin{cases} \frac{1}{2}\sqrt{\left|1 - \frac{4m_{K_\pm}^2}{s}\right|} + \frac{1}{2}\sqrt{\left|1 - \frac{4m_{K_0}^2}{s}\right|} & \text{if } s > 4m_{K_0}^2 \\ \frac{1}{2}\sqrt{\left|1 - \frac{4m_{K_\pm}^2}{s}\right|} - \frac{i}{2}\sqrt{\left|1 - \frac{4m_{K_0}^2}{s}\right|} & \text{if } 4m_{K_\pm}^2 < s < 4m_{K_0}^2 \\ -\frac{i}{2}\sqrt{\left|1 - \frac{4m_{K_\pm}^2}{s}\right|} - \frac{i}{2}\sqrt{\left|1 - \frac{4m_{K_0}^2}{s}\right|} & \text{if } s < 4m_{K_0}^2\,. \end{cases} \tag{8.14}$$

8.2.1.5 Complete Parametrization of Isobaric $\pi^-\pi^-\pi^+$ Decay Amplitudes

Merging the information of the three previous sections, the full amplitude $\Psi(\tau)$ of a produced state X decaying into $\pi^-\pi^-\pi^+$ via the isobar R, decaying further into pions 1 and 2, and the bachelor pion B, is constructed using equations (8.3) and (8.8). In the most

---

isobar. The parameters used for the $(\pi\pi)_S$ wave are optimized such, that the function is as much smooth as possible [Rya12], while the parameters of the resonance itself are taken from [PDG10].

[11] Average mass of K^0 and $K^\pm$.

general way, it is given as[12]

$$\begin{aligned}\Psi(\tau) = & \\ & \sum_{n=1,2} \sum_{M_R \lambda_B} D^{J_X}_{M_X,\lambda_X}(\theta_{n_X}, \phi_{n_X}, 0) \sqrt{2L_X+1} (L_X 0 s_X \lambda_X | J_X \lambda_X)(s_R \lambda_R s_B \lambda_B | s_X \lambda_X) F_{L,X} \Delta_X(m_{3\pi}) \\ & \cdot \sum_{\lambda_1 \lambda_2} D^{J_R}_{M_R,\lambda_R}(\theta_{n_R}, \phi_{n_R}, 0) \sqrt{2L_R+1} (L_R 0 S_R \lambda_R | J_R \lambda_R)(s_1 \lambda_1 s_2 \, \lambda_2 | s_R \lambda_R) F_{L,R} \Delta_R(m_{2\pi}) \,. \end{aligned} \tag{8.15}$$

As the pions (i.e. particles 1, 2, and B) carry spin $s_{1,2,B} = 0$, also their helicities $\lambda_{1,2,B}$ are 0. It follows also $\lambda_R = 0$ for the isobar decay in the helicity frame, while the helicity of the isobar in the GJF, denoted by M_R, can take values $\neq 0$. So equation (8.15) simplifies in a first step to

$$\begin{aligned}\Psi(\tau) = & \\ & \sum_{n=1,2} \sum_{M_R} D^{J_X}_{M_X,\lambda_X}(\theta_{n_X}, \phi_{n_X}, 0) \sqrt{2L_X+1} (L_X 0 s_X \lambda_X | J_X \lambda_X)(s_R M_R 00 | s_X \lambda_X) F_{L,X} \Delta_X(m_{3\pi}) \\ & \cdot D^{J_R}_{M_R,0}(\theta_{n_R}, \phi_{n_R}, 0) \sqrt{2L_R+1} (L_R 0 S_R 0 | J_R 0)(0000 | s_R 0) F_{L,R} \Delta_R(m_{2\pi}) \end{aligned} \tag{8.16}$$

The decay angles θ_X and ϕ_X are given in GJF, i.e. should be denoted as θ_{GJ} and ϕ_{GJ}, while θ_R and ϕ_R in the helicity frame are θ_{hel} and ϕ_{hel}. As the pion spin is 0, i.e. also $S_R = 0$, it follows also $L_R = J_R$, $J_R = S_X$ and $\lambda_X = M_R$, so that equation (8.16) finally simplifies to

$$\begin{aligned}\Psi(\tau) = & \sum_{n=1,2} \sum_{M_R} D^{J_X}_{M_X,M_R}(\theta_{n_{GJ}}, \phi_{n_{GJ}}, 0) \sqrt{2L_X+1} (L_X 0 J_R M_R | J_X M_R) F_{L,X} \Delta_X(m_{3\pi}) \\ & \cdot D^{J_R}_{M_R,0}(\theta_{n_{hel}}, \phi_{n_{hel}}, 0) \sqrt{2L_R+1} F_{L,R} \Delta_R(m_{2\pi}) \end{aligned} \tag{8.17}$$

While the mass dependence of the isobar $F_{L,R}\Delta_R(m_{2\pi})$ (see section 8.2.1.4) is explicitely stated, the mass dependence $\Delta_X(m_{3\pi})$ of the resonance X is assumed to be constant within the respective mass bin, and such set to a constant value of 1 in the mass-independent analysis. The angular momentum barrier factors $F_{L,X}$ of the decay of X are usually chosen according to equations (8.9), but can also be neglected, i.e. substituted by simplified p^L behaviour, for specific amplitudes. This option is chosen purely empirically when it is supposed to describe the data better[13] [Rya12].

The outer sum over $n = 1, 2$ introduces the Bose symmetrization, that respects that the two π^- are not distinguishable and can both potentially be the bachelor pion or decay particle of the isobar.

The amplitudes are calculated for both positive and negative values of M explicitely. The migration into the reflectivity basis subsequently restricts to $M \geq 0$, by introducing

---

[12] As the helicity formalism is used, the z-component of both L_R and L_X is zero. See the explanations following equation (8.8) for details. Furthermore, the isospin coupling present in equation (8.8) is omitted, as the 3π system must feature $I = 1$, and no $I = 2$ resonances are known to decay into $\pi^+\pi^-$.

[13] This might be the case if an amplitude collects mere background. It is also supposed to compensate a distorted shape of the isobar, i.e. when the parametrization does not match the form in the data well enough.

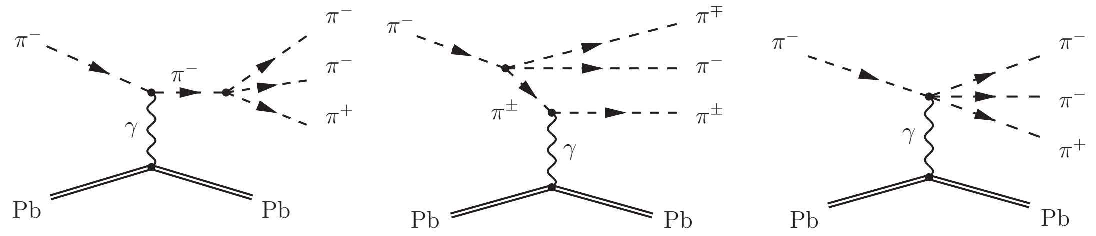

Figure 8.3: Leading order processes in ChPT [KF08] for the reaction $\pi^-\gamma \to \pi^-\pi^-\pi^+$, embedded in the Primakoff reaction contribution to $\pi^-\text{Pb} \to \pi^-\pi^-\pi^+\text{Pb}$.

the additional reflectivity quantum number $\epsilon = \pm 1$ which was already announced in section 8.1. The eigenstates of the reflectivity operator are given by [CT75]

$$\psi^{\epsilon}_{JM}(\tau) = c(M)\left[\Psi_{JM}(\tau) - \epsilon P(-1)^{J-M}\Psi_{J(-M)}(\tau)\right] \tag{8.18}$$

with $c(M)$ given by

$$c(M) = \begin{cases} 1/\sqrt{2}, & M > 0 \\ 1/2, & M = 0 \\ 0, & M < 0\,. \end{cases} \tag{8.19}$$

8.2.2 Non-Isobaric Amplitudes

Real data contains also events from processes that cannot properly be interpreted as isobaric decays of intermediate states emerging from an excited beam particle. For the following analysis of $\pi^-\pi^-\pi^+$ final states produced at very low t' to a lead target, especially non-resonant $\pi\pi$ scattering[14] in Primakoff interactions, and beam kaon decays into the $\pi^-\pi^-\pi^+$ final state prevail. The corresponding decay amplitudes are described in the following.

8.2.2.1 Amplitudes from ChPT

At low masses, i.e. at and just above the threshold of a specific multi-pion final state produced from pion beam, the only hadrons involved are pions interacting with each other. In the case of photons mediating in the scattering process[15], these scattering processes, including the coupling to a real photon, can be calculated from Chiral Perturbation Theory (see section 7.1.3). The fully differential form of these calculations can be used as an additional amplitude inside the PWA framework as depicted in the following for the $\pi^-\pi^-\pi^+$ final state.

---

[14] without any other states than pions involved

[15] E.g. the exchange of quasi-real photons occuring with pion scattering at heavy nuclear targets.

The tree diagrams that enter the ChPT calculations at leading order for $\pi^-\gamma \to \pi^-\pi^-\pi^+$, embedded in the Primakoff contribution to $\pi^-\mathrm{Pb} \to \pi^-\pi^-\pi^+\mathrm{Pb}$, are depicted in figure 8.3. The partial-wave amplitude for the leading-order scattering of a pion with a real photon in $\pi^-(p)\gamma(k) \to \pi^-(q_1)\pi^-(q_2)\pi^+(q_3)$ can be obtained from the calculation of the unpolarized cross-section of this process (equation (7.9) taken from [KF08]). This cross-section is worked out in the Gottfried-Jackson frame (GJF, as defined in section 8.2.1.2) and depends on the four-momenta k of the photon, p of the beam π^-, $q_{1,2}$ of the two final state π^- and q_3 of the final state π^+. In the following, $\vec{k}$ indicates the corresponding three-momentum vector of the photon ($\vec{q}_i$, $i \in 1,2,3$ accordingly), $\hat{k} = (0,0,-1)$ the corresponding unit vector, and $(\vec{q}_i)_j$, $j \in x,y,z$, the x, y or z component of the three-momentum vector $\vec{q}_i$, respectively. Thus the chiral amplitude on the tree-level, $\vec{\mathcal{A}}_{\text{chpt-tree}}$, is given as

$$\vec{\mathcal{A}}_{\text{chpt-tree}} = f0 \cdot \Big((\vec{q}_1 \times \hat{k}) \cdot f1 + (\vec{q}_2 \times \hat{k}) \cdot f2 + (\vec{q}_3 \times \hat{k}) \cdot f3 \Big) \tag{8.20}$$

using

$$f0 = \sqrt{\frac{s}{(s - m_\pi^2)^3}} \tag{8.21}$$

$$f1 = \Big(p_0(\sqrt{s} - \omega_2) - \sqrt{s}\omega_1 - \vec{k} \cdot \vec{q}_2 \Big) \Big/ \Big(\omega_1 - \vec{q}_1 \cdot \hat{k} \Big) \tag{8.22}$$

$$f2 = \Big(p_0(\sqrt{s} - \omega_1) - \sqrt{s}\omega_2 - \vec{k} \cdot \vec{q}_1 \Big) \Big/ \Big(\omega_2 - \vec{q}_2 \cdot \hat{k} \Big) \tag{8.23}$$

$$f3 = \Big(\sqrt{s}k_0 - p_0\omega_3 - \vec{k} \cdot \vec{q}_3 \Big) \Big/ \Big(\omega_3 - \vec{q}_3 \cdot \hat{k} \Big) \ . \tag{8.24}$$

Here $\sqrt{s} = m_{3\pi}$ is the total center-of-mass energy, $\omega_i = \sqrt{\vec{q}_i^{\,2} + m_\pi^2}$ the energy of the respective pion, $k_0 = (s - m_\pi^2)/2\sqrt{s}$ the energy of the photon, and $p_0 = (s + m_\pi^2)/2\sqrt{s}$ the energy of the beam pion. All mentioned quantities have already been used equivalently in equation (7.9).

The evaluation of the cross-products $\vec{q}_i \times \hat{k}$ in equation (8.20) leaves only $(\vec{q}_i)_y$ components to $(\vec{\mathcal{A}}_{\text{chpt-tree}})_x$, $(\vec{q}_i)_x$ components to $(\vec{\mathcal{A}}_{\text{chpt-tree}})_y$, and $(\vec{\mathcal{A}}_{\text{chpt-tree}})_z = 0$, as $\hat{k} = (0,0,-1)$ in the GJF. This means, the x- and y-components of $\vec{\mathcal{A}}_{\text{chpt-tree}}$ feature the properties of negative and positive reflectivity ϵ, respectively[16]. Thus the partial-wave amplitudes applied during the mass-independent PWA, which take into account the angular distributions calculated by ChPT on tree level, are given as

$$\psi^{\epsilon=+1}_{\text{chpt-trees}} = f0 \cdot (q_1[x] \cdot f1 + q_2[x] \cdot f2 + q_3[x] \cdot f3) \tag{8.25}$$

$$\psi^{\epsilon=-1}_{\text{chpt-trees}} = f0 \cdot (-q_1[y] \cdot f1 - q_2[y] \cdot f2 - q_3[y] \cdot f3) \tag{8.26}$$

As stated already in section 7.1.3, also higher order processes in ChPT, taking into account loop contributions, have been calculated [Kai10]. Examples for these processes,

---

[16] The reflectivity operator causes x components of the particles to remain and their y components to change the sign.

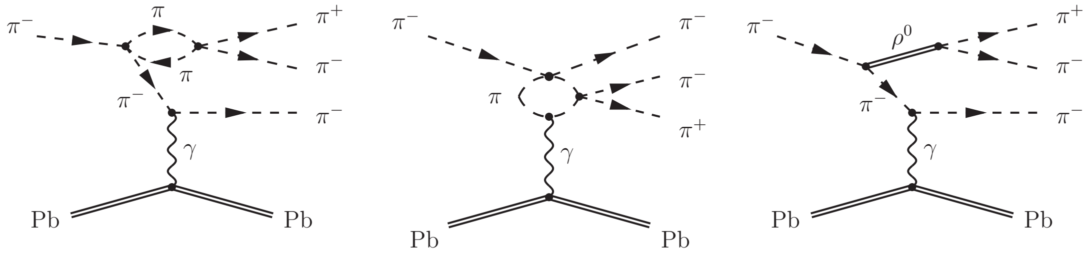

Figure 8.4: Examples for higher order processes in ChPT containing loops (left, middle) and explicit ρ (right) [Kai10, Kai11] for the reaction $\pi^-\gamma \to \pi^-\pi^-\pi^+$, embedded in the Primakoff reaction contribution to $\pi^-\text{Pb} \to \pi^-\pi^-\pi^+\text{Pb}$.

embedded in the $\pi^-\gamma$ Primakoff scattering, are depicted in figure 8.4 (left and middle). The differential form of their contribution to the cross-section can be implemented as an amplitude that takes into account both tree and loop diagrams. For higher masses than $m_{3\pi} \geq 5\,m_\pi$, also processes with explicit ρ contributions appear. An example is given in figure 8.4 (right), that develops from the process depicted in figure 8.4 (left). The ρ contributions can be either taken into account with an amplitude describing trees and ρ contributions, or with an amplitude describing trees and loops and the ρ [Kai11]. If these extended amplitudes are not yet used, the impact of loop and rho contributions has to be mimicked by using several isobaric waves using ρ or $(\pi\pi)_S$ wave as isobars. This is the case for the analysis presented in section 9.4.

As the total spin of quasi-real photons is $J = 1$, amplitudes related to quasi-real photon exchange have to provide the spin-projection $M = 1$. For the calculated ChPT amplitude, two amplitudes with opposite reflectivity $\epsilon = \pm 1$ are introduced, which are mathematically connected to the x- and y-components as explained above. As the amplitudes from ChPT are mathematically not orthogonal to isobaric $M = 1$ waves, simultaneous use with those is to be avoided as far as possible, as it would lead to double-counting and such destabilize the fit.

As the quasi-real photon in the analyzed data stems from the interaction with a lead target, the Weizsäcker-Williams equivalent-photon approximation given by equation (7.12) has to be taken into account for any evaluations of cross-sections. On the level of the mass-independent fit in comparatively small mass bins, however, it multiplies only constant terms to the chiral partial-wave amplitudes given by equations (8.25) and (8.26). These constant terms do obviously not influence angular distributions, so that they are neglected during the mass-independent PWA.

8.2.2.2 Kaon Decay Amplitude

A significant fraction of $\pi^-\pi^-\pi^+$ final state events, recorded at COMPASS at low momentum transfer, stems from decays of beam kaons $K^- \to \pi^-\pi^-\pi^+$ in the 3π-mass region around $0.5\,\text{GeV}/c^2$. These decays occur all along the spectrometer, also in the near target region (see also section 9.6.1). These kaon decay events cannot be treated properly in a traditional mass-independent PWA with mass bins in the order of $10 - 40\,\mathrm{MeV}/c^2$ in which the production strengths of all signals are assumed to be constant. Kaon decays form a sharp mass spectrum and follow the typical Dalitz plot of 3π coming from kaon decay. Thus a dedicated non-isobaric kaon decay amplitude is introduced, which takes into account these specific features. The mass dependence on $m_{3\pi}$ is modelled by two gaussians (adapted to the reconstructed data[17]) as

$$m_{K^-_{\text{model}}} = 846 \cdot \exp\left(-0.5\frac{(m_{3\pi} - 0.494)^2}{0.00175^2}\right) + 241 \cdot \exp\left(-0.5\frac{(m_{3\pi} - 0.495)^2}{0.008735^2}\right) . \tag{8.27}$$

The $K^- \to \pi^-\pi^-\pi^+$ Dalitz plot intensity $\mathcal{I}_{K^-,\text{dalitz}}$ is parametrized as (from [PDG10], page 752)

$$\begin{aligned} \mathcal{I}_{K^-,\text{dalitz}} &= 1 - 0.21134\,\frac{s_3 - s_0}{m_\pi^2} + 1.848\left(\frac{s_3 - s_0}{m_\pi^2}\right)^2 - 4.63\left(\frac{s_2 - s_1}{m_\pi^2}\right)^2 \\ \text{with}\quad s_i &= (p_K - p_i)^2 = (m_K - m_i)^2 - 2m_K T_i \\ s_0 &= \frac{1}{3}\sum_i s_i = \frac{1}{3}(m_K^2 + 3m_\pi^2) . \end{aligned} \tag{8.28}$$

p_K and p_i, $i = 1, 2, 3$, denote the four-vectors, m_K and m_i the mass, and T_i the kinetic energy, of the kaon or the pion i, respectively, where $i = 1, 2$ for the negative and $i = 3$ for the positive pion. Consequently, the complete kaon decay amplitude is given by

$$\mathcal{A}_{K^- \to \pi^-\pi^-\pi^+} = \sqrt{m_{K^-_{\text{model}}} \cdot \mathcal{I}_{K^-,\text{dalitz}}} . \tag{8.29}$$

This amplitude is added incoherently to the other amplitudes in equation (8.1), as interference with those is not supposed to appear.

8.2.2.3 Amplitudes Describing further Non-Isobaric Processes

Data contains more processes than those described in the two previous sections, which need to be described by non-isobaric amplitudes. An amplitude that is common to all current analyses [Wei08a, Jas12, Sch12, Neu12, Haa12] is a *background wave* describing the pure phase-space[18] decay of a state X into three pions without intermediate isobars. This amplitude is added incoherently in equation (8.1), and supposed to collect contributions that do not correspond to the other amplitudes.

An important non-isobaric process, that produces events with the same final state particles and the same quantum numbers as isobaric amplitudes, is the *Deck effect* as depicted in figure 8.5. Pions can act as exchange particles, e.g. between a single final state

---

[17] More precisely, the kaon mass spectrum consists of two parts: The mass resolution of kaons decaying downstream of the target material is significantly better than that of kaons, whose three decay products had to cross the target material. The same argument holds for the reconstructed momentum transfer distributions of the respective parts of the mass spectrum (roughly defined by the reconstructed decay vertex position).

[18] This amplitude is often called “flat wave”, as its behaviour is flat in phase space, but not with mass!

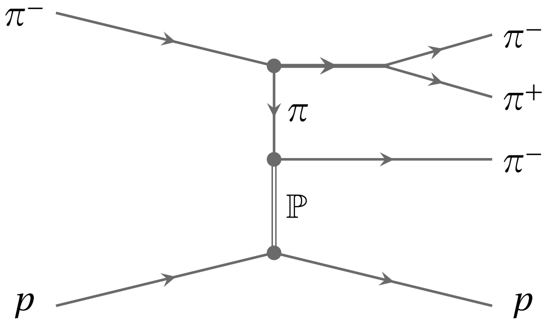

Figure 8.5: A possible contribution to Deck-like scattering, from [Haa12].

pion and a di-pion resonance, in addition to the one-Reggeon exchange with the target. This can significantly influence the mass spectrum and thus the extraction of resonance parameters if not taken into account separately. It is difficult to treat with a dedicated amplitude as well, as that amplitude would be mathematically not orthogonal to isobaric amplitudes. The Deck effect is equivalent to the scattering processes described in section 8.2.2.1. However, equivalent calculations of scattering amplitudes with pomeron exchange are not available owing to the problems of strong interaction at low energies. The Deck effect is not explicitely treated in the following analysis, but is studied with great care in the high-t' analysis (see [Haa12] for more information), where it has a significant impact to the search for spin-exotic resonances.

Calculations of rescattering of the final state particles are also subject of current efforts, but supposed not to be of major importance for the following analysis, so that they can be neglected.

8.2.3 t' Dependences of Decay Amplitudes

The t' dependences $f_i^\epsilon(t')$, which are multiplied on the decay amplitudes $\psi_i^\epsilon(\tau, m)$ in equation (8.1), are not related to the decay, but to the production mechanisms of the intermediate states X^-. Still, their application is supposed to make the fit result more stable, as they provide support for a more reliable description of the data. As they are, in the following PWA in mass bins presented in section 9.4.2, also predefined and not a fitting parameter, their parametrization is still described in this section.

The dependences of the cross-sections of various production mechanisms on t' are well-known for the physics processes exploited in the following analysis. For diffractive production holds $\sigma \propto t^{|M|}\mathrm{e}^{-bt}$ as stated in section 7.2, so that $f(t')$ is dependent most significantly on the spin-projection M of the produced states. Primakoff production features $\frac{d\sigma}{dt'} \propto \frac{t'}{(t'+|t|_{\text{min}})^2}$ as explained in section 7.3, i.e. provides a sharp peak near $t' = 0$ at $|t|_{\text{min}}$, which depends on m_{X^-}. Kaon decay features $t = 0$ as for all decay events. Especially the latter two are observed in experimental data heavily influenced by multiple scattering and resolution effects of the spectrometer, so that their actually observed forms have to be determined, usually directly from the data, and used in the PWA.

In the following analysis of $\pi^-\pi^-\pi^+$ events featuring very low t', diffractive production with $M \geq 1$ can be neglected, so only the $M = 0$ amplitudes stem from diffractive production, and the $M = 1$ amplitudes are exclusively associated to Primakoff production. As the latter forms only a small fraction of the data, its actual t' dependence cannot be obtained from the data directly, but only from a Monte Carlo simulation that takes as input the theoretical t' dependence, and applies proper distortion by resolution effects (see section 9.2.4). The actual t' dependence of the dominating diffractively produced data is obtained via a statistical subtraction of the Primakoff contribution (see section 9.3 for details). It is found that both cross-sections show exponential forms, with the Primakoff contribution featuring a much steeper slope b than the diffractive contribution. Both depend also, less significantly, on the invariant mass $m = m_{X^-}$, so that they can effectively be described by

$$\frac{\mathrm{d}\sigma}{\mathrm{d}t'} \propto \mathrm{e}^{-b(m)t'} \; . \tag{8.30}$$

Both slopes $b(m)$ are determined as explained above, so that the diffractive, i.e. $M = 0$, decay amplitudes, are multiplied by

$$\begin{aligned} f(t')_{\text{diffractive}} = f(t')_{M=0} =& \sqrt{\mathrm{e}^{-b_{\text{diff}}(m)t'}} \\ \text{with} \quad b_{\text{diff}}(m) =& 456.106 - 71.5904 \cdot m + 6.47228 \cdot m^2 \; , \end{aligned} \tag{8.31}$$

while the Primakoff, i.e. $M = 1$, decay amplitudes, are supposed to follow

$$\begin{aligned} f(t')_{\text{Primakoff}} = f(t')_{M=1} =& \sqrt{\mathrm{e}^{-b_{\text{Primakoff}}(m)t'}} \\ \text{with} \quad b_{\text{Primakoff}}(m) =& 2108.0 - 812.1 \cdot m + 46.4 \cdot m^2 \; . \end{aligned} \tag{8.32}$$

The mass dependence of the decay kaons features two components (see equation (8.27) in section 8.2.2.2), as their mass resolution depends on whether the kaon or its decay particles had to cross the target material. This translates equivalently to the resolution in t' (see section 9.6.1.1), so that both mass components feature their own t' dependence:

$$f(t')_{\text{kaon, 1}} \propto \mathrm{e}^{-3200.0\,t'} \quad \text{for} \quad m_{\text{kaon, 1}} \propto \exp\left(-0.5\frac{(m_{3\pi} - 0.494)^2}{0.00175^2}\right) \tag{8.33}$$

$$f(t')_{\text{kaon, 2}} \propto \mathrm{e}^{-1750.0\,t'} \quad \text{for} \quad m_{\text{kaon, 2}} \propto \exp\left(-0.5\frac{(m_{3\pi} - 0.495)^2}{0.008735^2}\right) \; . \tag{8.34}$$

8.3 Normalization Integrals

Normalization integrals are an important ingredient to the mass-independent PWA procedure. Such integrals used for the normalization of the decay amplitudes are described in the following, as well as the normalization integrals used in the log-likelihood fit.

8.3.1 Phase Space Integrals for Normalization of Decay Amplitudes

The phase space integrals

$$I^{\epsilon}_{ii}(m) = \sqrt{\int \left|\psi^{\epsilon}_{i}(\tau, m)\right|^{2} \mathrm{d}\tau} = \sqrt{\frac{1}{N_{\text{generated}}} \sum_{n}^{N_{\text{generated}}} \psi^{\epsilon}_{i}(\tau_n, m)\psi^{\epsilon\,*}_{i}(\tau_n, m)} \tag{8.35}$$

are used for the normalization of the decay amplitudes as given by equation (8.2), to compensate the relative mass dependences of different amplitudes ψ_i. They are calculated from $N_{\text{generated}}$ Monte Carlo events only respecting the phase space of the decay into the final state particles under investigation. These Monte Carlo events are usually generated at sharp values of m_X, i.e. at the upper limits of small mass bins Δm_{MC}, which are chosen as subintervals of the bins Δm_{fit} used during the fit. The mass dependence of an amplitude inside each Δm_{fit} is then approximated by a linear extrapolation between values at all m_X inside Δm_{fit}, and such compensated by the division by I^{ϵ}_{ii}. These integrals are not equal to 1 as the angular momentum barrier factors from equation (8.9) are also applied here.

8.3.2 Standard Normalization Integrals

The standard normalization integrals are used during the log-likelihood fit (see section 8.5). They normalize the PWA fit results in a way, that inside each mass bin Δm_{fit} the resulting total intensity is equal to the number of events, usually including acceptance corrections. These integrals $AccI^{\epsilon}_{ij}$ are given by

$$AccI^{\epsilon}_{ij} = \int \overline{f}^{\epsilon}_{i}(t')\,\overline{\psi}^{\epsilon}_{i}(\tau, m)\,\overline{f}^{*\epsilon}_{j}(t')\,\overline{\psi}^{*\epsilon}_{j}(\tau, m)\;Acc(\tau, m, t')\;\mathrm{d}\tau\,\mathrm{d}m\,\mathrm{d}t' \tag{8.36}$$

integrating over phase space τ and the kinematic variables m (inside Δm_{fit}) and the investigated region of t', for pairs of individual partial waves i and j. $f^{\epsilon}_{i}(t')\,\psi^{\epsilon}_{i}(\tau, m)$ are evaluated for phase space Monte Carlo events[19], and acceptance is taken into account by the factor $Acc(\tau, m, t')$ which uses the information from simulations of these events passing the spectrometer used for data taking[20].

In case of fitting without acceptance corrections, the integrals

$$NAccI^{\epsilon}_{ij} = \int \overline{f}^{\epsilon}_{i}(t')\,\overline{\psi}^{\epsilon}_{i}(\tau, m)\,\overline{f}^{*\epsilon}_{j}(t')\,\overline{\psi}^{*\epsilon}_{j}(\tau, m)\;\mathrm{d}\tau\,\mathrm{d}m\,\mathrm{d}t' \tag{8.37}$$

---

[19] Integration over phase space and kinematic variables means again the summation of an amount of MC events, that should exceed the number of experimental events significantly. Typically a factor of 5-10 of accepted events is chosen, so that the final uncertainty of the fit result is dominated by data and not by uncertainties of the integrals.

[20] Phase space events, that cannot be fully reconstructed after taking into account all experimental influences, like e.g. limited resolutions and active areas of detectors, are used for the correction of the final fit result for acceptance.

are used instead. It should be noted, that these integrals are zero for amplitudes i and j corresponding to different $J^{PC}M^{\epsilon}$, as those are orthogonal.

As none of these integrals contain any fitting parameters, they are pre-calculated once before being used for PWA fits. They have to be re-calculated only in case of acceptance-relevant changes in the event selection or other changes of the acceptance evaluations, e.g. due to improved simulations of the spectrometer.

8.3.3 Special Integrals

For most applications the decay amplitudes are normalized[21] according to equation (8.2), using equation (8.35), and subsequently the normalization integrals for the PWA fit are calculated according to equation (8.36). However, for special purposes, which are relevant for the following analysis, the compensation of the relative mass dependence can or should be omitted or modified.

This is the case, for example, in PWA fits in small bins of t' aiming at the extraction of t' dependences of amplitudes. These fits use broad mass bins, inside which significant changes of decay amplitudes appear, so that a mass dependence of an amplitude or even the full Breit-Wigner description of a resonance are preferably introduced during the calculation of the normalization integrals for the PWA fit. These mass dependences or Breit-Wigner descriptions are multiplied on the respective standard amplitude $\psi_i^{\epsilon}(\tau, m)$ (i.e. substitute $\Delta_X(m_{3\pi}) = 1$ in equation (8.17)) as given in the following exemplarily for three special cases, which are applied in the analysis given in section 9.4.3.

- The relative phase between two specific resonances, e.g. the $a_2(1320)$ and the $a_1(1260)$, is to be investigated depending on t', so that small bins of t' are used. In this case, only one broad mass range covering the full Breit-Wigner of the narrower resonance (here: the $a_2(1320)$; completely included in the mass range of the broader resonance, here the $a_1(1260)$) is subject of the PWA fit. Both the mass dependence and the change of the phase within this mass bin, of both compared resonances, are to be conserved in this case. So no phase-space integrals are used at all, i.e. the PWA fit is based on unnormalized decay amplitudes. In addition, the full Breit-Wigner forms of the $a_1(1260)$ and $a_2(1320)$ resonances are multiplied on their respective decay amplitudes. With the decay amplitude of the $a_1(1260)$ being the $J^{PC}M^{\epsilon}[isobar\ \pi]L = 1^{++}0^{+}[\rho\pi]S$ wave, and for $a_2(1320)$ the $J^{PC}M^{\epsilon}[isobar\ \pi]L = 2^{++}1^{+}[\rho\pi]D$ wave, this leads to

$$\psi_{a_1(1260)}(\tau, m) = \psi_{1^{++}0^{+}[\rho\pi]S}(\tau) \cdot BW_{a_1}(m) \quad \text{and} \tag{8.38}$$

$$\psi_{a_2(1320)}(\tau, m) = \psi_{2^{++}1^{+}[\rho\pi]D}(\tau) \cdot BW_{a_2}(m)\ . \tag{8.39}$$

---

[21] i.e. the relative differences of mass dependences of different ψ_i are compensated

The Breit-Wigners used for both resonances are given as

$$BW(m) = \frac{\sqrt{m_0\Gamma_0}}{m_0^2 - m_2 - im_0\Gamma(m)} \tag{8.40}$$

with the mass-dependent widths

$$\Gamma_{a_1}(m) = \Gamma_{0,a_1}\frac{m_{0,a_1}}{m}\frac{\int \psi^2 \mathrm{d}\tau}{0.2873} \tag{8.41}$$

$$\text{with} \quad m_{0,a_1} = 1.220\,\mathrm{GeV}/c^2\,, \quad \Gamma_{0,a_1} = 0.370\,\mathrm{GeV}/c^2 \quad \text{and}$$

$$\Gamma_{a_2}(m) = \Gamma_{0,a_1}\frac{m_{0,a_2}}{m}(0.8\frac{pF_{2,\rho\pi}(x)}{p_0F_{2,\rho\pi}(x_0)} + 0.2\frac{pF_{2,\eta\pi}(x)}{p_0F_{2,\eta\pi}(x_0)}) \tag{8.42}$$

$$\text{with} \quad m_{0,a_2} = 1.314\,\mathrm{GeV}/c^2\,, \quad \Gamma_{0,a_2} = 0.120\,\mathrm{GeV}/c^2\,. \tag{8.43}$$

Using $\int \psi^2 \mathrm{d}\tau$ for the mass-dependent width of the $a_1(1260)$ provides a more general approach than using $F_L(x)$ as given in equation (7.3). The constant division factor is chosen such, that the fraction is equal 1 at the nominal mass of the $a_1(1260)$. The mass-dependent width of the $a_2(1320)$ uses the Flatte-approch (equation (7.3)) and takes into account its most important decays into $\rho\pi$ and $\eta\pi$. These are the traditional parametrizations for the $a_1(1260)$ and $a_2(1320)$ resonances, respectively. They are used for the analysis of the dependence[22] of the $a_2(1320)$ phase with t', presented in section 9.4.3.2.

- t' dependences of amplitudes in the low-mass region are to be investigated, again in small bins of t', but accumulated in a comparatively broad mass region. As the investigated mass region covers the range just above threshold, non-resonating final states prevail, so the production phases are assumed to be constant[23], and no Breit-Wigner forms need to be introduced. Instead, the mass dependencies only are described by polynomials that have been obtained from fits to the data[24]. These polynomials contain also the phase space within the mass dependence, so that the phase space integrals used for the normalization of the decay amplitudes have to be calculated and used in the standard way. However, the amplitudes finally used in the PWA fit are multiplied subsequently with the square-roots of these polynomials, to keep the measured mass dependence:

$$\overline{\psi_i(\tau, m)} = \frac{\psi_i(\tau)\cdot\sqrt{(polynomial)_i(m)}}{\sqrt{\int |\psi_i(\tau)| \mathrm{d}\tau}}\,. \tag{8.44}$$

The polynomials used in the following analysis for each amplitude i, or sets of amplitudes, are stated in table 8.2. This parametrization is used for the investigation

---

[22] In addition, these are the standard parametrizations used for a mass-dependent PWA (see section 8.8).

[23] A PWA in mass bins shows, that the phases are poorly measured, but indeed flat on the resulting level of precision.

[24] More precisely, these polynomials have been obtained from the behaviour of the intensities of the respective waves, from a PWA fit in small mass bins, covering the range $t' < 0.001\,\mathrm{GeV}^2/c^2$.

amplitude(s) ($J^{PC}M^{\epsilon}[isobar\ \pi]L$ or sets)	$polynomial_i(m)$ employing $m[\mathrm{GeV}/c^2]$
$0^{-+}0^{+}[(\pi\pi)_S\pi]S$	$-0.0244 + 0.10821\,m - 0.16374\,m^2 + 0.088797\,m^3$
$0^{-+}0^{+}[\rho\pi]P$	$-0.15551 + 0.95872\,m - 1.9681\,m^2 + 1.3468\,m^3$
$1^{++}0^{+}[\rho\pi]S$	$-0.039814 + 0.19352\,m - 0.31127\,m^2 + 0.16620\,m^3$
$J^{PC}M = 1^{++}1$	$0.20655 - 0.63554\,m + 0.48634\,m^2$
$J^{PC}M = 1^{-+}1$	$0.12952 - 0.36402\,m + 0.25283\,m^2$
$J^{PC}M = 2^{++}1$	$0.077447 - 0.18955\,m + 0.11649\,m^2$
$J^{PC}M = 2^{-+}1$	$-0.40354 + 0.58341\,m$
ChPT	$0.026861 - 0.12709\,m + 0.15353\,m^2$
other amplitudes	$0.018724 - 0.14114\,m + 0.38217\,m^2 - 0.47945\,m^3 + 0.22053\,m^4$

Table 8.2: Polynomials describing the mass-dependence of decay amplitudes at low masses as used in the analysis in section 9.4.3.1

of the t' dependence of the ChPT amplitude in section 9.4.3.1.

- Phases and intensities are to be investigated dependent on t', in a mass region, where various resonances are present, with additional background known to appear in the same amplitudes as resonances of interest. Again PWA fits are carried out in very small bins of t', but in a broad mass bin, inside which both mass dependences and phases are to be conserved. The resonances are parametrized again by Breit-Wigners, and the background by exponentials in m. As the background can stem from tails of higher resonances, and such have a relative phase, this additional mass dependence is also complex. Breit-Wigners and background are summed to single complex terms, denoted in the following by $BWBKG_j(m)$. Their parameters are obtained again from a fit to the intensities concerned, at which the square of these $BWBKG_j(m)$ is fitted to the intensities. These sums are then multiplied on the decay amplitudes, which have been normalized in the standard way before. Such, similar to the previous item, the PWA is based on the following amplitudes

$$\overline{\psi_j}(\tau, m) = \frac{\psi_j(\tau) \cdot BWBKG_j(m)}{\sqrt{\int |\psi_j(\tau)| \mathrm{d}\tau}} \tag{8.45}$$

using

$$BWBKG_j(m) = p_{4,j} \frac{\sqrt{m_j \Gamma_j}}{m_j^2 - m^2 - i m_j \Gamma_j} + p_{5,j} \exp(-\alpha_j m) + i p_{6,j} \exp(-\alpha_j m) \tag{8.46}$$

with m_j the nominal mass, Γ_j the nominal width of the resonance, α_j describing the background, and $p_{4,j}$, $p_{5,j}$, and $p_{6,j}$ adjusted to the relative strengths of Breit-Wigner and background. All parameters are derived from fits to intensities in small mass bins, and given in table 8.3. The mass dependences of all minor waves not included in table 8.3 , but used in the PWA fit, are just described by a polynomial behaviour

amplitude(s) $J^{PC}M^{\epsilon}[isobar\ \pi]L$	m_j [GeV/c^2]	Γ_j [GeV/c^2]	α_j [(GeV/c^2)$^{-1}$]	$p_{4,j}$	$p_{5,j}$	$p_{6,j}$
$0^{-+}0^{+}[(\pi\pi)_S\pi]S$	1.8188	0.23117	4.5104	43.180	12512.0	-43305.0
$0^{-+}0^{+}[f_0(980)\pi]S$	1.8094	0.23515	-0.36871	28.042	3.0863	-0.57855
$0^{-+}0^{+}[\rho\pi]P$	1.5150	0.20004	1.1676	47.787	43.133	-162.45
$1^{++}0^{+}[\rho\pi]S$	1.3051	0.31616	7.3830	101.58	238700.0	23925.0
$1^{++}0^{+}[\rho\pi]D$	1.5943	0.26680	1.5255	53.629	-77.010	-524.38
$1^{++}0^{+}[(\pi\pi)_S\pi]P$	1.3763	0.74318	0.49296	89.914	76.893	-17.233
$1^{++}0^{+}[f_2(1270)\pi]P$	1.6815	0.25355	1.3663	34.721	-33.388	-232.13
$2^{-+}0^{+}[f_2(1270)\pi]S$	1.6497	0.23698	3.9694	43.674	4821.3	603.17
$2^{-+}0^{+}[f_2(1270)\pi]D$	1.7782	0.24392	3.1200	18.036	-1756.3	-284.26
$2^{-+}0^{+}[\rho\pi]P$	1.7142	0.43511	-0.29141	31.377	3.8596	0.14228
$2^{-+}1^{\pm}[f_2(1270)\pi]S$ $2^{-+}1^{\pm}[\rho\pi]P/F$	1.6909	0.24024	0.33177	9.1258	17.349	-3.7695

Table 8.3: Parameters used with equation 8.46 to describe the mass-dependence of decay amplitudes in the $\pi_2(1670)$ mass region, as used in the analysis in section 9.4.3.1

$$BWBKG_j(m) = \sqrt{0.19746 - 0.32710\,m + 0.18933\,m^2 - 0.037275\,m^3} \tag{8.47}$$

This parametrization is used for the investigation of t' dependences of intensities and phases in the $\pi_2(1670)$ mass region in section 9.4.3.3.

8.4 Ranks and Partial Coherence

By the summation over the rank $r = 1 \ldots N_r$ in equation (8.1), N_r sets of coherent cross-section contributions are summed up incoherently. This is eventually needed if different final states of the unobserved recoiling system are possible. Each of those terms contains the same set of decay amplitudes $\psi_i^{\epsilon}(\tau, m)$, on which different independent transition amplitudes T_{ir}^{ϵ} are multiplied, such that for each $\psi_i^{\epsilon}(\tau, m)$ N_r different T_{ir}^{ϵ} are fitted. This allows for different coeffients $T_{ir}^{\epsilon}T_{jr}^{\epsilon *}$ multiplied to the $\psi_i^{\epsilon}\psi_j^{\epsilon *}$, so that the relative phase of the partial waves (see section 8.6) can have a completely different behaviour in the distinct sets N_r. Thus the rank N_r is usually chosen according to the (in)coherence of the analyzed production process: Rank 1 is chosen for coherent scattering, as occuring with scattering at heavy nuclei at low t', while rank 2 is traditionally chosen for scattering processes at nucleons, so that both helicity-flip and helicity-non-flip processes at the recoil nucleon are taken into account [Wei08a, Haa12]. Rank 2 might also be chosen if the coherence of a process is distorted in the experimental data by limited resolution of the spectrometer[25]. N_r can exhibit at maximum the total number of decay amplitudes, which is then called *unlimited rank*.

Another way to account for breaking of coherence due to limited experimental resolution, is the concept of *partial coherence* instead of increased rank $N_r > 1$. This allows limited coherence between selected sets of decay amplitudes, and thus reweighting of individual off-diagonal terms in the coherent sum, illustrated by

$$\sum_{ij} T_i\, T_j^*\, \psi_i\, \psi_j^* \quad \rightarrow \quad \sum_{ij} \boxed{\mathrm{r}_{ij}}\, T_i\, T_j^*\, \psi_i\, \psi_j^* \,. \tag{8.48}$$

$\mathrm{r}_{ij} \leq 1$ is a real number that reflects the reduction of coherence between the decay amplitudes i and j, with $\mathrm{r}_{ij} = \mathrm{r}_{ji}$, and $\mathrm{r}_{ii} \equiv 1$ (see section 8.6 for explanations).

This approach is derived from the formula given for the general description of the total cross-section[26] [Han74], often referred to as the *Ascoli approach*:

(8.49)

$$\sigma = \sum_{\epsilon_A} \sum_{op} \sum_{kl} \underbrace{\rho^{\epsilon_A}_{op}}_{\rho-matrix} \underbrace{C^{\epsilon_A}_{ok}\, C^{\epsilon_A *}_{pl}}_{\hookrightarrow T_i} \psi^{\epsilon_A}_k\, \psi^{\epsilon_A *}_l = \sum_{\epsilon_A} \sum_{op} \rho^{\epsilon_A}_{op} \left(\sum_k C^{\epsilon_A}_{ok}\, \psi^{\epsilon_A}_k \right) \left(\sum_l C^{\epsilon_A *}_{pl}\, \psi^{\epsilon_A *}_l \right)$$

In this approach the $\psi^{\epsilon_A}_k$ refer to the decay part of the amplitude presently used, i.e. "$[isobar\ \pi]L$", and $C^{\epsilon_A}_{ok}$ to $J^{PC}M^{\epsilon}$. These are summed (over the index k or l, resp., defining the decay) coherently, so that the fitting parameters $C^{\epsilon_A}_{ok}$ define the relative strengths of the different decay modes[27] of a certain $J^{PC}M^{\epsilon}$, assuming that only one resonance is present with these quantum numbers in a certain mass range. The hermitian complex matrix $\rho^{\epsilon_A}_{op}$ contains another set of fit parameters, that define the relative strengths between different $J^{PC}M^{\epsilon}$, so that it was called *spin-density matrix*[28]. The coherence in this approach is not predetermined. The sum over ϵ_A reflects the sum over the incoherent contributions, i.e. technically different *blocks* are defined (one for each value of ϵ_A), allowing internally only coherent summation. It should be noted that each combination of $C^{\epsilon_A}_{mk}\psi^{\epsilon_A}_k$ is different, which means it is allowed to appear only in one specific block.

In the course of technical development of partial-wave analysis methods this approach has been modified [Rya12], so that different blocks are nowadays used for both different

---

[25] Historically, rank 2 was in fact chosen for the first iterations of the PWA presented in section 9.4, where the decay particles are detected at very small angles, so that the reconstruction of their decay angles is challenging.

[26] The analyses, in whose context this formalism was developped, were also carried out in mass bins. The parameters of mass and phase spase are omitted here for better readability of the formula.

[27] It is assumed that a resonance does not remember its production, so that its decay is independent from the way it was produced. This means, the parameters $C^{\epsilon_A}_{ok}$ are constant for the mass region of a specific resonance, which is true if one of them is fixed, so that the others are well related to it [Rya12].

[28] This is the historical origination of the notation "spin-density matrix". For its nowadays' meaning and interpretations see section 8.6.

ranks r and reflectivities ϵ ($\epsilon_A \rightarrow r, \epsilon$), while decay amplitudes may be repeated ($\psi_k^{\epsilon_A} \rightarrow \psi_i$) with ranks $N_r > 1$. The ρ_{op} are typically set to 1, and the $C_{op}^{\epsilon_A}$ remain as the only fitting parameters, renamed to T_{ir}^{ϵ}.

For the analysis presented in the following, the original technique has been partly recovered, so that the matrix ρ_{op} is re-established containing real numbers r_{ij} as mentioned above. These r_{ij} decrease the contribution (i.e. the absolute value, but not the phase) of the interference of the amplitudes i and j (or sets of amplitudes that are internally treated with rank 1, i.e. fully coherent) for $\mathrm{r}_{ij} < 1$. This is achieved without introducing additional phases (with respect to a rank 1 fit, as would result from a rank 2 fit). These parameters r_{ij} can be either predeterminded and then fixed, or also subject of the fitting procedure.

The choice of a certain rank N_r, or "initial rank 1 with partial coherence" and its appropriate number of $\mathrm{r}_{ij} < 1$, for a specific PWA fit should be a subject of thorough investigations, to find the model that fits the data best. Ideally these studies are supported by of a dedicated Monte Carlo study, that reflects the influence of the experimental resolution properly.

8.5 Extended Log-Likelihood Fit

The physics understanding of the data is developped in terms of trivial *models*, which use all ingredients described in the previous sections and are based on equation (8.1). Within these models, the transition amplitudes T_{ir}^{ϵ} have now to be optimized individually for each mass bin such that the best possible agreement of $\mathcal{I}_m(\tau, t')$ with the real data covering this mass bin is achieved. This is realized by applying the extended log-likelihood method, maximizing the following expression, which subtracts the integral of the normalized models from the sum of the experimental events (for details see e.g. [Neu12]):

$$\ln \mathcal{L} = \sum_{n=1}^{N_{\text{events}}} \ln \mathcal{I}_{m_n}(\tau_n, t'_n) - \underbrace{\int \mathcal{I}_m(\tau, t')\ Acc(\tau, m, t') \mathrm{d}\tau \mathrm{d}m \mathrm{d}t'}_{=N_{\text{events}} \text{ for optimized parameters, i.e. } \mathcal{I}=\mathcal{I}_{\text{opt}}}$$

(8.50)

$$= \sum_{n=1}^{N_{\text{events}}} \ln \left[\sum_{\epsilon,r} \sum_{ij} T_{ir}^{\epsilon} T_{jr}^{\epsilon *} \overline{f}_i^{\epsilon}(t'_n)\, \overline{\psi}_i^{\epsilon}(\tau_n, m_n) \overline{f}_j^{\epsilon *}(t'_n)\, \overline{\psi}_j^{\epsilon *}(\tau_n, m_n) \right] - \sum_{\epsilon,r} \sum_{ij} T_{ir}^{\epsilon} T_{jr}^{\epsilon *} Acc I_{ij}^{\epsilon}$$

with $Acc I_{ij}^{\epsilon}$ the pre-calculated normalization integrals given by equation (8.36).

The fitting procedure is carried out for each mass bin individually, with typically 10-50 independent fit attempts per mass bin, until the best fit yields independent optimized sets of T_{ir}^{ϵ} with their statistical errors (see [Wei08a] for details on those) for each mass bin Δm_{fit}.

The PWA program used is based on the "Ascoli fitter" [Asc70], originating in the 1970s and featuring plenty of modifications and improvements nowadays.

8.6 Interpretation of Fit Results

Physical parameters cannot be derived from the optimized set of complex numbers T^{ϵ}_{ir} directly, but from the elements of the *spin-density matrix*, which is given by

$$\rho^{\epsilon}_{ij} = \sum_r T^{\epsilon}_{ir} T^{\epsilon *}_{jr} \,. \tag{8.51}$$

The total number of acceptance corrected events in a certain mass bin used in the fit can now be written as

$$N_{\text{corr}} = \int \mathcal{I}_{m,\text{opt}}(\tau, t') \mathrm{d}\tau \mathrm{d}m \mathrm{d}t' = \sum_{\epsilon} \sum_{ij} \rho^{\epsilon}_{ij} \, NAccI^{\epsilon}_{ij} \tag{8.52}$$

with $NAccI^{\epsilon}_{ij}$ the normalization integrals that do not take into account the experimental acceptance, given by equation (8.37).

The diagonal elements of the spin-density matrix constitute the *intensities* of the single amplitudes

$$\text{Intens}^{\epsilon}_{i} = \rho^{\epsilon}_{ii} \tag{8.53}$$

which are real numbers. With the chosen normalization given in section 8.3.2, they can be interpreted as the (acceptance corrected) effective number of events associated with an intermediate state with the decay channel i.

The *interferences* between single amplitudes are contained in the off-diagonal complex elements $\rho^{\epsilon}_{ij,\, i \neq j}$. They are usually accessed using the relative *phase* Φ^{ϵ}_{ij} and the degree of *coherence* $\text{Coh}^{\epsilon}_{ij}$ between two different amplitudes i and j, defined by

$$\rho^{\epsilon}_{ij} = |\rho^{\epsilon}_{ij}| \, \mathrm{e}^{i \Phi^{\epsilon}_{ij}} \quad \text{and} \tag{8.54}$$

$$\text{Coh}^{\epsilon}_{ij} = |\rho^{\epsilon}_{ij}| \Big/ \sqrt{\rho^{\epsilon}_{ii}} \sqrt{\rho^{\epsilon}_{jj}} = \sqrt{(\text{Re}\, \rho^{\epsilon}_{ij})^2 + (\text{Im}\, \rho^{\epsilon}_{ij})^2} \Big/ \sqrt{\rho^{\epsilon}_{ii} \rho^{\epsilon}_{jj}} \,. \tag{8.55}$$

Another important quantity is the *overlap* $\text{Overlap}^{\epsilon}_{ij}$, describing the integrated interference[29] between two amplitudes i and j, given by

$$\text{Overlap}^{\epsilon}_{ij} = 2 \, \text{Re} \, (\rho^{\epsilon}_{ij} \, NAccI^{\epsilon}_{ij}) \tag{8.56}$$

which is zero for amplitudes i and j with different quantum numbers $J^{PC}M^{\epsilon}$ as those are orthogonal with respect to each other, so that their $NAccI^{\epsilon}_{ij} = 0$. The interference itself instead is expressed by $\rho^{\epsilon}_{ij} \neq 0$, allowing for e.g. the measurement of phases also for orthogonal amplitudes.

So-called *total intensities* can be obtained by adding all intensities $\text{Intens}^{\epsilon}_{i}$ and non-zero overlaps $\text{Overlap}^{\epsilon}_{ij}$ that feature the same quantum numbers J^{PC}, M and/or ϵ. They might

---

[29] related to the number of events in the interference region of these two amplitudes

be preferred to the individual intensities when they give a clearer picture of resonances, or distinguish between certain physics processes. In the following analysis for example, especially the comparison of $M = 0$ and $M = 1$ total intensities is relevant, as those can be attributed to different interaction mechanism in the analyzed kinematic range.

It is obvious from the equations above that in case of working with "initial rank 1 with partial coherence" $\mathrm{r}_{ij,i\neq j} \leq 1$, i.e. the spin-density matrix is modified from equation (8.51) to

$$\rho^{\epsilon}_{ij} = \mathrm{r}_{ij} T^{\epsilon}_{i} T^{\epsilon *}_{j}, \tag{8.57}$$

the intensities $\mathrm{Intens}^{\epsilon}_{i}$ and the phases Φ^{ϵ}_{ij} are not controlled artificially, while the coherences are given by $\mathrm{Coh}^{\epsilon}_{ij} = \mathrm{r}_{ij}$. The overlaps are also reduced technically, but non-zero only for amplitudes with the same quantum numbers $J^{PC}M^{\epsilon}$, between which the coherences are usually not reduced, as those are supposed to be coherent.

For the physics interpretation, the above mentioned quantities are ususally plotted for a specific t' range analyzed, combining all different independently fitted mass bins into one common histogram, that depicts the mass-dependence of a certain quantity like an intensity or a phase between two amplitudes (for examples see section 9.4.2). Like this, resonances can show up as Breit-Wigner shaped structures in the intensities of certain amplitudes, and characteristic phase motions with respect to other amplitudes (that might also contain resonances) can be observed. Vice versa, the combination of different independent fits in bins of t' for a defined mass range can also be exploited to investigate t' dependences (see section 9.4.3), if the available statistics is not enough for a two-dimensional fit in both m_X and t'.

8.7 Quality Checks

The quality of the result of a mass-independent PWA fit can traditionally be judged by different methods. One obvious approach is the comparison[30] of the log-likelihood $\ln \mathcal{L}$ (equation (8.50)) of fits with different models (e.g. different sets of decay amplitudes or different ranks) that may help to chose the model that describes the data best. Another important procedure focuses on the comparison of various kinematical distributions, e.g. momentum distributions in the laboratory system or decay angles θ and ϕ in a certain analyzing frame. These should agree on a certain level[31] between data and intensity of the optimized model for the analyzed mass range given by equation (8.1). The latter is usually referred to as *weighted Monte Carlo*[32] and basically described in the following.

"Weighted Monte Carlo" denotes phase-space Monte Carlo that has been weighted with

---

[30] If fits with different number of fitting parameters are compared, $\ln \mathcal{L}$ has to be normalized to the number of degrees of freedom before the comparison, of course.

[31] Agreement is desired typically on the level of a few percent.

[32] In former times also the notation "predict plots/results" was commonly used, as the executable from the employed program that carries out the weighting procedure is named `predictmc.exe`.

both acceptance and the parameters found by the best PWA fit. It is based on Monte Carlo events that have been generated homogeneous in the phase-space variables τ (i.e. that neither resonances nor other cuts in phase space are present), and that are judged whether being accepted after having passed a simulation of the experimental apparatus[33]. Hereby acceptance is fulfilled, if events can be fully reconstructed from the simulated detector response, so that they fulfill the selection criteria of the real data events. In addition the optimized intensity (with the fit result ρ_{ij} depending on m) is calculated for each event. The Monte Carlo events are weighted accordingly and summed up using all related information. Now any relevant kinematical distribution can be obtained from the weighted MC events, normalized to the total number of events from data, and be compared to the corresponding distribution from real data. For examples see sections C.1.3 and C.2.

It has to be stressed that the approach of weighted Monte Carlo evaluates the quality of the fitting model and the acceptance corrections simultaneously, as the fitting parameters T^{ϵ}_{ir} are obtained during a PWA fit that takes into account the experimental acceptance. This means that an incomplete description of the setup can lead to wrong angular distributions that might influence the fit result as well. Examples for improvements in the acceptance descriptions, initiated by distributions of weighted Monte Carlo events poorly matching those from real data, are given in appendix C.

8.8 Mass-Dependent PWA

After the results of the mass-independent PWA have converged to some level of log-likelihood for each mass bin, they can be used to extract and confirm resonances and their parameters from the full analyzed mass range. This is based on all information available, i.e. uses both intensities and interferences. This means, the second step of a full PWA takes as input also the non-diagonal elements of the spin-density matrix $\rho^{\epsilon}_{ij} = \sum_r T^{\epsilon}_{ir} T^{\epsilon *}_{jr}$, which can also be expressed as

$$\rho^{\epsilon}_{ij} = \sum_{r=1}^{N_r} \left(\sum_k C^{\epsilon}_{ikr} \, BW_k(m) \sqrt{\int \left|\psi^{\epsilon}_i(\tau, m)\right|^2 \mathrm{d}\tau} \right) \left(\sum_l C^{\epsilon}_{jlr} \, BW_l(m) \sqrt{\int \left|\psi^{\epsilon}_j(\tau, m)\right|^2 \mathrm{d}\tau} \right)^{*} . \tag{8.58}$$

Equation (8.58) contains the transition amplitudes C^{ϵ}_{ikr}, and the mass-dependence is now described by $BW_k(m)$, which can be Breit-Wigner or background functions dependent on mass $m = m_X$. Thus they contain new fitting parameters related to mass m_0 and width Γ_0 of a resonance X, or the shape of the background, which is usually parametrized by $\mathrm{e}^{-\alpha p^2}$ [ACC81], with α the fitting parameter and p the break-up momentum of the resonance X, respectively. In this step, a specific Breit-Wigner function might be used to fit several different intensities ρ^{ϵ}_{ii} and their interferences ρ^{ϵ}_{ij}, while any given amplitude i might also

---

[33] For a reasonable simulation of the spectrometer response, some quantities like decay vertex positions are predefined, but the decay itself is generated to be flat in phase space (see also section 9.2.1).

be fitted by more than one Breit-Wigner and coherent background. Usually the same rank N_r is chosen is this step as for the mass-independent fit, to allow for the same level of coherence between different amplitudes. Still, it might be desirable to add incoherent background to the intensity of a specific amplitude, which is technically equivalent of working with an even higher rank (i.e. $N_r \to N_r + 1$). As the computational evaluation of the method described is quite CPU consuming, usually only a well-defined subset of all amplitudes, i.e. presumably the most important ones, are chosen for the extraction of resonance parameters by the mass-dependent χ^2 fit applied to equation (8.58). More information on this technique, illustrated in conjunction with the analyses it has been applied with, can be found in [Wei08a, Neu12, Haa12].

Chapter 9

Analysis of 2004 $\pi^-\pi^-\pi^+$ Data at Low Momentum Transfer

Results from an analysis of $\pi^-\pi^-\pi^+$ events, produced from a pion beam impinging on a lead target, are presented in this chapter. Thereby the main focus is placed on the kinematic regime of low momentum transfer t' to the target, where Primakoff interactions (see section 7.3) are expected in addition to diffractive dissociation (see section 7.2). If these are reliably separated, the measurement of processes calculated by Chiral Perturbation Theory (see section 7.1.3), as well as of Primakoff-produced resonances, is possible. Section 9.1 starts with the introduction of the analyzed data set and the event selection, including the basic kinematic distributions. In section 9.2 the Monte Carlo simulations carried out in the course of this analysis are described. They cover simulations of the COMPASS spectrometer for the acceptance corrections to be applied during the partial-wave analysis (PWA), including the evaluation of the acceptance, as well as simulations of resolution effects most strongly affecting events featuring the pure Primakoff momentum transfer distribution.

A statistical subtraction method as a first access to the Primakoff-produced contribution to the data is described in section 9.3. The results from the mass-independent PWA, as introduced in chapter 8, are presented in section 9.4. First the impact of the non-isobaric amplitudes, implemented specifically for this PWA of events featuring smallest $t' < 10^{-3}\,\mathrm{GeV}^2/c^2$, is shortly discussed, followed by the various PWA fits. While intensities and phases analyzed in mass bins provide access to the discrimination of diverse resonances and non-resonant structures, an analysis in bins of t' gives an insight to the production mechanisms of these (non-)resonant structures. A short leakage study dealing with the impact of resolution effects at $t' \approx 0$ on the PWA results is depicted in section 9.5.

As a main result, the first measurement of the total cross-section $\pi^-\gamma \to \pi^-\pi^-\pi^+$, as calculated in leading order by ChPT, is presented in section 9.6. An important ingredient to this measurement is the determination of the beam flux, which is obtained from the free decays of beam kaons. The cross-section derived from the corresponding intensity from PWA via the kaon normalization is then compared to the prediction from ChPT.

9.1 Data Set and Event Selection

The data presented in the following were recorded during the COMPASS Pilot Hadron Run in autumn 2004 (see section 2.2.2 and [Din10] for a brief history and the details of the data taking conditions). The analyzed data set covers only runs with a 190 GeV/c π^- beam on lead targets during which the diffractive trigger was activated. This trigger fired when a threshold of 1.5 MIP[1] in a scintillator disk ("Multiplicity Counter") downstream of the target, and a fixed threshold of a few[2] GeV energy deposit in the hadronic calorimeter HCAL2, were exceeded, while less than two of the three beam killers in the downstream part of the spectrometer were hit. The data set, effectively collected in less than three days, consists of 15 runs with the 3 mm lead target (from the range of run numbers 42820-42840) and 58 runs with the $2 + 1$ mm lead targets (run numbers 43191-43323) inserted into the beam. In the latter period also the online filter was in stable operation, resulting in increased purity of the data, so that about 85 % of the statistics entering the PWA was collected then.

In the following the selection criteria for exclusive $\pi^-\text{Pb} \to \pi^-\pi^-\pi^+\text{Pb}$ events are described, including the characteristics of the different ranges of momentum transfer. The event selection is deduced from the analysis of "high t'" events (discussed in detail in [Wei08a]) and slightly adapted according to the peculiarities of the "low t'" data concentrated on here. 3π invariant mass spectra for all ranges of t' and Dalitz plots for $t < 10^{-3}\,\text{GeV}^2/c^2$ give a first global impression of the "very low t'" data treated with the PWA focussed on later. The kaon contributions to the $\pi^-\pi^-\pi^+$ data are also summarized, concerning both the decay of beam K^- and unidentified kaons in the final state.

9.1.1 Basic Cuts, Exclusivity and t' Ranges

As a basic requirement, the **diffractive trigger** bit has to be set in the trigger mask[3] of an event entering the further analysis. Events that were triggered *only* by other triggers were rejected, as for those the acceptance corrections would have been much more delicate due to e.g., in case of the Primakoff triggers, high but poorly reproducible thresholds in the electromagnetic calorimeters potentially leading to artefacts in the 3π acceptance. The diffractive trigger instead, generally selecting events with at least two charged outgoing particles with scattering angles less than about 50 mrad, does not introduce significant artificial cuts into the 3π acceptance (see e.g. figure 9.7) and can such be regarded as a minimum bias trigger for the 3π analysis.

The **online filter**, which is closely related to the trigger (see section 2.2.2.4), was still being tuned during the data taking period with the 3 mm target, so that it could not

---

[1] Energy deposit of a **M**inimum **I**onizing **P**article in a certain material

[2] The exact threshold is not documented. The data suggest a threshold of about 4 GeV, which corresponds to 6 GeV in the Monte Carlo simulation if shapes of spectra are compared. A proper calibration is missing here.

[3] Bitmap that contains the information which trigger(s) fired for a particular event.

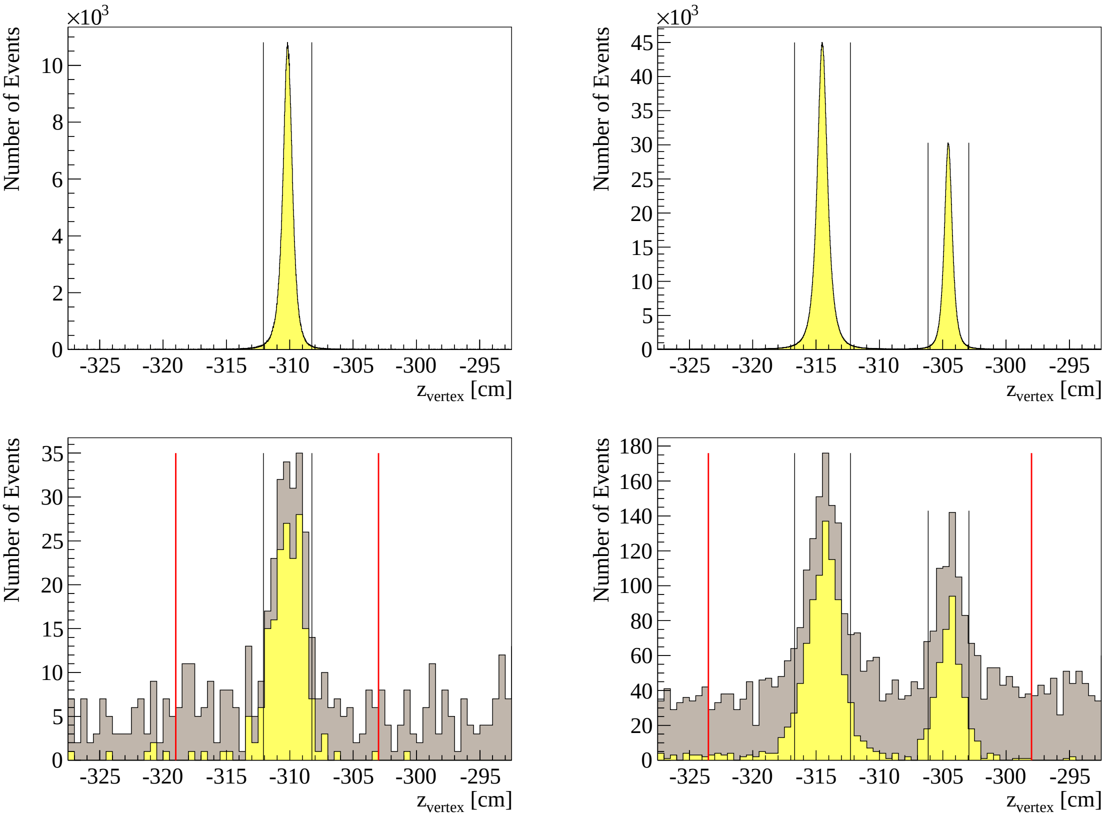

Figure 9.1: z-position of the primary vertices for 3 mm (left) and 2+1 mm (right) lead target, respectively, for all exclusive events (top) and for exclusive events with $t' < 10^{-3}\,\mathrm{GeV}^2/c^2$ and $m_{3\pi} < 0.6\,\mathrm{GeV}/c^2$ (bottom). For the yellow histograms in the bottom line, the decay of beam kaons is excluded by an additional cut on $m_{3\pi} > 0.51\,\mathrm{GeV}/c^2$.

be applied. During the $2 + 1$ mm period, the filter was actively filtering for one part of this period, in the other it worked in *mark-only* mode, i.e. not disregarding any event, but still providing the information whether an event was supposed to be accepted by the filter. Consequently, the filter could be applied reliably during the event selection and the subsequent acceptance corrections within the PWA for the full second period. Similar to the diffractive trigger, the online filter did not cut significantly into the 3π acceptance. It was found to have only a small impact for 3π masses above $1.7\,\mathrm{GeV}/c^2$ (see section 9.2.2).

The desired event signature is further specified by requiring exactly one **primary vertex** formed by an incoming beam particle and three outgoing, correctly charged $(- - +)$, particles, which is reconstructed in the vicinity of the respective lead targets. It has to be stressed, that in the analysis at hand these four reconstructed particles contributing to the vertex were simply assumed to be pions, as reliable particle identification was neither available for particles in the beam line nor in the spectrometer, as already stated in section 2.2.2.

The precise position of the lead targets is obtained by a gaussian fit to the vertex distribution in the corresponding z region[4]. The position of the single 3 mm target is found to be at $z = -310.169\,\mathrm{cm}$ with $\sigma = 0.468\,\mathrm{cm}$, the 2 mm disk and the 1 mm disk of the segmented target at $z = -314.490\,\mathrm{cm}$ and $z = -304.547\,\mathrm{cm}$, with $\sigma = 0.551\,\mathrm{cm}$ and $\sigma = 0.402\,\mathrm{cm}$, respectively [Wei08a]. For previous analyses of these data, a cut of $\pm 4\sigma$ around the mean position of each target, was applied and supposed not to cut into the acceptance of low masses (even at "low t'", i.e. $t' \in [10^{-3}, 10^{-2}]\,\mathrm{GeV}^2/c^2$). The vertex distributions for all events with three outgoing charged particles are shown in figure 9.1, with the 4σ cut indicated. Yet it was found that the resolution of the vertex reconstruction is significantly worse for exclusive events featuring $t' < 10^{-3}\,\mathrm{GeV}^2/c^2$ and masses below $m_{3\pi} \approx 0.7\,\mathrm{GeV}/c^2$, and in addition worse for reconstructed Monte Carlo events than for reconstructed experimental data (see sectin 9.2.3). Consequently the cut on the reconstructed vertex position is significantly broadened for the present analysis to allow for more precise acceptance corrections for low masses at $t' < 10^{-3}\,\mathrm{GeV}^2/c^2$, which is of major importance for the measurement of the cross-section $\pi^-\gamma \to \pi^-\pi^-\pi^+$ presented in section 9.6. The broadened cuts are not determined in terms of σ anymore, which is due to the non-symmetric reconstructed distribution, but derived from the comparison between real data and Monte Carlo resolution. Figure 9.1 (bottom line) shows the vertex distribution for the relevant real-data events featuring even $m_{3\pi} < 0.6\,\mathrm{GeV}/c^2$ (grey) and those with additionally $m_{3\pi} > 0.51\,\mathrm{GeV}/c^2$ (yellow; to roughly exclude the continuous background from decays of beam kaons (see section 9.1.3). The black thin lines mark the previous "4σ" cuts, the red lines the broadened cuts, i.e. $z \in [-319.0, -303.0]\,\mathrm{cm}$ for the 3 mm setup, and $z \in [-323.5, -298.0]\,\mathrm{cm}$ for the 2+1 mm setup.

The next important requirement an event has to fulfill is **exclusivity**. This means, that all the particles participating in the reaction are well-known. On the one hand, beam and all outgoing particles have to be properly reconstructed and attributed to the vertex and no (neutral) particle is lost, and, on the other hand, the target particle recoils without being excited or destroyed. This is assured by checking energy conservation. The energy of the beam particles was not measured in the beam line, but their direction is precisely known from measurements in the beam telescope. In addition no recoil particle detector was available yet. To apply an exclusivity cut nevertheless, and to calculate the momentum transfer t' using equation (7.7), the energy of the beam particle E_{beam} is calculated as the sum $E_{3\pi}$ of the energies of the three pions in the final state. The resulting energy spectrum shows a clear peak at 190 GeV (the nominal beam energy) with a shoulder at about 187 GeV, that turned out to be a feature of the 2004 beam[5]. The exclusivity cut is then in first order defined as $185\,\mathrm{GeV} < E_{\mathrm{beam}} = E_{3\pi} < 193\,\mathrm{GeV}$. This can be further refined when t' is determined, assuming the scattering mechanism changes from coherent scattering on lead nuclei to scattering off the individual nucleons in a certain region of t', presumably between 10^{-2} and $0.1\,\mathrm{GeV}^2/c^2$. Typically the nucleon mass is used for the target for $t' > 0.1\,\mathrm{GeV}^2/c^2$ instead of the mass of the lead nucleus. Taking into account this assumption on the target mass, the measured scattering angle θ, $E_{3\pi}$ and the presupposition, that the target particle remains intact during the scattering process,

---

[4] z is the coordinate in beam direction in the COMPASS main reference system.

[5] This second momentum component was caused by a wrongly set quadrupole magnet in the beam line.

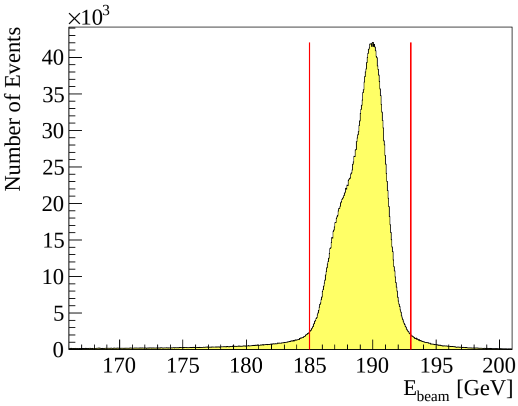

Figure 9.2: Beam energy spectrum with exclusivity peak for $t' < 10^{-2}\,\text{GeV}^2/c^2$.

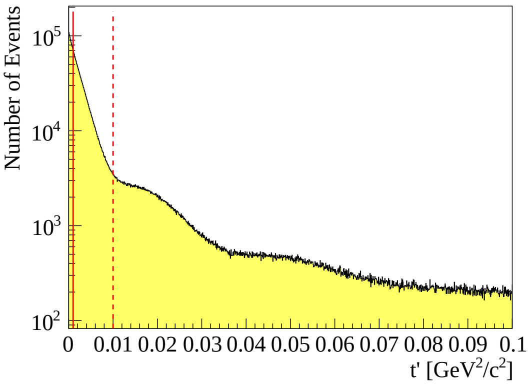

Figure 9.3: Momentum transfer spectrum showing coherent diffraction of the beam pions on lead nuclei.

the beam energy can be recalculated more precisely using equation (B.8) in [Wei08a]. A difference of this recalculated beam energy from the simple sum $E_{3\pi}$ is remarkable only at higher t' for scattering off nucleons. Figure 9.2 depicts the beam energy spectrum for $t' < 10^{-2}\,\text{GeV}^2/c^2$, containing the t' region of interest, with the clear exclusivity peak containing only very little background from non-exclusive events, and the corresponding exclusivity cut.

As already mentioned in the previous paragraphs, the basic quantity for the selection of certain physics processes potentially emerging in $\pi^-\text{Pb} \to \pi^-\pi^-\pi^+\text{Pb}$ is the **momentum transfer t'**. Its spectrum can be divided into different ranges according to the physics processes that contribute, as summarized in the following:

- For $t' < 10^{-2}\,\text{GeV}^2/c^2$, coherent scattering off the lead nucleus is analyzed and profundly dominated by diffractive production.
    - For $t' < 10^{-3}\,\text{GeV}^2/c^2$, here referred to as “very low t'” or “Primakoff t'”, Coulomb production contributes significantly to the spectrum, interfering with the strong interaction production. Furthermore, the limited experimental resolution makes a precise (partial-wave) analysis very challenging in this range.
    - At $10^{-3}\,\text{GeV}^2/c^2 < t' < 10^{-2}\,\text{GeV}^2/c^2$, called “low t'”[6], coherent scattering off the lead nuclei is referred to almost pure diffractive production. A first analysis of these data was presented already in [Gra05, Wei08a].
- Between $10^{-2}\,\text{GeV}^2/c^2$ and $0.1\,\text{GeV}^2/c^2$ nuclear excitations and nuclear breakup contribute in addition.

  The whole spectrum for these three t' ranges included in $t' < 0.1\,\text{GeV}^2/c^2$ shows a diffraction pattern for scattering off the lead nucleus, that can be understood as a

---

[6] In this specific respect, “low t'” excludes the “Primakoff t'” range, while the general notation ‘low t'’ is ususally meant to include it, i.e. covering all data up to $10^{-2}\,\text{GeV}^2/c^2$, which is still sometimes restricted to lower parts of this range.

black disk in optics (see figure 9.3, the solid red line indicates $10^{-3}\,\mathrm{GeV}^2/c^2$ and the dashed red line $10^{-2}\,\mathrm{GeV}^2/c^2$).

- At $0.1\,\mathrm{GeV}^2/c^2 < t' < 1.0\,\mathrm{GeV}^2/c^2$, called "high t'", dominately scattering off individual nucleons takes place. The analysis including a full PWA of this t' range is presented in [Wei08a].

9.1.2 Mass Spectra and Dalitz Plots

Figure 9.4 presents the invariant mass of the $\pi^-\pi^-\pi^+$ system for all t' and for the different t' ranges introduced in the previous section. The production of three major resonances can be already concluded from this plot. While the $a_1(1260)$ and the $\pi_2(1670)$ are present in all selected t' intervals, the $a_2(1320)$ is visible only for $t' > 0.1\,\mathrm{GeV}^2/c^2$ and $t' < 10^{-3}\,\mathrm{GeV}^2/c^2$.

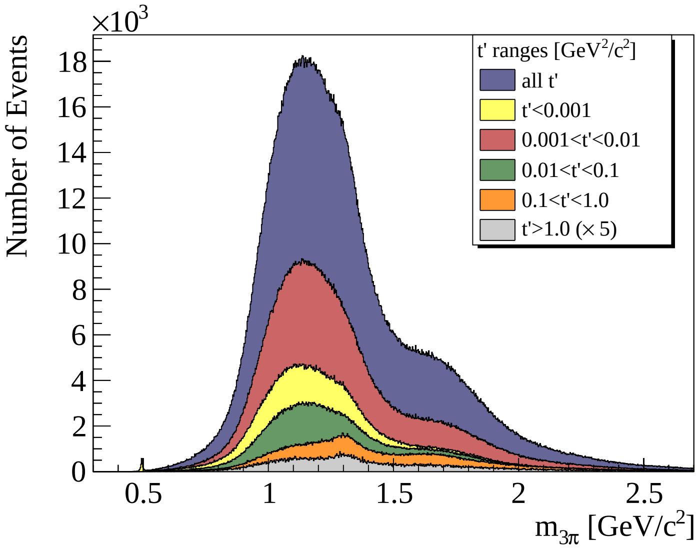

Figure 9.4: Invariant mass of the 3π system for different t' bins.

A first impression of the decay channels of these resonances, or more generally, of the data contained in a specific mass range, is included in *Dalitz plots*. The squared invariant masses of two subsystems, i.e. here the two possible $\pi^+\pi^-$ pairs, are plotted versuch each other. This is depicted in figure 9.5 for the mass regions containing the $a_2(1320)$ (left) and $\pi_2(1670)$ (right), with a cut of the nominal width Γ applied around the respective nominal masses. The Dalitz plot of the $a_2(1320)$ exhibits the dominant $\rho(770)\pi$ decay. The Dalitz plot of the $\pi_2(1670)$ shows the decay channels into $\rho(770)\pi$ and $f_2(1270)\pi$.

To identify the produced resonances, detailed information about both the mass and the quantum numbers of the resonances, as contained in the angular distributions, is mandatory.

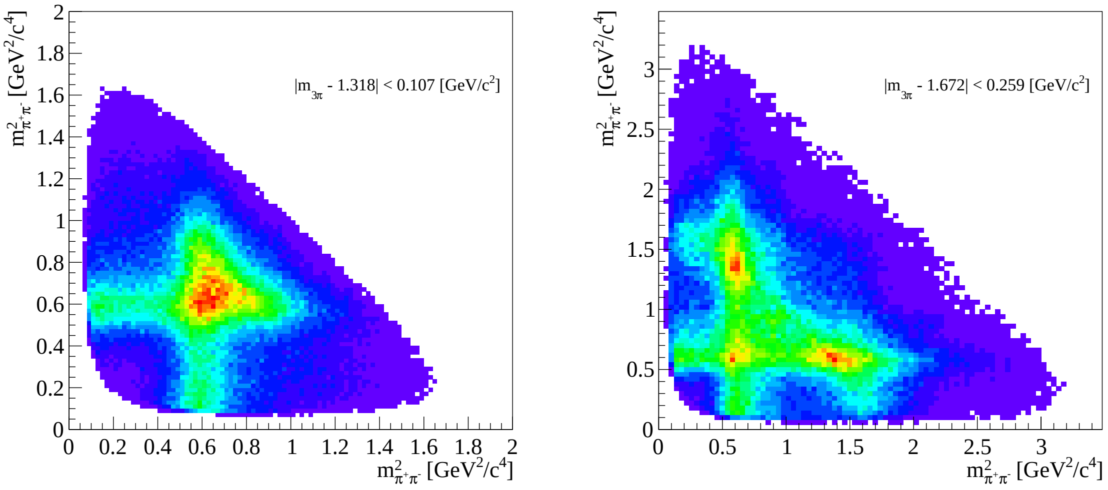

Figure 9.5: Dalitz plots for mass regions containing $a_2(1320)$ and $\pi_2(1670)$ with $t' < 10^{-3}\,\mathrm{GeV}^2/c^2$. $1\,\Gamma$ cuts around nominal masses.

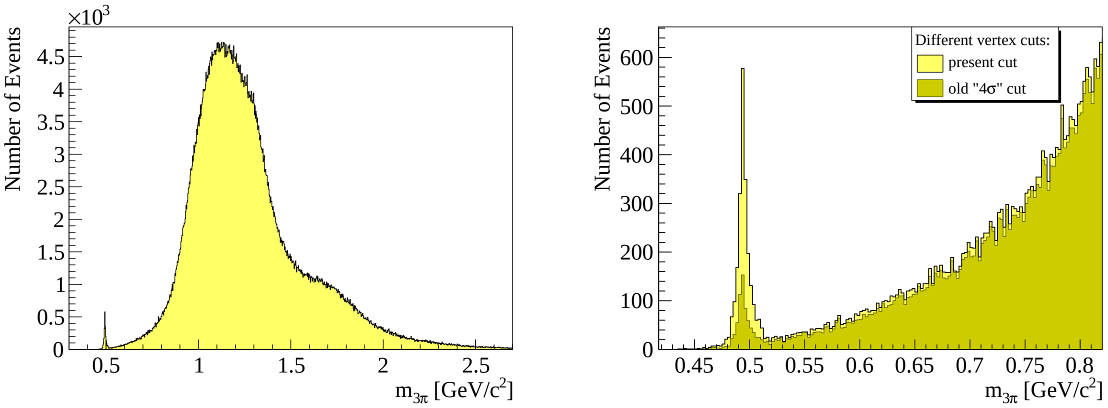

Figure 9.6: Invariant mass of the 3π system for exclusive events with $t' < 10^{-3}\,\mathrm{GeV}^2/c^2$ (left). A comparison between the old and the new vertex cuts, which depicts the change in kaon peak, is given in the zoomed plot (right).

9.1.3 Kaon Contributions

Kaons contribute in different ways to the analyzed data set. As already mentioned, particle identification could not be applied for the analysis, neither for the beam particles nor for the particles in the spectrometer, so that they have all been assumed to be pions. This leads to potential background from kaon dissociation, i.e. $K^-\mathrm{Pb} \to K^-\pi^-\pi^+\mathrm{Pb}$, or from intermediate states decaying into $\pi^-K^-K^+$. Both possibilities have been checked by assigning the kaon mass to one or two of the outgoing particles, but no signals confirming the respective hypothesis have been observed [Wei08a].

In addition, kaons feature a hadronic decay channel $K^- \to \pi^-\pi^-\pi^+$, so that the decay of beam kaons naturally contributes to the mass spectrum for $t' \approx 0$. The kaon peak is visible at $m_{3\pi} \approx 0.5\,\mathrm{GeV}/c^2$ in figure 9.6, where the full three-pion mass spectrum for $t' < 10^{-3}\,\mathrm{GeV}^2/c^2$ is shown on the left, with an additional zoom into the low-mass region $m_{3\pi} < 0.82\,\mathrm{GeV}/c^2$ emphasizing the kaon peak on the right. In the latter, the spectrum is shown for two different cuts on the reconstructed vertex. With the broader cut, the kaon peak becomes significantly more prominent, while the rest of the mass spectrum is marginally influenced by this cut. This contribution from $K^- \to \pi^-\pi^-\pi^+$ is used for the determination of the luminosity, which is explained in section 9.6.1, where more information on these decays is available.

9.2 Monte Carlo Simulations

In the course of the analysis, several Monte Carlo (MC) simulations of the COMPASS spectrometer have been carried out for different purposes. A PWA needs the information of the acceptance conditions in the five-dimensional[7] phase space, which is evaluated from the simulation of events decaying flat in phase space in the respective spectrometer. The acceptance of beam kaon decays, which is an important input to the luminosity determination based on them, is obtained from equivalent simulations of kaons decaying in the relevant spectrometer region. The simulation of these kaon decays is evaluated in section 9.6.1.2. In addition, resolution effects occuring particularly for Primakoff-produced $\pi^-\pi^-\pi^+$ events have been studied with a dedicated simulation. Before the simulated data sets and their evaluation is presented, some technical background on the event generation is given.

9.2.1 Event Generation

The event generator is part of the PWA software framework. It generates the three-pion events with the correct kinematic distributions according to their decays in phase space [Jam68]. For the studies and acceptance corrections presented in the following, events are generated with the following input from experimental data:

- Position of the targets (exact positions from the distribution of the reconstructed primary vertices, with thicknesses of 3 mm and 2+1 mm, respectively. The decay vertizes are generated evenly distributed along z, exclusively within these ranges.)
- Approximate statistical ratio between 3mm and 2+1mm target events (fine adjustment subsequently in the PWA)
- Energy profile, position, spread and divergence of the beam (using the full correlations between beam momenta and vertex positions of a subsample of the data with $t' < 10^{-3}\,\mathrm{GeV}^2/c^2$, that features the least possible background under the exclusivity peak. The beam energy range was restricted such ($E_{\mathrm{input}} \in (189.0 \pm 3.5)\,\mathrm{GeV}$), that the shape of the tails of the reconstructed beam energy is equivalent to the one observed in the experimental data, so that the same cut of $189 \pm 4\,\mathrm{GeV}$ can be applied. In addition, extreme cases of beam divergence are rejected.)
- Momentum transfer distribution, with $t'(m)$ determined individually for each mass bin instead of using a global t' distribution:
    - For the acceptance studies and corrections, the t' distribution is determined from the set of the experimental data with $t' < 10^{-3}\,\mathrm{GeV}^2/c^2$ that enters the PWA.

---

[7] Three-particle decays are fully determined by five phase space variables.

  - For the t' resolution studies, the theoretical Primakoff t' distribution from equation (9.1) is used.
  - Kaon decays are generated with $t' \equiv 0$.

With these ingredients, events are generated in mass bins of typically $10\,\mathrm{MeV}/c^2$ with $m_{3\pi}$ equally distributed in the respective bin, and separately for each target setup.

For the acceptance corrections, 240 000 events of phase-space MC have been simulated for the t' region $t' < 10^{-3}\,\mathrm{GeV}^2/c^2$ in each $10\,\mathrm{MeV}/c^2$ mass bin in the mass range $0.43\,\mathrm{GeV}/c^2 < m_{3\pi} < 2.5\,\mathrm{GeV}/c^2$ (i.e. in total $\approx$ 50 000 000 events). The amount of reconstructed MC events that survive all cuts exceeds six times the statistics that is obtained from the experimental data in the mass bin with the maximum number of events, so that the influence of the MC uncertainties to the error bars of the PWA fits can be assumed to be negligible.

The studies of the t' resolution of events featuring the Primakoff t' dependence were carried out with 30 000 events in $10\,\mathrm{MeV}/c^2$ mass bin in the mass range $0.42\,\mathrm{GeV}/c^2 < m_{3\pi} < 2.5\,\mathrm{GeV}/c^2$.

For the studies of kaon decays about 360 000 events have been simulated. They have been generated at a sharp mass point at $m_{3\pi} = m_{K^-} = 0.49368\,\mathrm{GeV}/c^2$.

9.2.2 Evaluation of Acceptances

For each simulated event, the MC truth and, if available, the reconstructed information are stored. Each reconstructed MC event is treated with PHAST equivalently to real data events, and the corresponding cuts are applied, from which several acceptance flags are derived.

First of all, a reconstructed primary vertex with three outgoing particles of correct charges is required, and the cuts on vertex position[8] and exclusivity are applied. The diffractive trigger is simulated by asking for at least two of the simulated outgoing particles crossing the multiplicity counter, and requiring at least 6 GeV energy of a reconstructed cluster in HCAL2. Also the full information of the beam killers (veto if at least two out of three are hit) is used. The algorithm of the online filter is applied using the MC truth information of the silicon detectors downstream of the target.

In addition, a geometrical cut for particles crossing the material of the downstream Sandwich (SW) veto detector is introduced. From the data it was concluded, that this veto was either inefficient or not for the whole data taking period implemented as a veto (see section C.1), so that the simulation would have been quite delicate, and a hard cut on both data and MC was considered to be the most reliable solution.

In figures 9.7 and 9.8 the overall COMPASS acceptance is shown for the 3π mass, the $\pi^+\pi^-$ subsystem mass, and the decay angles $\cos\theta_{GJ}$ and ϕ_{TY}, as defined in section 8.2.1.2,

---

[8] The choice of the vertex cut parameters is explained in section 9.2.3.

of the decay of the intermiated state into a single π^- and a neutral two-pion state (for the two possible combinations of $\pi^+\pi^-$ pairs of each event). The acceptance distributions are based on the MC truth. A histogram containing the MC truth for all events fulfilling the acceptance conditions is normalized to a histogram filled with the MC truth of all simulated events.

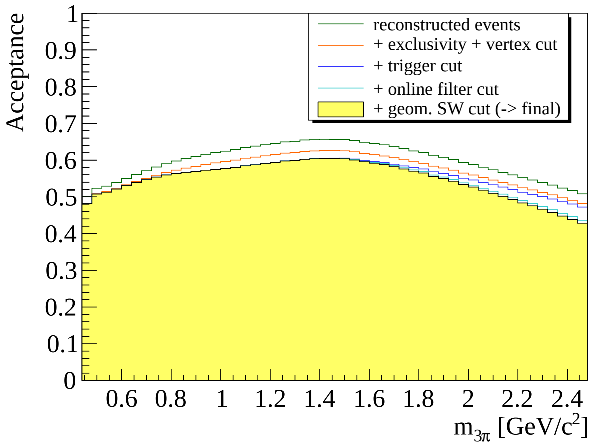

Figure 9.7: Acceptance versus 3π mass for $t' < 10^{-3}\,\mathrm{GeV}^2/c^2$.

One can see that most of the acceptance is defined by the ability of the COMPASS spectrometer to reconstruct certain types of events at all, and the vertex and exclusivity cuts. The trigger, online filter and the additional cut on the geometry of the SW veto detector have only small effect. The plots show the simulated data with a cut on the 3π mass ($0.8\,\mathrm{GeV}/c^2 < m_{3\pi} < 2.0\,\mathrm{GeV}/c^2$, i.e. the mass range covered by the significant part of the data). This cut is applied for all distributions except the 3π mass itself, to achieve an overall picture which is closer to data, and not biased by extreme cases. COMPASS features a quite flat acceptance, which was in the 2004 setup only slightly lowered at masses above $1.5\,\mathrm{GeV}/c^2$ by the SW veto detector.

The acceptances of the $\pi^-\pi^+$ subsystems, $\cos\theta_{GJ}$, and ϕ_{TY} in the mass range $0.44\,\mathrm{GeV}/c^2 < m_{3\pi} < 0.72\,\mathrm{GeV}/c^2$, i.e. the mass range[9] that is analyzed for the comparison to the ChPT prediction (see section 9.6), are shown in figure 9.9. For these low masses the acceptance also slightly drops, which can be explained by more difficult conditions for the reconstruction algorithms, due to the very small angles the three pions are emitted with. So there are less reconstructed events in general, but also worse resolution compared to events featuring higher invariant masses. This becomes obvious particularly in the resolution of the vertex reconstruction, where too narrow cuts significantly cut into the acceptance (see figure 9.10 and, for more details, section 9.2.3).

The acceptances of the $\pi^-\pi^+$ subsystems, $\cos\theta_{GJ}$ and ϕ_{TY} of two selected mass ranges, namely $1.26\,\mathrm{GeV}/c^2 < m_{3\pi} < 1.38\,\mathrm{GeV}/c^2$ containing the $a_2(1320)$ and $1.50\,\mathrm{GeV}/c^2 <$

---

[9] As the plots are based on MC events, they take into account a flat mass distribution in the mass range $0.44\,\mathrm{GeV}/c^2 < m_{3\pi} < 0.72\,\mathrm{GeV}/c^2$, so that (compared to the mass distribution present in the data) they overestimate the constribution of lowest masses.

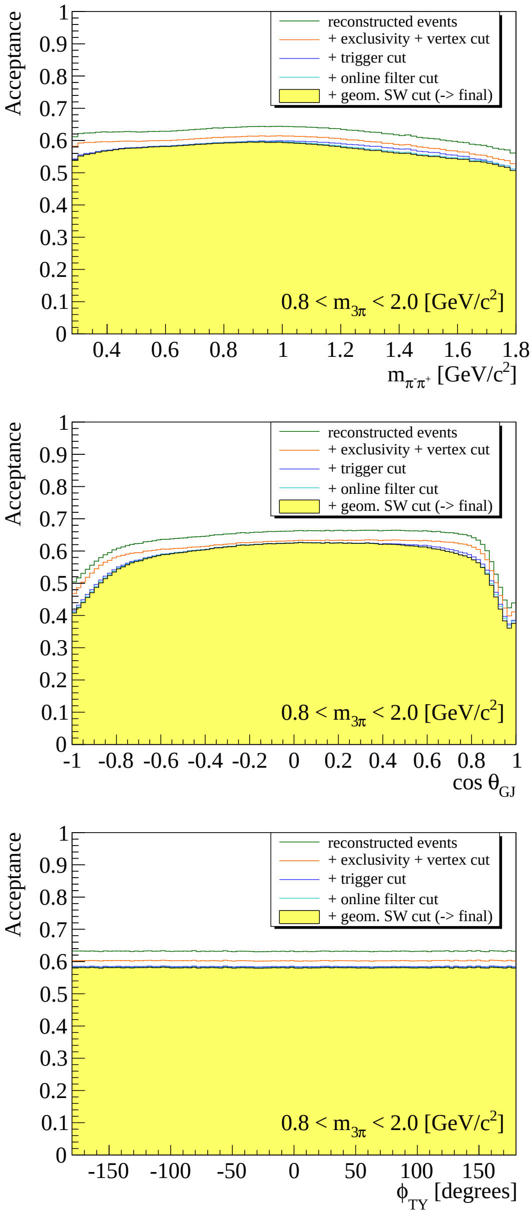

Figure 9.8: Acceptance for 2π subsytems (top), $\cos\theta_{GJ}$ (middle) and ϕ_{TY} (bottom) for the mass range covering significant part of the data ($t' < 10^{-3}\,\mathrm{GeV}^2/c^2$).

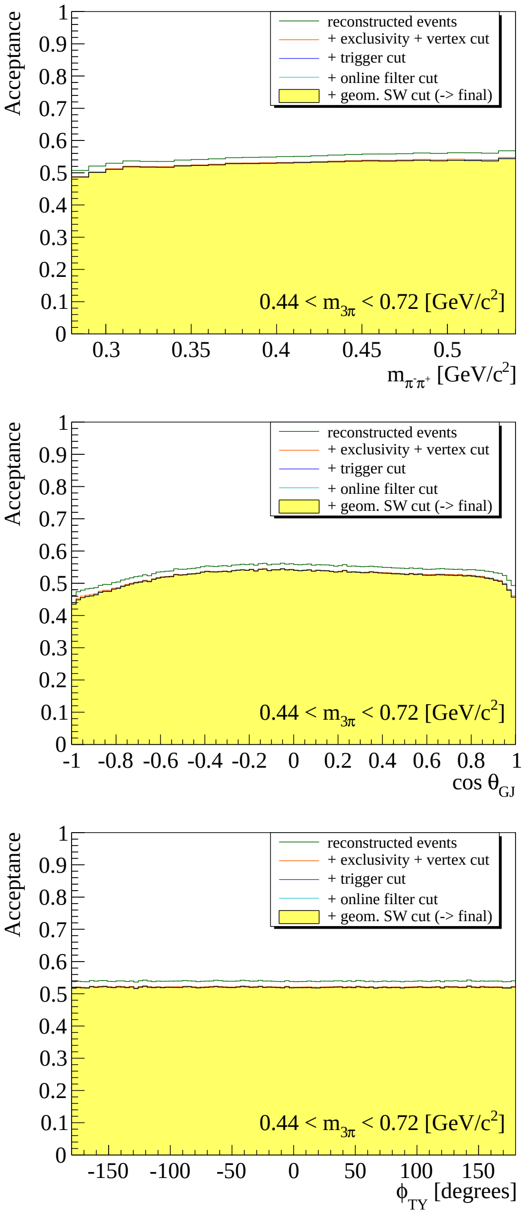

Figure 9.9: Acceptance for 2π subsytems (top), $\cos\theta_{GJ}$ (middle) and ϕ_{TY} (bottom) for the range of low masses ($t' < 10^{-3}\,\mathrm{GeV}^2/c^2$).

$m_{3\pi} < 1.92\,\mathrm{GeV}/c^2$ containing the $\pi_2(1670)$, are shown in figure 9.11. While the acceptances for the $\pi^-\pi^+$ subsystems and ϕ_{TY} are flat in both cases, the dips at $\cos\theta_{GJ} \pm 1$ are significantly more pronounced for the range of higher mass, which can be explained again by the SW veto cutting into the acceptance.

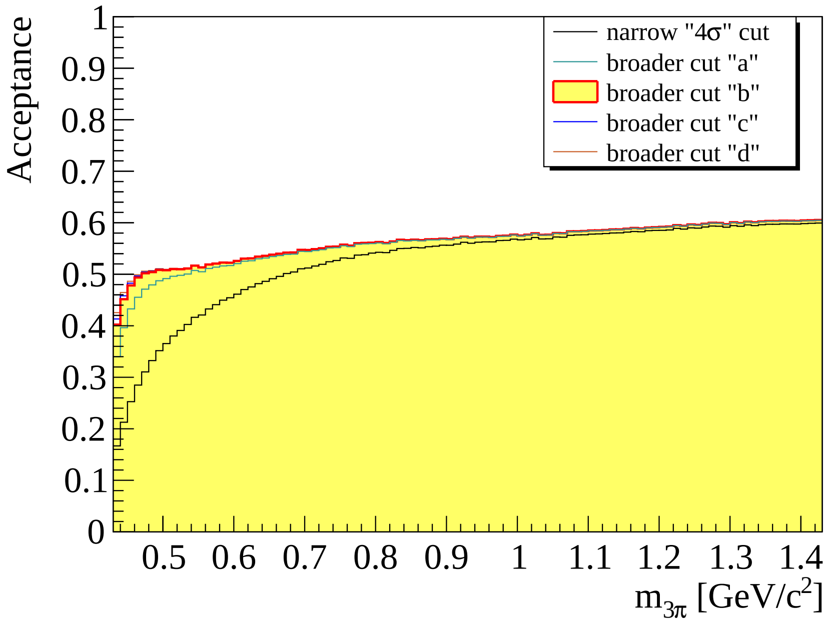

Figure 9.10: Acceptance for low masses for different cuts on reconstructed vertex positions. The cut sets “a”, “b”, and “c” are indicated each with the same color in figure 9.12, the cut “d” is even outside of the range given in figure 9.12.

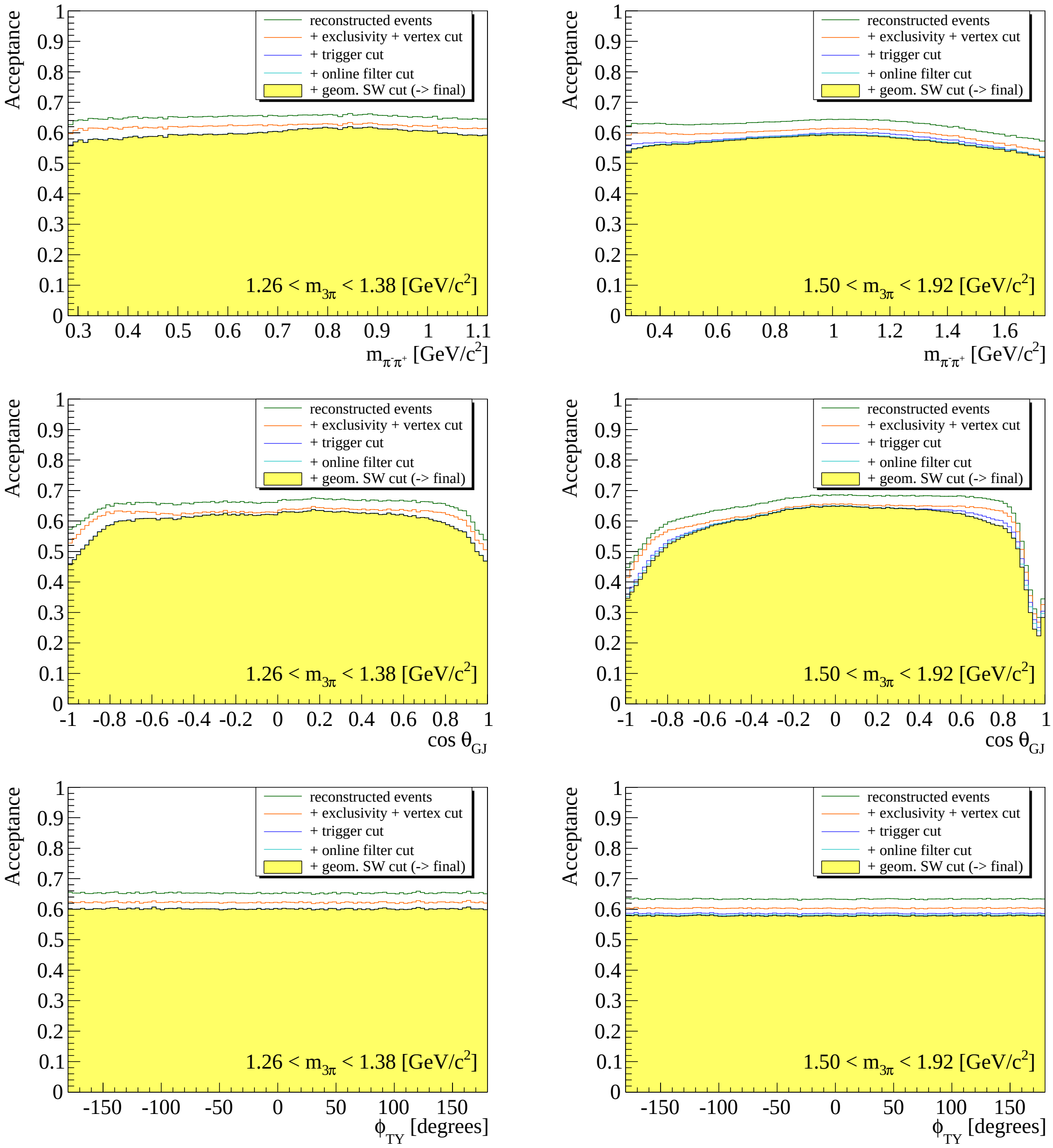

Figure 9.11: Acceptance for 2π subsytems (top row), $\cos\theta_{GJ}$ (middle row) and ϕ_{TY} (bottom row) for the two mass ranges containing the $a_2(1320)$ (left) and the $\pi_2(1670)$ (right column) ($t' < 10^{-3}\,\mathrm{GeV}^2/c^2$).

9.2.3 Study of Vertex Resolution

Another topic concerning vertex reconstruction affects differences in the resolution of reconstructed vertices in experimental data and MC events. From a comparison of vertex distributions of data and weighted MC[10], we can see that the resolution of reconstructed MC events is visibly worse than for data (see figure 9.12). This leads to slightly wrong acceptance corrections, if vertex positions are cut on the slopes of the distributions, as it was the case for the old 4σ cut (indicated in black, lead to slight over-corrections). So finally the limits are chosen such that they are supposed not to distort the acceptance corrections (figure 9.12, red lines), and at the same time the acceptance itself does not change appreciably any more in this range (figure 9.10, that features the same color code for the cut sets).

9.2.4 Simulation of Primakoff t' Distribution

The knowledge of the experimenatally observed t' distribution of events produced by quasi-real photon exchange is an important input to a PWA of data (presumably) containing such events. Their contribution (and such their t' dependence) cannot be extracted directly from the data in a reliable way due to the large diffractive background (see section 9.3), but the t' distribution is theoretically known and can be precisely computed. For photon exchange in the reaction $\pi^- \mathrm{Pb} \to \pi^-\pi^-\pi^+ \mathrm{Pb}$, using the Weizsäcker-Williams equivalent-photon approximation, the cross section is given as

$$\frac{d\sigma}{ds\, dt'} = \frac{\alpha \cdot Z^2}{\pi(s - m_\pi^2)} \cdot F_{\mathrm{eff}}^2(t') \cdot \frac{t'}{(t' + t_{\mathrm{min}})^2} \cdot \sigma_r(s) \tag{9.1}$$

with $F_{\mathrm{eff}}^2(t')$ the elastic form factor of lead and $\sigma_r(s)$ the unpolarized cross-section $\pi^-\gamma \to \pi^-\pi^-\pi^+$ (for details see section 7.3). Assuming the MC simulation reproduces the resolution effects appearing in the experimental data sufficiently well, one can thus learn about the experimentally observed t' dependence of events produced by quasi-real photon exchange. Events are simulated with a t' dependence according to equation (9.1) and processed with the complete MC chain.

Such events have been simulated in $10\,\mathrm{MeV}/c^2$ mass bins in the range $0.43 < m_{3\pi} < 2.50\,\mathrm{GeV}/c^2$ evenly distributed in mass (i.e. neglecting $\sigma_r(s)$ which does not influence the result in such small mass bins) with a subsequent phase space decay into the 3π final state. Then the t' distributions of the reconstructed events are fitted in the respective mass bins (of $40\,\mathrm{MeV}/c^2$ bin width), as the shapes depend significantly on $m_{3\pi}$ (they peak much more strongly at $t' \approx 0$ for lower masses, see figure 9.13 and figure 9.14). The reconstructed t' dependences, with experimental resolution applied, is evaluated for two different purposes using different ranges of t'.

---

[10] "Weighted MC" refers to phase space MC events, that are weighted by a PWA fit result concerning angular distributions and Dalitz plots, so that they describe the data in the best possible way, see also section 8.7.

Firstly, the t' dependence for Primakoff events for the PWA of data featuring $t' < 10^{-3}\,\mathrm{GeV}^2/c^2$ is obtained from the reconstructed t' distributions in the range $t' < 10^{-3}\,\mathrm{GeV}^2/c^2$. They can be described reasonably well with $\mathrm{d}\sigma/\mathrm{d}t' \propto \exp(-b_{\mathrm{prim}}(m)t')$. The development of these fits with rising $m_{3\pi}$ is depicted for selected mass bins in figure 9.13. For each mass bin, the t' distribution (from MC truth) of all simulated events is shown in light blue, the t' distribution of the MC truth of all reconstructed events in black, and the t' distribution (after reconstruction) of all reconstructed events in red, with the mentioned fit for $t' < 10^{-3}\,\mathrm{GeV}^2/c^2$. The resulting fit parameters $b_{\mathrm{prim}}(m)$ are collected in the bottom line of figure 9.13, which shows a smooth curve (of values between 1600 and 400) that is fitted by a second order polynomial. The resulting parametrization is used for the respective t' dependence in PWA (see also section 8.2.3).

In addition, the Primakoff t' dependence is also used in the statistical subtraction method presented in section 9.3. This procedure provides both a first access to the Primkoff produced $m_{3\pi}$ spectrum, and the diffractive slope $b_{\mathrm{diff}}(m)$ that is also an important ingredient to the PWA. For this purpose a description of the differential cross-section w.r.t. t' covering $t' < 6 \cdot 10^{-3}\,\mathrm{GeV}^2/c^2$ is necessary, which is not possible anymore by a single exponential. It has been found empirically that the spectra are fitted reasonably well (for the full range of mass bins) by $c(m)/(t' + \epsilon(m))^{3.9}$ (see figure 9.14, color scheme same as for figure 9.13). The resulting values of $\epsilon(m)$ are presented in the bottom line of figure 9.14, which is fitted by a fifth order polynomial.

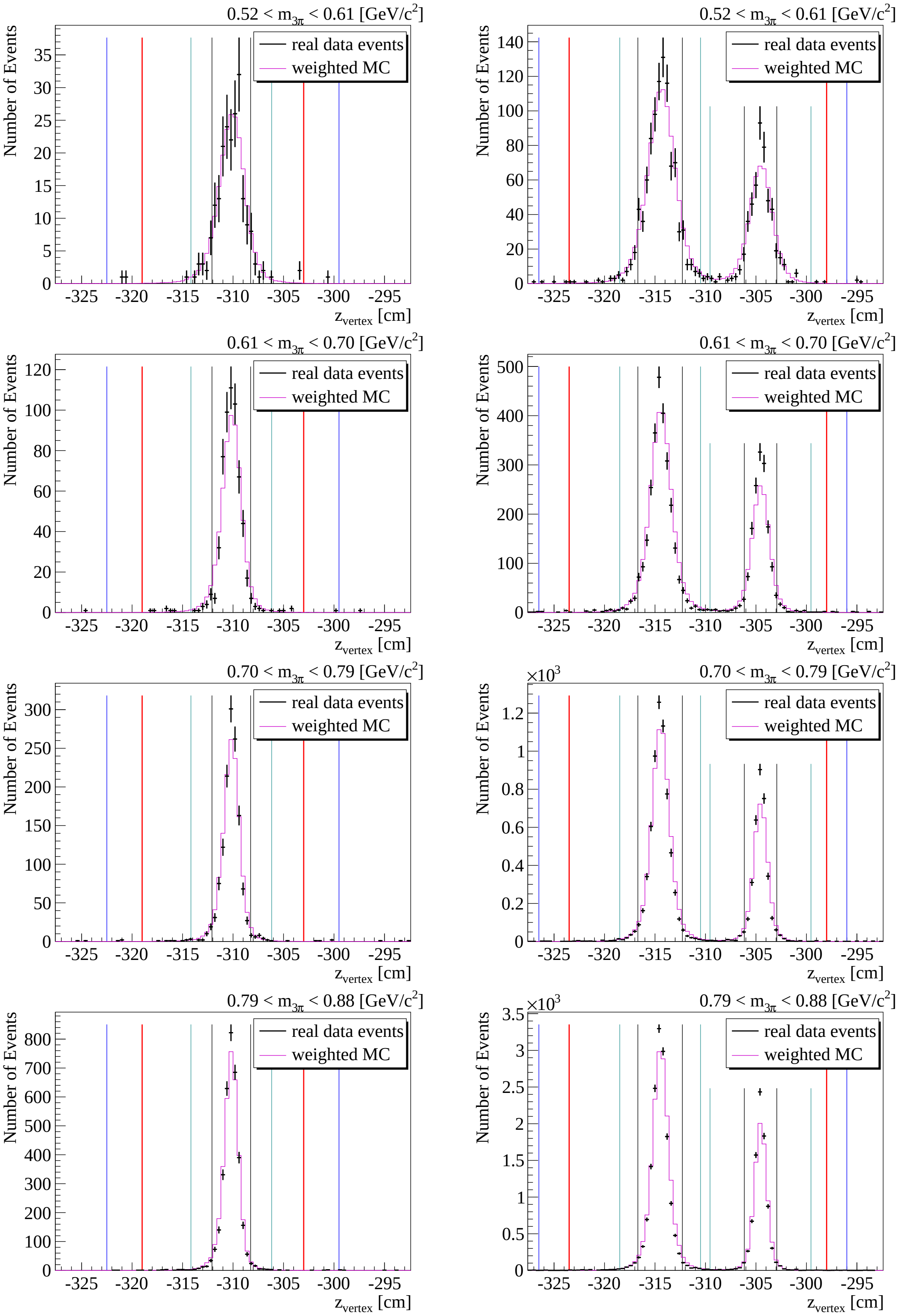

Figure 9.12: Comparison of vertex distribution in data and weighted MC for the single 3 mm target setup (left column) and the segmented 2+1 mm target setup (right column) for various ranges of $m_{3\pi}$ as indicated.

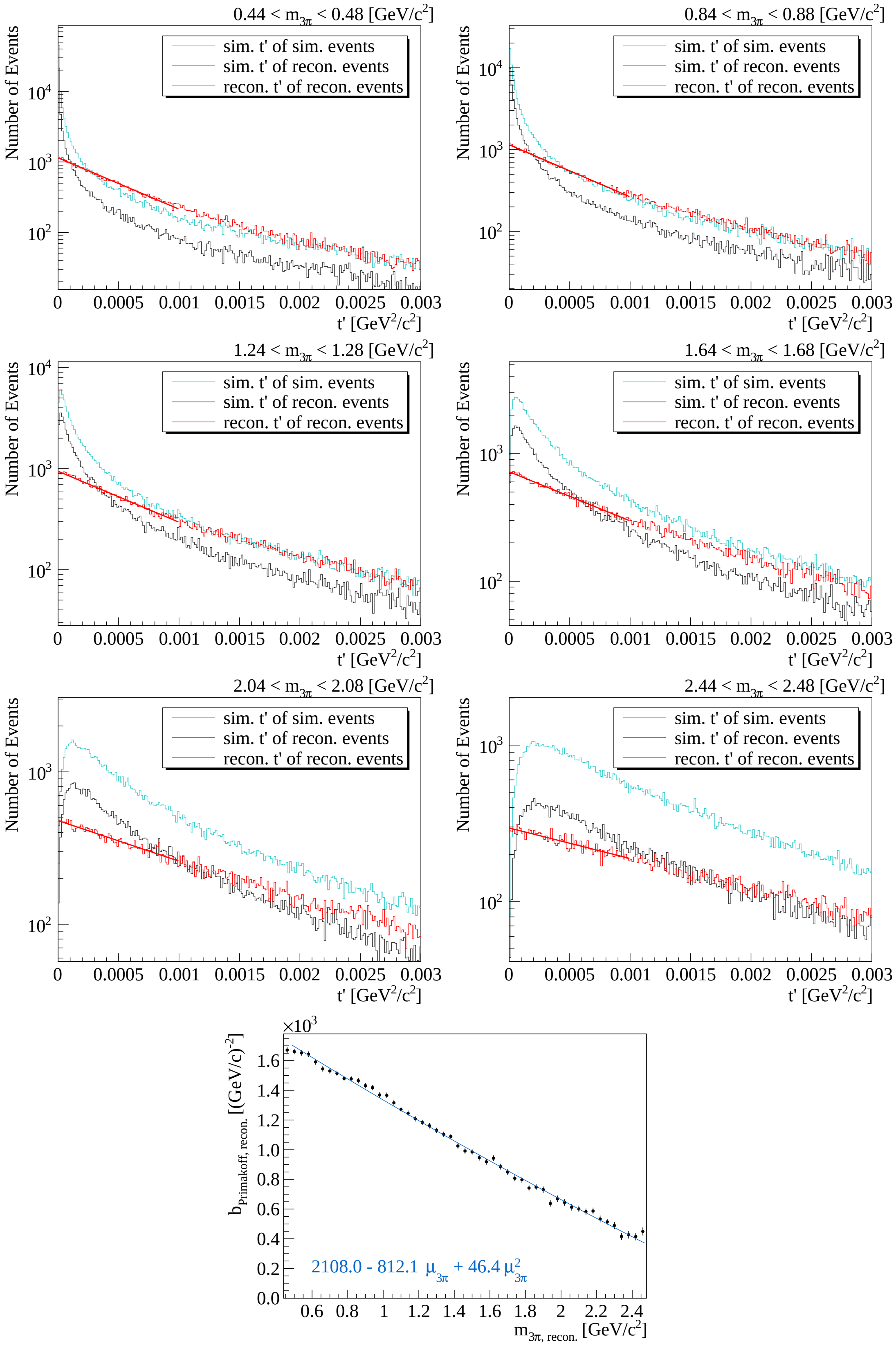

Figure 9.13: Simulation of the Primakoff t' distribution evaluated for $t' < 10^{-3}\,\mathrm{GeV}^2/c^2$ with a single exponential fit for different invariant mass ranges. The resulting slope parameter distribution $b_{\mathrm{Prim}}(m)$ is shown in the bottom line, using $\mu_{3\pi} = m_{3\pi}/[\mathrm{GeV}/c^2]$.

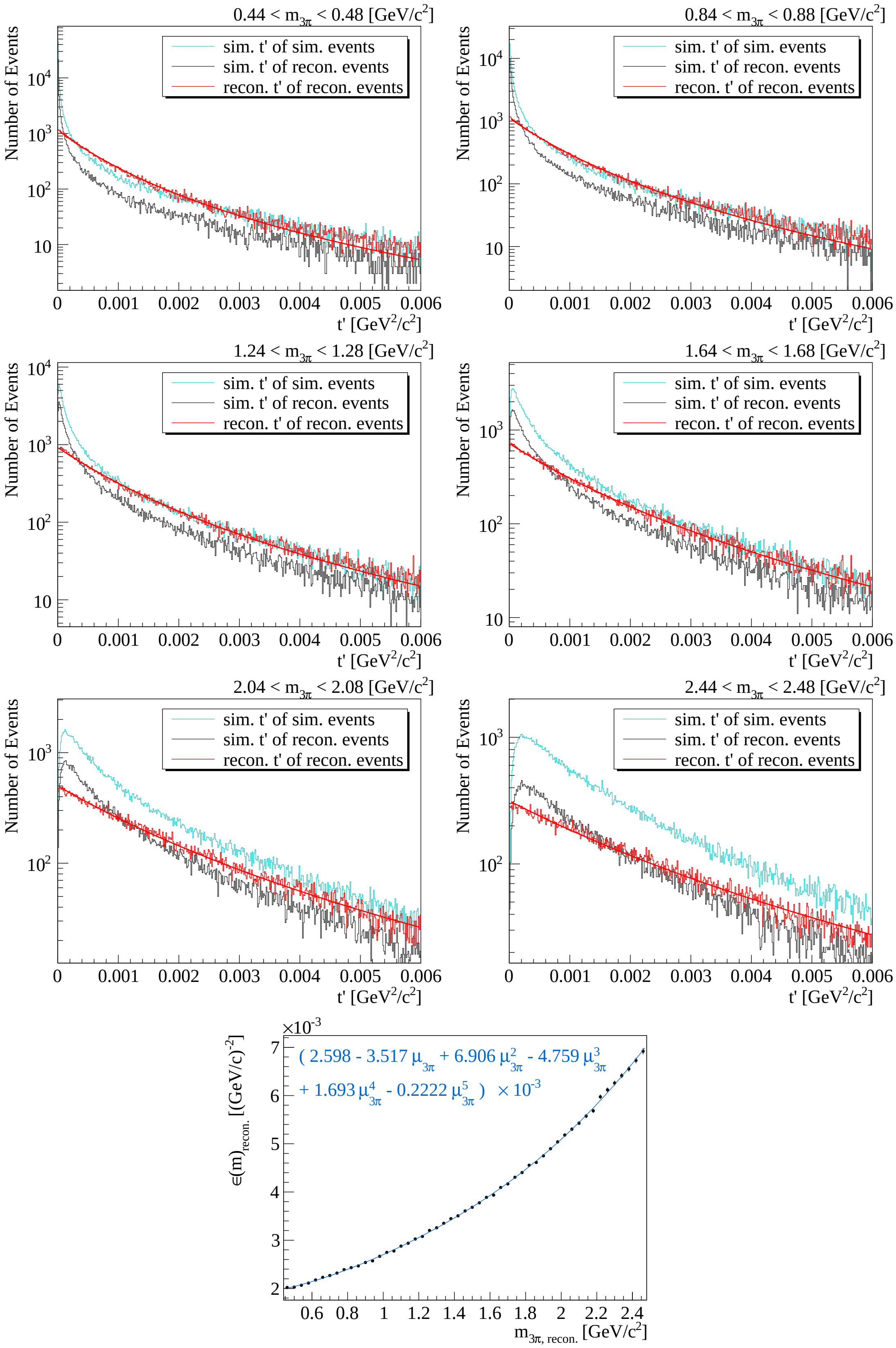

Figure 9.14: Simulation of the Primakoff t' distribution evaluated for $t' < 6 \cdot 10^{-3}\,\mathrm{GeV}^2/c^2$ with $c(m)/(t' + \epsilon(m))^{3.9}$ for different invariant mass ranges. The resulting distribution of the parameter $\epsilon(m)$ is shown in the bottom line, using $\mu_{3\pi} = m_{3\pi}/[\mathrm{GeV}/c^2]$.

9.3 Statistical Subtraction of the Diffractive Contribution at $t' < 10^{-3}\,\mathrm{GeV}^2/c^2$

As introduced in chapter 7, the high-energetic beam pion can be excited by pomeron exchange with a target nucleus, and subsequently decay into 3π, but the same final state can also be obtained from the exchange of a quasi-real photon (Primakoff-production). In the latter case, the cross-section strongly peaks at $t' \approx 0$, and the experimental spectrum is dominated by the resolution. This leads effectively to a dependence on t' which is much steeper than the diffractive cross-section with $\mathrm{d}\sigma(t')/\mathrm{d}t' \propto \mathrm{e}^{-b_{\mathrm{diff}}t'}$ ($b_{\mathrm{diff}} \approx 400\,(\mathrm{GeV}/c)^{-2}$ for lead[11]). Primakoff-produced events cannot be extracted easily by applying cuts on the data set on an event-by-event basis, but their presence is visible as an additional contribution to the t' spectrum at $t' \lesssim 10^{-3}\,\mathrm{GeV}^2/c^2$. A steeper slope is observed there, compared to the adjacent range $10^{-3}\,\mathrm{GeV}^2/c^2 < t' < 10^{-2}\,\mathrm{GeV}^2/c^2$.

The overall t' spectrum for $t' < 6 \cdot 10^{-3}\,\mathrm{GeV}^2/c^2$ can be fitted well with the sum of two exponentials, while for $t' \gtrsim 6.5 \cdot 10^{-3}\,\mathrm{GeV}^2/c^2$ the influence of the diffraction pattern (as shown in figure 9.3) starts to be visible in logarithmic scale (see figure 9.15). From those two exponentials a first glimpse of the contribution of Primakoff and diffractive production to the data at $t' \approx 0$ can be extracted. Figure 9.16 shows the t' distribution of events attributed to Primakoff production, i.e. the exponential curve attributed to diffractive production has been statistically subtracted here. Even an impression of the mass spectrum of the Primakoff-produced events can be derived, if such fits are carried out in the different mass bins and the statistically extracted Primakoff contribution is integrated in each mass bin. This procedure obviously neglects interference effects, but is still able to provide a first approximate insight.

On the level of available statistics, it turned out not to be possible to obtain the experimentally observed Primakoff t' distribution reliably from the data. So the presumed experimental distribution is obtained from MC simulations of events featuring the theoretical correlations and passing the COMPASS spectrometer (see section 9.2.4). The resulting t' distribution serves as input for the following fitting and subtraction procedure.

To execute this procedure in a mathematically stable way, the t' distribution of Primakoff production has been fixed to the parameter that had been obtained from this MC simulation for the respective mass bin. The diffractive slope parameter b_{diff} is still kept as a fitting parameter in every single mass bin, as it also turned out to depend slightly on the invariant mass.

For each of the $40\,\mathrm{MeV}/c^2$ mass bins for $0.44\,\mathrm{GeV}/c^2 < m_{3\pi} < 2.48\,\mathrm{GeV}/c^2$ separately, the t' spectrum after subtraction is obtained and then integrated from $t' = 0$ to $t' = 10^{-3}\,\mathrm{GeV}^2/c^2$. The resulting mass spectrum is shown in figure 9.17. It contains a clear peak at $m_{3\pi} \approx 1.3\,\mathrm{GeV}/c^2$, steming from the Primakoff-produced $a_2(1320)$. The broad bump from around $1\,\mathrm{GeV}/c^2$ to $2\,\mathrm{GeV}/c^2$ can presumably be attributed to an extension of

---

[11] The diffractive slope parameter b_{diff} depends on the size of the diffracting object, i.e. the target material, as given in section 7.2

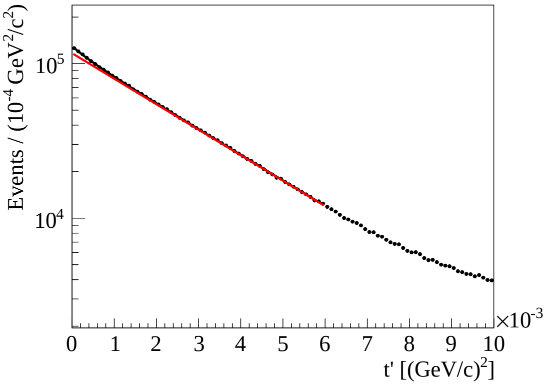

Figure 9.15: t' spectrum for all masses (black), with two exponential fit (black) and contribution of diffractive background (red).

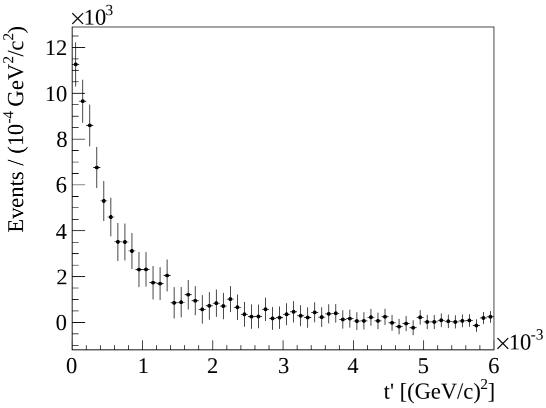

Figure 9.16: t' spectrum after subtraction of diffractive background.

the low-energy processes calculated in ChPT, including ρ contributions. Equivalent mass spectra have already been obtained by the Selex Collaboration for carbon, copper and lead targets, and fitted with a sum of pure Coulomb contribution and smooth background [SELEX01], see also figure 9.18.

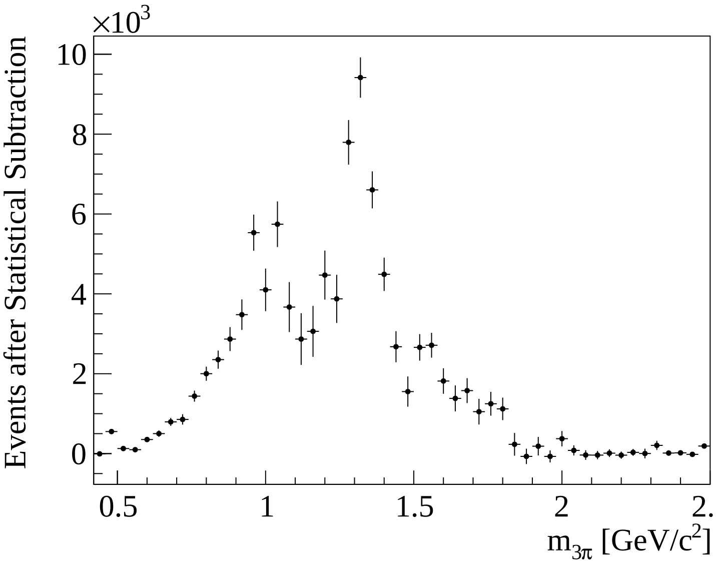

Figure 9.17: Mass spectrum after statistical subtraction of diffractive background for $t' < 10^{-3}\,\mathrm{GeV}^2/c^2$.

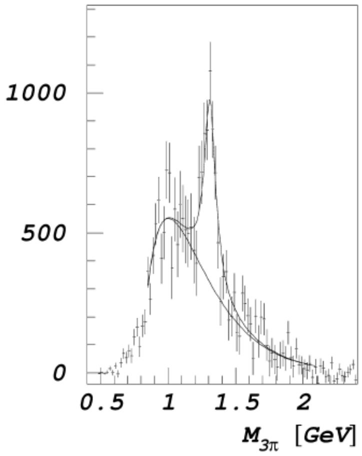

Fig. 3. $M_{3\pi}$ mass distribution for the Cu target after subtraction of diffractive background. The curve shows fit with a sum of pure Coulomb contribution and smooth background.

Figure 9.18: Mass spectrum after statistical subtraction of diffractive background for copper target (from [SELEX01]).

Another interesting result of this investigation is presented in figure 9.19. The slope $b_{\mathrm{diff}}(m)$ of the subtracted diffractive background, that is obtained from independent fits for each mass bin, changes significantly with the invariant mass of the 3π system between $b(m_{3\pi} = 0.44\,\mathrm{GeV}/c^2) \approx 500\,(\mathrm{GeV}/c)^{-2}$ and $b(m_{3\pi} = 2.5\,\mathrm{GeV}/c^2)) \approx 300\,(\mathrm{GeV}/c)^{-2}$. It can be parameterized by a quadratic polynomial. This relation enters the t' dependence of the decay amplitudes of waves attributed to diffractive production for the PWA (see section 8.2.3).

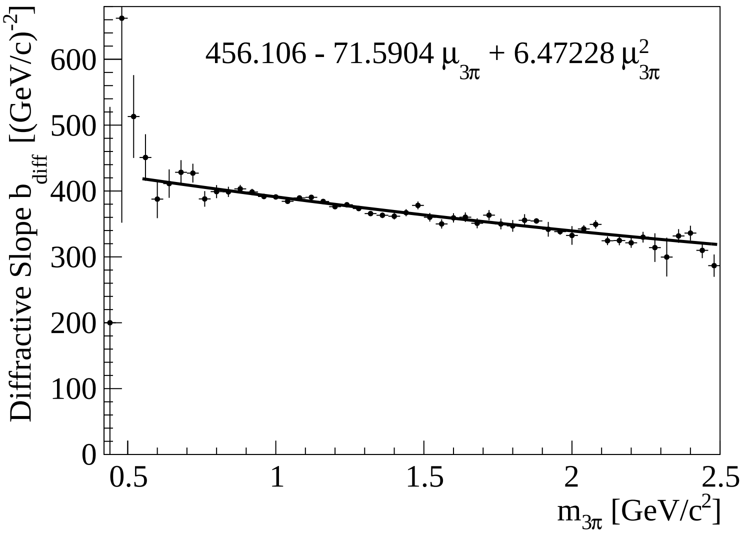

Figure 9.19: Mass-dependence of the diffractive slope "$b_{\text{diff}}(m)$" from fits containing a fixed Primakoff parameter and a free exponential diffractive component (fits to $t' < 6 \cdot 10^{-3}\,\text{GeV}^2/c^2$), using $\mu_{3\pi} = m_{3\pi}/[\text{GeV}/c^2]$.

9.4 Results from PWA

Based on the event selection introduced in section 9.1, and applying acceptance corrections based on the MC simulations presented in section 9.2.2, a mass-independent partial-wave analysis has been performed to decompose the invariant three-pion mass spectrum from figure 9.6 (left) into its contributions from resonances and non-resonant intermediate states. In this whole section, all isobaric amplitudes are identified by their quantum numbers and the isobar, i.e. by $J^{PC}M^{\epsilon}[isobar\ \pi]L$ as introduced in section 8.2.1.1. In the beginning, the new amplitudes introduced specifically for this analysis are presented with their effect to the fit result. Several partial-wave analysis fits in bins of both mass and t' are shown in the following, which reveal strong indications for several resonances and changes of their production mechanisms with t'. An outlook to the future extensions of the present PWA is given in section 9.4.4, and the first glimpse on a PWA with an extension of one of the introduced amplitudes is given in section 9.4.5.

9.4.1 PWA Fits with Amplitudes from ChPT Calculations and Kaon Decays

The two new non-isobaric amplitudes cover calculations from ChPT (see section 8.2.2.1) and the free decay of beam kaons $K^- \to \pi^-\pi^-\pi^+$ (see section 8.2.2.2). In the following, fits result including them are compared to fits results before their introduction, i.e. where their intensity had to be picked up by other amplitudes.

9.4.1.1 ChPT Amplitude

The impact of the use of the amplitude from the ChPT calculations, often called chiral amplitude, in the PWA (instead of isobaric $M = 1$ waves for masses below $m_{3\pi} = 0.7\,\mathrm{GeV}/c^2$) is depicted in figure 9.20. The two fitting models[12] (see tables 9.1 and 9.2) are directly compared for selected intensities of $M = 1$ waves or the spin totals: The intensities of the $1^{++}1^{+}(\pi\pi)_s\pi P$ and the $1^{++}1^{+}\rho\pi S$ waves are shown top left and right, the $M = 1$ spin total and the spin total of the chiral amplitude bottom left and right, respectively. The red data points refer to a fit without the chiral amplitude (i.e. it is completely absent in all mass bins), the black data points to the fit with the chiral amplitude used in all mass bins and the isobaric $M = 1$ waves thresholded as indicated by the border between white and grey regions.

Comparing the behaviour of the fits in the low mass region (indicated by the white background, i.e. either the chiral wave or several isobaric $M = 1$ waves are part of the respective fitting model), one can clearly see that the intensities of the isobaric waves feature huge error bars, indicating difficulties of the fit to distinguish between them (red points in upper two plots). The intensity of the chiral spin total, on the other hand, shows a

---

[12] The mass range fitted here is different from the one used for the fits detailed later, i.e. the fit started only at $m_{3\pi} > 0.5\,\mathrm{GeV}/c^2$. This comparison had been carried out before the kaon amplitude, described in section 9.4.1.2, was introduced.

$J^{PC}M^{\epsilon}$	L	Isobar π	Thresh. [GeV]
$0^{-+}0^{+}$	S	$(\pi\pi)_s\pi$	-
$0^{-+}0^{+}$	P	$\rho\pi$	-
$1^{++}0^{+}$	S	$\rho\pi$	-
$1^{++}0^{+}$	P	$(\pi\pi)_s\pi$	-
$1^{++}0^{+}$	D	$\rho\pi$	1.05
$1^{++}1^{+}$	S	$\rho\pi$	0.70
$1^{++}1^{+}$	P	$(\pi\pi)_s\pi$	0.78
$1^{-+}1^{+}$	P	$\rho\pi$	0.70
$2^{++}1^{+}$	D	$\rho\pi$	0.70
$2^{-+}0^{+}$	P	$\rho\pi$	0.80
$2^{-+}0^{+}$	D	$(\pi\pi)_s\pi$	-
$2^{-+}1^{+}$	S	$f_2\pi$	0.98
$2^{-+}1^{+}$	P	$\rho\pi$	0.70
$2^{-+}1^{+}$	D	$(\pi\pi)_s\pi$	0.78
$2^{-+}1^{+}$	F	$\rho\pi$	0.98
$3^{++}0^{+}$	F	$(\pi\pi)_s\pi$	-
chiral $\epsilon = +1$			
$1^{++}1^{-}$	S	$\rho\pi$	0.70
$1^{++}1^{-}$	S	$(\pi\pi)_s\pi$	0.78
$1^{-+}0^{-}$	P	$\rho\pi$	-
$1^{-+}1^{-}$	P	$\rho\pi$	0.70
$2^{++}0^{-}$	D	$\rho\pi$	-
$2^{++}1^{-}$	D	$\rho\pi$	0.70
$2^{-+}1^{-}$	S	$f_2\pi$	0.98
$2^{-+}1^{-}$	P	$\rho\pi$	0.70
$2^{-+}1^{-}$	D	$(\pi\pi)_s\pi$	0.78
$2^{-+}1^{-}$	F	$\rho\pi$	0.98
chiral $\epsilon = -1$			
Background			

Table 9.1: Exemplary Set of Amplitudes used for $m_{3\pi} < 1.1\,\mathrm{GeV}/c^2$ and $t' < 10^{-3}\,\mathrm{GeV}^2/c^2$, with the chiral amplitude replacing isobaric $M = 1$ waves at low masses (used for fit presented in Fig. 9.20, black points).

$J^{PC}M^{\epsilon}$	L	Isobar π	Thresh. [GeV]
$0^{-+}0^{+}$	S	$(\pi\pi)_s\pi$	-
$0^{-+}0^{+}$	P	$\rho\pi$	-
$1^{++}0^{+}$	S	$\rho\pi$	-
$1^{++}0^{+}$	P	$(\pi\pi)_s\pi$	-
$1^{++}0^{+}$	D	$\rho\pi$	1.05
$1^{++}1^{+}$	S	$\rho\pi$	-
$1^{++}1^{+}$	P	$(\pi\pi)_s\pi$	-
$1^{-+}1^{+}$	P	$\rho\pi$	-
$2^{++}1^{+}$	D	$\rho\pi$	-
$2^{-+}0^{+}$	P	$\rho\pi$	0.80
$2^{-+}0^{+}$	D	$(\pi\pi)_s\pi$	-
$2^{-+}1^{+}$	S	$f_2\pi$	0.98
$2^{-+}1^{+}$	P	$\rho\pi$	-
$2^{-+}1^{+}$	D	$(\pi\pi)_s\pi$	-
$2^{-+}1^{+}$	F	$\rho\pi$	0.98
$3^{++}0^{+}$	F	$(\pi\pi)_s\pi$	-
$1^{++}1^{-}$	S	$\rho\pi$	-
$1^{++}1^{-}$	S	$(\pi\pi)_s\pi$	-
$1^{-+}0^{-}$	P	$\rho\pi$	-
$1^{-+}1^{-}$	P	$\rho\pi$	-
$2^{++}0^{-}$	D	$\rho\pi$	-
$2^{++}1^{-}$	D	$\rho\pi$	-
$2^{-+}1^{-}$	S	$f_2\pi$	0.98
$2^{-+}1^{-}$	P	$\rho\pi$	-
$2^{-+}1^{-}$	D	$(\pi\pi)_s\pi$	-
$2^{-+}1^{-}$	F	$\rho\pi$	0.98
Background			

Table 9.2: Exemplary Set of Amplitudes used for $m_{3\pi} < 1.1\,\mathrm{GeV}/c^2$ and $t' < 10^{-3}\,\mathrm{GeV}^2/c^2$ without using the chiral amplitude, but several isobaric $M = 1$ waves starting at $0.5\,\mathrm{GeV}/c^2$ (used for fit presented in Fig. 9.20, red points).

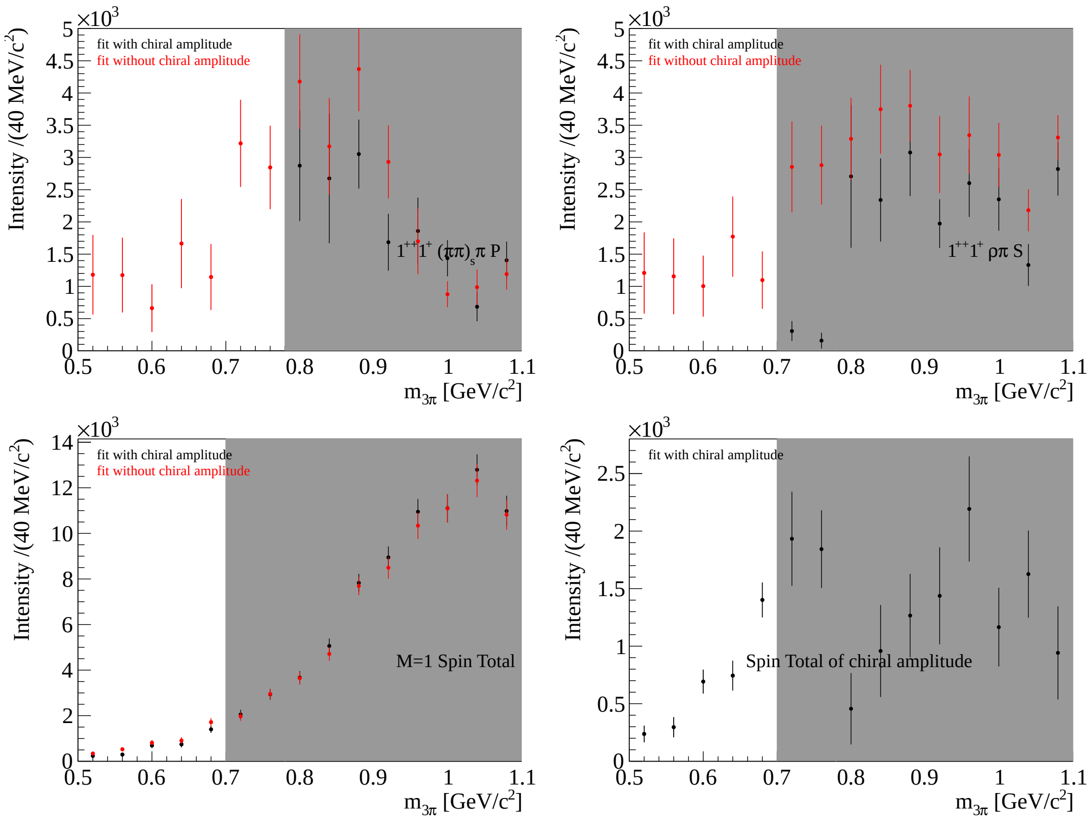

Figure 9.20: Intensities of selected waves with $M = 1$ for fit with chiral amplitude replacing other $M = 1$ waves at low mass (black) compared to fit with isobaric $M = 1$ waves (red).

smooth behaviour with much smaller statistical error bars (dark points in bottom right plot). The resulting $M = 1$ spin total (bottom left) of both fitting models are well in agreement, indicating that the chiral amplitude is equivalently capable of determining the Primakoff-produced fraction of the data as several isobaric $M = 1$ waves. The fit quality in the low mass region is also compatible.

For the best fit, which is used for the determination of the cross-section (see section 9.6), the fitting model was reduced by the $3^{++}0^{+}(\pi\pi)_s\pi F$, $1^{-+}0^{-}\rho\pi P$ and $2^{++}0^{-}\rho\pi D$ waves with respect to table 9.1, the wave describing the beam kaon decay (see section 9.4.1.2 was added, and rank 2 is used. The resulting total intensity of the ChPT amplitudes for $0.44 < m_{3\pi} < 0.72\,\mathrm{GeV}/c^2$ is presented in figure 9.21.

9.4.1.2 Kaon Decay Amplitude

Previous partial-wave analyses of data at small t' had to exclude the low-mass range $m_{3\pi} < 0.5\,\mathrm{GeV}/c^2$ due to the contribution of decaying beam kaons in the mass region just below this value. The fit had attributed this kaon contribution to isobaric waves, as indicated in figure 9.22. To extend the PWA fit in the lower mass region, a dedicated amplitude describing the decay $K^- \to \pi^-\pi^-\pi^+$ was introduced based on the experi-

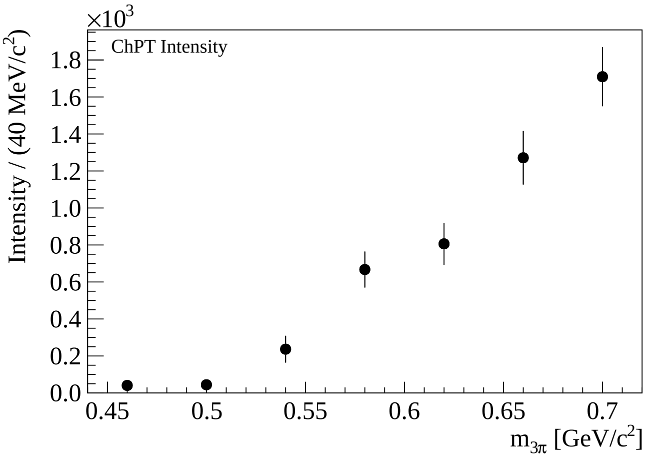

Figure 9.21: Total intensity of the ChPT amplitude.

mentally observed kaon mass distribution and the kaon decay Dalitz plot, as presented in section 8.2.2.2. Figure 9.23 shows, that the huge intensity in the respective mass region is now indeed attributed to the kaon decay amplitude.

9.4.2 PWA in Mass Bins

The mass-independent PWA has been carried out for the mass range $0.44\,\mathrm{GeV}/c^2 < m_{3\pi} < 2.48\,\mathrm{GeV}/c^2$. The fitting model is given in table D.1: It includes the decay amplitudes derived from ChPT and takes into account the decay of beam kaons in the relevant mass range. It respects the mentioned t' dependence of decay amplitudes given in section 8.2.3. The data are fitted with $N_r = 1$ with one free coherence parameter between all $M = 0$ and all $M = 1$ waves (as explained in detail in section 8.4). Intensities of selected Spin Totals and individual waves are presented here, as well as selected phases between waves. A comprehensive overview of the complete fit result is given in section D.

9.4.2.1 Total Intensities (“Spin Totals”)

The total intensities for $M = 0$ and $M = 1$ are presented in figure 9.24. It is worth stressing that the $M = 0$ total intensity collects most of the statistics (and such reflects the shape of the total mass spectrum), while the summed intensity of $M = 1$ waves has a similar shape, as the mass spectrum presented in figure 9.17. The latter was obtained by simple statistical subtraction of the diffractive background, which is a completely different approach. This plot shows again a clear peak at $1.3\,\mathrm{GeV}/c^2$,

Figure 9.25 opposes these two mass spectra. The $M = 1$ total intensity from the PWA is here divided by its acceptance, so that the intensities of the two mass spectra can be directly compared: They feature equivalent intensity at $m_{3\pi} \approx 1.3\,\mathrm{GeV}/c^2$, i.e. they both select the $a_2(1320)$ equally. In contrast, the bump at $m_{3\pi} \approx 1.1\,\mathrm{GeV}/c^2$ is more pronounced in the PWA plot, which might still give a hint to leakage (from $a_1(1260)$) to the

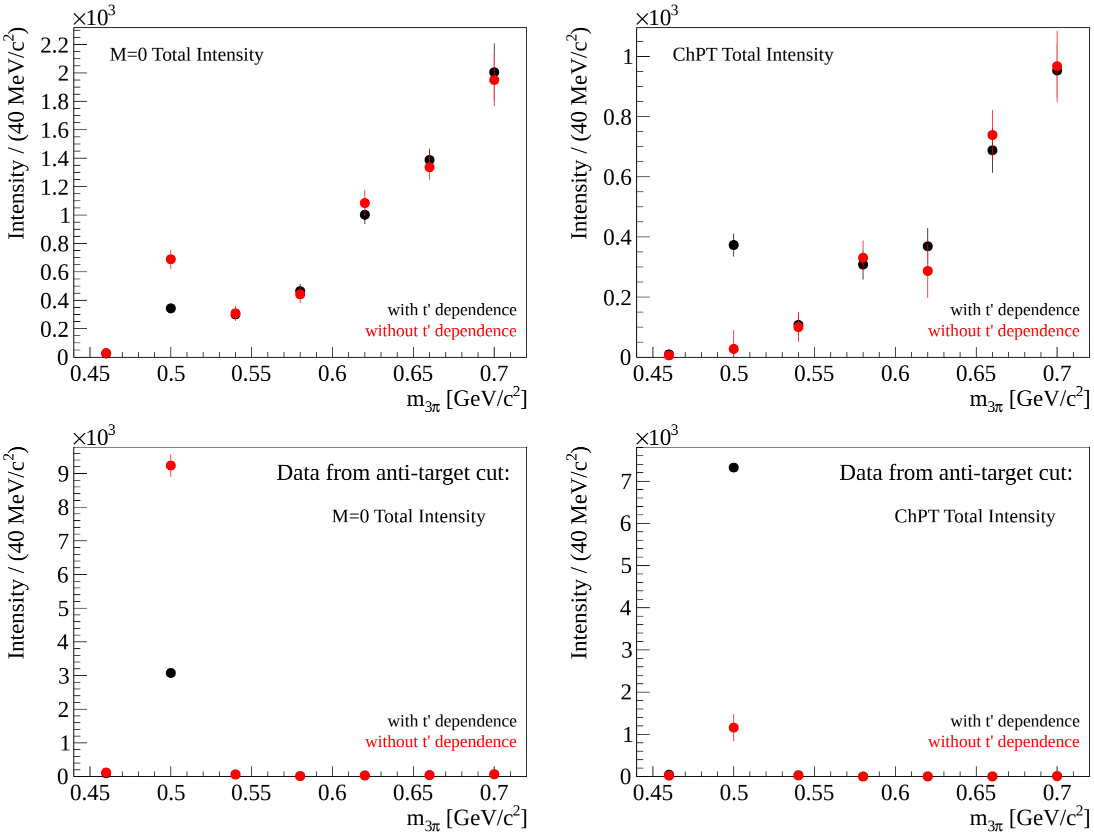

Figure 9.22: Attribution of the kaon decay component to total intensities in the bin at $m_{3\pi}$ before the introduction of the kaon decay amplitude: Significant intensity is attributed to $M = 0$ amplitudes, and when t' dependences are used, most intensity ends up in the $M = 1$ (=ChPT) amplitudes. This is even more pronounced for data with an anti-target cut as shown in the bottom row. The fits were carried out without acceptances corrections, which explains the reduced intensities compared to the ones from figure 9.23.

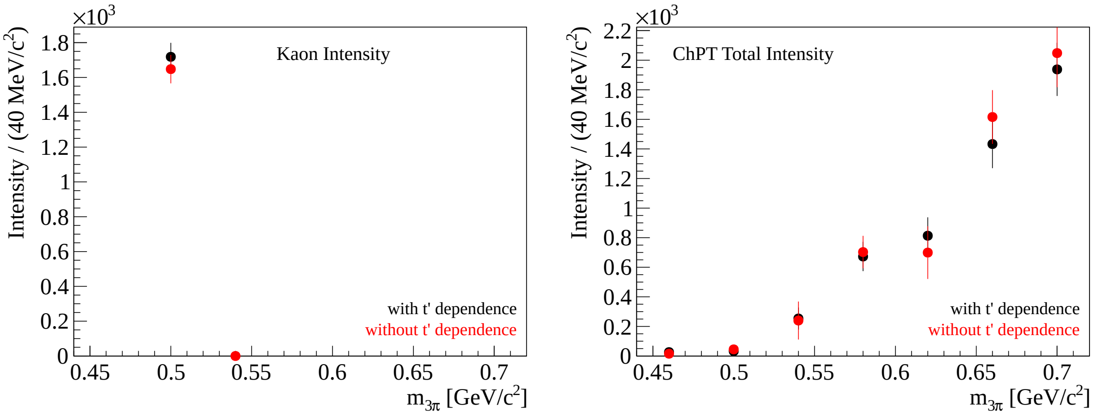

Figure 9.23: The kaon amplitude (left) collects a reasonable intensity both for fits with and without t' dependent amplitudes. No kaon peak is visible in the $M = 1$ (ChPT) intensities any more.

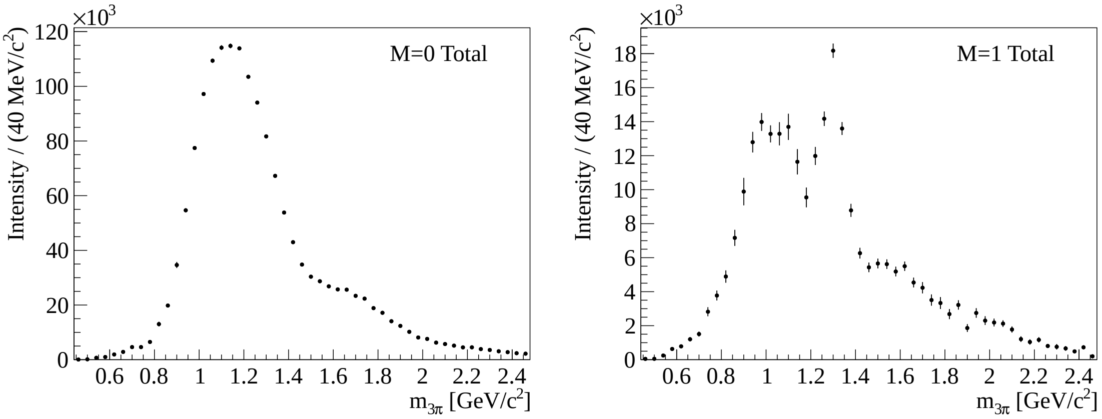

Figure 9.24: Spin Total for M=0 (left) and M=1 (right) for $t' < 10^{-3}\,\mathrm{GeV}^2/c^2$.

relatively small $M = 1$ waves, or it might as well point to difficulties the statistical subtraction method has with the huge statistics around $1.1\,\mathrm{GeV}/c^2$. In any case, the PWA puts upper limits to the contribution of production via quasi-real photon exchange.

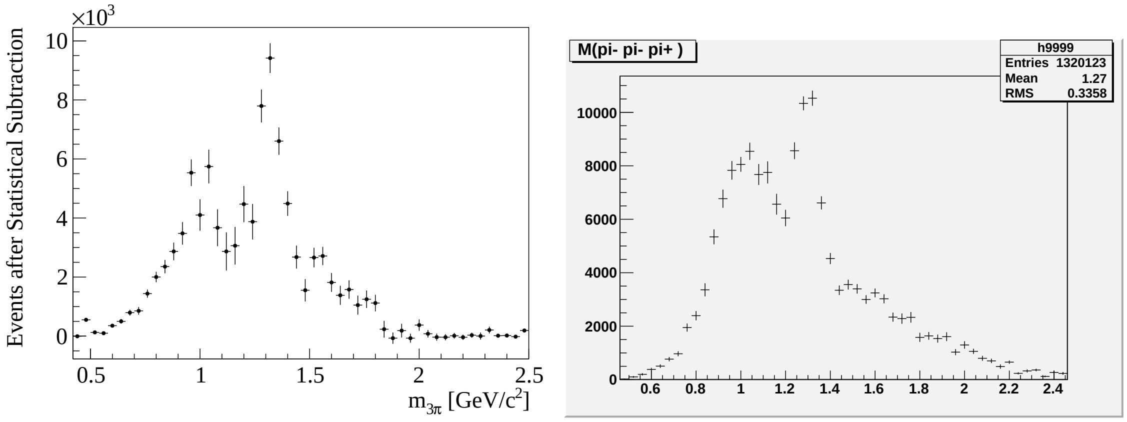

Figure 9.25: Comparison of the statistical substraction (left) and the $M = 1$ Spin Total from PWA divided by acceptance (right, from [Rya11]) for $t' < 10^{-3}\,\mathrm{GeV}^2/c^2$.

Figure 9.26 shows the contributions of different J^{PC} total intensities with $M = 1$, which are the relevant quantities for the determination of the amount of produced states like the $a_2(1320)$ in the $2^{++}1$ total intensity (bottom left) or $\pi_2(1670)$ in the $2^{-+}1$ total intensity (bottom right). As shown in section 9.5, at very low momentum transfer both positive and negative reflectivity $M = 1$ intensities contain physical events and thus can and have to be added. The $1^{++}1$ total intensity (top left) and $1^{-+}1$ total intensities are also presented, for potential interpretation see section 9.4.2.2.

9.4.2.2 Intensities of Selected Waves

The intensities of six selected amplitudes are presented in figure 9.27 for $t' < 0.001\,\mathrm{GeV}^2/c^2$. Phases between those amplitudes will be shown later. The intensity of

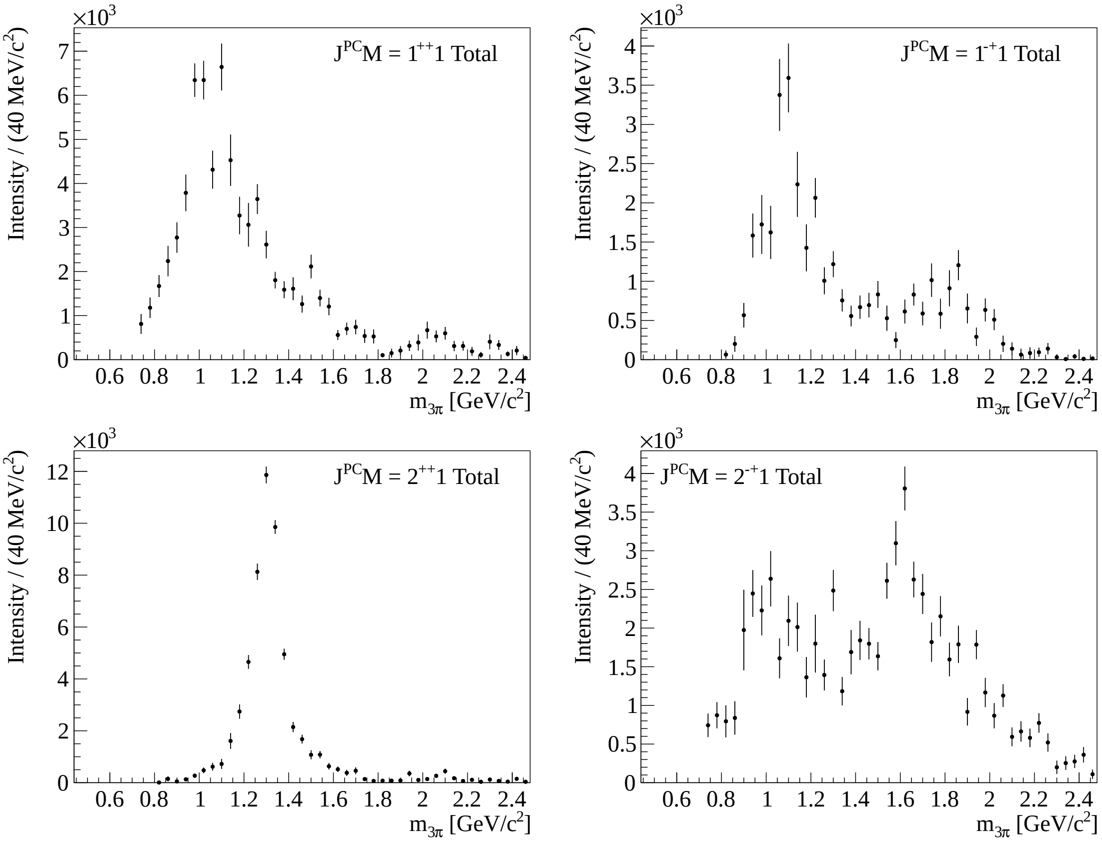

Figure 9.26: Spin Total for M=1 with different J^{PC} for $t' < 10^{-3}\,\mathrm{GeV}^2/c^2$: $1^{++}1$ and $1^{-+}1$ (top left and right), $2^{++}1$ and $2^{-+}1$ (bottom left and right) total intensities.

the $1^{++}0^{+}\rho\pi S$ wave contains the major part of the total intensity, peaking at around $1.1\,\mathrm{GeV}/c^2$, that might contain the $a_1(1260)$ (but not exclusively, top row left plot). The intensity of the $2^{++}1^{+}\rho\pi D$ wave depicts a very clear and sharp bump at around $1.3\,\mathrm{GeV}/c^2$, that is related to the $a_2(1320)$ (top row right plot). The intensities of the $2^{-+}0^{+}f_2\pi S$ and $2^{-+}1^{+}f_2\pi S$ waves (middle row, left and right plot) show both bumps at around $1.7\,\mathrm{GeV}/c^2$, that can be (presumably) correlated to the $\pi_2(1670)$ resonance. While the $\pi_2(1670)$ with $M = 0$ from diffractive production is an established resonance, the $2^{-+}1^{+}f_2\pi S$ (with $M = 1$) is a candidate for Primakoff production of $\pi_2(1670)$, which has not been clearly seen before. The $1^{++}1^{+}\rho\pi S$ wave shows a bump at around $1.1\,\mathrm{GeV}/c^2$ and is a potential candidate for the $a_1(1260)$ produced by photon exchange (that has been quoted by [Zie84], bottom row left plot), while the $1^{-+}1^{+}\rho\pi P$ wave shows two bumps at around $1.1\,\mathrm{GeV}/c^2$ and $1.9\,\mathrm{GeV}/c^2$, that might possibly point to Primakoff-produced spin-exotic resonances.

9.4.2.3 Relative Phases between Selected Waves

Figure 9.28 shows the phase motions of the $2^{++}1^{+}\rho\pi D$, $2^{-+}0^{+}f_2\pi S$ and $2^{-+}1^{+}f_2\pi S$ amplitudes (whose intensities are shown in figure 9.27) relative to $1^{++}0^{+}\rho\pi S$, which in-

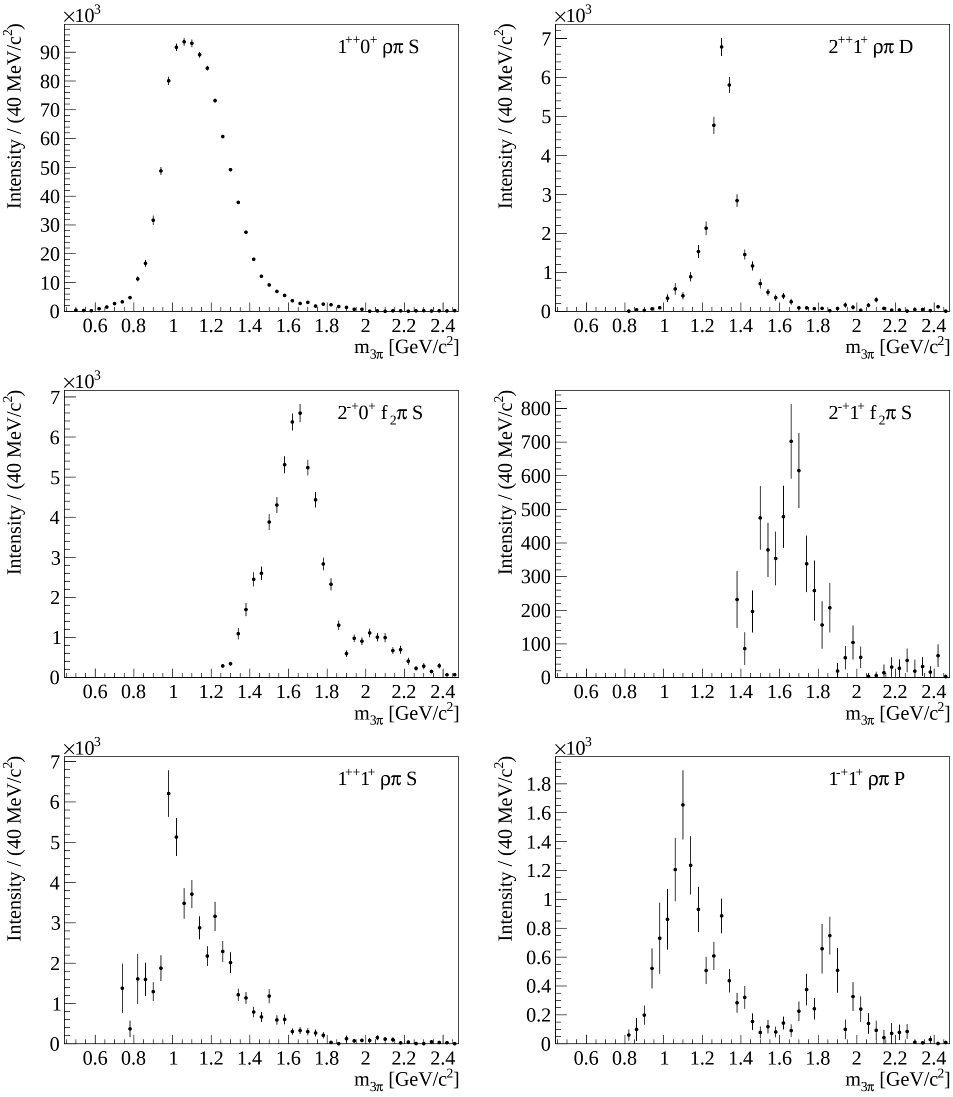

Figure 9.27: Intensities of $1^{++}0^{+}\rho\pi S$, $2^{++}1^{+}\rho\pi D$, $2^{-+}0^{+}f_2\pi S$, $2^{-+}1^{+}f_2\pi S$, $1^{++}1^{+}\rho\pi S$, and $1^{-+}1^{+}\rho\pi P$, (from left top to right bottom) for $t' < 10^{-3}\,\mathrm{GeV}^2/c^2$.

dicate resonant behaviour of all three amplitudes in the mass range around $1.3\,\mathrm{GeV}/c^2$ ($a_2(1320)$) and $1.7\,\mathrm{GeV}/c^2$ ($\pi_2(1670)$), respectively, with respect to the $a_1(1260)$ (top left, top right and bottom left). The phase between $2^{-+}0^{+}f_2\pi S$ and $2^{-+}1^{+}f_2\pi S$ is constant in the mass range of the $\pi_2(1670)$, which points to the same resonating behaviour of both waves. The absolute difference between the two phases (around 120 degrees) indicates Primakoff production of the $\pi_2(1670)$ in the $M = 1$ amplitude.

Figure 9.29 presents the phases of the $1^{++}1^{+}\rho\pi S$, and $1^{-+}1^{+}\rho\pi P$ amplitudes (intensities also shown in figure 9.27) relative to $1^{++}0^{+}\rho\pi S$. While the first one is falling in the mass range populated by $a_1(1260)$ resonances, the second one is more or less flat, so that there is no clear indication for resonances as “$a_1(1260)$ produced by photon-exchange” or “spin-exotic resonance from Primakoff production” (top row left and right plot). The phase of $2^{++}1^{+}\rho\pi D$ relative to $1^{++}1^{+}\rho\pi S$ (bottom plot) shows a phase motion of about 180 degrees in the mass region around $1.3\,\mathrm{GeV}/c^2$, which describes the full Breit-Wigner shape of the $a_2(1320)$ resonances without any compenstation by another Breit-Wigner, so that there is again no indication for a resonance occuring in the $1^{++}1^{+}\rho\pi S$ wave around $1.2 - 1.3\,\mathrm{GeV}/c^2$. The significant intensity of the $1^{++}1^{+}\rho\pi S$ wave in figure 9.27 presumably points to contributions of the non-resonating processes described by ChPT with ρ exchange, that are not included yet in the tree-level chiral amplitude described in section 8.2.2.1 (see also section 9.4.5). Those are supposed to contribute significantly around $1.0\,\mathrm{GeV}/c^2$, so that in the present fitting model their intensities likely ends up in $\rho\pi$ amplitude like the one depicted here.

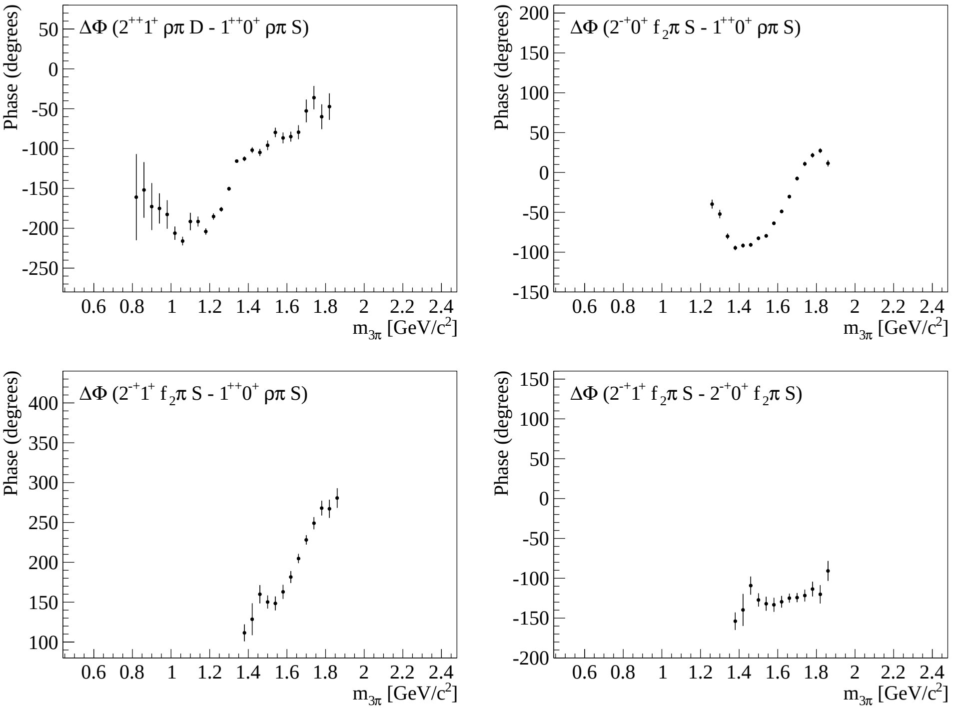

Figure 9.28: Phases of $2^{++}1^{+}\rho\pi D$, $2^{-+}0^{+}f_2\pi S$ and $2^{-+}1^{+}f_2\pi S$ with respect to $1^{++}0^{+}\rho\pi S$ (left top, right top, left bottom) for $t' < 10^{-3}\,\mathrm{GeV}^2/c^2$. Phase between $2^{-+}1^{+}f_2\pi S$ and $2^{-+}0^{+}f_2\pi S$ shows constant offset (right bottom).

9.4.2.4 Selected Intensities and Phases for separated t' ranges

Both the "low t'" ($10^{-3} < t' < 10^{-2}\,\mathrm{GeV}^2/c^2$) data (see [Wei08a]) and the "Primakoff t'" ($t' < 10^{-3}\,\mathrm{GeV}^2/c^2$) data show clear indication for the presence of the $a_2(1320)$ in the respective data. Its quantum number $M = 1$ suggests, that the $a_2(1320)$ is created by different production mechanisms, that should be distinguishable roughly by t': Photon-exchange for $t' < 10^{-3}\,\mathrm{GeV}^2/c^2$, pomeron exchange for $t' > 10^{-3}\,\mathrm{GeV}^2/c^2$. To get a clear picture, clearly separated regions of the two t' ranges have been chosen, that is $t' < 0.5 \cdot 10^{-3}\,\mathrm{GeV}^2/c^2$ and $1.5 \cdot 10^{-3}\,\mathrm{GeV}^2/c^2 < t' < 10^{-2}\,\mathrm{GeV}^2/c^2$. For both a mass-

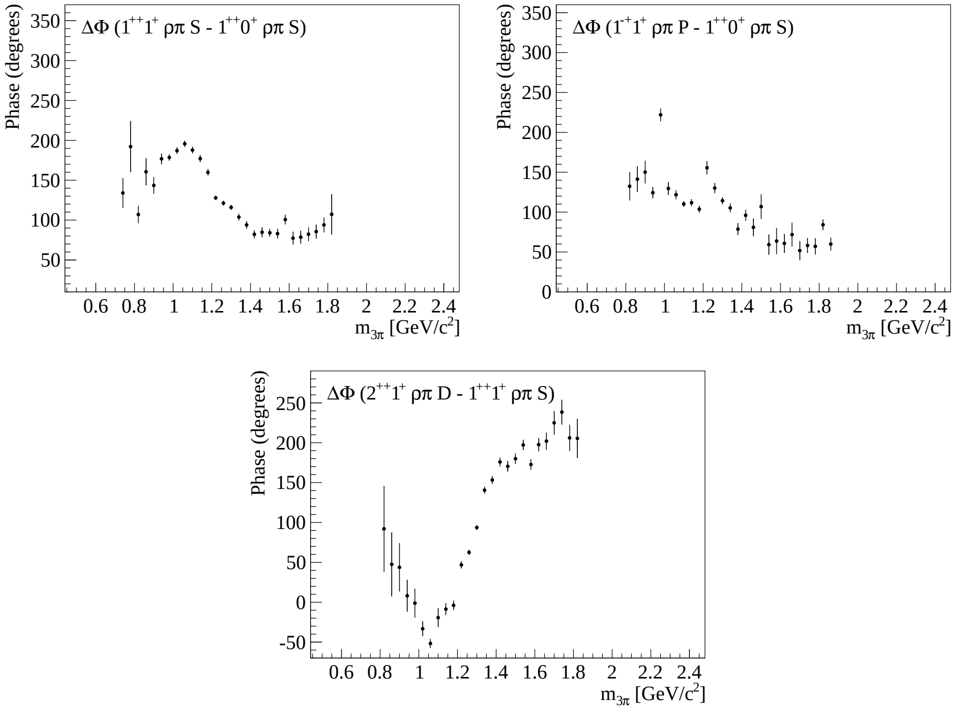

Figure 9.29: Phases of $1^{++}1^{+}\rho\pi S$ and $1^{-+}1^{+}\rho\pi P$ with respect to $1^{++}0^{+}\rho\pi S$ (top) and of $2^{++}1^{+}\rho\pi D$ with respect to $1^{++}1^{+}\rho\pi S$ for $t' < 10^{-3}\,\mathrm{GeV}^2/c^2$.

independent partial-wave analysis is performed with the goal to look at the phase between the $a_2(1320)$ and the $a_1(1260)$, presented by their prominent decay amplitudes $2^{++}1^{+}\rho\pi D$ and $1^{++}0^{+}\rho\pi S$. The fitting model with one free coherence parameter between the $M = 0$ and $M = 1$ waves, which are internally connected by rank 1, is chosen for both t' ranges. No t' dependence of the decay amplitudes is taken into account at this stage. Figure 9.30 (left column) shows this fit for $t' < 0.5 \cdot 10^{-3}\,\mathrm{GeV}^2/c^2$ in red and the one for $1.5 \cdot 10^{-3}\,\mathrm{GeV}^2/c^2 < t' < 10^{-2}\,\mathrm{GeV}^2/c^2$ in black. The relative phase between the two amplitudes grows in both cases, but is shifted overall by about 90° (bottom left plot). This leads to the speculation, that the production phase can be considered constant for the narrow mass of a_2, but changes with t'. Thereby the $a_1(1260)$ production stays the same, but the $a_2(1320)$ production changes from photon exchange (purely real amplitudes) to Pomeron exchange (purely imaginary amplitudes) with growing t'.

An equivalent observation is made for the $\pi_2(1670)$, presented by its decay to $f_2\pi S$ amplitudes, but with $M = 0$ and $M = 1$, which is shown in figure 9.32 (right column). The phases between these two waves are constant in the relevant range at $\approx 1.6\,\mathrm{GeV}/c^2$ in both t' ranges, which is explained by the observation of the same resonance in both amplitudes. The shift by an offset of about $90\,^{\circ}$ is again interpreted as a change of the production of the $\pi_2(1670)$ from Primkoff to diffractive production between the two t' ranges.

For a better quantification, PWA fits have been carried out in small bins of t' as presented

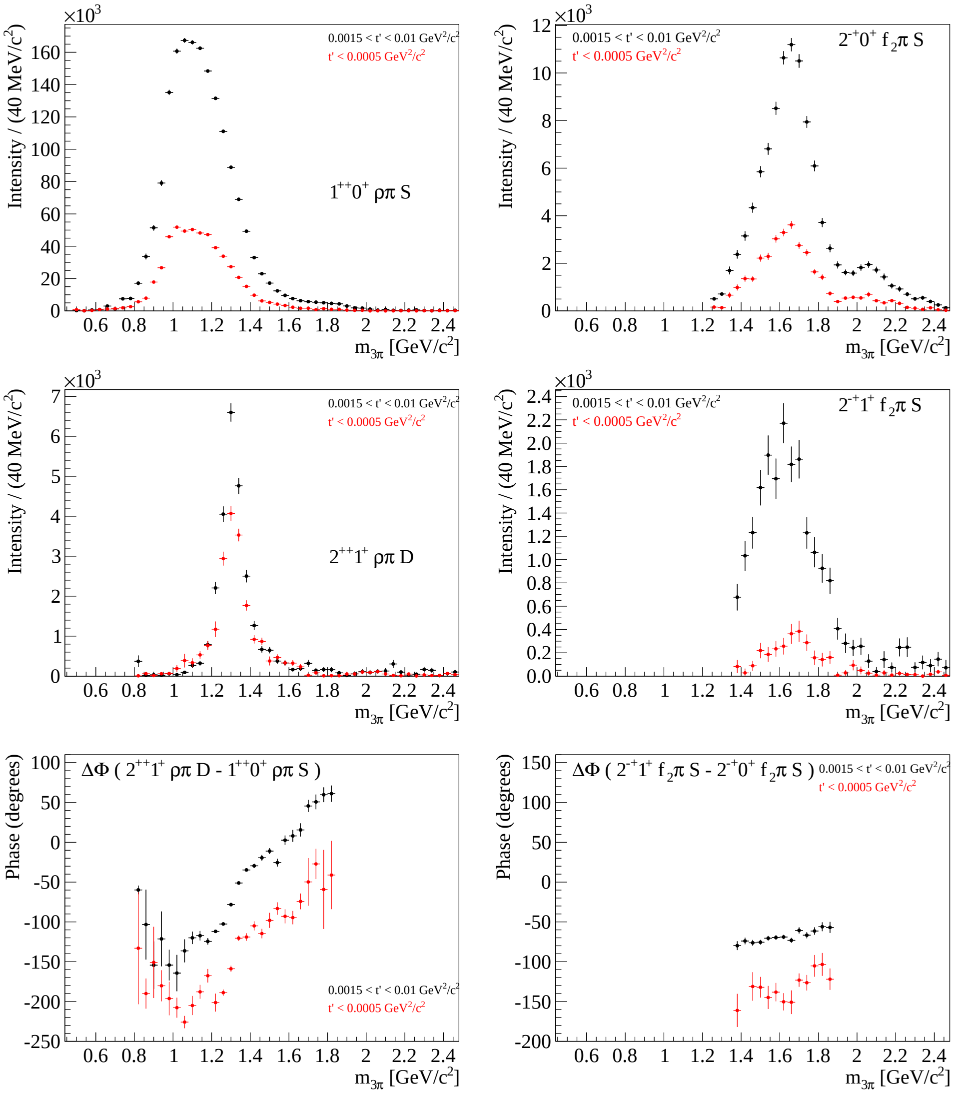

Figure 9.30: Production phase of $a_2(1320)$ (left column) and $\pi_2(1670)$ (right column) for two separated t' regions (Top row: Intensities of $1^{++}0^{+}\rho\pi S$ (left) and $2^{-+}0^{+}f_2\pi S$ (right); middle row: $2^{++}1^{+}\rho\pi D$ (left) and $2^{-+}1^{+}f_2\pi S$ (right); Bottom row: Relative phases between the respective two waves.

in section 9.4.3.

9.4.3 PWA in t' Bins

For the investigation of production mechanisms featuring distinct t' dependences, PWA fits are performed in small bins of t'. Due to the limited statistic of the presented data, one mass bin, which is significantly broader than 40 MeV/c^2, is chosen. Consequently the mass cannot be treated constant inside this bin any more, but its dependence has to be modeled by polynomials or Breit-Wigner functions (see section 8.3.3 for the technical implementation). In return, no predetermined t' dependence of the decay amplitudes is taken into account for these fits.

9.4.3.1 t' Dependence of ChPT Amplitude

The t' dependence of the chiral amplitude has been investigated with a dedicated set of PWA fits in the low mass region ($0.51\,\mathrm{GeV}/c^2 < m_{3\pi} < 0.72\,\mathrm{GeV}/c^2$). This whole mass region is used as one mass bin, with a polynomial describing the mass dependence of the chiral amplitude multiplied on its decay amplitude. The fits are carried out in small bins of t' but without taking into account any t' dependences of the single waves. Figure 9.31 shows the intensities of the chiral spin total (left) and the $M = 0$ spin total (right) dependent on t'. Both intensities are fitted with an exponential ($\mathrm{d}\sigma(t')/\mathrm{d}t' \propto \mathrm{e}^{-bt'}$) for $t' < 10^{-3}\,\mathrm{GeV}^2/c^2$. While the $M = 0$ spin total features a slope $b \approx 400\,(\mathrm{GeV}/c)^{-2}$ which is typical for diffractive production at a lead target, the slope of the chiral spin total shows $b \approx 1560\,(\mathrm{GeV}/c)^{-2}$ which is in agreement with Primakoff production (i.e. the theoretical shape convolved with resolution, as confirmed by the dedicated MC sample presented in section 9.2.4). This confirms the Primakoff nature of the events collected by the chiral amplitude.

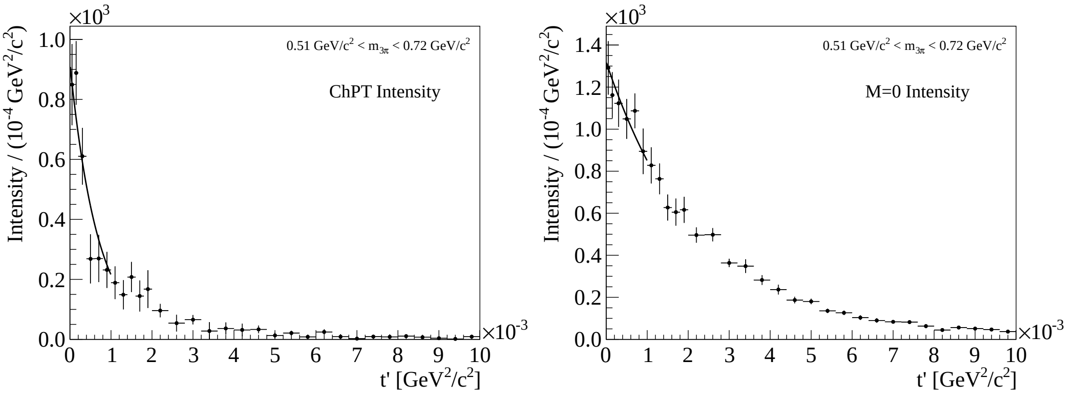

Figure 9.31: Intensities of Spin Totals dependent on t': Slope of chiral intensity (left) is significantly shaper than the slope of the $M = 0$ intensity (right), confirming the Primakoff nature of the chiral amplitude.

9.4.3.2 Mass range containing $a_2(1320)$

To measure the production phase of the $a_2(1320)$, a set of PWA fits was performed in the region of the a_2 mass ($1.26\,\mathrm{GeV}/c^2 < m_c < 1.38\,\mathrm{GeV}/c^2$), that is used as a single mass bin. For these fits the t' range $t' < 0.01\,\mathrm{GeV}^2/c^2$ was divided into several bins of different width (narrower bins for small t'). Due to the broad mass bin, coherence is lost even for higher t', but also significantly for the very narrow t' bins at $t' = 0$, so that a fitting model with $N_r = 1$ between the $M = 0$ amplitudes, but with free coherence parameters between all $M = 1$ waves (in positive reflectivity, $N_r = 2$ in negative reflectivity) is used. There is no overall t' dependence taken into account, but mass dependent Breit-Wigner terms (without adding the Deck-effect, as this does presumably not influence the phase) are multiplied on the $a_1(1260)$ and $a_2(1320)$ decay amplitudes instead. Figure 9.32 shows the intensities of the two selected waves (positive reflectivities, which is necessary to investigate the phase) dependent on t', and the coherence and the production phase of the $a_2(1320)$ changing with t'. One can clearly see a smooth motion of the production phase, that reproduces the offset for the two t' ranges used before, and indicates a smooth changeover of the two different production mechanisms.

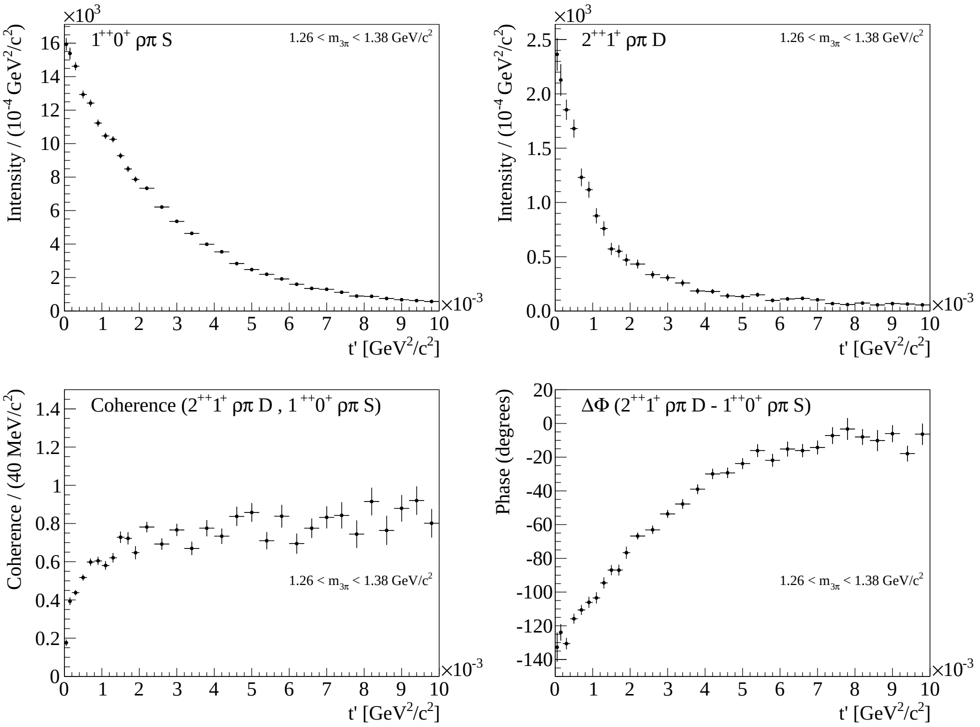

Figure 9.32: Production phase of $a_2(1320)$ dependent on t' (Top row:Intensites of $1^{++}0^{+}\rho\pi S$ (left) and $2^{++}1^{+}\rho\pi D$ (right), Bottom row: Coherence (right) and relative phase between the two amplitudes (left).

In addition, figure 9.33 shows the intensity of $a_2(1320)$ fitted by negative reflectivity, and the Spin Total (that contains the incoherent sum of the intensities of both the positive and the negative reflectivity). The intensity of the negative reflectivity shows the same magnitude as the one of positive reflectivity at $t' = 0$, but vanishes at $t' \approx 10^{-3}\,\mathrm{GeV}^2/c^2$, so that there is no intensity of negative reflectivity in the diffractive region, while the positive reflectivity propagates there. As confirmed by the leakage study (see section 9.5), the Spin Total corresponds to the total number of produced $a_2(1320)$ resonances. It can be fitted by a sum of two exponentials reflecting the contribution of Primakoff and diffractive production of the $a_2(1320)$ (see right bottom plot, blue and grey curve): $\exp(-b_{\mathrm{prim}}t')$ and $t'\exp(-b_{\mathrm{diff}}t')$, respectively, which reproduce approximately the numbers for $b_{\mathrm{prim}}(m)$ and $b_{\mathrm{diff}}(m)$ that one expects for $m_{3\pi} \approx 1.3\,\mathrm{GeV}/c^2$ (see sections 9.2.4 and 9.3). By this fit the shape of the spectrum can be roughly explained, but the interference effects from Pri-

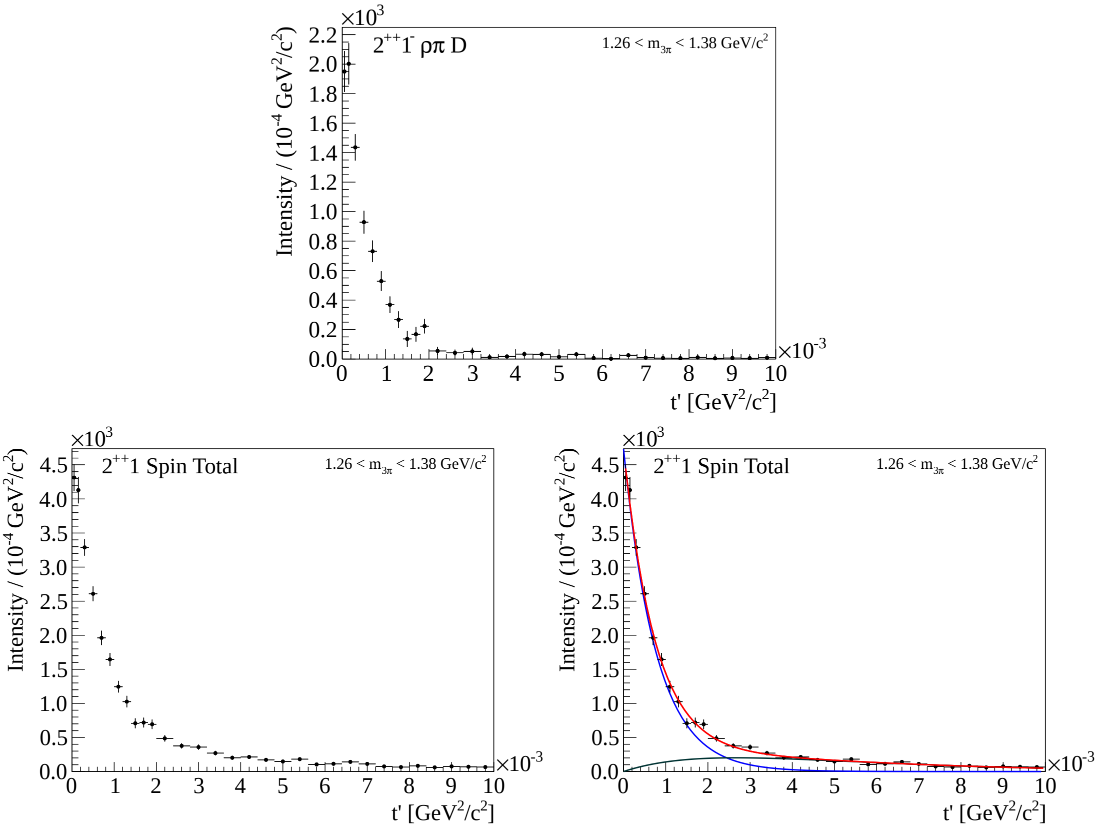

Figure 9.33: Primakoff production of $a_2(1320)$: Intensities dependent on t'. Intensity of $2^{++}1^-\rho\pi D$ (top) and $2^{++}1$ Spin Total (bottom).

makoff and diffractive production in the data can obviously not be taken into account[13].

9.4.3.3 Mass range containing $\pi_2(1670)$

An equivalent procedure as presented in the previous section, was also carried out in the mass range $1.50 < m_{3\pi} < 1.92\,\mathrm{GeV}/c^2$ to investigate the production phase of the $2^{-+}1^+f_2\pi S$, i.e. the amplitude offering a candidate for the $\pi_2(1670)$ produced by quasi-real photon exchange. The same fitting model with free coherence between the $M = 0$ waves (that are internally treated by rank 1) and all individual $M = 1$ waves is applied. Due to the broad mass range, the decay amplitudes of the significant waves[14] are multiplied by Breit-Wigner terms plus background as given by the Stodolski approximation [ACC81]. Here individual parameters, obtained from fits to the data, are used for each channel. As the data is fitted in small bins of t', no t' dependence of amplitudes is taken

---

[13] The ansatz with a two exponential fit is not perfectly correct, as the MC simulation of the Primakoff t' distribution has shown, that the exponential fit to its reconstructed values is only reasonable for $t' < 10^{-3}\,\mathrm{GeV}^2/c^2$. Including higher values of t', the reconstructed Primakoff t' spectrum gets flatened. So a reasonable fit is obtained with a too sharp Primkoff contribution, which might be a hint for destructive interference between Coulomb and Primakoff production.

[14] Non-significant waves, i.e. small waves without structures, are just multiplied by complex polynomials.

into account again.

Figure 9.34 shows the intensities of three single waves ($1^{++}0^{+}\rho\pi S$ (top left), $2^{-+}0^{+}f_2\pi S$ (top right) and $2^{-+}1^{+}f_2\pi S$ (bottom)) and figure 9.35 the total intensities of 1^{++} $M = 0$ (top left), 2^{-+} $M = 0$ (top right) and 2^{-+} $M = 1$ (bottom) in the indicated mass region dependent on t'. All show approximately the same slope, which is expected in this mass range also for Primakoff production, as the numbers for $b_{\text{prim}}(m)$ and $b_{\text{diff}}(m)$ are less different than for lower masses. The 2^{-+} $M = 1$ total intensity can be fitted by a sum of $\exp(-b_{\text{prim}}t')$ and $t' \exp(-b_{\text{diff}}t')$ with fixed slope parameters $b_{\text{prim}} = 350$ and $b_{\text{prim}} = 880$ (numbers taken from figures 9.19 and 9.13), but this ansatz is probably as oversimplified as for the $2^{++}1$ total in the previous section.

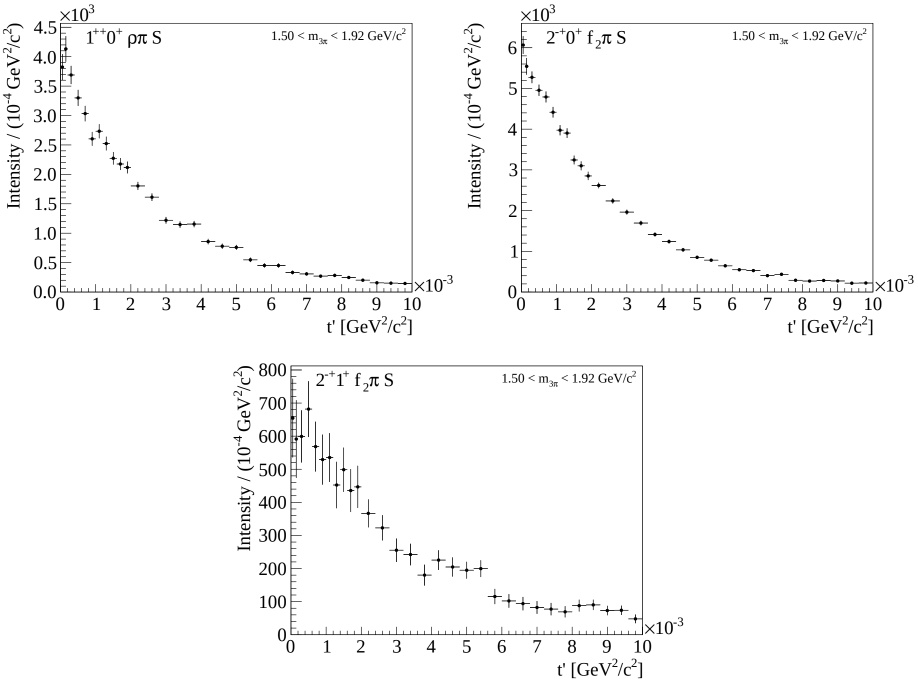

Figure 9.34: Intensities of $1^{++}0^{+}\rho\pi S$, $2^{-+}0^{+}f_2\pi S$ and $2^{-+}1^{+}f_2\pi S$ for $1.50 < m_{3\pi} < 1.92\,\text{GeV}/c^2$ dependent on t'.

Figure 9.36 shows the relative phases between the three amplitudes presented in figure 9.34. The smooth motion of the production phase of the $2^{-+}1^{+}f_2\pi S$ with respect to the $1^{++}0^{+}\rho\pi S$ and $2^{-+}0^{+}f_2\pi S$ waves indicates a change of its production mechanism from Primakoff to diffractive production with t' (top left and right plots). The production phase between the two $M = 0$ waves does not change with t', which is a confirmation for the same (i.e. the diffractive) production mechanism of these both waves (bottom plot). For the first time a clear indication for Primakoff production of the $\pi_2(1670)$ at $t' \approx 0$ is observed in the COMPASS data.

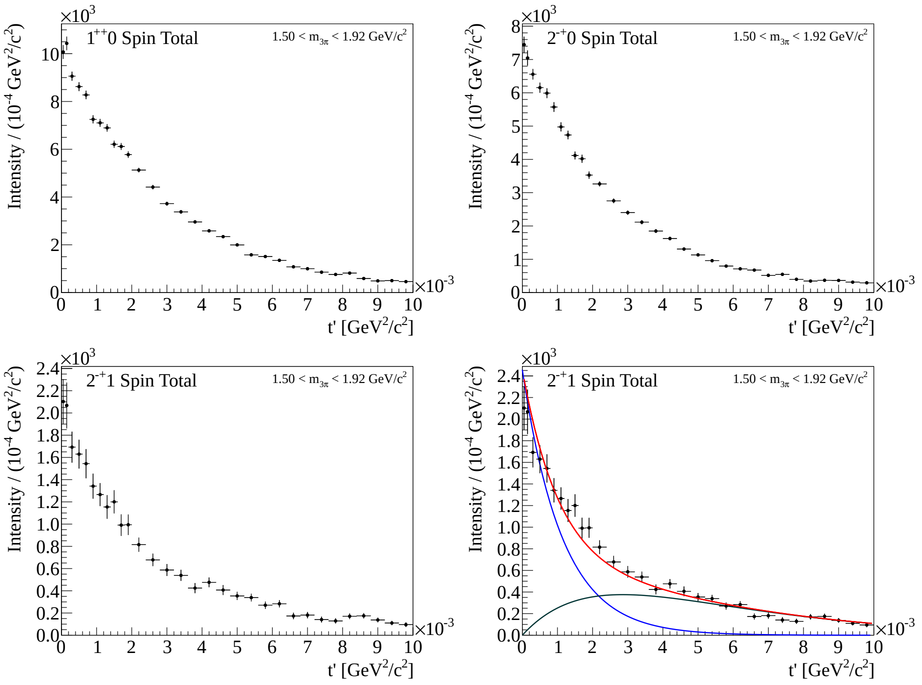

Figure 9.35: Total intensities of $1^{++}0$, $2^{-+}0$ and $2^{-+}1$ for $1.50 < m_{3\pi} < 1.92\,\mathrm{GeV}/c^2$ dependent on t'.

9.4.4 Outlook: Future Extensions of the present PWA

In section 9.4.2.4 it was shown, that the production phase of the two amplitudes showing strong evidence for the $a_2(1320)$ and the $\pi_2(1670)$ with $M = 1$ changes by about 90 degrees between two fixed ranges around $t' \approx 0$ and $t' \approx 10^{-2}\,\mathrm{GeV}^2/c^2$, while the phase motion itself remains the same. This change is in agreement with the observation of Primakoff (i.e. electromagnetic) interaction featuring a real-amplitude scattering at $t' \approx 0$, and diffractive (i.e. strong) production featuring an imaginary amplitude at higher t', for the same resonance. The more detailed results based on the analysis in small bins of t' in section 9.4.3 reveal a smooth phase shift between values even larger than 90 degrees and 0 dependent on t'. From these results the interference between Primakoff and diffractive production can be investigated in detail, so that the nature of the Pomeron can be studied ([Fri12] and references therein).

The observation of the radiative coupling of the $a_2(1320)$ and the $\pi_2(1670)$ allows for the quantification of their radiative widths. The radiative width of the $a_2(1320)$ has been measured already with similar conditions [SELEX01]. The determination of the radiative width of the $\pi_2(1670)$ can be done with the present data for the first time. The knowledge of the absolute cross-section of the Primakoff production of these resonances is mandatory. The normalization will be obtained analogously from the beam kaon decays as presented in section 9.6. However, as slightly different parts of the spectrometer are involved for the detection of higher-mass particles[15], the shortcomings of the simulation

---

[15] The $a_2(1320)$ and the $\pi_2(1670)$ feature significantly higher masses than the mass range in which the

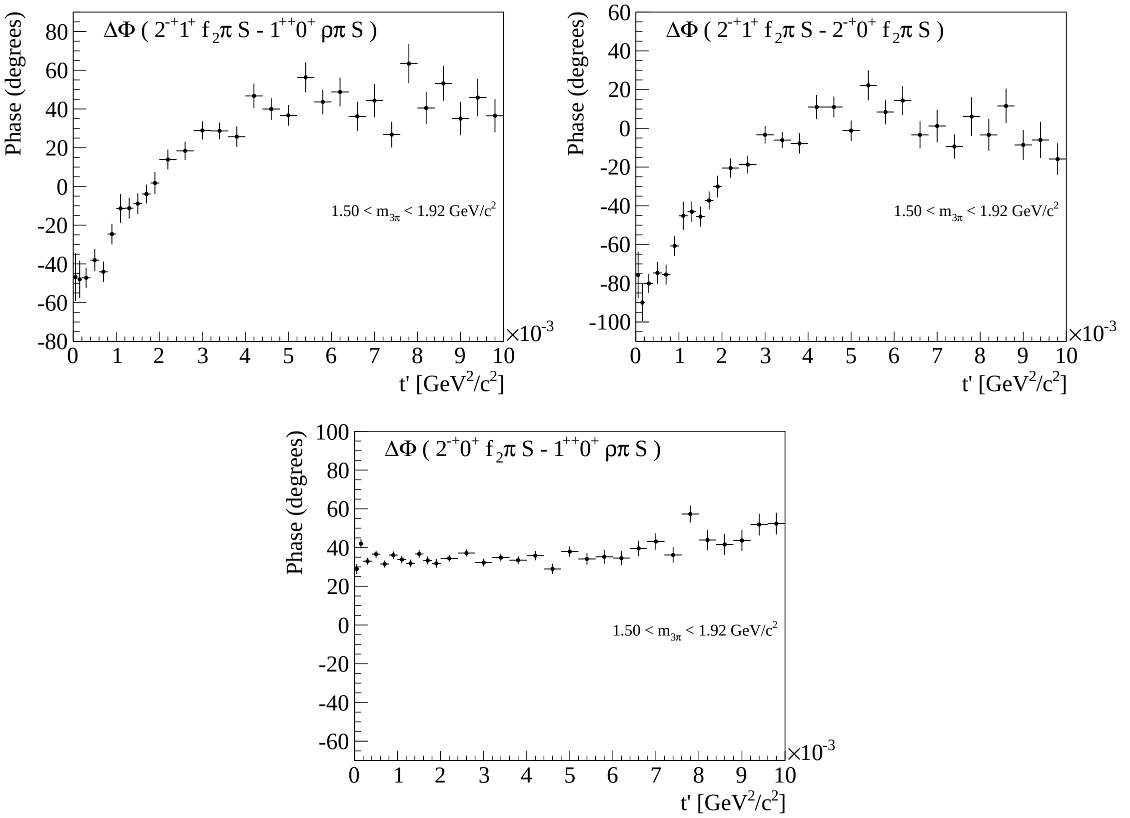

Figure 9.36: Primakoff Production of $\pi_2(1670)$: Relative phases between $1^{++}0^{+}\rho\pi S$, $2^{-+}0^{+}f_2\pi S$ and $2^{-+}1^{+}f_2\pi S$ for $1.50 < m_{3\pi} < 1.92\,\text{GeV}/c^2$ dependent on t'. The smooth motion of the production phase of the $2^{-+}1^{+}f_2\pi S$ with respect to the two $M = 0$ waves indicates a change of its production mechanism from Primakoff to diffractive production with t' (top left and right plots). The production phase between the two $M = 0$ waves does not change with t' (bottom plot).

for low masses (see C.1.3) have to be better understood and carefully quantized. Furthermore, the naive two-exponential fits to the total intensities $J^{PC} = 2^{++}1$ (figure 9.33) and $J^{PC} = 2^{-+}1$ (figure 9.35) point out, that the $\pi_2(1670)$ features a remarkable diffractive component already for $t' < 10^{-3}\,\text{GeV}^2/c^2$ (unlike the $a_2(1320)$), so that a quantification of the interference between Primakoff and diffractive production will be required for the determination of the radiative width of the $\pi_2(1670)$.

In addition, a mass-dependent fit will be necessary for the definite determination of the resonances present in the data, and their masses and widths. It has to be sorted out how the $M^{\epsilon} = 1^{-}$ contribution caused by resolution (see section 9.5), which do mathematically not interfere with the positive reflectivity contributions, can be taken into account. A summary of the resonances present in the data, in addition to the ones discussed before, is available in appendix D, where the intensities of all amplitudes used in the mass-independent PWA fit are plotted.

---

cross-section is determined in section 9.6, which includes the kaon mass.

9.4.5 First Glimpse on PWA with the extended ChPT Amplitudes

The amplitude from ChPT, which has been used in the fits presented in this thesis, is given by the first order calculations ([KF08], see also section 8.2.2.1). Their description does not take into account contributions from pion-loops or explicit ρ, which are mimicked by isobaric waves with ρ or $(\pi\pi)_S$ as isobars. In the following, results from the first exercises with amplitudes from ChPT, which take into account also pion-loops and the ρ [Kai10, Kai11] (in the following denoted as "extended ChPT amplitudes", are presented.

In the first iteration, the leading-order ChPT amplitudes have been replaced by extended ones. An overview of the $M = 1$ total intensities, where an impact is expected for masses between $0.7\,\mathrm{GeV}/c^2 < m_{3\pi} < 1.2\,\mathrm{GeV}/c^2$, is given in figure 9.37. There is significant impact on the $J^{PC}M = 1^{-+}1$, and $J^{PC}M = 2^{-+}1$ total intensities, where a huge part of the intensities observed in the standard fit are attributed to the extended ChPT amplitudes if provided. The $J^{PC}M = 2^{++}1$ does not change, which is expected as only the $a_2(1320)$ resonance is visible, but no background. Also the $J^{PC}M = 1^{++}1$ does not change yet, but it has to be stated, that the amplitude set is overdetermined, as isobaric amplitudes are still used in parallel to the extended ChPT amplitude.

The improvement of the fitting model was carried out by rejecting (i.e. thresholding) of the isobaric amplitudes where this seemed to be applicable. It turned out, that the spin-exotic $J^{PC}M = 1^{-+}1$ amplitudes can be omitted up to $1.5\,\mathrm{GeV}/c^2$, which is in agreement with the assumption, that there is no resonant behaviour in the intensity in this mass range. The same is true for the $J^{PC}M = 2^{-+}1$ amplitudes below $1.3\,\mathrm{GeV}/c^2$. For the $J^{PC}M = 1^{++}1$, the fit quality became significantly worse when both amplitudes with ρ or $(\pi\pi)_S$ as isobars were omitted, but the use of only one of them did also not describe the data well. Still non-resonant contributions in these intensities are assumed, and they can be explained by explicit contributions of the $(\pi\pi)_S$ [Sze11], which are not included in the available ChPT calculations . The obtained total intensities are presented in figure 9.38.

It has to be stressed that this result is very preliminary, and serious technical checks, systematic studies and further optimizations of the fitting models will have to be carried out before the result can be settled.

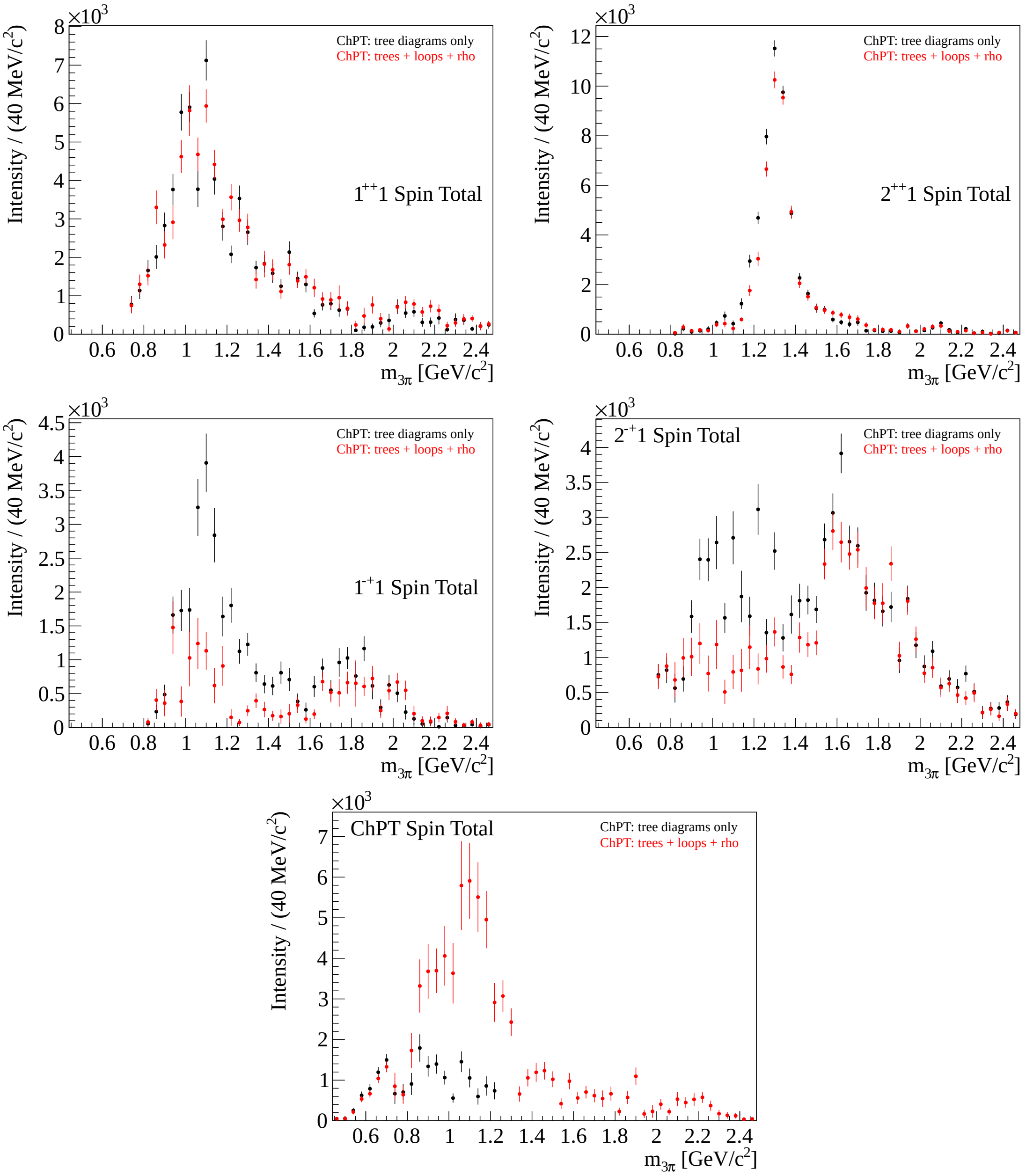

Figure 9.37: Total intensities for $J^{PC}M = 1^{++}1$, $J^{PC}M = 2^{++}1$, $J^{PC}M = 1^{-+}1$, $J^{PC}M = 2^{-+}1$, and the ChPT amplitudes, compared for fits with the leading-order ChPT amplitudes and the extended ChPT amplitudes.

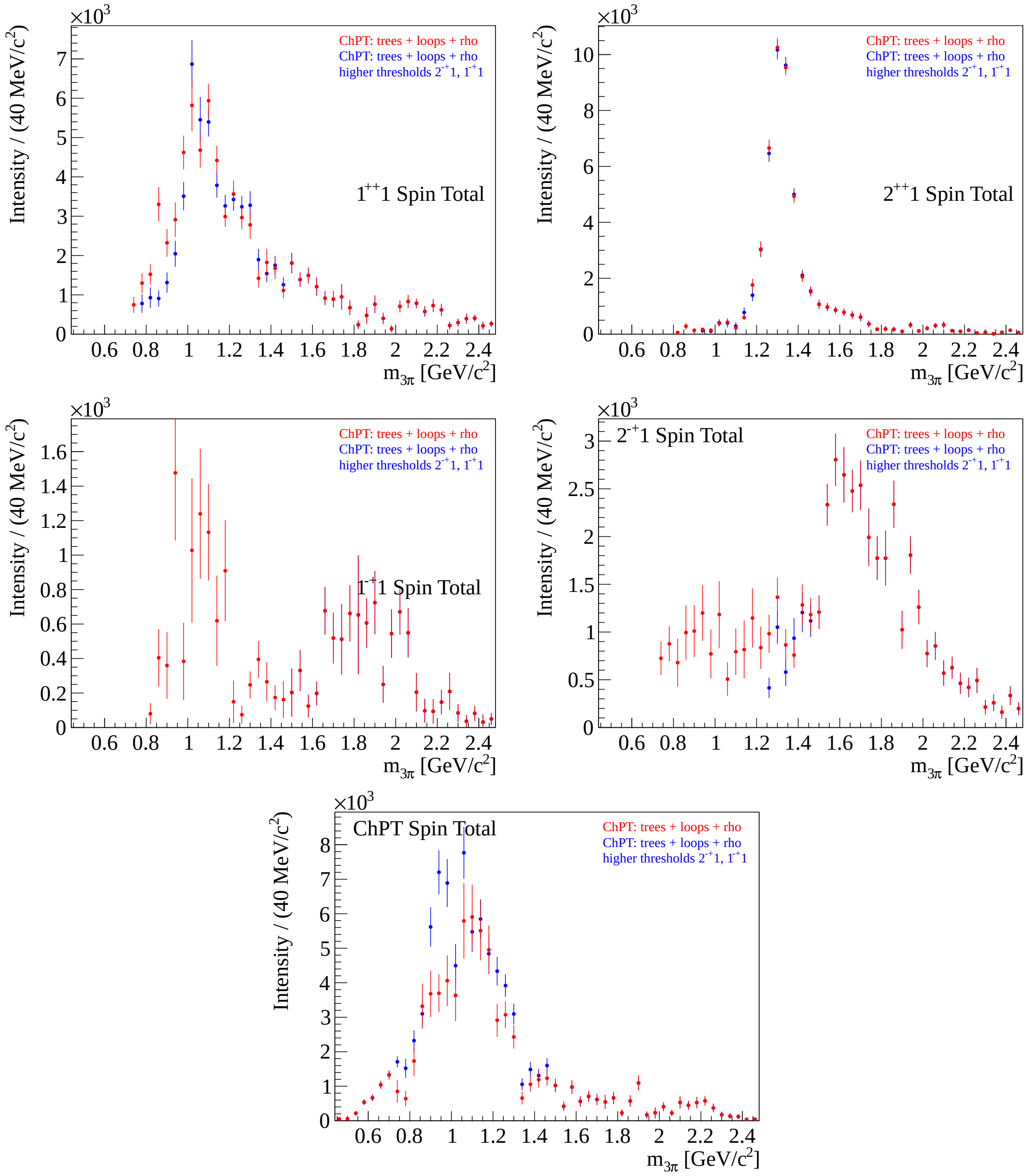

Figure 9.38: Total intensities for $J^{PC}M = 1^{++}1$, $J^{PC}M = 2^{++}1$, $J^{PC}M = 1^{-+}1$, $J^{PC}M = 2^{-+}1$, and the extended ChPT amplitudes, compared for fits using the extended chiral amplitudes, with and without higher thresholds for several isobaric waves applied.

9.5 Leakage Study

The purpose of a leakage study is to verify a certain fitting model (whose purpose is to describe nature) for a given task. That means, it is used as a basis for judging how well a known input data set, which is affected by the impact of the spectrometer, can be described by the PWA fit using this model.

For the analyses presented in this work, the main purpose of the leakage study is to confirm the changes to the input due to the impact of the resolution of the spectrometer that is supposed to be the reason for effects seen in the fits of reconstructed experimental data. For scattering processes at heavy nuclei at very low momentum transfer (here $t' < 10^{-3}\,\mathrm{GeV}^2/c^2$), nature should be described by coherent sums of amplitudes (strong interaction dominated by $M^\epsilon = 0^+$, Primakoff production by $M^\epsilon = 1^+$). However, the values of coherence measured by the PWA of the experimental data are reduced. Obviously ϕ_{TY} cannot be properly measured any more, so that the intensities of $M^\epsilon = 1^+$ waves migrate also to $M^\epsilon = 1^-$ waves. To get the "real" total intensities of $M = 1$ waves as the $a_2(1320)$, the intensities of the positive and negative reflectivity can (and have to) be summed. This conclusion has to be confirmed by a leakage study based on MC, as it is an important prerequisite to cross-section measurements as the one presented in section 9.6. As the measured values of coherence between $M = 0$ waves internally are not significantly below 1, and a similar effect can be seen for $M = 1$ waves internally, this suggests to use a fitting model which is more advanced than the traditional rank $N_r = 1$ or $N_r = 2$ fit with free coherence parameters (see section 8.4). This alternative model, as well as the choice of the wave set, have also to be verified by the leakage study, and to be chosen such that the fit result describes the input data best.

A leakage study including the full COMPASS MC chain is carried out in the way presented in the following. A PWA fit result to the respective data is used as input. Events are then generated in phase space, but weighted with the angular distributions and Dalitz plots that correspond to the cross-sections of single amplitudes as they are measured by the mentioned PWA fit, and with the supposed unsmeared t' distributions[16]. Due to the assumption, that the $M^\epsilon = 1^-$ intensities are populated just due to resolution, but not by nature, their intensities are neglected as input to the simulation, but the intensities of the corresponding $M^\epsilon = 1^+$ waves are scaled accordingly (by the factor 1.8). The intensities of $M = 0$ waves are used unchanged, while the flat background amplitude does not enter the simulation. The generated events are passed through the standard COMGEANT+CORAL chain, and analyzed and fitted equivalently to the data. Then the PWA fits to both the MC truth and the reconstructed MC are compared to the input.

Selected intensites from the leakage study made are presented in figures 9.39, 9.40 and 9.41. In all these plots the input to the simulation, i.e. the result of the PWA fit that served as basis, are plotted in black. For better comparison, the intensities of the black points (all amplitudes) have been scaled such that the $M = 0$ total intensity features approximately the same intensity, and the $M^\epsilon = 1^+$ intensities have been multiplied with

---

[16] This means particulary, that formula (7.12) is used for $M = 1$ waves produced by photon exchange.

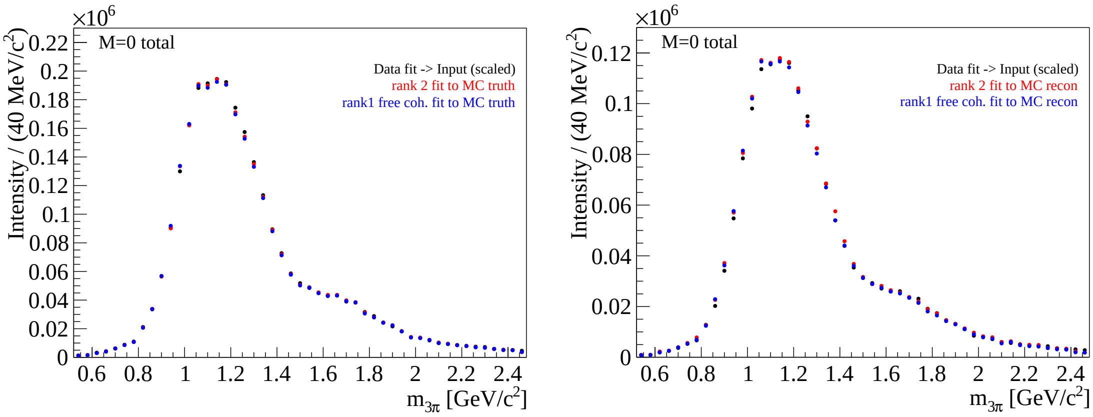

Figure 9.39: Total intensity of $M^\epsilon = 0^+$ waves as obtained from PWA fits to the MC truth (left) and the reconstruced MC events (right).

the additional scaling factor used during the generation of events a second time, and the $M^\epsilon = 1^-$ of this fit have been neglected for plotting. The red and blue points correspond to fits with the same wave set as used for the input fit, but with rank $N_r = 2$ for the red and rank $N_r = 1$ with one additional free coherence parameter for the blue case.

Figure 9.39 presents the $M = 0$ total intensity from fits to MC truth and to reconstructed MC. On this level, both fitting models seem to be equivalent, and the reconstructed events do not seem to suffer significantly from resolutions effects.

Figure 9.40 shows the intensities of the $2^{++}\rho\pi D$ waves (referring to the $a_2(1320)$). In the fit to the MC truth (left column), most intensity is attributed to the $M^\epsilon = 1^+$ wave, only very little to the $M^\epsilon = 1^-$ wave[17], and the total intensity matches perfectly, so that the input is completely reproduced. In the fit to the reconstructed MC (right column) instead, the intensity attributed to the $M^\epsilon = 1^+$ wave is only slightly more than half of the input intensity, and the remaining part ends up in the $M^\epsilon = 1^-$ wave, while the total intensity is again in quite good agreement. The same conclusions as for the $a_2(1320)$ are also true for the $M^\epsilon = 1^+$, $M^\epsilon = 1^-$ and $M = 1$ total intensities (figure 9.41).

From this study, it is concluded that it is well justified to assume that for $t' < 10^{-3}\,\mathrm{GeV}^2/c^2$, the intensities of $M^\epsilon = 1^-$ waves occur due to resolution effects only in the data, and should be added to the corresponding $M^\epsilon = 1^+$ waves if the amount of intensity matters. Even the relative amount of $M^\epsilon = 1^+$ and $M^\epsilon = 1^-$ intensities in the reconstructed MC reflect the relative amount seen in the data very well. In addition, it turned out that the fit with rank $N_r = 1$ and one free coherence parameter between $M^\epsilon = 0^+$ and $M^\epsilon = 1^+$waves only, seems to be the most reliable model for the purpose of the PWA of data featuring $t' < 10^{-3}\,\mathrm{GeV}^2/c^2$, as the rank $N_r = 2$ fit shows more instabilites.

---

[17] The intensity of the negative reflectivity in the MC truth fit can be presumably correlated to the fact, that the fit to the MC truth, that is presented here, was carried out with the usual cuts on the reconstructed values, and then corrected again for acceptance, which has been proven to introduce some uncertainties.

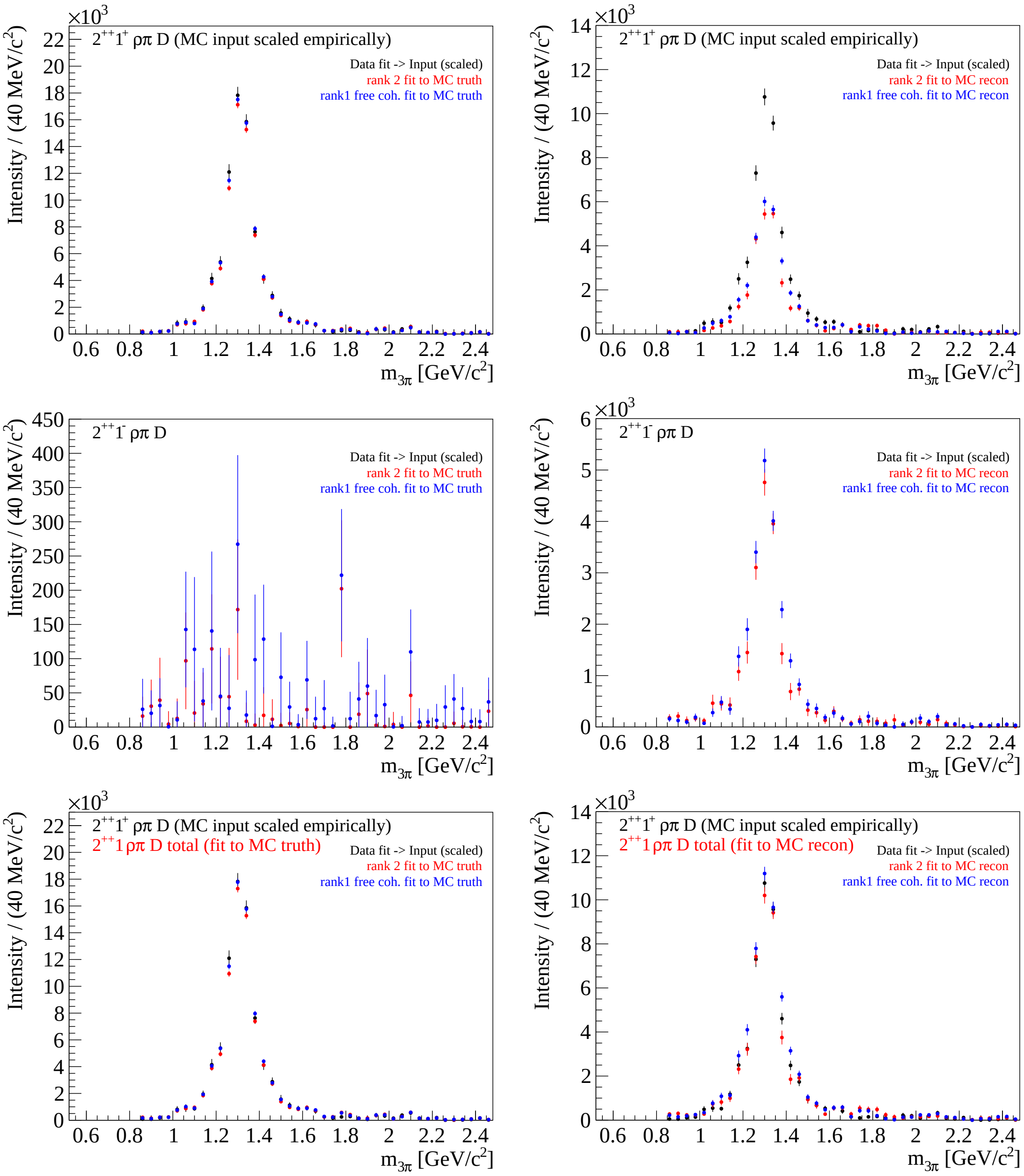

Figure 9.40: Intensities of $2^{++}\rho\pi D$ waves (referring to the $a_2(1320)$) fitted by positive reflectivity $M^{\epsilon} = 1^{+}$ (top row), negative reflectivity $M^{\epsilon} = 1^{-}$ (middle row) and the total intensity of both (bottom row) from PWA fits to the MC truth (left column) and the reconstructed MC events (right column), resp.

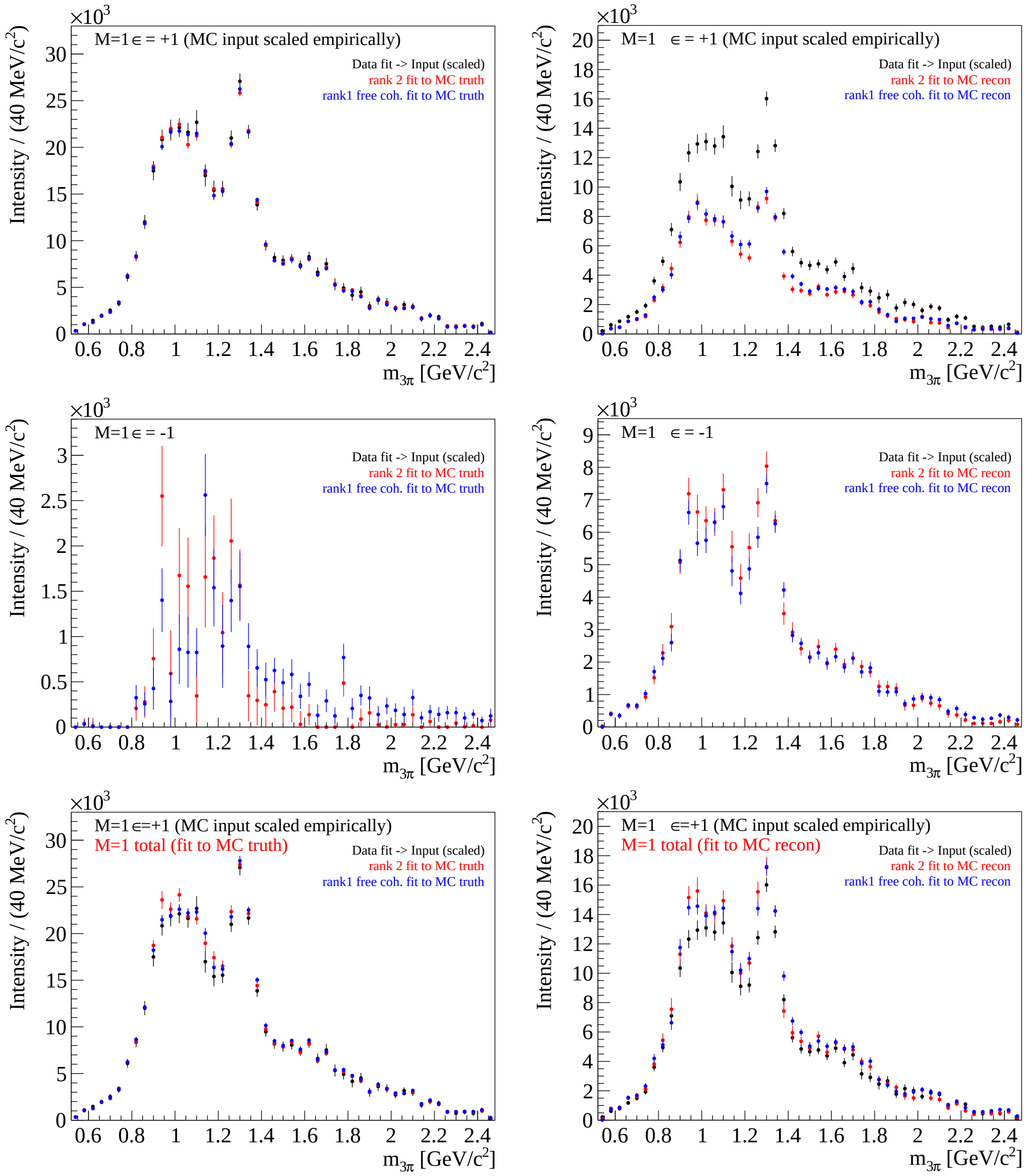

Figure 9.41: Total intensity of $M = 1$ waves fitted by positive reflectivity ($M^\epsilon = 1^+$) (top row), negative reflectivity ($M^\epsilon = 1^-$) (middle row) and the total intensity of both (bottom row) from PWA fits to the MC truth (left column) and the reconstructed MC events (right column), resp.

9.6 Total Cross-Section of the ChPT Prediction

The absolute cross-section σ_{abs} of a specific reaction is related to the number of events that are observed in the experiment via

$$\text{Number of reactions (events)} = \epsilon \cdot \int \mathcal{L}\mathrm{d}t \cdot \sigma_{abs} \tag{9.2}$$

with ϵ being the efficiency of the experiment to observe the reaction (i.e. the acceptance) and $\int \mathcal{L}\mathrm{d}t$ the integrated luminosity during the respective time of data taking.

This can also be used for specific kinematic variables, e.g. in this analysis for a particular bin in $m_{3\pi}$:

$$\text{Events}_{bin(m(3\pi))} = \epsilon_{bin(m(3\pi))} \cdot \int \mathcal{L}\mathrm{d}t \cdot \sigma_{abs} \; . \tag{9.3}$$

As the COMPASS 190 GeV/c π^- beam features a known fraction of K^- (and also $\bar{p}$, see section 2.2.1), the beam flux can be calculated from the number of K^- decays into $\pi^-\pi^-\pi^+$. If these kaon decay events are selected using the same criteria (i.e. especially the same trigger) as the events used in the respective analysis, the beam flux can be directly used as a scaling factor to determine cross-sections. This procedure implies that the acceptance of the kaon decays and the investigated final state must be equally well described in the simulation.

In this section the absolute cross-section for $\pi^-\gamma \to \pi^-\pi^-\pi^+$ is determined from the intensity of the ChPT amplitudes, obtained from a PWA fit to COMPASS data, and compared to the prediction of the leading-order calculations from ChPT.

9.6.1 Luminosity Determination from $K^- \to \pi^-\pi^-\pi^+$ Decays

The integrated beam flux can be calculated from the number of observed beam kaon decays $N(K^-\text{decays})$ in the following way (taken from [Nag08]):

$$\epsilon \cdot \int \Phi \mathrm{d}t = \frac{N(K^-\text{decays})}{(1 - e^{-s/\beta\gamma\tau}) \cdot BR \cdot \left(\frac{K^-}{\pi^- K^- \bar{p}}\right)} \; . \tag{9.4}$$

Here ϵ denotes the acceptance of beam kaons that decay into $\pi^-\pi^-\pi^+$ in a certain region of the spectrometer, which is obtained from a dedicated MC simulation. It has to be stressed that the selection of accepted events is performed in exactly the same way as the beam kaons are selected from real data, i.e. the same cuts are applied.

$\int \Phi \mathrm{d}t$ is the integrated beam flux, i.e. the value which is calculated and translated into the integrated luminosity.

The length of the kaon decay volume, s, and its position are chosen such, that a reasonable reconstruction efficiency can be expected from the detectors present in the regions concerned, and a reasonable amount of statistics is provided to work with it. These conditions are fulfilled in the COMPASS target region. $\beta\gamma\tau$ denotes the K^- decay length, which is 1429 m for kaons with 190 GeV/c momentum.

The branching ratio BR of $K^- \to \pi^+\pi^-\pi^-$ amounts to $(5.59 \pm 0.04\,\%)$ [PDG10].

The K^- fraction in the beam at the COMPASS target, $\frac{K^-}{\pi^- K^- \bar{p}}$, is 2.43 %, with an estimated relative uncertainty of 5% (calculated from [Ath80], see [Nag08]).

9.6.1.1 $K^- \to \pi^-\pi^-\pi^+$ from Real Data

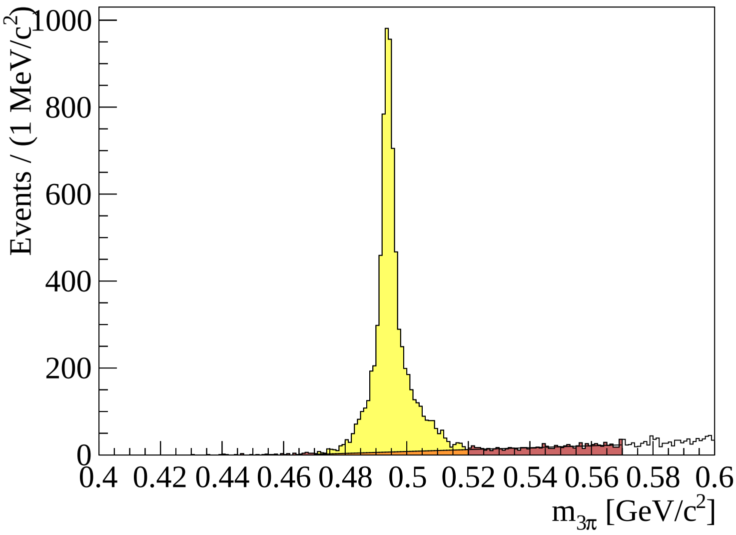

Figure 9.42: Invariant mass of reconstructed beam K^- from data.

The beam kaon decays that are used for the normalization are part of the $\pi^-\pi^-\pi^+$ data described in section 9.1, but are observed in a quite wide range of 80 cm along z around the lead target position. Kaon candidates are chosen by requiring the diffractive trigger condition, having a reconstructed primary vertex[18] with three correctly charged outgoing particles in $|z + 310\,\mathrm{cm}| < 40\,\mathrm{cm}$.

The usual exclusivity cut ($|E_{3\pi} - 189\,\mathrm{GeV}| < 4\,\mathrm{GeV}$) is applied, and decay candidates are selected by requiring $t' < 1.5 \cdot 10^{-3}\,\mathrm{GeV}^2/c^2$, taking into account resolution effects of the spectrometer. Figure 9.42 shows the distribution of the invariant 3π mass for the selection mentioned, including the wide vertex cut. One can clearly see a peak at $m_{3\pi} \approx 0.5\,\mathrm{GeV}/c^2$ indicating a clean kaon signal. The small background contribution below this peak is roughly estimated by a linear fit to the mass spectrum near the peak, which is

---

[18] As introduced in section 9.1, the lead targets are positioned around $z \approx -310\,\mathrm{cm}$. The region of decay vertices is limited by the multiplicity counter at $z = -247\,\mathrm{cm}$, which was a releveant part of the diffractive trigger, and the downstream silicon detector of the beam telescope at $z = -400\,\mathrm{cm}$, which needs to see the single particle (before it decays) for proper determination of the decay vertex. A window inside these maximum boundaries is chosen to ensure flat reconstruction efficiency (checked with MC).

then extended below the peak. After subtraction of this background contribution, 7530 beam kaons decaying into $\pi^-\pi^-\pi^+$ are obtained in the relevant spectrometer region.

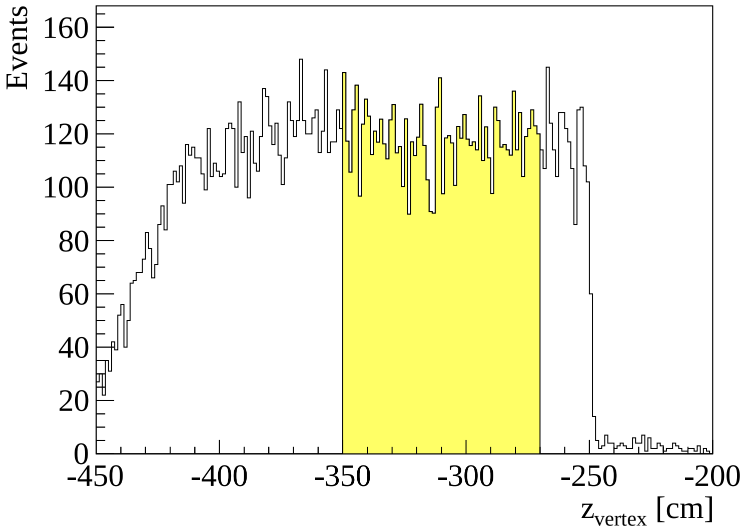

Figure 9.43: Reconstructed vertex positions of K^- decays from data.

The distribution of reconstructed kaon decay vertices, obtained by a cut of $|m_{3\pi} - 0.495\,\text{GeV}/c^2| < 0.025\,\text{GeV}/c^2$, is depicted in figure 9.43. The contribution of the small background in this mass region is obtained from the vertex distribution in the neighboring mass region, scaled accordingly, and subtracted statistically. The resulting distribution is quite flat, as expected, but shows a small drop in the region just upstream of the lead target. This can be explained by the distortion of the three pion tracks in the lead, adding some broadening to the decay vertex reconstruction, which only impacts decays upstream of the lead disks. The effect of the lead material to the mass resolution of the kaon is shown in figure 9.44. Kaons reconstructed upstream of the lead target feature a mass resolution which is about three times worse than for decays downstream of the lead. This leads to the broadening at the bottom of the overall mass spectrum[19] shown in figure 9.42.

The overall momentum transfer distribution of the reconstructed beam kaons is given in figure 9.45 (left). It is fitted with an exponential ($\mathrm{d}\sigma(t')/\mathrm{d}t' \propto \mathrm{e}^{-bt'}$) for $t' < 10^{-3}\,\text{GeV}^2/c^2$, which gives a slope paramter $b \approx 2900\,(\text{GeV}/c)^{-2}$. As in a decay process no momentum transfer to an external particle is involved, this number gives direct access to the resolution of the COMPASS spectrometer. It should be stressed, that the resolution in t' is significantly different for kaons decaying upstream and downstream of the lead target, leading to $b \approx 1800\,(\text{GeV}/c)^{-2}$ and $b \approx 4000\,(\text{GeV}/c)^{-2}$, respectively, for the two cases (see figure 9.45, left).

---

[19] These two components of the spectrum of the reconstructed kaon mass are taken into account in the kaon decay amplitude, see section 8.2.2.2.

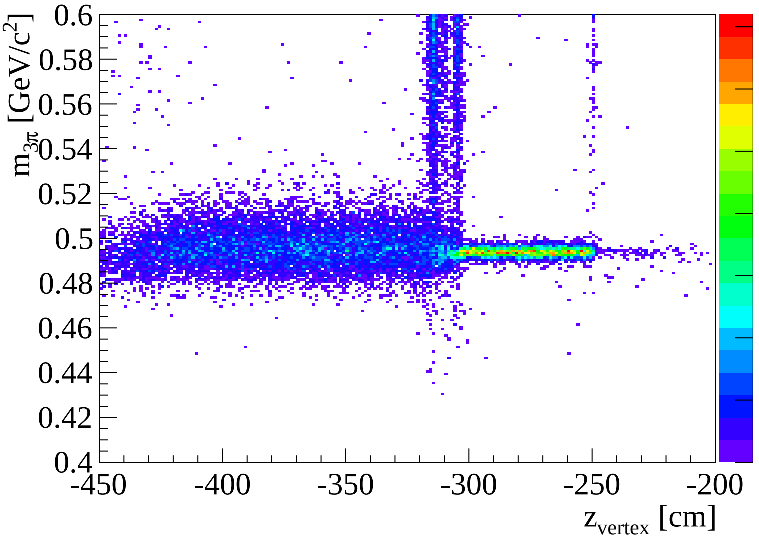

Figure 9.44: Mass resolution of reconstructed beam K^- before and after the lead target (at $z \approx -310\,\text{cm}$) from data.

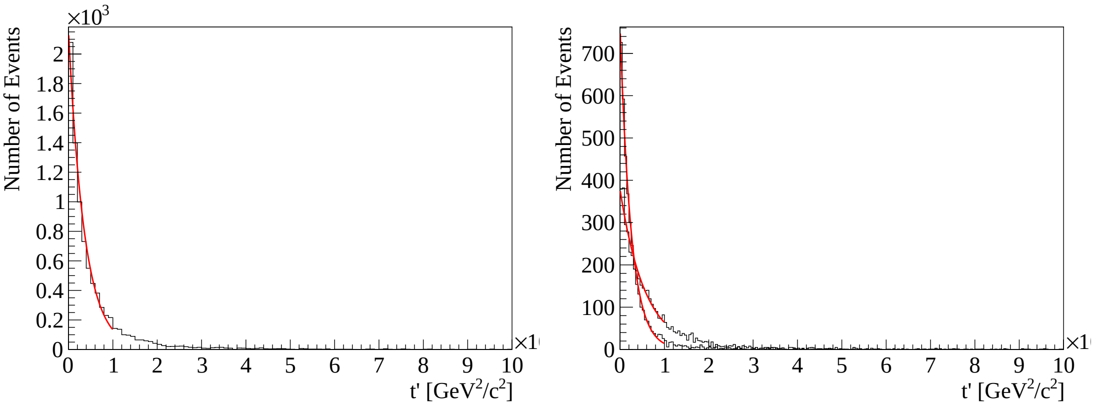

Figure 9.45: Momentum transfer t' of reconstructed beam kaons from data (left), separated between decays upstream and downstream of the target (right).

9.6.1.2 Simulation of $K^- \to \pi^-\pi^-\pi^+$

For the determination of the reconstruction efficiency of beam kaon decays in the COMPASS spectrometer, a dedicated simulation has been carried out. Kaon decays have been generated along the relevant region of the spectrometer, using the properties of the COMPASS beam as kinematic input in the lab system. The events have been passed through the standard MC chain (as described in section B.2) applying the usual acceptance criteria like the trigger and reconstruction requirements. Apart from these, the same cuts (exclusivity, t', position of reconstructed vertex) have been applied as for the determination of the number of kaons from the experimental data.

Figure 9.46 shows the distribution of both generated and reconstructed decay vertex po-

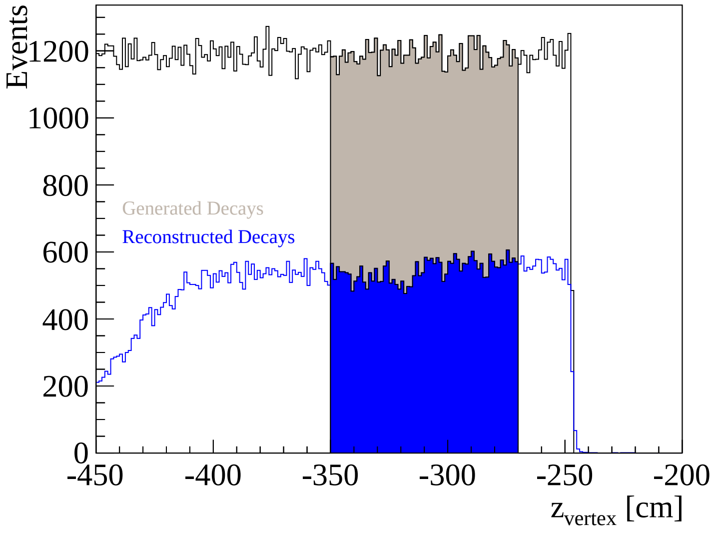

Figure 9.46: Generated and reconstructed vertices of K^- decays.

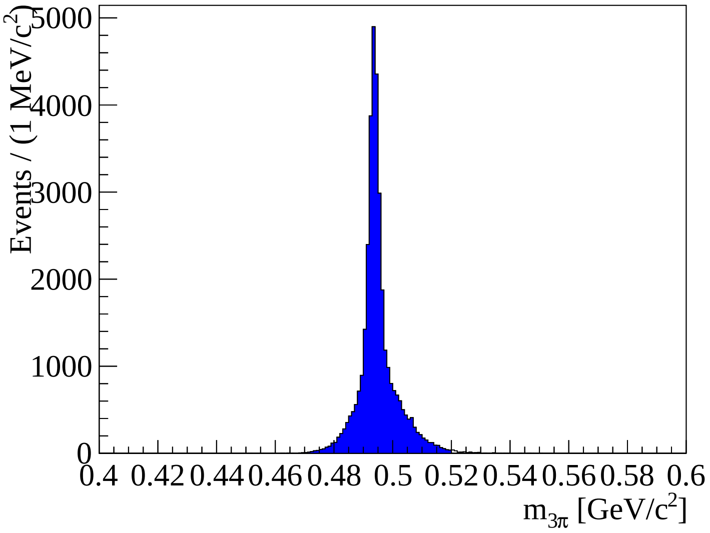

Figure 9.47: Invariant mass of reconstructed beam K^- from MC.

sitions (grey and blue, respectively). One can clearly see the same effect on the vertex reconstruction upstream of the lead disks as for real data (figure 9.43). Figure 9.47 shows the mass spectrum of the kaons itself, withouth a background from reactions in the lead target. The mass resolution (figure 9.48) is affected by the material of the lead disks in a comparable way as we observed in experimental data. Also the momentum transfer distribution (see figure 9.49) is equivalent to the one from real data, with the same difference in sharpness for kaons decaying upstream and downstream of the lead target.

The acceptance for kaon decays ϵ is given as the ratio of the number of reconstructed kaon decays (with all cuts applied) to the number of generated decays in the same spec-

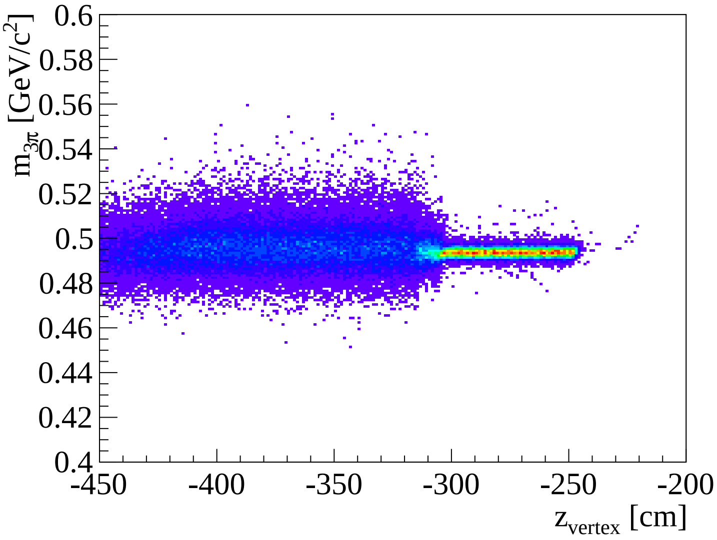

Figure 9.48: Mass resolution of reconstructed beam K^- before and after the lead target (at $z \approx -310\,\text{cm}$) from MC.

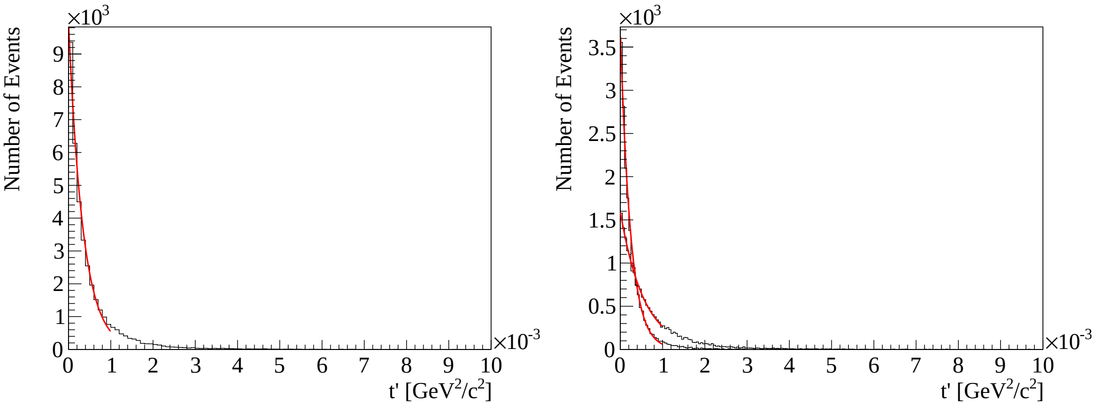

Figure 9.49: Momentum transfer t' of reconstructed beam kaons from MC (left), separated between decays upstream and downstream of the target (right).

trometer region $|z + 310\text{cm}| < 40\,\text{cm}$ as used for the real data analysis. Figure 9.46 shows that the reconstruction efficiency is quite flat in the selected region, so that this selection is reasonable for this purpose. With the cuts mentioned, an acceptance of $\epsilon \approx 45.9\%$ is obtained for the kaon decays.

9.6.1.3 Determination of Luminosity

With 7530 reconstructed decays of beam kaons into $\pi^-\pi^-\pi^+$ in our data set, an acceptance for these decays of $\epsilon \approx 45.9\%$, and the numbers given for the other components of equation (9.4), the beam flux amounts to $\int \Phi dt = 9.90 \cdot 10^9$ negative beam particles passing the COMPASS target region during the time range covered by our data, with an estimated relative uncertainty of 6 % (see table 9.3 for details; the statistical uncertainty is added quadratically to the other two uncertainties, which are summed linearly).

Contribution	Estimated Relative Uncertainty
K^- fraction	5 %
BR of $K^- \to \pi^+\pi^-\pi^-$	$< 1\,\%$
Number of K^- decays from data	$< 1\,\%$

Table 9.3: Contributions to systematic errors of luminosity determination

Taking into account the amount of target particles in a lead disk of 3 mm thickness ($9.9 \cdot 10^{21}$ lead nuclei / cm^2), the integrated luminosity is determinated to be

$$\int \mathcal{L}\mathrm{d}t = \int \Phi \mathrm{d}t \cdot \frac{\text{target particles}}{\text{area}} = 9.55 \cdot 10^4 \frac{\text{events}}{\text{mbarn}} \tag{9.5}$$

9.6.2 Total Cross-Section: Comparison of the Data to the ChPT Prediction

With equation (9.3) the cross-section of the reaction $\pi^-\gamma \to \pi^-\pi^-\pi^+$ near threshold obtained from a PWA fit of COMPASS data for $0.44\,\mathrm{GeV}/c^2 < m_{3\pi} < 0.72\,\mathrm{GeV}/c^2$ can be presented. As the data is integrated for $t' < 10^{-3}\,\mathrm{GeV}^2/c^2$, and need to be compared to the theory curve integrated over the same t' range, the migration of events in fact having $t' < 10^{-3}\,\mathrm{GeV}^2/c^2$ but being reconstructed in the range $t' > 10^{-3}\,\mathrm{GeV}^2/c^2$ has to be taken into account. This can also be learned from the MC simulation of Primakoff t' distributions presented in section 9.2.4. The effect is exemplarily shown for a selected $m_{3\pi}$ mass range in figure 9.50, that compares the simulated and the reconstruced t' distributions of reconstructed events, with the indicated range $t' < 10^{-3}\,\mathrm{GeV}^2/c^2$. One can see that a significant ratio (i.e. $\approx 20\,\%$) of events migrate, so that the data points have to be rescaled to recover this loss.

Figure 9.51 displays the incoherent sum of the two amplitudes calculated from the tree diagrams of ChPT (often referred to as "spin total of chiral amplitudes") converted into its cross-section (black data points, with the statistical errors from the PWA fit).

The systematic errors contributing to the cross-section are given as bands at the bottom of figure 9.51. The lower grey-green curve reflects the error from the luminosity determination (for details see table 9.3), while for the upper blue curve, which shows the full systematic error, the systematic error obtained from the differences due to different fitting models is added linearly. A potential contribution from the MC systematics is assumed to be negligible, as the MC samples for kaon decays and phase-space three-pion events at a comparable mass region are supposed to cover the same mechanisms (i.e. the same detectors in the setup) so that any systematic effects from $\epsilon_{bin(m(3\pi))}$ (see equation (9.3)) and ϵ (see equation (9.4)) practically cancel each other. In addition, the statistics of the MC samples are high enough (reconstructed statistics is 10 and 5, respectively, times

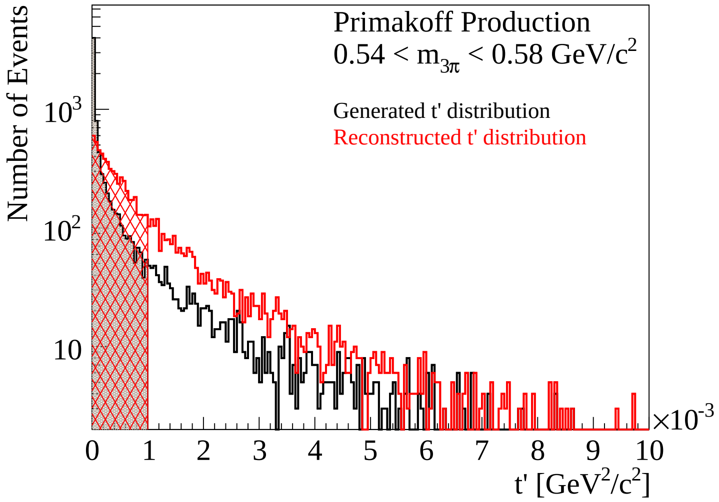

Figure 9.50: Illustration of event migration due to smeared t' distribution of reconstructed events.

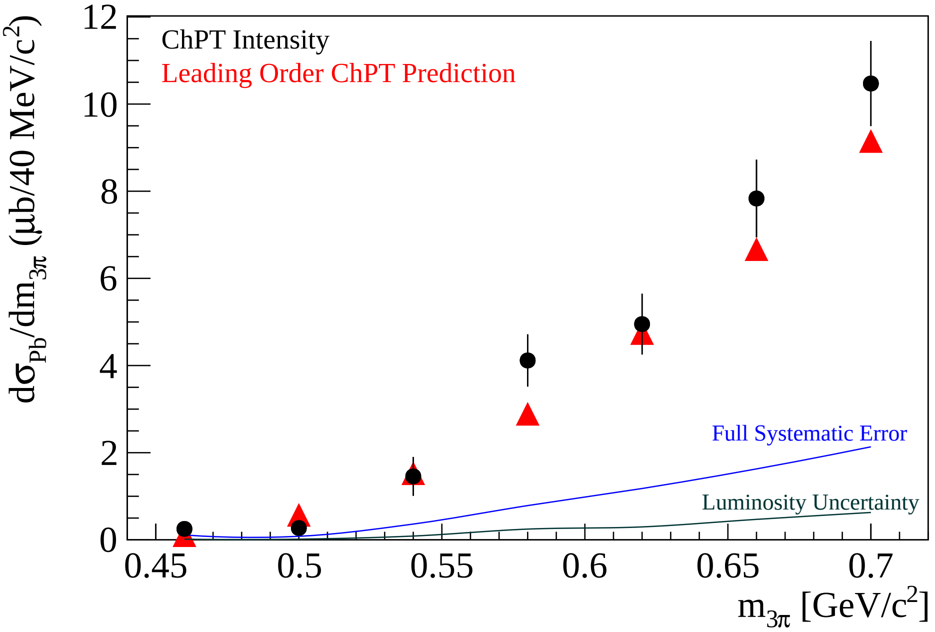

Figure 9.51: Measured absolute cross-section of $\pi^-\mathrm{Pb} \rightarrow \pi^-\pi^-\pi^+\mathrm{Pb}$ induced by photon exchange compared to ChPT prediction.

larger than the corresponding data sample) so that a contribution to the error from MC statistics is also negligible. The red triangles in figure 9.51 represent the corresponding cross-section from theoretical calculation (from [KF08], the theory curves in the plots are based on a numerical integration in a dedicated MC, provided by [Rya11]). Both the data points and the theory points present integrals over the three-pion mass within bins of $40\,\mathrm{MeV}/c^2$, and are centered at the given positions.

The absolute cross-section of the real photon scattering $\pi^-\gamma \to \pi^-\pi^-\pi^+$ is presented in figure 9.52. The measured points at the presented $m_{3\pi}$ have been obtained from the intensity in the respective bin by dividing out the quasi-real photon density factor as given by equation (7.12), and are attributed to the center of the bin. The data is in very good agreement with the tree-level ChPT prediction of the cross-section, in terms of the shape in $m_{3\pi}$ as well as the absolute values, on the level of the experimental precision of 20 %. This result constitutes the first measurement of the absolute cross-section $\pi^-\gamma \to \pi^-\pi^-\pi^+$ and is a confirmation of the theoretical calculations of ChPT.

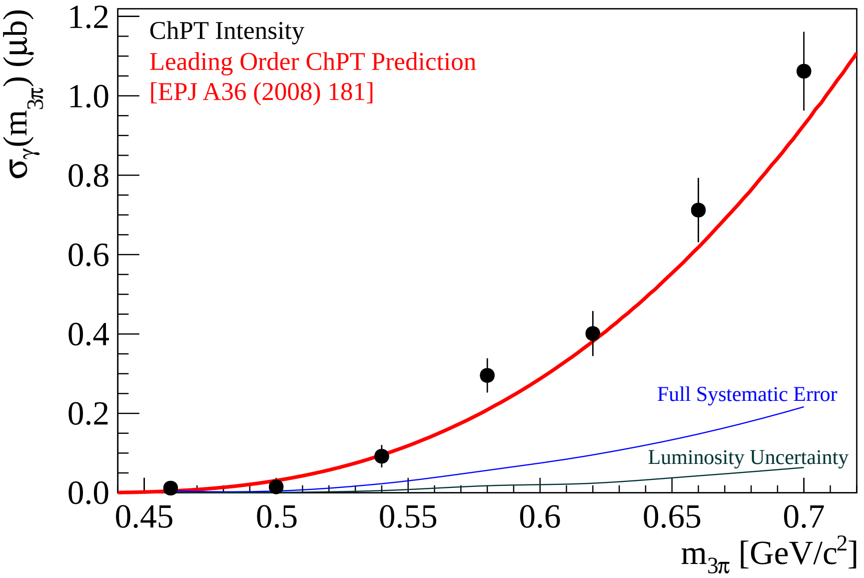

Figure 9.52: Measured absolute cross-section of $\pi^-\gamma \to \pi^-\pi^-\pi^+$ (from COMPASS π^-Pb $\to \pi^-\pi^-\pi^+$Pb data) compared to ChPT prediction, as published in [COM12a].

Chapter 10

Conclusions and Outlook

Two different topics have been worked on in the course of this thesis: The long-term cryogenic operation of the COMPASS silicon detectors has been established, and partial-wave analyses of $\pi^-\pi^-\pi^+$ events produced at lowest momentum transfer have been performed.

The development of the **cryogenic silicon detectors** had already been started in the beginning of the COMPASS experiment, when the operation at 130 K had been foreseen in order to increase the charge collection efficiency of irradiated detectors. This was triggered by the contemporary discovery of the Lazarus effect. The cooling of the COMPASS silicon detectors to cryogenic temperatures is achieved by the evaporation of liquid nitrogen in thin capillaries which are attached to the silicon detector modules close to the sensor. Various modifications have been applied to the detector module, mainly to compensate the different thermal expansion coefficients of the single components, and such to increase the mechanical stability when the modules are cooled. At the coldest part, the supporting PCB has been cut to a pad-like structure, which allows more local shrinking and prevents the accumulation of big forces that can break the silicon sensor. The capillary, which is soldered point by point to the created pads, is curled for the same reason, with the additional benefit of a more turbulant nitrogen flow that improves the heat transfer between the wall and the nitrogen. In addition, the material budget of the module has been minimized again by soldering cables directly instead of using a commercial connector, and substituting the connector's rigidity by a light carbon-fiber reinforced stabilization structure.

The detectors are now operated at 200 K, since the primary objectives of the cooling (lower noise and a better spatial stability) can be achieved already there. Subsequently, the previously problematic readout of the cold APV25 readout chips was found to have stabilized. Still, it could not yet be investigated if this is the result of their higher operating temperatures, or, more likely, connected to the better electronic contact of soldered cables compared to cold connectors. This requires further readout tests with detectors operated at 130 K. The detector performance can presumably also profit in addition from dedicated readout tests to optimize the APV settings for the cold readout.

The cryostats that house the silicon detectors were partly refurbished to better prevent vacuum connections with o-rings becoming cold, to increase the stability of the vacuum window, and to adapt to the changed dimensions of the electronics vacuum feedthrough connectors. A dedicated, conically shaped, cryostat for the spectrometer silicon stations has been designed and built, and also refurbished for liquid nitrogen cooling of the detectors it houses. A phase separator significantly improves the cooling stability by separating the gaseous from the liquid part of the nitrogen just before the liquid enters the capillaries to the detectors. Temperature fluctuations of less than 1 K could be reached for the detectors in the beam station cryostats.

The radiation impact to the COMPASS silicon detectors was re-estimated. Neither the previous warm nor the current cryogenic silicon detectors have been exposed yet to radiation in the order of magnitude, $10^{14}\,\mathrm{n_{eq}/cm^2}$, where the Lazarus effect becomes necessary to be exploited. Still, increased noise and leakage currents were observed for the warm detectors, becoming significant with an estimated radiation impact of about $5 \cdot 10^{12}\,\mathrm{n_{eq}/cm^2}$. Conclusions of the impact of the cryogenic operation to these observables cannot be drawn yet, as a comparable radiation impact is not yet reached. Nevertheless, the cryogenic operation of the silicon detectors leads to a better reconstruction performance. For the cryogenic detectors used in 2009, compared to the warm detectors used in 2004, the time resolution could be improved from $2.0 - 3.0$ ns to $1.4 - 1.8$ ns and the spatial resolution from $5 - 6\,\mu$m and $9 - 14\,\mu$m for two-strip and one-strip clusters, respectively, to $4 - 6\,\mu$m and $7 - 11\,\mu$m. This can be traced back to the faster signals of cold APV chips, and an improved charge sharing thanks to an enhancement of the signal-to-noise ratio of about 33 %, compared to warm operation.

A **partial-wave analysis** (PWA) was carried out for $\pi^-\pi^-\pi^+$ events at very low momentum transfer $t' < 10^{-3}\,\mathrm{GeV}/c$. The analyzed data set was recorded during the COMPASS hadron run 2004 with $190\,\mathrm{GeV}/c$ π^- beam on a lead target, and consists of one million events. Most of these events are produced by diffractive dissociation, but a significant part is also produced by Primakoff interaction, i.e. the exchange of a quasi-real photon with the high-Z target nucleus. The Primakoff contribution was extracted both by a simple statistical subtraction and by means of mass-independent PWA. The PWA in mass bins revealed the expected signatures of well-known resonances, i.e. the diffractively produced $a_1(1260)$ and $\pi_2(1670)$, and the Primakoff-produced $a_2(1320)$, but indicates also Primakoff production of $\pi_2(1670)$ for the first time. Significant intensities are also observed in $J^{PC} = 1^{++}$ and $J^{PC} = 1^{-+}$ amplitudes featuring spin-projection $M = 1$, i.e. presumably Primakoff-produced, at the mass range around $1.2\,\mathrm{GeV}/c^2$, but those seem to be related to non-resonant processes and not to indicate resonances.

Several Monte Carlo studies have been carried out to improve and approve assumptions made in the analysis. Those are related to resolution effects occuring in the experimental data due to the extremely small scattering and decay angles of the investigated final state. The presumably experimentally observed t' dependence of Primakoff produced final states was obtained from the simulation, as it could not be reliably extracted from the data. A basic leakage study showed, that the observed intensity in $M = 1$ amplitudes with negative reflectivity can be traced back to the limited resolution for the reconstruction of the ϕ_{TY} angle for the Primakoff events, and needs to be summed with the respective intensities with positive reflectivity to obtain the effective intensity.

Two new amplitudes have been successfully implemented for this PWA to improve the description of the data at low masses just above the three-pion threshold. A specific kaon amplitude describes the decay of beam kaons into the same final state, so that its application allows the extension of the analyzed mass range below $m_{3\pi} = 0.5\,\mathrm{GeV}/c^2$. A novel so-called "chiral amplitude", provided by the fully differential form of the tree-level calculations of $\pi\gamma \to 3\pi$ scattering in ChPT, substitutes now the previously-used six isobaric $M = 1$ amplitudes which were not motivated physically, but used empirically, in the mass range $m_{3\pi} \leq 0.72\,\mathrm{GeV}/c^2$. This substitution leads to the same total signal strength for $M = 1$ and a comparable likelihood as observed in PWA fits with the previously used amplitudes. The total intensity of the chiral amplitude in seven bins in $0.44\,\mathrm{GeV}/c^2 \leq m_{3\pi} \leq 0.72\,\mathrm{GeV}/c^2$, where the calculated cross-section does not change when pion-loop and ρ contributions are added, was then normalized to the target thickness and the effective luminosity, which is derived from the recorded free decays of beam kaons, $K^- \to \pi^-\pi^-\pi^+$. The absolute cross-section was found to be in good agreement with the ChPT prediction on the level of the experimental precision of 20 %.

Investigations of the behaviour of different ranges of t' or trends dependent on t', respectively, suggest that the interference of Primakoff and diffractive production of both $a_2(1320)$ and $\pi_2(1670)$ is apparent in the COMPASS data, and can be studied also quantitatively. Their relative strengths will also be important for the determination of the radiative widths of the $a_2(1320)$ and the $\pi_2(1670)$ from the relative strengths of Primakoff production in their absolute cross-sections. After the last remaining shortcomings in the simulation will be sorted out, the radiative widths of the $a_2(1320)$ and the $\pi_2(1670)$ will be extracted and published in the near future.

A mass-dependent PWA has still to be performed to finally confirm the indicated resonances and to extract their parameters. The technical aspects for the proper treatment of the unphysical $M^\epsilon = 1^-$ component caused by resolution need to be sorted out. The mass-dependent PWA will also be useful to make a solid statement about the (non-)-presence of a Primakoff-produced spin-exotic resonance.

A preliminary analysis with the extended chiral amplitude, taking into account also contributions from loops and explicit ρ and such providing presumably a more complete description for $m_{3\pi} \geq 0.72\,\mathrm{GeV}/c^2$, indicates already that indeed non-resonant processes are related to the observed strength in the $J^{PC} = 1^{++}$ and $J^{PC} = 1^{-+}$ intensities with $M = 1$.

The COMPASS 2009 data with lead target features about two times the statistics presented here and will be useful for more precise statements. In addition, ChPT calculations for the $\pi^-\pi^0\pi^0$ final state exist, where the cross-section changes significantly already for events with $m_{3\pi} \leq 0.72\,\mathrm{GeV}/c^2$ if loops are taken into accout. The analysis of this final state from the 2009 data will allow for a first confirmation of the tree and loop contributions to the measured absolute cross-section.

Appendix A

Technical Information related to the Silicon Detectors

The most relevant technical information concerning the COMPASS silicon detectors, collected in the course of this thesis, is summarized here. This concerns particularly the detector modules built in winter 2008 and winter 2009[1] for the cryogenic operation. Which detector modules were used when and where in the experiment for the beam times 2007 to 2012 is stated here, followed by detailed overviews of the properties of all assembled detetor modules.

A.1 Overviews of Detector Modules

A.1.1 Detector Modules in the Experiment

Beam Stations:

The warm beam stations already used before [Din10] have been kept for 2007, and due to delays in the commissioning of the new cryostats, also during the hadron run 2008.

In the course of changing over to liquid nitrogen cooling in the beginning of the hadron beam time 2009 all cryostats, i.e. all modules as well, have been successively exchanged with freshly assembled ones. This process was completed by the exchange of `SI01` on July 13th 2009.

Due to an incident in September 2009, making SI02X partly unusable, the detector module of `SI02XY` had to be exchanged before the 2010 beam time. This configuration was kept until at least 2012, see table A.1.

Conical Cryostat:

The conical cryostat has been equipped with newly produced detector modules, and was still operated warm in 2008.

---

[1] In the following, the *2008 production* refers to the production already initiated in November 2006 for the first prototype, but effectively started in October 2007 and completed in May 2008. The *2009 production* was carried out in the beginning of 2009.

		SI01		SI02		SI03	
		UV	XY	UV	XY	UV	XY
2007	muon	SIL 11	SIL 10	SIL 08	SIL 12	SIL 16	SIL 13
2008	hadron	SIL 11	SIL 10	SIL 08	SIL 12	SIL 16	SIL 13
2009	hadron	SI 2.02	SI 2.05	SI 1.04	SI 1.09	SI 2.03	SI 2.01
2010	muon	SI 2.02	SI 2.05	SI 1.04	SI 1.14	SI 2.03	SI 2.01
2011	muon	SI 2.02	SI 2.05	SI 1.04	SI 1.14	SI 2.03	SI 2.01
2012	hadron	SI 2.02	SI 2.05	SI 1.04	SI 1.14	SI 2.03	SI 2.01

Table A.1: Silicon modules installed in the beam telescope during the COMPASS beam times 2007 – 2012.

		SI04		SI05	
		UV	XY	UV	XY
2008	hadron	SI 1.13	SI 1.12	SI 1.11	SI 1.08
2009	hadron	SI 1.11	SI 1.08	SI 1.12	SI 1.13
2012	hadron	SI 1.11	SI 1.08	SI 1.12	SI 1.13

Table A.2: Silicon modules installed downstream of the target during the COMPASS hadron beam times 2008, 2009, and 2012.

During the rearrangement inside the conical cryostat due to the preparation of the liquid nitrogen cooling, the detector modules of `SI04` and `SI05` have been swapped before 2009.

During an incident in the commissioning phase in 2012 one APV chip of `SI05U`, half of `SI05V`, and half of `SI04X` were damaged. Nevertheless the detector modules concerned have not been exchanged due to the limited number of spare modules. The overview of all modules installed in the conical cryostat is given in table A.2. More details on single modules are given in table A.3.

A.1.2 Properties of Detector Modules Produced in 2008 and 2009

This section summarizes relevant information on all the detector modules produced in 2008 and 2009 at `HighTec`. Peculiarities of the two different productions, concerning both the material used and the work steps, are stated in the following. For each detector module, which properties or handling had an impact to the assembly of future detector modules, the story is also given. Everything noted down in the overview tables A.3 and A.4 is also available in the TUM-E18-silicon project space on nfs, and in the TUM-E18-silicon wiki (where it has potentially been updated, the status given here is dated from July 2012).

All modules feature the properties mentioned in section 4.1, i.e. a curled capillary, a cable directly soldered to the PCB, and the stabilization bridge (unless stated otherwise). The assembly of the single L-Boards (including the soldering of the capillary) was done at TUM. The assembly of the complete modules, i.e. the gluing of L-Boards and sensors, the gluing of APVs and pitch adapters, the gluing of the epoxy connectors, and the bonding, was carried out at `HighTec`. The finalizing steps, i.e. attaching the temperature sensors, HV capacitors, carbon-fiber bridges, and the soldering of the cables were done at TUM afterwards.

The modules from the 2008 production use sensors made by HLL (i.e. they feature intermediate strips also on the n-side). This production used 15 silicon sensors, with related modules `SI 1.00` to `SI 1.14` (see table A.3). The first two produced modules still had ERNI connectors. The L-Boards used for the modules of this production were equipped with additional unneccessary capacitors by mistake[2]. These capacitors caused higher noise, especially at the centers but also on the borders of the single APV chips. This is depicted in figure A.1, comparing the common-mode corrected noise of both readout sides of module `SI 1.14`, with and without these capacitors, in the lab. Particularly the 8chip-side shows a noise level of more than four ADC channels at some neighbouring channels[3], which can cause inefficiencies, as four-sigma cuts are applied to the data, but cluster amplitudes, which might be divided unevenly between two readout strips, only feature around 50 ADC channels. The unneccessary capacitors were identified as the source of this problem only quite late in 2009, so that they were removed only after the 2009 beam time.

At three modules (`SI 1.03` to `SI 1.05`), the APVs had been glued with a wrong conduction glue, which was not suitable for cryogenic temperatures and cracked, so that the APVs partly lifted off after cooling, and were fixed by silicone glue afterwards (modules affected are marked with "G"). These modules were suspected to show higher noise, as

---

[2] These capacitors had been optionally foreseen in the original design of the PCBs, i.e. alternatively to a set of resistors, to filter noise on the ground lines. This option was never used, but the corresponding soldering pads were not removed from the PCBs [Kon12].

[3] The high noise at chip 10 of the 10-side and chip 1 of the 8-side are related to shorter readout strips to which a part of the channels of the affected APVs are connected to. This causes problems for the current common-mode correction algorithm, and is a feature of all silicon detector modules operated in the COMPASS experiment.

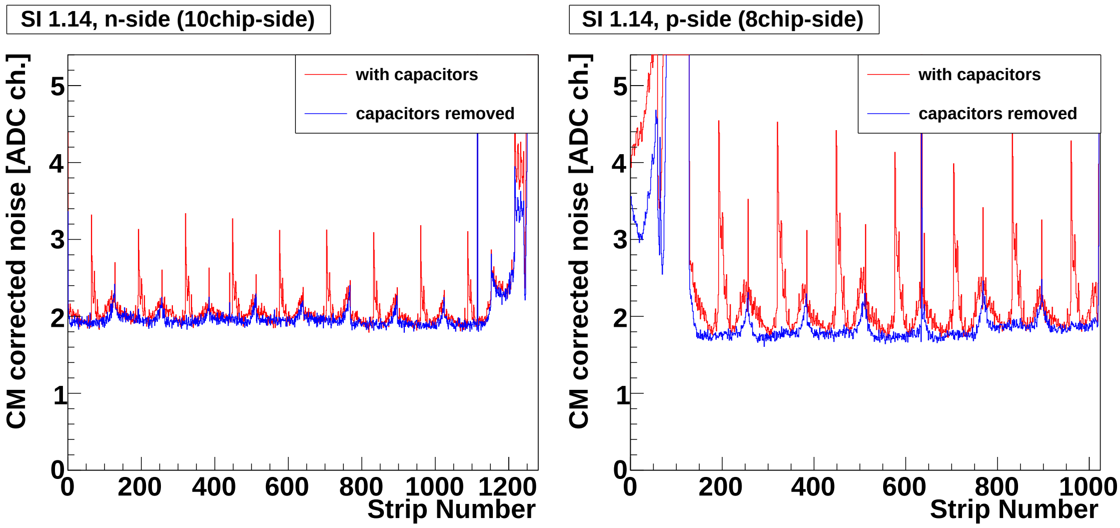

Figure A.1: Common-mode corrected noise for the 10chip-side (left) and the 8chip-side (right) of the detector module `SI 1.14`, with and without the unneccessary capacitors, with a bias voltage of 130 V in the lab. The improvement after the removal of these capacitors is obvious especially for the 8chip-side. The high noise at chip 10 of the 10-side and chip 1 of the 8-side is related to the shorter readout strips a part of these channels are connected to, and their treatment in the common-mode correction algorithm, and thus present for all silicon detector modules operated in the COMPASS experiment.

the grounding of the APV chips was expected to be worse. This is obviously not the case for `SI 1.04` which is the only one of the three modules concerned that is used in the experiment. Still, its chip 5 at the 10chip-side shows instabilites of the baseline when cooled: The chip seems to stay warm after cooling down, and to become cold only within about two days. This makes a regular adjustment of the VPSP setting necessary to stay within the dynamic range of the ADC (see section 4.6) and obtain reasonable data from this chip.

The sensor of the first detector module without ERNI connector, i.e. `SI 1.03`, cracked during one of the first cooling attempts. This incident was later explained by mechanical stress to the sensor, as the previously underestimated stability induced by the ERNI connector was missing now, and the module was additionally squeezed by the screws fixing it to the shuriken. This triggered the development of the stabilization bridge made from carbon-fiber reinforced plastic, which was glued to all successive detector modules just next to the cables, as depicted in section 4.1.

Module `SI 1.07` was delivered with a blocked capillary. The removal and regluing of the epoxy connector solved this blockage. But the sensor cracked in the next cooling attempt already at 180 K. This was later traced back to a glue connection between the capillary and the L-Board introduced during the repair, causing the PCB to become much colder in this corner than usually, and such to bend. Thus, obvious explanations for the cracked sensors of both `SI 1.03` and `SI 1.07` exist, which are not related to the general design, but to particular problems of these two modules. Still, the spare detector situation became critical when the second of these two detectors was lost, so that it was decided to cool the detectors to only 200 K as a precaution measure.

Some of the modules, which had cracked before for other reasons, were destroyed in an indicent with an imploding window of the conical cryostat during the commissioning phase beginning of the 2008 beam time (marked with "CC").

The four modules in the conical cryostat were exposed to incidents with presumably bias voltage discharges[4] during the commissioning phase in 2012. Consequently, the APV chip 9 of `SI05U` (10chip-side of module `SI 1.11`) dose not deliver data any more. Half of the plane `SI05V` (8chip-side of module `SI 1.11`) shows a significantly higher noise, so that the threshold (the multiplicity of the noise value) needed to be lowered to not loose too much signals. Half of the plane `SI04X` (10chip-side of module `SI 1.12`) does not show any amplification, i.e. no noise but also no reasonable signals.

The modules from the 2009 production use sensors obtained from SINTEF. As their quality was not guaranteed and unknown, the sensors have been tested for leakage current development at room temperature, before the best ones were delivered to `H`ighTec. Also the L-Boards have been equipped with APVs and tested before the sensors were glued to them, to avoid problems as present at `SI 1.10`. Seven modules were fully assembled and named `SI 2.01` to `SI 2.07`, and two modules only partly, i.e. the finalizing steps to be done in Munich are still missing. Despite the leakage current measurements of the sensors before assembly some of the new detectors show high noise at parts only, so that they are not suitable for being used in the experiment (see table A.4). The noise and readout tests of the two detector modules without cables have been carried out with the clamping support that had been used for the L-Board tests at `HighTec` as well, so that only one readout side could be tested at the same time.

---

[4] Sudden application (or discharges) of the bias voltage to the detectors, that caused high currents over the silicon bulk and the bonds, are the currently most probable explanation for the observed damages. Those are supposed to be prevented by a HV capacitor combined with a 10 kΩ resistor, placed outside of the cryostat, for each bias voltage. Before the 2012 run, new connecting cables were manufactured. Those were found to have unreliable contacts later, so that the connection between a charged capacitor and the silicion detector could happen suddenly inside the circuit. The cryostat could not be opened yet for an inspection of the affected modules, but a destruction of relevant bonds seems to be the most reasonable explanation for the observed effects.

ID	Location	Comments	Marks
SI 1.00	-	used as a bonding / gluing sample at `HighTec`	
SI 1.01	-	first prototype, due to unaligned capillaries the wafer was broken during the attachement of the epoxy connector	CC
SI 1.02	MUC	first prototype, still with ERNI connectors, extensively tested in the lab, tests in COMPASS beam in november 2007, many noisy channels on 10-side	
SI 1.03	MUC	sensor broken in the cooling incident, which triggered the implementation of the stabilization bridge; only 10-side with cable	G
SI 1.04	CERN	baseline of APV chip 5 at 10-side instable (needs regular adjustment of VPSP setting)	G
SI 1.05	CERN	after the first cooling the wafer corner under the silicone-glued Pt100 shows irragularity (probably a crack). HV can still be applied, but with high leakage current ($\approx 50\,\mu A$)	G
SI 1.06	CERN	APV chip 2 at 8-side is not LOADable and shows synchronization problems (i.e. lower half of detector is missing with old ADC firmware)	
SI 1.07	-	sensor broke when cooling (after exchange of epoxy connector, glue connection to PCB → cold bridge)	CC
SI 1.08	CERN		
SI 1.09	CERN	chip 1 (0x21) at 10-side burned in incident in fall 2009, i.e. right half of detector not synchronized	
SI 1.10	CERN	chip 6 at 10-side: shortcut on PCB	
SI 1.11	CERN	chip 9 at 10-side does not deliver data any more, and the second half of the 8-side has significantly higher noise, since an indicent in May 2012	
SI 1.12	CERN	second half of the 10-side does not show any amplification since an incident in May 2012	
SI 1.13	CERN	-	
SI 1.14	CERN	APV chip 10 at 10-side has to be addressed as 0x37 (instead of 0x33)	

Table A.3: Detector modules from 2008 production. The IDs of the modules that have been used in the experiment are given in bold letters.

ID	Location	Sensor (leakage current)	Comments
SI 2.01	CERN	Sensor 12 (1.5 µA @ 100 V, 10 µA @ 112 V	chip 7 at 10-side needs adjustment of VPSP settings after cooling down
SI 2.02	CERN	Sensor 38 (0.3 µA @ 100 V, 10 µA @ 230 V)	
SI 2.03	CERN	Sensor 115 (1.0 µA @ 100 V, 10 µA @ 200 V)	
SI 2.04	MUC	Sensor 13 (3.5 µA @ 100 V, 10 µA @ 130 V)	develops extremely high noise at chip 5 (8-side) and chip 9 (10-side) when HV is increased above 60 V
SI 2.05	CERN	Sensor 94 (1.6 µA @ 100 V, 10 µA @ 210 V)	
SI 2.06	CERN	Sensor 17 (1 µA @ 100 V, 10 µA @ 155 V)	develops high noise in the middle of planes when HV is increase above 73 V
SI 2.07	CERN	Sensor 93 (2.0 µA @ 100 V, 10 µA @ 145 V)	T-Sensor, HV capacitor and stabilization bridges still missing. According to the `wiki`, it develops noise on two channels at the edge when HV is on - should be checked again!
-	MUC	Sensor 57 (3.5 µA @ 100 V, 10 µA @ 135 V) Sensor has similar leakage current as sensor 13 in module SI 2.04, thus supposed to be not usable.	Cables are not soldered yet. T-sensors, HV capacitor and stabilization bridges still missing. Tests showed some increased noise in the central chips at 96 V, which disappered at 108 V again.
-	MUC	Sensor 88 (10 µA @ 100 V) Sensor supposed to be a "bad quality" sensor.	Cables are not soldered yet. T-sensors, HV capacitor and stabilization bridges still missing. Test showed the development of high noise already at 27 V; no higher bias voltage has been applied.
-	HighTec	Sensor 99 (0.3 µA @ 100 V, 10 µA @ 250 V)	was a good spare sensor, not assembled to a module (yet)

Table A.4: Detector modules from 2009 production. The IDs of the modules that have been used in the experiment are given in bold letters.

Appendix B

Technical Information related to the Data Analysis

B.1 Analysis of the Experimental Data

The presented data has been processed with the CORAL version with the CVS tag `hprod_nov05_1` in winter 2005/2006 centrally at CERN. The following data analysis was carried out with PHAST version 7.062.

The employed PWA program is called *compassPWA* and based on the Ascoli fitter. The program is maintained by Dmitri Ryabchikov and available in the SVN repository located at `/nfs/hicran/project/compass/sw/PWA/repository/compassPWA`. For the mainstream fits presented in this thesis, revision 270 was employed. For the studies with the extended ChPT amplitude, revision 292 was used.

B.2 Monte Carlo Simulations

The **event generation** was carried out with the phase-space event generator which is provided by the PWA program. The input to the simulation based on kinematical distributions from the experimental data is summarized in section 9.2.1. The events used for the acceptance corrections (see section 9.2.2) and the t' resolution studies (see section 9.2.4) were generated with revision 264. The kaon decay events used for the flux determination (see section 9.6.1.2) were generated with revision 270, using a dedicated feature for the proper generation of this decay according to the kaon decay Dalitz plot.

The generated events were processed partly with **COMGEANT** 7.03.10, partly with COMGEANT revision 167. In both cases the geometry of the 2004 hadron setup (taking into account the best current knowledge of the setup) was used, that can be found in the official COMGEANT repository starting with revision 167. Compared to the geometry that had been used to obtain the MC samples for the acceptance corrections of previous PWAs of 2004 data [Wei08a], the following improvements have been introduced (see also chapter C):

- Significant correction of size and position of the downstream Sandwich veto detector
- Correction of the RICH beam pipe material (steel)
- Addition of material around the spectrometer silicon detectors
- Fine tuning of target positions

The simulated events were reconstructed with the **CORAL** version that was used for the production of the real data (CVS tag: `hprod_nov05_1`) including some minor compilation fixes. The dictionary file has been created with the following grid parameters (taken from [Wei08b]):

- 12 -120 120 ! x
- 6 -120 120 ! y
- 15 -1.5 1.5 ! 1/p
- 18 -0.30 0.30 ! tanx
- 12 -0.30 0.30 ! tany

The resulting mDSTs were analyzed with PHAST version 7.106, with an equivalent user code like the one that was used for the real data analysis.

Appendix C

Improvements of the Simulation

One important input to the judgement of the quality of a PWA fit and the applied model is the comparison between the data and "weighted Monte Carlo" (see section 8.7). For this purpose, kinematical distributions like the position of reconstructed vertices (see section 9.2.3), momentum distributions of the outgoing particles, and the invariant mass distributions of the 2π subsystems are checked, as well as the distributions of $\cos\theta$ and ϕ_{TY} of the two-body decays. This approach relies on a solid description of the spectrometer in the simulation, as it evaluates the fitting model and the acceptance correction at the same time. On the other hand, a PWA fit is even able to "accomodate" to a bad description of the setup by adapting the fit such that it matches the acceptance, which distorts the fit result.

In the course of this work, several shortcomings of the material description of the spectrometer in COMGEANT and the simulation of the trigger have been identified. An exhaustive overview of weighted-MC plots has been checked repeatedly for the presented PWA fits, and finally found to be in good agreement. Instead of a full collection of these, a selection of plots is presented in the following, that stresses the effects achieved by the improvement of the MC description. These plots have been collected during the workflow, thus they cover also data with higher t' than those presented in the analysis part. In particular, several effects have also been found for the high-t' data, i.e. covering $0.1\,\mathrm{GeV}^2/c^2 < t' < 1.0\,\mathrm{GeV}^2/c^2$.

C.1 Improvements of Variables in the Laboratory System

Several quantities are selected in the following, that show clear effects in the laboratory system. The plots are shown for different conditions to achieve a clear depiction of the "best effect". They partly show the pure phase space MC, and partly the weighted MC, compared to data. The effects of the corrected position of the Sandwich veto detector, the corrected material of the rich beam pipe, and the proper use of the beam killer information are presented.

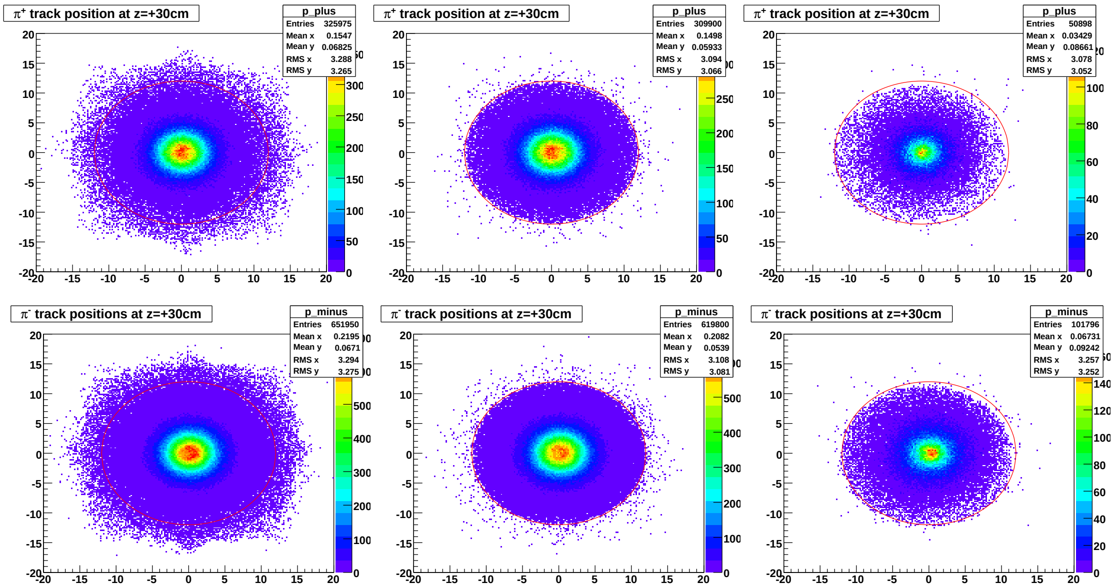

Figure C.1: Positions of tracks in lab system for the previous MC, the MC with a corrected SW position, and the data.

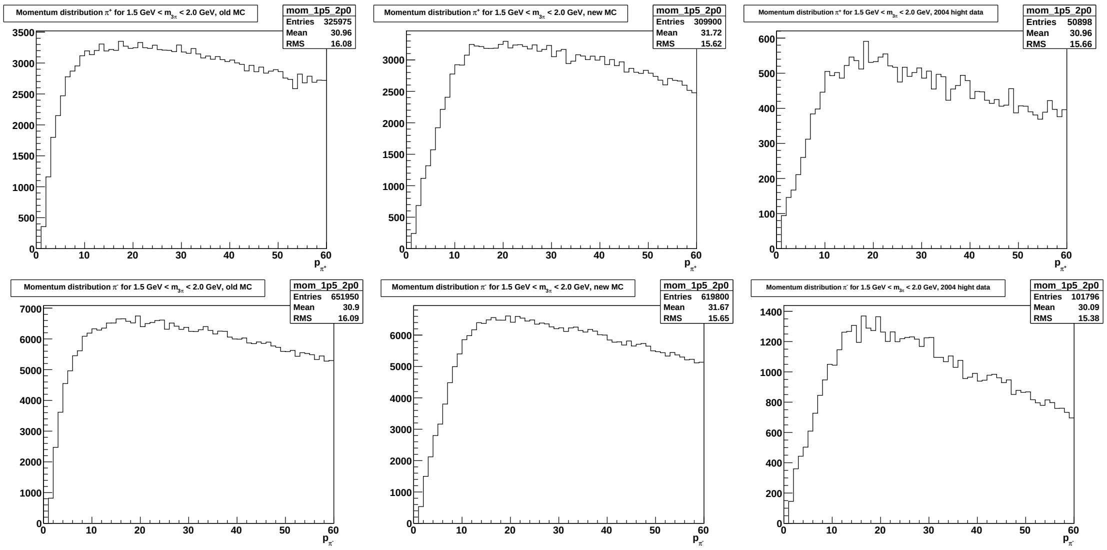

Figure C.2: Momenta of tracks in lab system for the previous MC, the MC with a corrected SW position, and the data.

C.1.1 Sandwich Veto Position

In the previous MC description, the second SW veto had been positioned at $z = -208\,\text{cm}$, just downstream of the other SW. In an improved version, that was indicated by photos of the target region and achieved by comparison to the data, this detector was placed at $z = 30\,\text{cm}$. In addition, it is centered at $x = 0$ and $y = 0$, so that the final position had also to be obtained from data. The improvement is prominent already in the comparison of the data with phase-space MC. Figure C.1 presents the positions of tracks in the lab system, i.e. at $z = 30\,\text{cm}$, for high-t' data and MC, and masses $1.5\,\text{GeV}/c^2 < m_{3\pi} < 2.0\,\text{GeV}/c^2$. Figure C.2 presents the corresponding momenta distributions. In both figures, the left colums shows the previous MC, the center column the MC with the SW at $z = 30\,\text{cm}$ but centered at $x = 0$ and $y = 0$, and the right column the data. The top and bottom row distinguish between the positive and the negative outgoing pions, respectively. The red circle features a diameter of 24 cm, that represent the hole in the detector, i.e. outside which particles are expected to be rejected. The description of the acceptances of masses above $m_{3\pi} = 1.5\,\text{GeV}/c^2$ and low momentum tracks has been improved significantly.

In the MC processing just the material of the SW was present, but active vetoing was not simulated. The experimental distributions are well reproduced, though, which indicate that the veto featured inefficiencies or was not actively participating in the trigger. Thus it was decided to apply geometrical cuts on the track positions on both the data and the MC used for the acceptance corrections.

In the final geometry version, that was settled after a cross-checked with a manual drawing eventually found in the documents of the technical coordinator [Gey11], the SW veto is implemented with a hole with 29 cm diameter at $z = 92\,\text{cm}$, which covers the same angular acceptance as the setup in the presented comparison.

C.1.2 Rich Beam Pipe Material

The material of the Rich beam pipe, which separates the radiator gas from the beam pipe filled with helium (see section 2.2.2.3), was stated to be made of aluminum in the previous MC, while it was in fact made of stainless steel. This pipe is present in the spectrometer in the region of $z \approx 750\,\text{cm}$ and has a diameter of 10 cm. Figure C.3 presents the effect on the slow negatively charged pions, where the data shows a decreased reconstruction efficiency for pion tracks passing this z position at a radial distance of 5 cm. The MC shows that this effect was visibly underestimated in the description with aluminum (left bottom), but seems more correct after the change of the material description (right bottom, compared to the data shown in the top plot).

C.1.3 Beam Killer Information

An important topic was the beam killer information to be taken into account in the trigger decision. This was previously not simulated, so that events with a forward outgoing

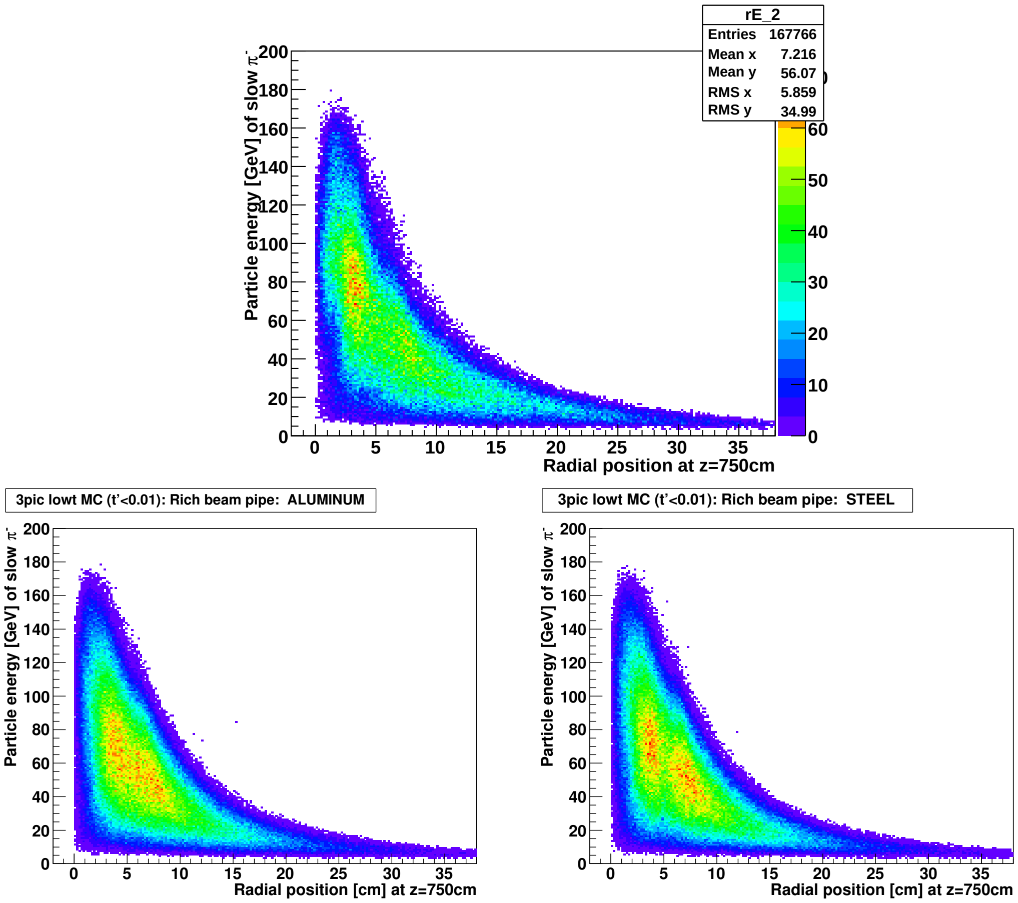

Figure C.3: Effect of the Rich beam pipe material: Data (top) compared to a MC description with aluminum (bottom left) and the improved description with stainless steel (bottom right).

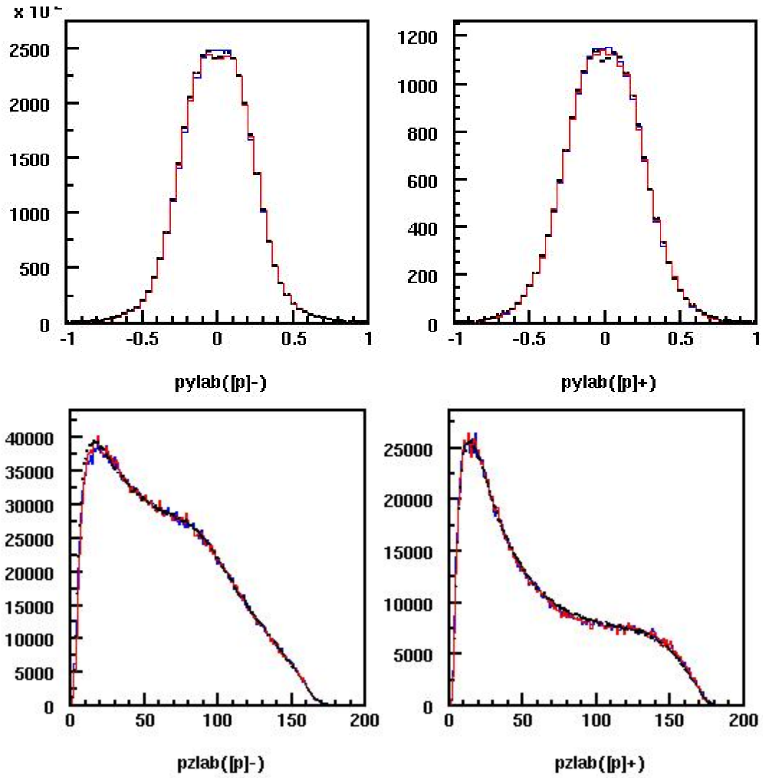

Figure C.4: Momenta in y (top) and z (bottom) direction in laboratory system, for π^- (left) and π^+ (right). Data (black) is compared to weighted MC for low t', without (blue) and with (red) including the beam killer information.

pion, that hit at least two of the beam killer scintillators, were not properly rejected. This was visible in the comparison of the momentum distributions in the laboratory system, as depicted in figure C.4. In the top row, the momentum distributions in y direction, and in the bottom row in z direction, are compared between the data (black) and weighted MC (blue for the previous simulation, red including the beam killer information), for negative pions in the left and positive pions in the right column. In the data, a dip at p_y is visible for both charges, which was not at all described in the previous description, and is in a large part present now. Still the data is not described in the optimal way. As this dip was found to affect mainly low masses, this issue has to be better clarified before an absolute cross-section of particles at $m_{3\pi} > 1.2\,\mathrm{GeV}/c^2$ can be carried out with the kaon ($m_{3\pi} = m_K \approx 0.5\,\mathrm{GeV}/c^2$) normalization. There are first hints that the corrected description of the dead zone of a large area tracking detector (found by [Nag12]) might improve this, but further detailed studies are needed for the final clarification.

C.2 Improvements of Angular Distributions

The most important check of a fitting model is related to the description of the angular distributions. However, the PWA accomodates its result to a bad description of the setup,

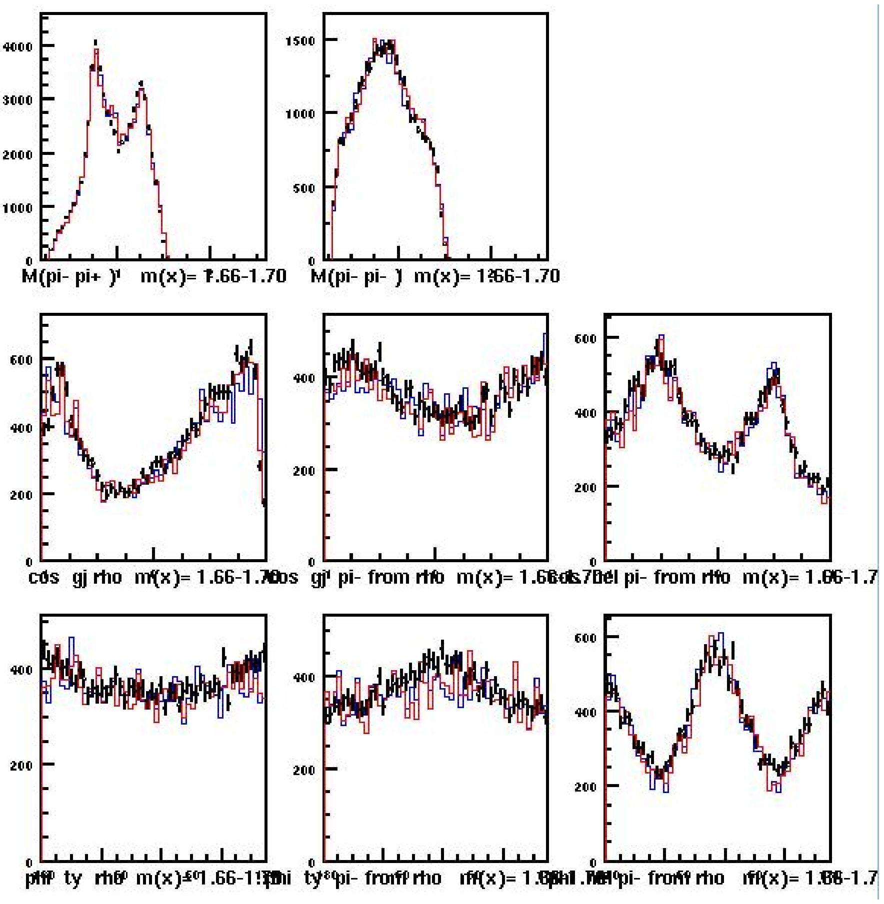

Figure C.5: Comparison of the angular distributions for $m_{3\pi} \approx 1.6\,\mathrm{GeV}/c^2$ at low t': Data (black) is compared to weighted MC for "low t'", with the previous (blue) and the updated (red) SW veto position. The improvement for $\cos\theta_{\mathrm{GJ}} = 1$ is apparent.

so that only minor effects in these angular distributions have been observed. Most effect is seen for the masses around $m_{3\pi} \approx 1.6\,\mathrm{GeV}/c^2$, where a sharp dip at $\cos\theta = 1$ could not be reproduced by the fits using the previous acceptance corrections. This dip could be traced back to the wrong positon of the SW veto. The effect is exemplarily depicted in figure C.5, which covers the mass range $1.66\,\mathrm{GeV}/c^2 < m_{3\pi} < 1.70\,\mathrm{GeV}/c^2$ for low t'. In all plots, the data points are black, the weighted MC from the previous simulation is blue, and the weighted MC for the improved simulation is plotted in red. The upper row shows the invariant masses of the $\pi^-\pi^+$ and the $\pi^-\pi^-$ subsystems, respectively. The other six plots show angular distributions, i.e. $\cos\theta_{\mathrm{GJ}}$ of the isobar in the GJF, $\cos\theta_{\mathrm{GJ}}$ for the pion from the isobar decay, and $\cos\theta_{\mathrm{hel}}$ for the pion from the isobar decay in the helicity frame in the middle row. The bottom row shows ϕ_{TY} accordingly. The improved descripton at $\cos\theta_{\mathrm{GJ}} = 1$ of the isobar in the GJF (left plot in the middle row) is obvious, and complements now the good agreement of the other quantities between data and weighted MC.

C.3 Comparison of Overall Acceptance Effects

The overall acceptance is compared for the previous and the improved MC description in the following for both low t' (figure C.6) and hight t' data (figure C.7). For both t' ranges, the acceptance with $m_{3\pi}$, and the acceptance for $\cos\theta_{\mathrm{GJ}}$ and ϕ_{TY} (with a cut on $0.8\,\mathrm{GeV}/c^2 < m_{3\pi} < 2.0\,\mathrm{GeV}/c^2$) are given, equivalently as in section 9.2.2. The sandwich veto detector, now at the correct position in the MC, cuts into the acceptance for masses above $m_{3\pi} > 1.5\,\mathrm{GeV}/c^2$ in a similar way for both ranges of t'. The angular distributions are affected by a consistent overall drop.

C.4 Comparison of Selected Fit Results

The effect of the improved acceptance description to PWA is depicted exemplarily for few selected intensities. Figure C.8 presents the result of three total intensities, namely $J^{PC}M^{\epsilon} = 1^{++}0^{+}$, $J^{PC}M^{\epsilon} = 1^{++}1^{+}$, and $J^{PC}M^{\epsilon} = 2^{-+}0^{+}$ for a PWA fit to the low t' data. Figure C.9 shows the $M = 0$ and $M = 1$ total intensities for a fit to high t' data. The black points are the results obtained with the previous acceptance corrections, and the red points with the improved acceptance corrections. As expected, the acceptance corrections influence the mass range $m_{3\pi} > 1.5\,\mathrm{GeV}/c^2$, where the losses in the SW veto are now corrected for. The corrections are much more pronouced for $M = 0$ amplitudes than for $M = 1$ amplitudes, which can be related to the decay particles of $M = 1$ states going much more foreward, so that they hit the SW veto only rarely [Rya11].

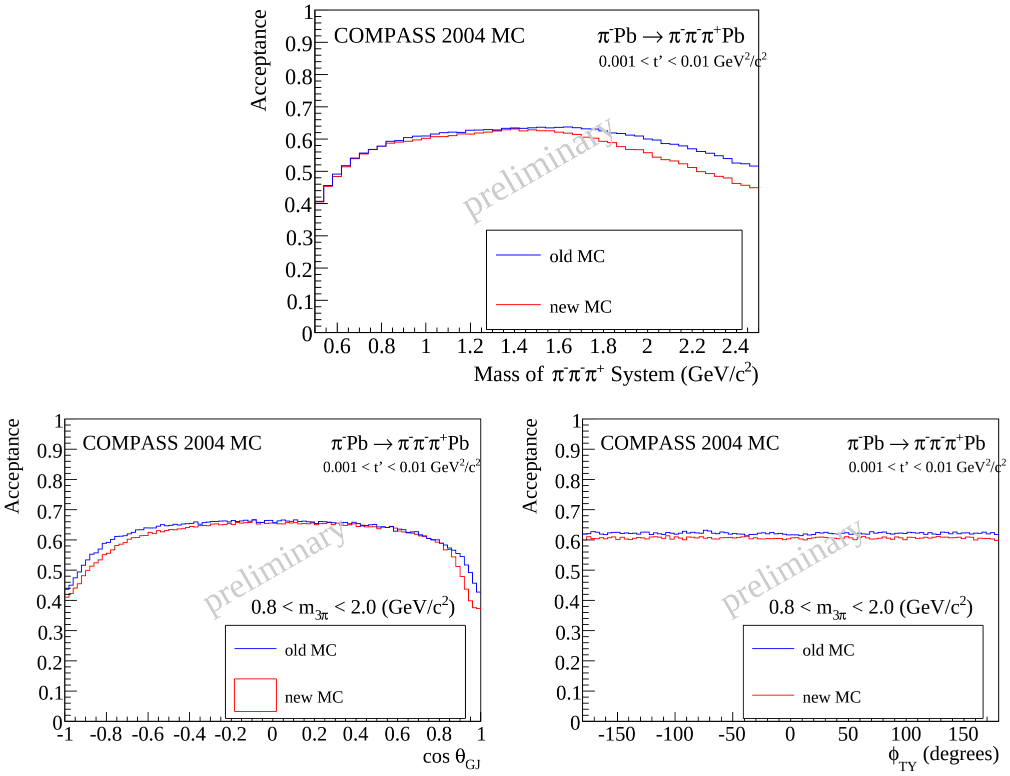

Figure C.6: Comparison of the acceptance with $m_{3\pi}$, $\cos\theta_{\mathrm{GJ}}$ and ϕ_{TY} for low t', for the previous and the corrected SW veto position.

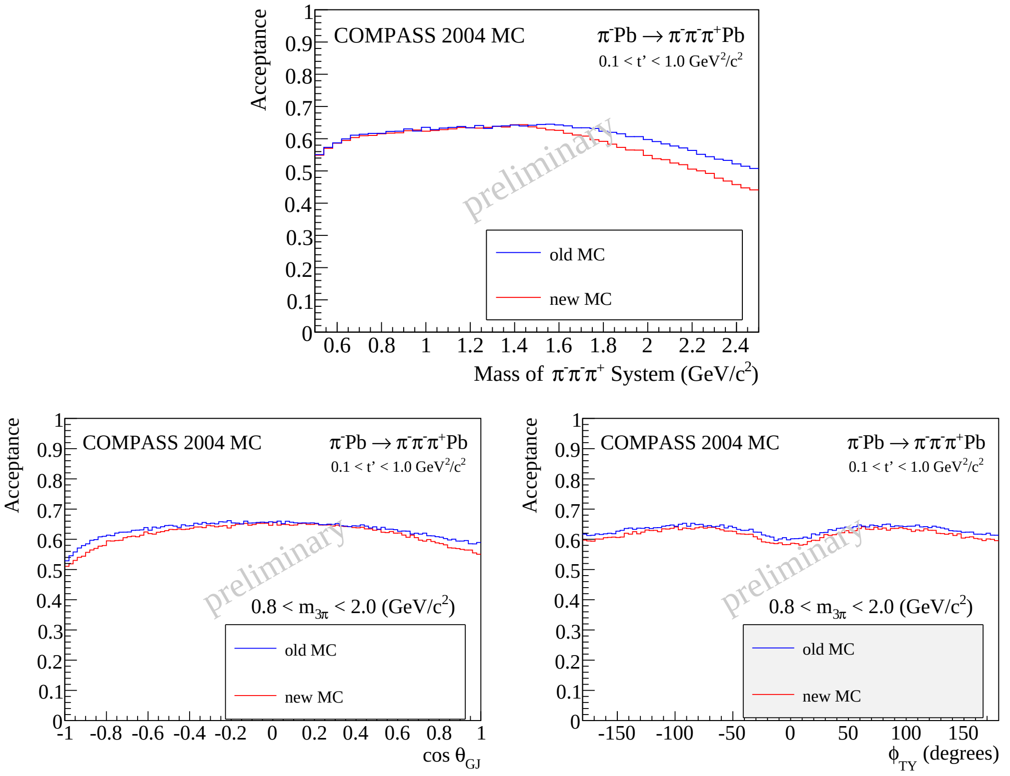

Figure C.7: Comparison of the acceptance with $m_{3\pi}$, $\cos\theta_{\mathrm{GJ}}$ and ϕ_{TY} for high t', for the previous and the corrected SW veto position.

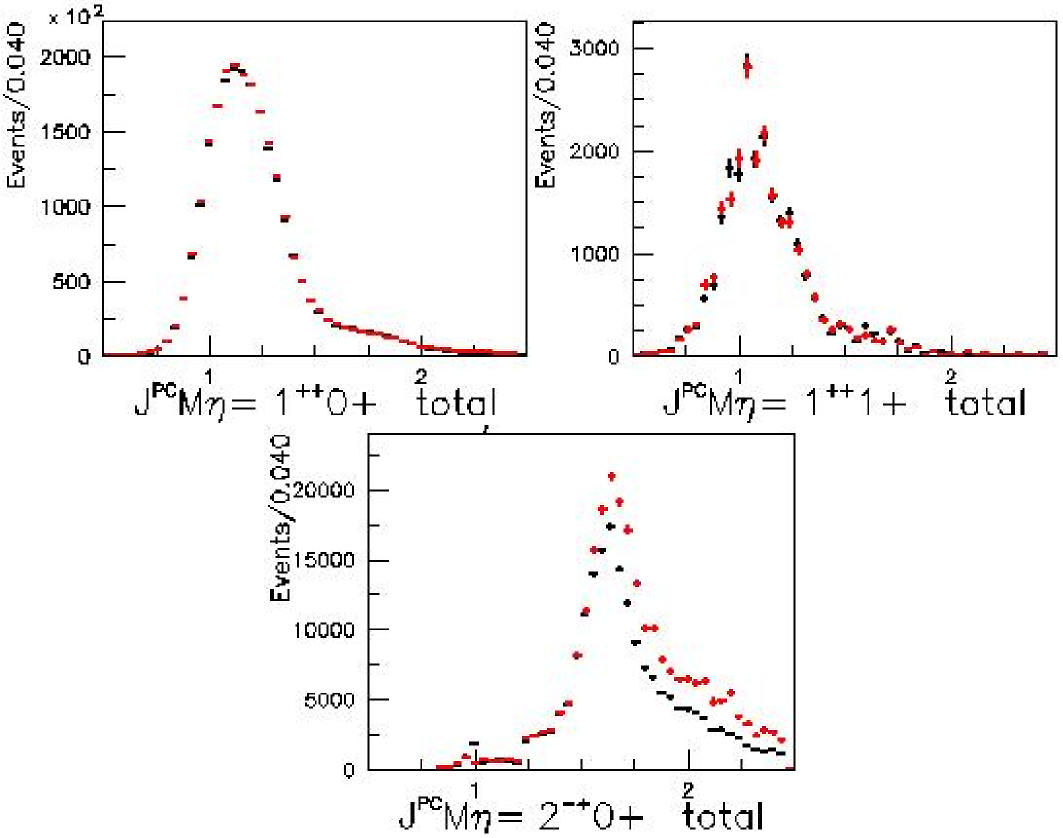

Figure C.8: Comparison of the total intensities obtained from a PWA of low t' data, for the previous and the corrected SW veto position.

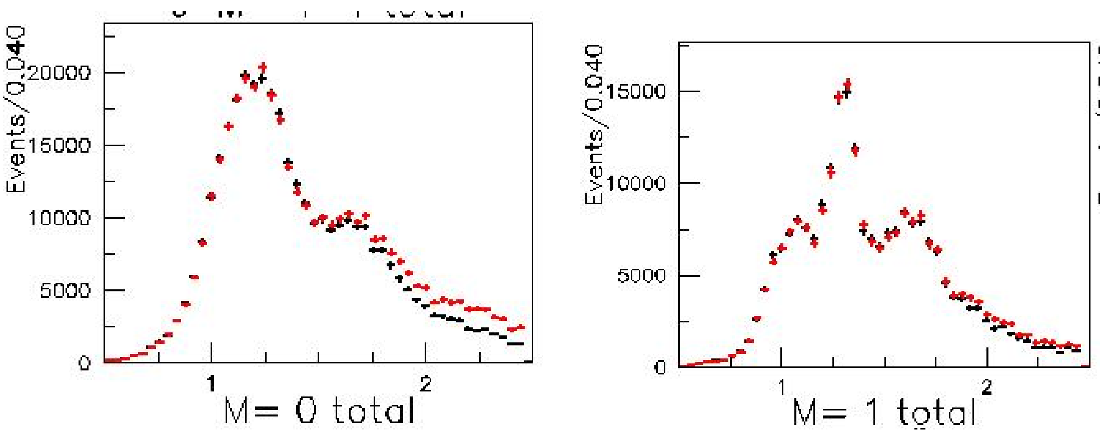

Figure C.9: Comparison of $M = 0$ and $M = 1$ total intensities obtained from a PWA of high t' data, for the previous and the corrected SW veto position.

Appendix D

Comprehensive Result of the PWA for $t' < 10^{-3}\,\mathrm{GeV}^2/c^2$

In this chapter a more comprehensive overview of the result of the mass-independent PWA presented in section 9.4.2, i.e. the fit in mass bins for the full range $t' < 10^{-3}\,\mathrm{GeV}^2/c^2$, is given. The used set of decay amplitudes is given in table D.1, including the applied thresholds. The parametrization of the t' dependence of the decay amplitudes as given in section 8.2.3 was used. The fitting model used rank $N_r = 1$ with one free coherence parameter between all $M = 0$ and all $M = 1$ waves (as explained in detail in section 8.4).

The interpretation of the major results relevant for this work is presented already in the section 9.4.2 and not repeated here again. The listings of all intensities and a broader selection of relative phases between selected amplitudes is meant for completeness and an outlook for resonance candidates that can potentially be extracted from this data.

The overview starts with total intensities: The total intensity of all amplitudes, the $M = 0$ and $M = 1$ total intensities, the $M^\epsilon = 1^\pm$ total intensities, and the total intensity of the ChPT amplitudes are collected in figure D.1. Total intensities of $J^{PC}M$ are presented in figure D.2.

The intensities of the single 37 employed amplitudes are depicted in the figures D.3, D.4, D.5, D.6, and D.7. They are listed in the same order as given in table D.1. The amplitude set covers 26 amplitudes with $\epsilon = +1$ (i.e. which are allowed to interfere with each other) and 9 amplitudes with $\epsilon = -1$ (which also interfere with each other), which leads to 361 independent relative phases in the fit. Not all of them are plotted in the following. Only the most interesting phases have been selected (figures D.8 and D.9). The selection criteria are based on the analysis of this work and the additional findings on the low-t' analysis presented in [Wei08a]. The latter found indications for the $a_1(1640)$ in the $1^{++}0^+ f_2\pi P$ and the $1^{++}0^+\rho\pi D$ amplitudes, which is still quoted to need confirmation [PDG10], and for the $\pi(1800)$ in the $0^{-+}0^+ f_0(980)\pi S$ amplitude. The $\pi(1300)$ can maybe be seen in the $0^{-+}0^+\rho\pi P$. The $2^{-+}0^+ f_2\pi D$ amplitude showed a significant intensity, but also a phase motion with respect to the $2^{-+}0^+ f_2\pi S$, so that an interpretation as the hybrid candiate $\pi_2(1880)$ was suggested. The resonant nature of these candidates, and their properties, can also be investigated based on the presented fit, but requires an additional mass-dependent PWA, which was not the focus of this thesis.

$J^{PC}M^{\epsilon}$	L	Isobar π	Thresh. [GeV]
$0^{-+}0^{+}$	S	$(\pi\pi)_s\pi$	-
$0^{-+}0^{+}$	S	$f_0(980)\pi$	1.12
$0^{-+}0^{+}$	P	$\rho\pi$	-
$0^{-+}0^{+}$	D	$f_2\pi$	1.24
$0^{-+}0^{+}$	S	$f_0(1500)\pi$	1.64
$1^{++}0^{+}$	S	$\rho\pi$	0.48
$1^{++}0^{+}$	P	$f_2\pi$	1.40
$1^{++}0^{+}$	P	$f_0(980)\pi$	1.24
$1^{++}0^{+}$	P	$(\pi\pi)_s\pi$	-
$1^{++}0^{+}$	D	$\rho\pi$	1.04
$1^{++}1^{+}$	S	$\rho\pi$	0.72
$1^{++}1^{+}$	P	$(\pi\pi)_s\pi$	0.72
$1^{-+}1^{+}$	P	$\rho\pi$	0.80
$2^{++}1^{+}$	D	$\rho\pi$	0.80
$2^{-+}0^{+}$	S	$f_2\pi$	1.24
$2^{-+}0^{+}$	P	$\rho\pi$	0.80
$2^{-+}0^{+}$	D	$(\pi\pi)_s\pi$	1.32
$2^{-+}0^{+}$	D	$f_2\pi$	1.52
$2^{-+}0^{+}$	F	$\rho\pi$	1.28
$2^{-+}1^{+}$	S	$f_2\pi$	1.38
$2^{-+}1^{+}$	P	$\rho\pi$	0.72
$2^{-+}1^{+}$	D	$(\pi\pi)_s\pi$	1.24
$2^{-+}1^{+}$	F	$\rho\pi$	1.52
$3^{++}0^{+}$	P	$f_2\pi$	1.52
$3^{++}0^{+}$	D	$\rho\pi$	1.52
chiral $\epsilon = +1$			< 1.24

$J^{PC}M^{\epsilon}$	L	Isobar π	Thresh. [GeV]
$1^{++}1^{-}$	S	$\rho\pi$	0.72
$1^{++}1^{-}$	P	$(\pi\pi)_s\pi$	0.72
$1^{-+}1^{-}$	P	$\rho\pi$	0.80
$2^{++}1^{-}$	D	$\rho\pi$	0.80
$2^{-+}1^{-}$	S	$f_2\pi$	1.36
$2^{-+}1^{-}$	P	$\rho\pi$	0.72
$2^{-+}1^{-}$	D	$(\pi\pi)_s\pi$	1.24
$2^{-+}1^{-}$	F	$\rho\pi$	1.52
chiral $\epsilon = -1$			< 1.24
kaon decay			< 0.56
Background			

Table D.1: The complete set of amplitudes used for the mass-independent PWA presented in section 9.4.2.

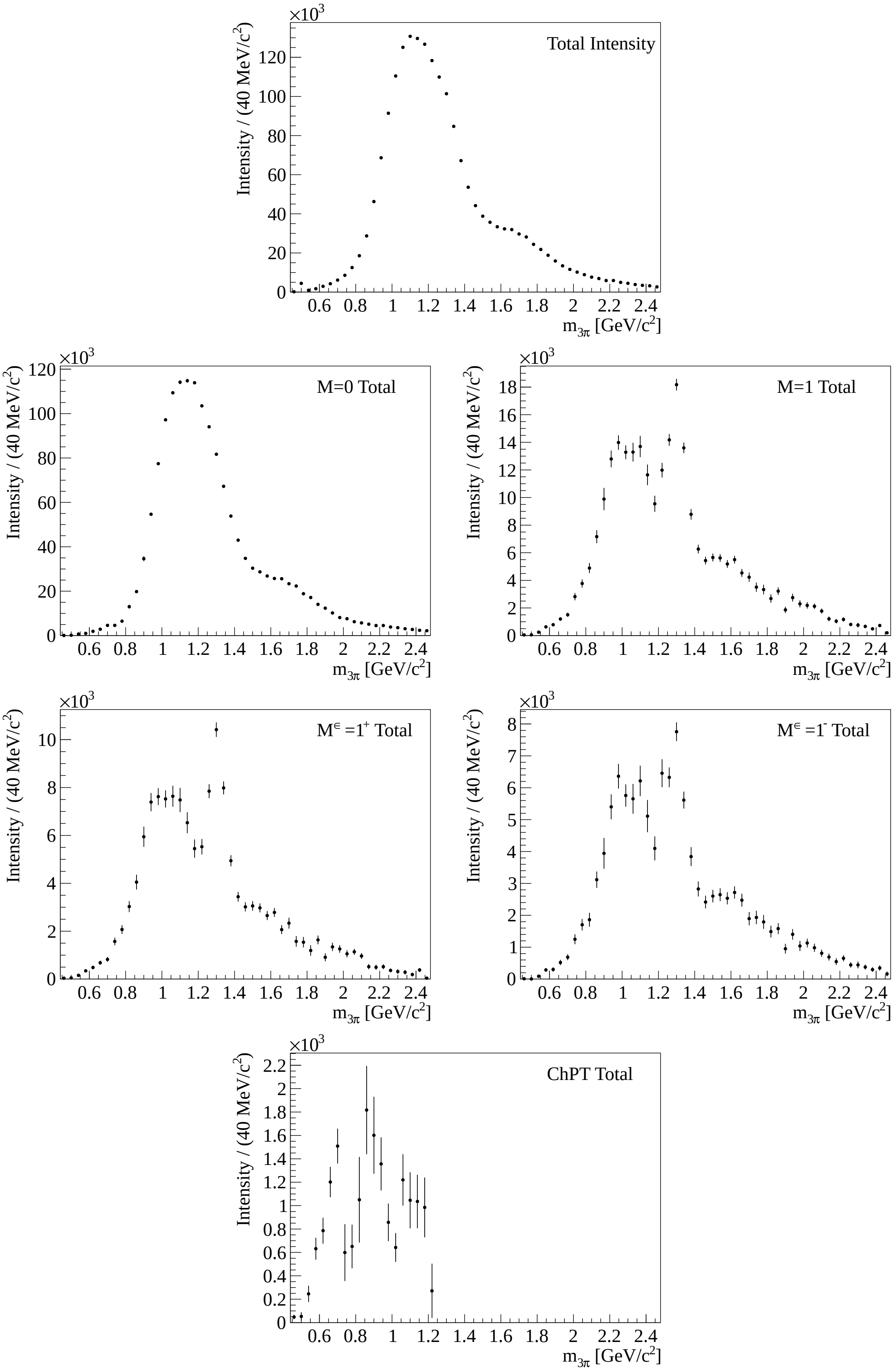

Figure D.1: Comprehensive overview of the PWA fit result for $t' < 10^{-3}\,\mathrm{GeV}^2/c^2$: Total intensities (1).

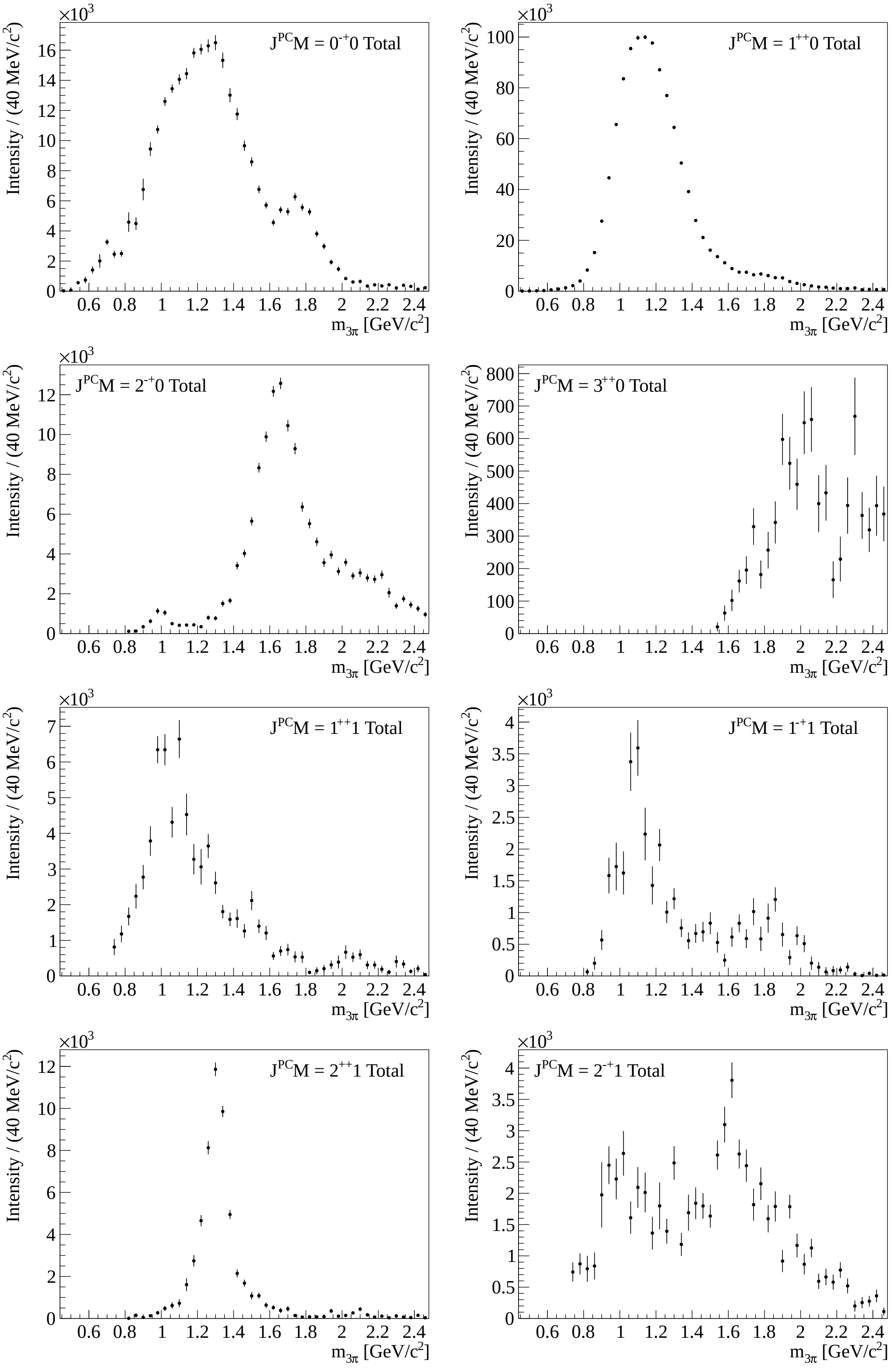

Figure D.2: Comprehensive overview of the PWA fit result for $t' < 10^{-3}\,\mathrm{GeV}^2/c^2$: Total intensities (2).

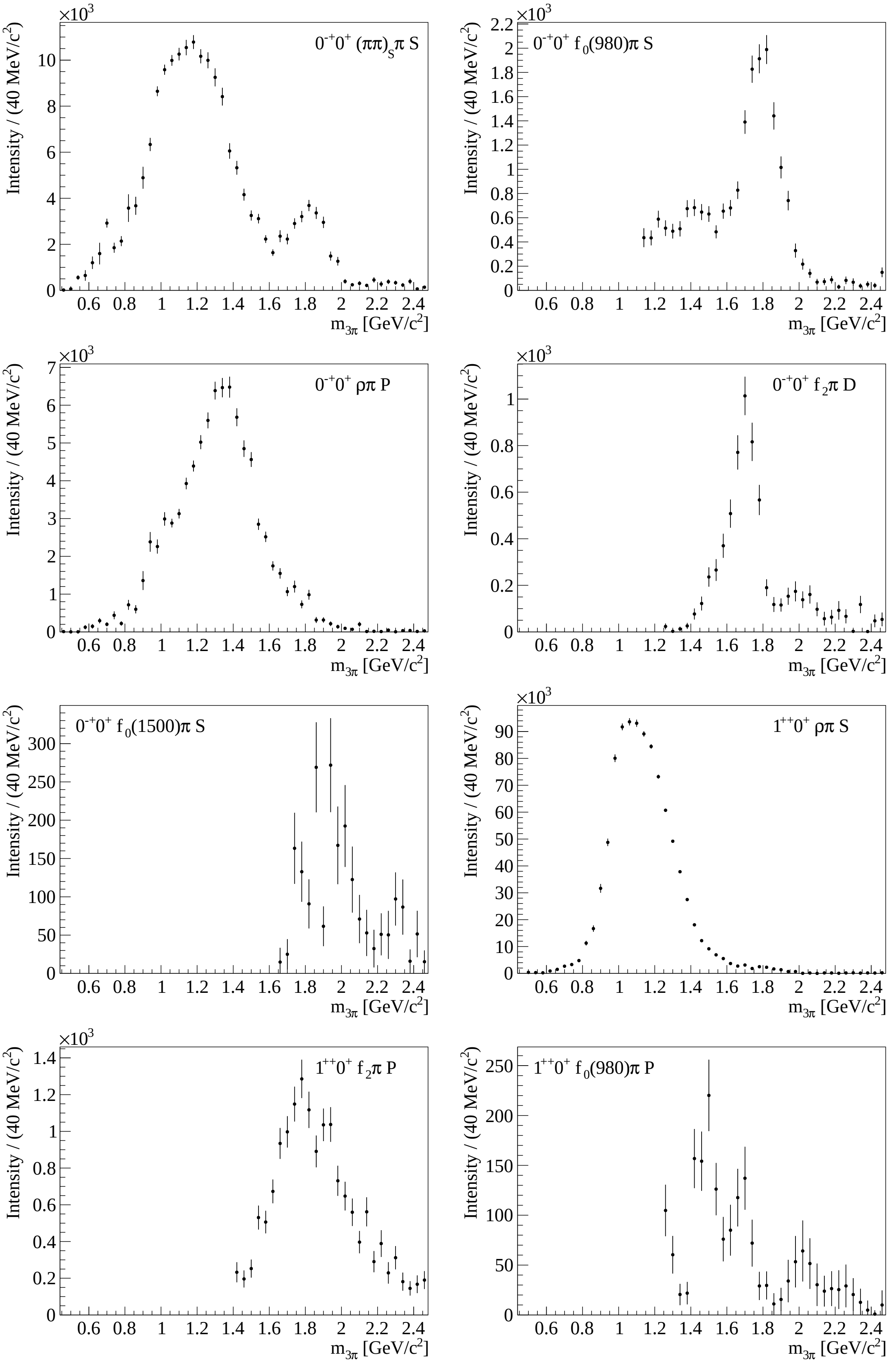

Figure D.3: Comprehensive overview of the PWA fit result for $t' < 10^{-3}\,\mathrm{GeV}^2/c^2$: Intensities of single amplitudes (1).

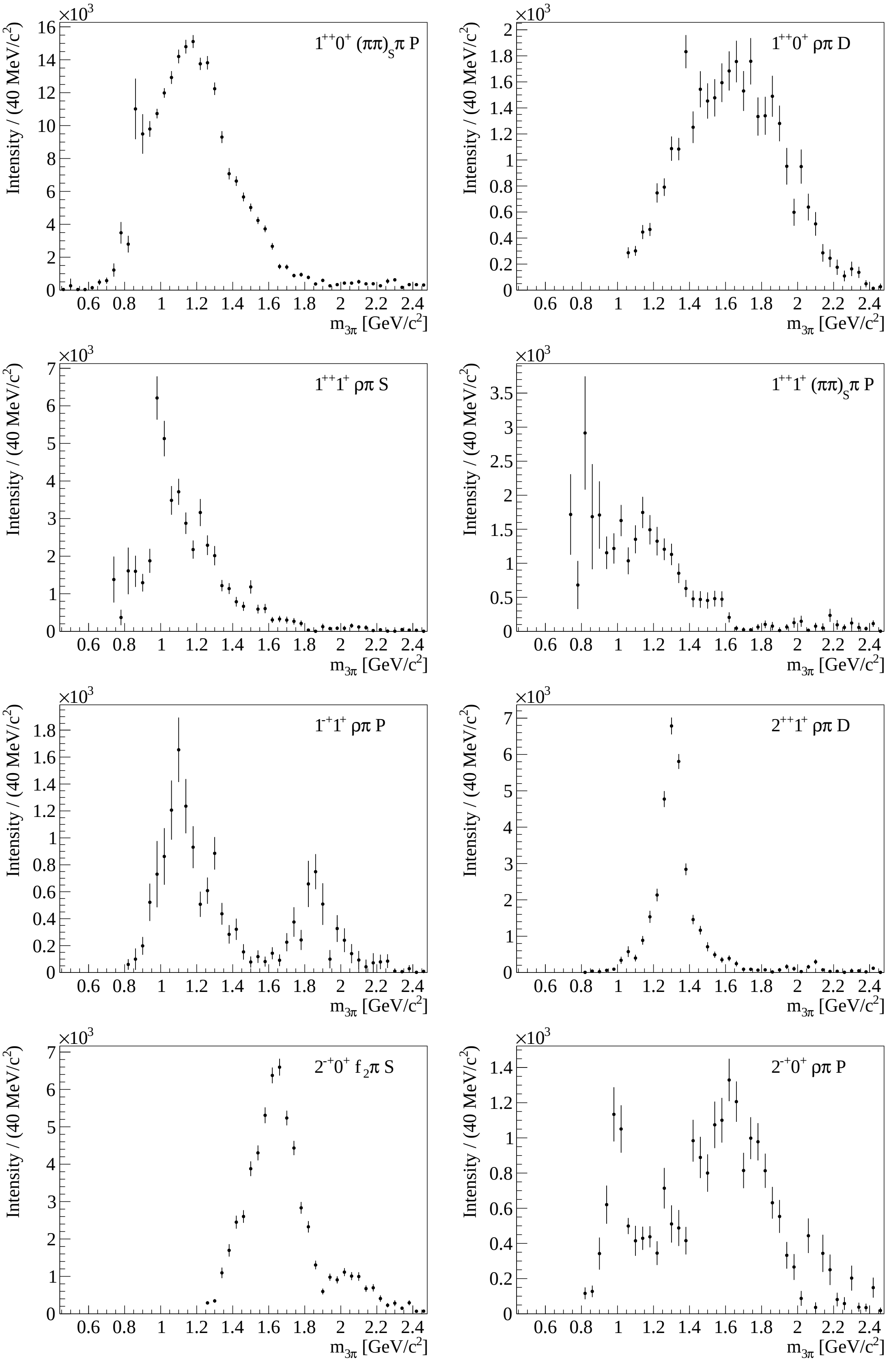

Figure D.4: Comprehensive overview of the PWA fit result for $t' < 10^{-3}$ GeV$^2/c^2$: Intensities of single amplitudes (2).

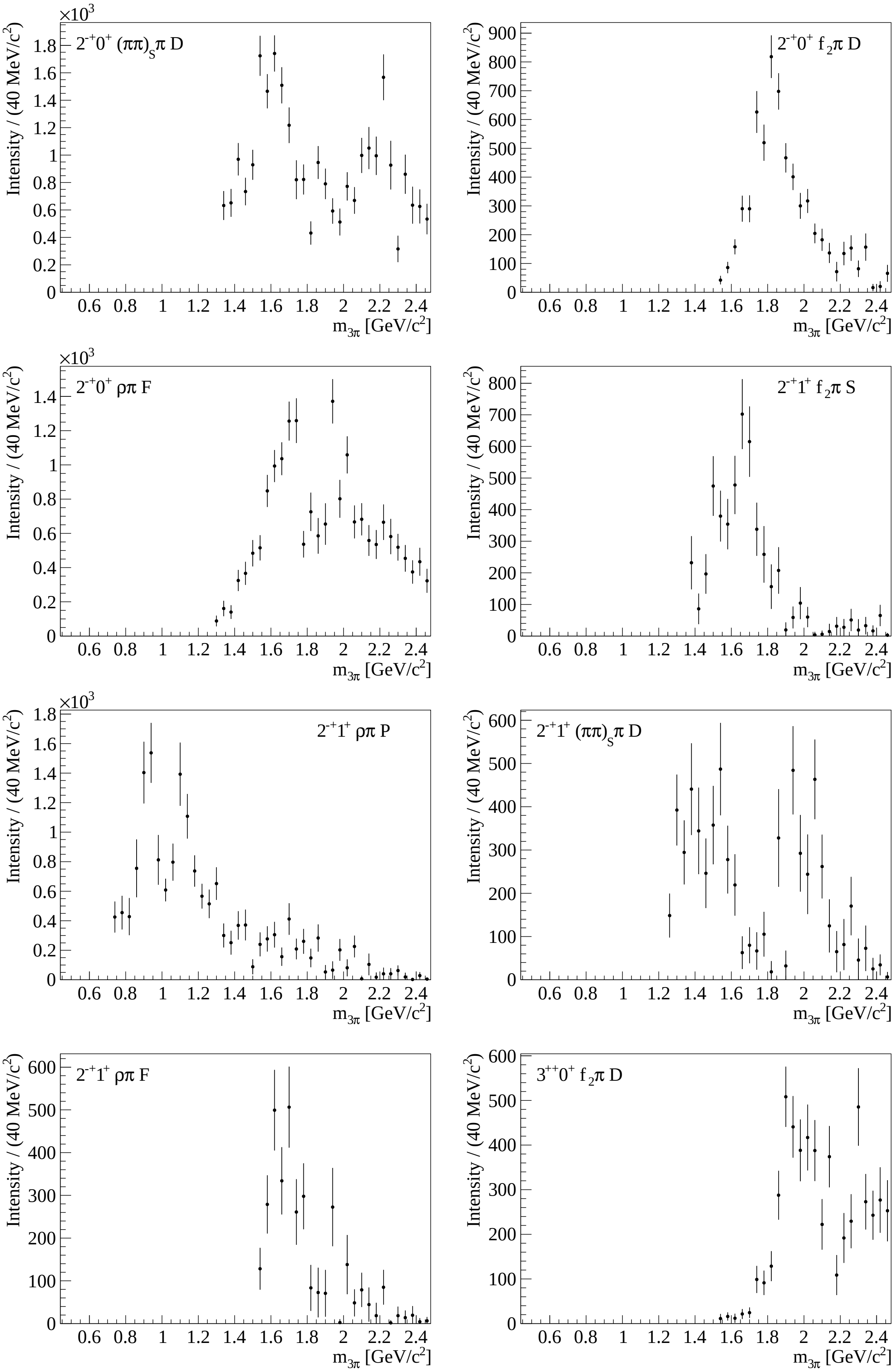

Figure D.5: Comprehensive overview of the PWA fit result for $t' < 10^{-3}\,\mathrm{GeV}^2/c^2$: Intensities of single amplitudes (3).

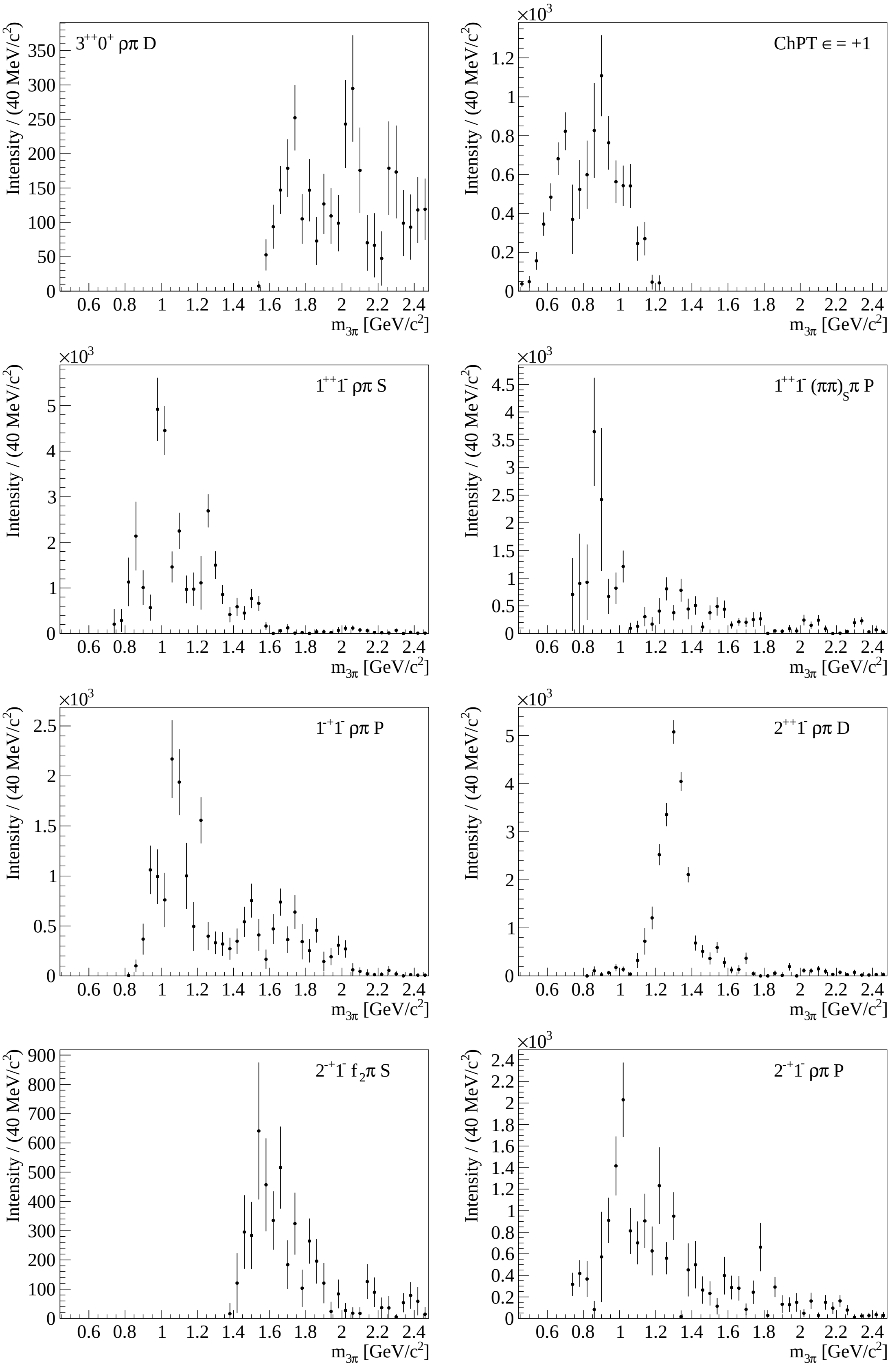

Figure D.6: Comprehensive overview of the PWA fit result for $t' < 10^{-3}$ GeV$^2/c^2$: Intensities of single amplitudes (4).

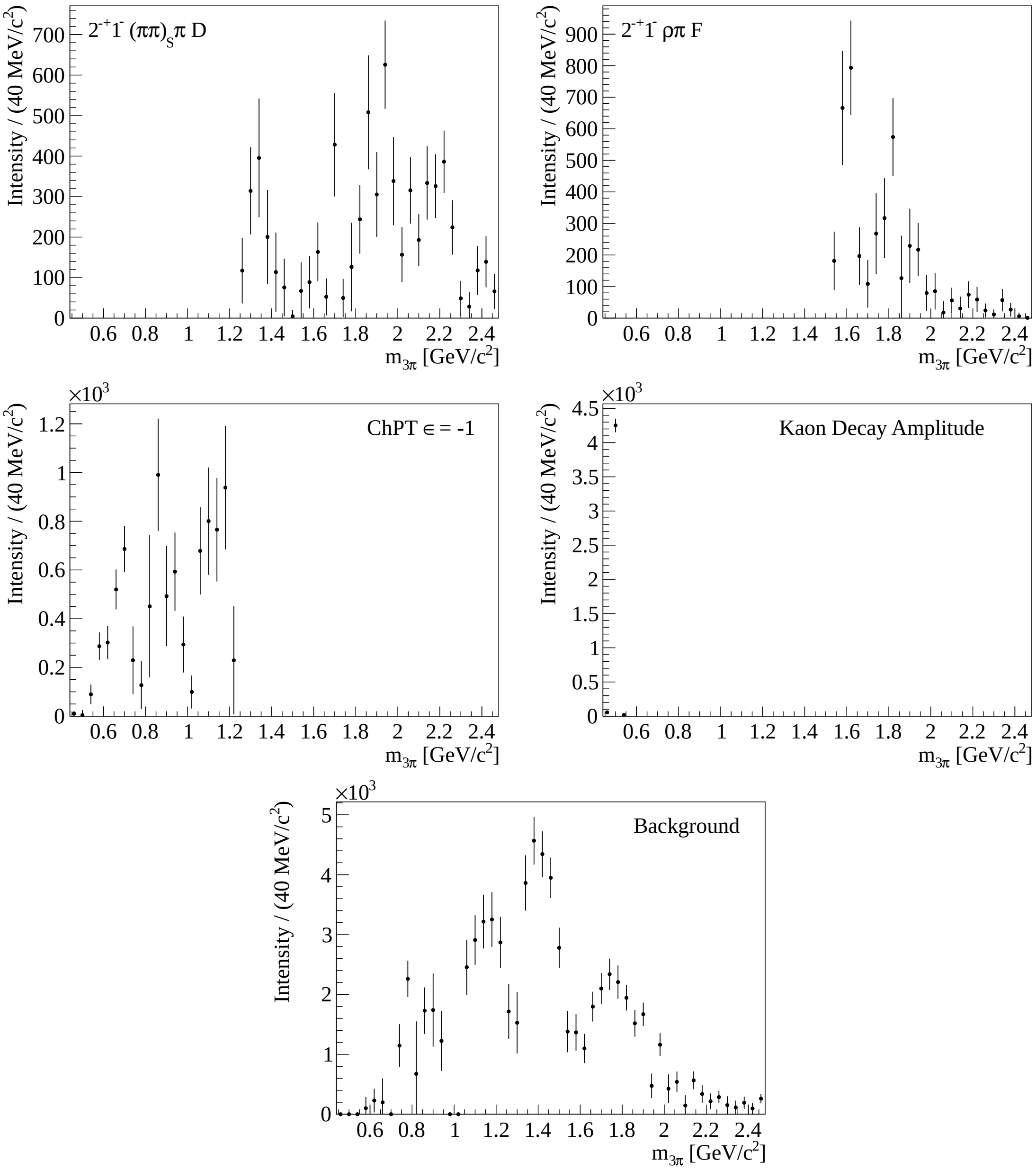

Figure D.7: Comprehensive overview of the PWA fit result for $t' < 10^{-3}\,\mathrm{GeV}^2/c^2$: Intensities of single amplitudes (5).

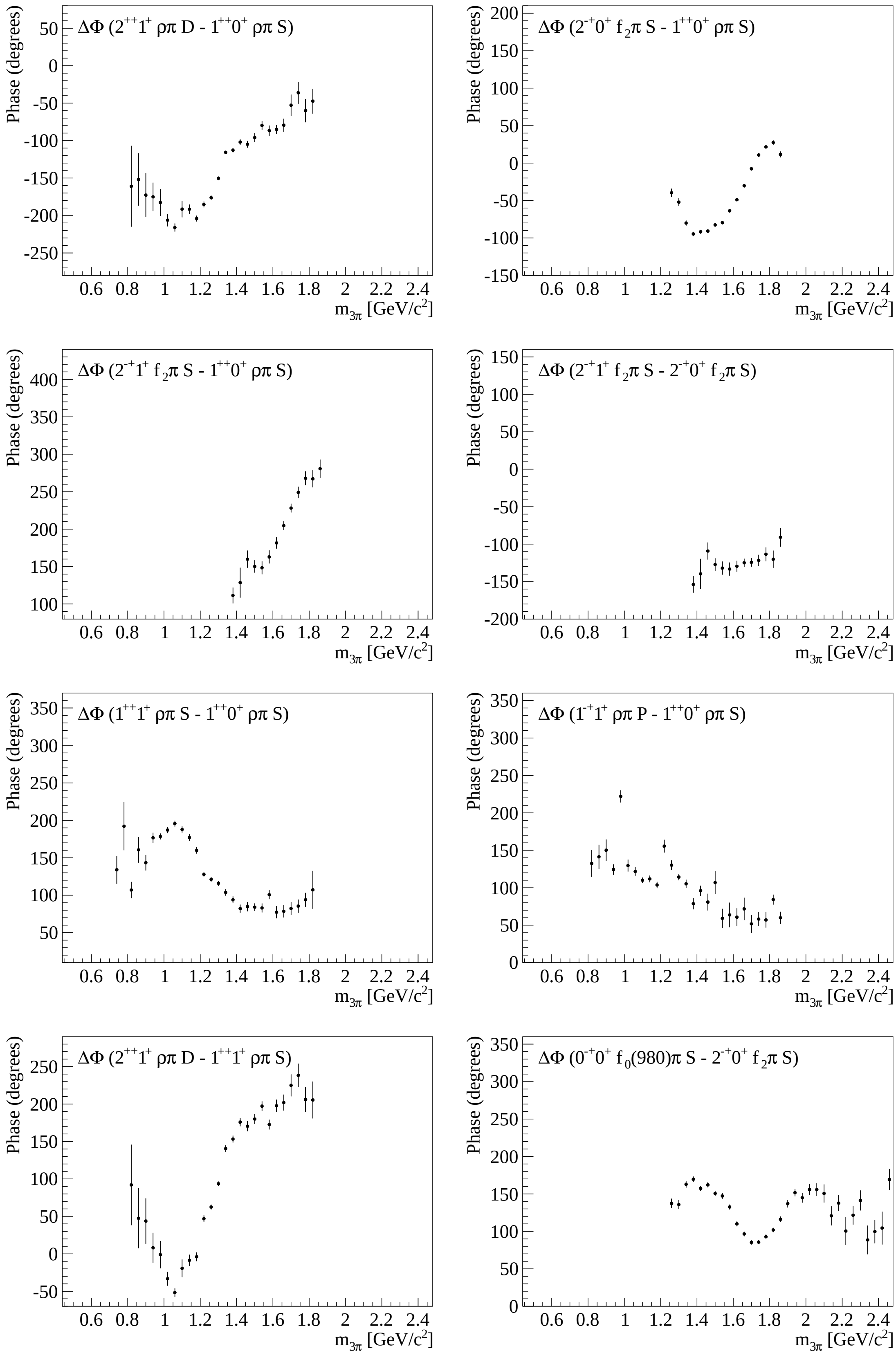

Figure D.8: Comprehensive overview of the PWA fit result for $t' < 10^{-3}\,\mathrm{GeV}^2/c^2$: Selected phases (1).

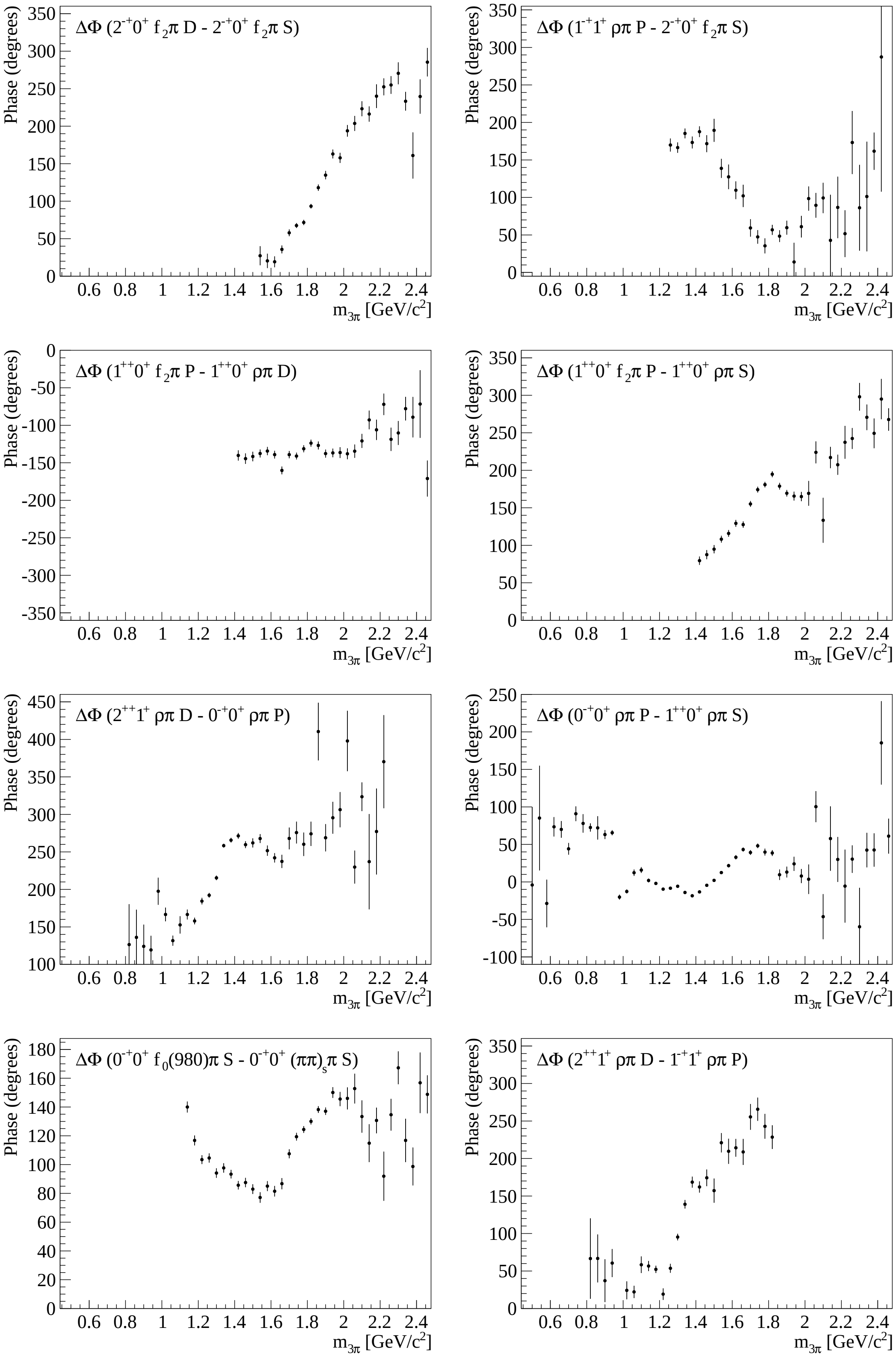

Figure D.9: Comprehensive overview of the PWA fit result for $t' < 10^{-3}\,\mathrm{GeV}^2/c^2$: Selected phases (2).

List of Figures

List of Tables

Bibliography

[Abt98] I. Abt et al. Gluing silicon with silicone. *Nucl. Instrum. Meth.* **A 411**, 191–196 (1998). (Cited on page 25.)

[Abt00] I. Abt et al. Double-sided microstrip detectors for the high radiation environment in the HERA-B experiment. *Nucl. Instrum. Meth.* **A 439**, 442–450 (2000). (Cited on page 23.)

[ACC81] C. Daum and others [The ACCMOR collaboration]. DIFFRACTIVE PRODUCTION OF 3 pi STATES AT 63 GeV AND 94 GeV. *Nucl. Phys.* **B182**, 269 (1981). (Cited on pages 108 and 146.)

[AJM76] U. Amaldi, M. Jacob, and G. Matthiae. Diffraction of hadronic waves. *Ann. Rev. Nucl. Sci.* **26**, 385–456 (1976). (Cited on page 80.)

[Ame01] L. Ametller, M. Knecht, and P. Talavera. Electromagnetic corrections to $\gamma\pi^{\pm} \to \pi^{0}\pi^{\pm}$. *Phys. Rev. D* **64**, 094009 (2001). (Cited on page 77.)

[AMP87] K. L. Au, D. Morgan, and M. R. Pennington. Meson dynamics beyond the quark model: Study of final-state interactions. *Phys. Rev. D* **35**, 1633–1664 Mar 1987. (Cited on pages 90 and 91.)

[APV01] L.L. Jones et al. APV25-S1 User Guide Version 2.2. http://cdsweb.cern.ch/record/1069892, 2001. (Cited on page 31.)

[Asc70] G. Ascoli, D. V. Brockway, H. B. Crawley, L. B. Eisenstein, R. W. Hanft, M. L. Ioffredo, and U. E. Kruse. Partial-wave analysis of the 3π decay of the A_2. *Phys. Rev. Lett.* **25**, 962–965 Oct 1970. (Cited on page 105.)

[Ath80] H.W. Atherton et al. Precise Measurement of Particle Production by 400 GeV/c Protons on Beryllium Targets. *CERN Yellow Report* **CERN 80-07** (1980). (Cited on page 158.)

[Bau00] C. Bauer et al. The HERA-B vertex detector system. *Nucl. Instrum. Meth.* **A 453**, 103–108 (2000). (Cited on page 24.)

[Bau02] C. Bauer et al. Radiation hardness of the HERA-B double-sided strip detectors. *Nucl. Instrum. Meth.* **A 485**, 116–120 (2002). (Cited on page 24.)

[Bec04] M. Becker. *Setup of a Cryogenic System for Silicon Microstrip Detectors in the COMPASS Experiment*. Diploma thesis, Technische Universität München, September 2004. (Cited on page 33.)

[Bic11] K. Bicker. *Construction and Commissioning of a Cooling and Support Structure for the Silicon Detectors for the COMPASS Experiment*. Diploma thesis, Technische Universität München, January 2011. (Cited on pages 37, 40, 41, and 47.)

[Bor00a] K. Borer et al. Charge collection efficiency and resolution of an irradiated double-sided silicon microstrip detector operated at cryogenic temperatures. *Nucl. Instrum. Meth.* **A 440**, 17–37 (2000). (Cited on page 33.)

[Bor00b] K. Borer et al. Charge collection efficiency of irradiated silicon detector operated at cryogenic temperatures. *Nucl. Instrum. Meth.* **A 440**, 5–16 (2000). (Cited on page 33.)

[Bru97] R. Brun and F. Rademakers. ROOT: An object oriented data analysis framework. *Nucl. Inst. Meth.* **A389**, 81 (1997). (Cited on page 17.)

[Bur96] U. Burgi. Charged pion polarizabilities to two loops. *Phys. Lett.* **B377**, 147–152 (1996). (Cited on page 77.)

[CB95] C. Amsler et al. High statistics study of $f_0(1500)$ decay into $\eta\eta$. *Phys. Lett. B* **353**, 571–577 (1995). (Cited on page 6.)

[CB98] A. Abele et al. Exotic $\eta\pi$ state in $\bar{p}d$ annihilation at rest into $\pi^-\pi^0\eta p_{\text{spectator}}$. *Phys. Lett. B* **423**, 175 (1998). (Cited on page 6.)

[CERN] CERN web site, `http://www.cern.ch/`. (Cited on page 3.)

[CHE95] E. Nappi et al. CHEOPS - CHarm Experiment with Omni-Purpose Setup. *CERN/SPSLC 95-22, SPSLC/I 202* (1995). (Cited on page 3.)

[Che06] Y. Chen et al. Glueball spectrum and maxtrix elements on anisotropic lattices. *Phys. Rev. D* **73**, 014516 (2006). (Cited on page 6.)

[Chu71] S.-U. Chung. Spin formalisms. *CERN Yellow Report* **1971-08** (1971). (Cited on pages 86, 88, and 89.)

[Chu97] S.-U. Chung. Techniques of amplitude analysis for two-pseudoscaler systems. *Physical Review D* **56**, 7299–7316 (1997). (Cited on page 85.)

[Clo95] F.E. Close and P.R. Page. The Production and Decay of Hybrid Mesons by Flux-Tube Breaking. *Nucl. Phys. B* **443**, 233–254 (1995). (Cited on page 6.)

[COM] COMPASS web site, `http://wwwcompass.cern.ch/`. (Cited on pages 3 and 12.)

[COM96] The COMPASS Collaboration. A proposal for a Common Muon and Proton Apparatus for Structure and Spectroscopy. *CERN* **SPSLC 96-14** (1996). (Cited on pages 3, 8, and 51.)

[COM05a] The COMPASS Collaboration. First Measurement of the Transverse Spin Asymmetries of the Deuteron in Semi-inclusive Deep Inelastic Scattering. *Physical Review Letters* **94 202002** (2005). (Cited on page 9.)

[COM05b] The COMPASS Collaboration. Measurement of the spin structure of the deuteron in the DIS region. *Physics Letters B* **612**, 154–164 (2005). (Cited on page 9.)

[COM06] The COMPASS Collaboration. Gluon polarization in the nucleon from quasi-real photoproduction of high-p_t hadron pairs. *Phys. Lett. B* **633**, 25–32 (2006). (Cited on page 8.)

[COM07a] The COMPASS Collaboration. COMPASS Programme 2007 to 2010. *CERN* **SPSC-2007-002, SPSC-M-754** January 2007. (Cited on page 30.)

[COM07b] The COMPASS Collaboration. The deuteron spin-dependent structure function g_1^d and its first moment. *Physics Letters B* **647**, 8–17 (2007). (Cited on page 9.)

[COM07c] The COMPASS Collaboration. A new measurement of the Collins and Sivers asymmetries on a transversely polarized deuteron target. *Nucl. Phys. B* **765**, 31–70 (2007). (Cited on page 9.)

[COM07d] The COMPASS Collaboration. Spin asymmetry A_1^d and the spin-dependent structure function g_1^d of the deuteron at low values of x and Q^2. *Physics Letters B* **647**, 330–340 (2007). (Cited on page 9.)

[COM07e] The COMPASS Collaboration. The COMPASS Experiment at CERN. *NIM* **A 577**, 455–518 (2007). (Cited on pages 10, 15, 17, and 23.)

[COM08] The COMPASS Collaboration. The polarised valence quark distribution from semi-inclusive DIS. *Physics Letters B* **660**, 458–465 (2008). (Cited on page 9.)

[COM09a] The COMPASS Collaboration. Collins and Sivers asymmetries for pions and kaons in muon-deuteron DIS. *Phys. Lett. B* **673**, 127–135 (2009). (Cited on page 9.)

[COM09b] The COMPASS Collaboration. Flavour separation of helicity distributions from deep-inelastic muon-deuteron scattering. *Physics Letters B* **680**, 217–224 (2009). (Cited on page 9.)

[COM09c] The COMPASS Collaboration. Gluon Polarisation in the Nucleon and Longitudinal Double Spin Asymmetries from Open Charm Muoproduction. *Phys. Lett. B* **676**, 31–38 (2009). (Cited on page 8.)

[COM09d] The COMPASS Collaboration. Measurement of the longitudinal spin transfer to Λ and $\bar{\Lambda}$ hyperons in polarised muon DIS. *Eur. Phys. J. C* **64**, 171–179 (2009). (Cited on page 9.)

[COM10a] The COMPASS Collaboration. COMPASS-II Proposal. *CERN* **SPSC 2010-14** (2010). (Cited on pages 3, 5, 9, and 10.)

[COM10b] The COMPASS Collaboration. Measurement of the Collins and Sivers asymmetries on transversely polarized protons. *Phys. Lett. B* **692**, 240–246 (2010). (Cited on page 9.)

[COM10c] The COMPASS Collaboration. Observation of a $J^{PC} = 1^{-+}$ Exotic Resonance in Diffractive Dissociaton of 190 GeV π^- into $\pi^-\pi^-\pi^+$. *Phys. Rev. Lett.* **104**, 241803 (2010). (Cited on page 7.)

[COM10d] The COMPASS Collaboration. Quark helicity distributions from longitudinal spin asymmetries in muon-proton and muon-deuteron scattering. *Physics Letters B* **693**, 227–235 (2010). (Cited on page 9.)

[COM12a] The COMPASS Collaboration. First Measurement of Chiral Dynamics in $\pi^-\gamma \rightarrow \pi^-\pi^-\pi^+$. *Phys. Rev. Lett.* **108**, 192001 (2012). (Cited on pages 7, 165, and 223.)

[COM12b] The COMPASS Collaboration. Leading order determination of the gluon polarisation from DIS events with high-p_t hadron pairs. *submitted to Phys. Lett. B, arXiv:1202.4064* (2012). (Cited on page 8.)

[COM12c] The COMPASS Collaboration. The COMPASS Setup for Physics with Hadron Beams. *to be published* (2012). (Cited on pages 10, 11, 23, and 47.)

[CORAL] CORAL web site, `http://coral.cern.ch/`. (Cited on page 18.)

[CT75] S.-U. Chung and T. L. Trueman. Positivity conditions on the spin density matrix: A simple parametrization. *Physical Review D* **11 3**, 633–646 (1975). (Cited on pages 85 and 93.)

[Din10] A.-M. Dinkelbach. *Precision Tracking and Electromagnetic Calorimetry Towards a Measurement of the Pion Polarisabilities at COMPASS*. PhD thesis, Technische Universität München, 2010. (Cited on pages 5, 26, 27, 28, 29, 59, 60, 65, 67, 68, 69, 72, 112, and 171.)

[dMa04] R. de Masi. *Development of a cryogenic silicon detector system and study of strange particle production in deep inelastic scattering*. PhD thesis, Technische Universität München, July 2004. (Cited on page 33.)

[Dzi06] A.R. Dzierba et al. Partial wave analysis of the $\pi^-\pi^-\pi^+$ and $\pi^-\pi^0\pi^0$ systems and the search for a $J^{PC} = 1^{-+}$ meson. *Phys. Rev. D* **73**, 072001 (2006). (Cited on page 6.)

[E85297] D.R. Thompson et al. Evidence for Exotic Meson Production in the Reaction $\pi^- p \rightarrow \eta\pi^- p$ at 18 GeV/c. *Phys. Rev. Lett.* **79**, 1630 (1997). (Cited on page 6.)

[E85298] G.S. Adams et al. Observation of a New $J^{PC} = 1^{-+}$ Exotic State in the Reaction $\pi^- p \rightarrow \pi^+\pi^-\pi^- p$ at 18 GeV/c. *Phys. Rev. Lett.* **81**, 5760 (1998). (Cited on page 6.)

[E85201] E.I. Ivanov et al. Observation of Exotic Meson Production in the Reaction $\pi^- p \rightarrow \eta'\pi^- p$ at 18 GeV/c. *Phys. Rev. Lett.* **86**, 3977 (2001). (Cited on page 6.)

[E85204] J. Kuhn et al. Exotic meson production in the $f_1(1285)\pi^-$ system observed in the reaction $\pi^- p \to \eta\pi^+\pi^-\pi^- p$ at 18 GeV/c. *Phys. Lett. B* **595**, 109 (2004). (Cited on page 6.)

[E85205] Lu M. et al. Exotic Meson Decay to $\omega\pi^0\pi^-$. *Phys. Rev. Lett.* **94**, 032002 (2005). (Cited on page 6.)

[EPA61] I.Ya. Pomeranchuk and I.M. Shmushkevich. On Processes in the Interaction of γ-Quanta with Unstable Particles. *Nucl. Phys.* **23**, 452–467 (1961). (Cited on page 80.)

[Fri11] J.M. Friedrich, `jan@tum.de`. Private communication, 2011. (Cited on page 24.)

[Fri12] J.M. Friedrich. *Chiral Dynamics in Pion-Photon Reactions*. Habilitation Thesis, Technische Universität München, 2012. (Cited on page 148.)

[Fuc03] A. Fuchs (married Dinkelbach). *Setup of a low Temperature Silicon Detector for the COMPASS Experiment*. Diploma thesis, Technische Universität München, December 2003. (Cited on pages 33 and 48.)

[Gas06] J. Gasser, M. A. Ivanov, and M. E. Sainio. Revisiting $\gamma\gamma \to \pi^+\pi^-$ at low energies. *Nucl. Phys.* **B745**, 84–108 (2006). (Cited on page 77.)

[GEANT] GEANT Detector Description and Simulation Tool, `http://wwwasdoc.web.cern.ch/wwwasdoc/pdfdir/geant.pdf`. (Cited on page 19.)

[Gey11] R. Geyer, `reiner.geyer@cern.ch`. Private communication, 2011. (Cited on page 183.)

[GJ64] K. Gottfried and J. Jackson. On the connection between production mechanism and decay of resonances at high energies. *Il Nuovo Cimento (1955-1965)* **33**, 309–330 (1964). 10.1007/BF02750195. (Cited on page 88.)

[Gra05] S. Grabmüller. *Studies of Diffractive Particle Production at COMPASS*. Diploma thesis, Technische Universität München, December 2005. (Cited on page 115.)

[Gru01] B. Grube. *The Trigger Control System and the Common GEM and Silicon Readout for the COMPASS Experiment*. Diploma thesis, Technische Universität München, December 2001. (Cited on page 32.)

[Gru06] B. Grube. *A Trigger Control System for COMPASS and A Measurement of the Transverse Polarization of Hyperons from Quasi-Real Photo-Production*. PhD thesis, Technische Universität München, 2006. (Cited on page 9.)

[Gus12] A. Guskov. TCS phase and systematics. *mail to `coral-weekly@cern.ch`, July 6th 2012* (2012). (Cited on page 70.)

[Haa12] F. Haas. *in preparation*. PhD thesis, Technische Universität München, 2012. (Cited on pages 7, 74, 90, 96, 97, 104, and 109.)

[Han74] J.D. Hansen et al. Formalism and assumptions involved in partial-wave analysis of three-meson systems. *Nuclear Physics B* **81**, 403–430 (1974). (Cited on pages 88, 89, and 104.)

[HiT] HighTec MC AG, Fabrikstrasse 9, 5600 Lenzburg, Switzerland, `http://www.hightec.ch`. (Cited on page 26.)

[HMC95] E. Nappi et al. Semi-inclusive muon scattering from a polarised target. *CERN/SPSLC 95-27, SPSC/I 204* (1995). (Cited on page 3.)

[Isg85] N. Isgur and J. Paton. Flux-tube model for hadrons in QCD. *Phys. Rev. D* **31**, 2910 (1985). (Cited on page 6.)

[Jac99] J. D. Jackson. *Classical Electrodynamics*. John Wiley & Sons, Inc., New York, 3rd edition, 1999. (Cited on page 80.)

[Jam68] F. James. Monte Carlo Phase Space. *CERN* **68-15** (1968). (Cited on page 119.)

[Jas12] P. Jasinski. *Analysis of diffractive dissociation of K^- into $K^-\pi^+\pi^-$ on a liquid hydrogen target at the COMPASS spectrometer*. PhD thesis, Johannes-Gutenberg-Universität Mainz, 2012. (Cited on pages 7, 11, and 96.)

[Kai10] N. Kaiser. Chiral corrections to $\pi^-\gamma \to 3\pi$ processes at low energies. *Nucl. Phys. A* **848**, 198–217 (2010). (Cited on pages 77, 78, 79, 94, 95, and 150.)

[Kai11] N. Kaiser, `nkaiser@ph.tum.de`. Private communication, 2011. (Cited on pages 78, 79, 95, and 150.)

[KF08] N. Kaiser and J.M. Friedrich. Cross-sections for low-energy $\pi^-\gamma$ reactions. *Eur. Phys. J. A* **36**, 181–188 (2008). (Cited on pages 6, 77, 78, 93, 94, 150, and 164.)

[Kon12] I. Konorov, `igor.konorov@cern.ch`. Private communication, 2012. (Cited on page 173.)

[Lee11] M. Leeb. *Optimization of the Clustering and Tracking Algorithms of the Silicon Microstrip Detectors for the COMPASS Experiment*. Diploma thesis, Technische Universität München, November 2011. (Cited on pages 24, 25, 59, 60, 63, 64, 65, 68, 69, 70, and 72.)

[McN06] C. McNeile and C. Michael. Decay width of light quark hybrid meson from the lattice. *Phys. Rev. D* **73**, 074506 (2006). (Cited on page 6.)

[Mol99a] M. Moll. *Radiation Damage in Silicon Particle Detectors - microscopic defects and macroscopic properties -*. PhD thesis, DESY-THESIS-1999-040, Universität Hamburg, 1999. (Cited on pages 52, 53, and 204.)

[Mol99b] M. Moll et al. Leakage current of hadron irradiated silicon detectors - material dependence. *Nucl. Instrum. Meth.* **A 426**, 87–93 (1999). (Cited on page 57.)

[Nag05] T. Nagel. *Cinderella: an Online Filter for the COMPASS Experiment*. Diploma thesis, Technische Universität München, January 2005. (Cited on pages 60 and 63.)

[Nag08] T. Nagel. 2004 hadron data: Investigating beam K^- decays for fun and profit. *Talk at the COMPASS analysis meeting November 2008* (2008). (Cited on pages 157 and 158.)

[Nag12] T. Nagel. *Measurement of the Charged Pion Polarizability at COMPASS*. PhD thesis, Technische Universität München, 2012. (Cited on pages 5 and 185.)

[NEE] Silikonkleber NEE001. Dr. Neumann Peltiertechnik GmbH, Gautinger Strasse 45, 82061 Neuried, Germany, `http://www.dr.neumann-peltier.de`. (Cited on page 25.)

[Ner11] F. Nerling. *in Proceedings of the XIV International Conference on Hadron Spectroscopy (hadron2011), Munich, 2011, edited by B. Grube, S. Paul and N. Brambilla, eConf C110613 (2011) [arXiv:1108.5969]* (2011). (Cited on page 7.)

[Neu12] S. Neubert. *First Amplitude Analysis of Resonant Structures in the 5-Pion Continuum at COMPASS*. PhD thesis, Technische Universität München, 2012. (Cited on pages 7, 74, 96, 105, and 109.)

[Pal98] V.G. Palmieri et al. Evidence for charge collection efficiency recovery in heavily irradiated silicon detectors operated at cryogenic temperatures. *Nucl. Instrum. Meth.* **A 413**, 475–478 (1998). (Cited on page 22.)

[PDG10] K. Nakamura et al (Particle Data Group). Review of Particle Physics. *Journal of Physics G: Nuclear and Particle Physics* **37 7A**, 075021 (2010). (Cited on pages 78, 91, 96, 158, and 191.)

[Pei92] A. Peisert. Silicon microstrip detectors. *Instrumentation in High Energy Physics, Advanced Series on Directions in High Energy Physics, World Scientific, Singapore* **9**, 1–79 (1992). (Cited on page 22.)

[Pfl11] S. Pflüger. *Investigations of the Light Meson Spektrum with COMPASS using Final States containing Neutral Particles*. Diploma thesis, Technische Universität München, July 2011. (Cited on page 7.)

[PHA] PHAST web site, `http://ges.home.cern.ch/ges/phast/`. (Cited on page 18.)

[QuH72] Frank von Hippel and C. Quigg. Centrifugal-barrier effects in resonance partial decay widths, shapes, and production amplitudes. *Phys. Rev. D* **5**, 624–638 Feb 1972. (Cited on page 89.)

[RD50] The RD50 collaboration, `http://cern.ch/rd50/`. (Cited on page 22.)

[ROOT] R. Brun, F. Rademakers, et al. ROOT home page, `http://root.cern.ch`. (Cited on page 17.)

[ROOT09] I. Antcheva et al. ROOT – A C++ framework for petabyte data storage, statistical analysis and visualization. *Comput. Phys. Commun.* **180**, 2499–2512 (2009). (Cited on page 17.)

[Ros57] M. E. Rose. *Elementary Theory of Angular Momentum.* John Wiley & Sons, Inc., New York, 1957. (Cited on page 88.)

[ROSE] The ROSE collaboration (RD48), `http://cern.ch/rd48/`. (Cited on page 22.)

[ROSE97] A. Vasilescu. The NIEL scaling hypothesis applied to neutron spectra of irradiation facilities and in the ATLAS and CMS SCT. *ROSE technical report* **ROSE/TN/97-2** (1997). `http://cern.ch/rd48/`. (Cited on pages 53 and 204.)

[Rya11] D. Ryabchikov, `dmitri.riabtchikov@cern.ch`. Private communication, 2011. (Cited on pages 138, 164, 187, and 206.)

[Rya12] D. Ryabchikov, `dmitri.riabtchikov@cern.ch`. Private communication, 2012. (Cited on pages 90, 91, 92, and 104.)

[Sch12] T. Schlüter. *The $\pi^-\eta$ and $\pi^-\eta'$ Systems in Exclusive* 190 *GeV $\pi^- p$ Reactions at COMPASS (CERN).* PhD thesis, Ludwig-Maximilians-Universität München, 2012. (Cited on pages 7 and 96.)

[See04] D. Seeharsch. *A Microcontroller based Steering Mechanism for the COMPASS Silicon Detector Cooling System.* Schriftliche Hausarbeit, Technische Universität München, August 2004. (Cited on page 33.)

[SELEX01] V.V. Molchanov et al. Radiative width of the a_2 meson. *Phys. Lett.* **B 521**, 171 (2001). (Cited on pages 73, 131, 148, and 206.)

[Sin] SINTEF, `http://www.sintef.no`. (Cited on page 24.)

[Spi05] H. Spieler. *Semiconductor detector systems.* Oxford Science Publications, 2005. (Cited on page 22.)

[Sze84] S.M. Sze. *Physics of Semiconductor Devices.* Wiley, 1984. (Cited on page 57.)

[Sze11] A. Szczepaniak, `aszczepa@indiana.edu`. Private communication, 2011. (Cited on page 150.)

[VES93] Beladidze G.M et al. Study of $\pi^- N \to \eta\pi^- N$ and $\pi^- N \to \eta\pi^- N$ reactions at 37 GeV. *Phys. Lett. B* **313**, 276 (1993). (Cited on page 6.)

[VES00] Y. Khoklov et al. Study of $x(1600)$ 1^{-+} hybrid. *Nucl. Phys. A* **663**, 596 (2000). (Cited on page 6.)

[VES05] D.V. Amelin et al. Investigation of Hybrid States in the VES Experiment at the Institute for High Energy Physics (Protvino). *Phys. Atom. Nucl.* **68**, 359 (2005). (Cited on page 6.)

[WA10200] D. Barberis et al. A study of the $f_0(1370)$, $f_0(1500)$, $f_0(2000)$ and $f_2(1950)$ observed in the centrally produced 4π final states. *Phys. Lett. B* **474**, 423–426 (2000). (Cited on page 6.)

[Wei08a] Q. Weitzel. *Precision Meson Spectroscopy: Diffractive Production at COMPASS and Development of a GEM-based TPC for PANDA*. PhD thesis, Technische Universität München, 2008. (Cited on pages 17, 74, 76, 86, 87, 96, 104, 105, 109, 112, 114, 115, 116, 117, 141, 179, and 191.)

[Wei08b] Q. Weitzel et al. Release Note on PWA of $\pi^-\pi^-\pi^+$ Events from Diffractive Dissociation at COMPASS, Version -II-. *COMPASS release note* (2008). (Cited on page 180.)

[Wie04] M. Wiesmann. *A Silicon Microstrip Detector for COMPASS and a First Measurement of the Transverse Polarization of the Lambda-Hyperons from Quasi-Real Photo-Production*. PhD thesis, Technische Universität München, January 2004. (Cited on pages 22, 26, 30, and 33.)

[Zem65] Charles Zemach. Use of angular-momentum tensors. *Phys. Rev.* **140**, B97–B108 Oct 1965. (Cited on page 86.)

[Zie84] M. Zielinski et al. Evidence for the Electromagnetic Produktion of the A_1. *Phys. Rev. Lett.* **52**, 1195 (1984). (Cited on page 139.)

[Zim11] P. Zimmerer. *Performance of cryogenic silicon microstrip detectors at the COMPASS experiment*. Diploma thesis, Technische Universität München, January 2011. (Cited on pages 59, 60, 62, 65, 68, and 69.)

Own Contributions

During the development and commissioning of the cryogenic operation of the silicon detectors in COMPASS I was involved in all aspects of this project which is lead by Jan Friedrich. This concerns primarily the enhancements of the new silicon detector modules and the organization of their production at an external company. I was responsible for manufacturing and preparation of all components involved, for the planning and scheduling of the assembly at HighTec, and for the subsequent readout tests and electronics commissioning of the detectors. I adapted several mechanical parts related to the vacuum and cooling infrastructure of the cryostats. In extensive test series with a laboratory setup, both at Munich and at CERN, I worked on the cooling stability together with Jan Friedrich and Jean-Yves Roussé and his team. I carried out the commissioning of the cold APV readout chips in close contact with Igor Konorov. I carried out the first long-term cooling test with the first cold silicon station in the COMPASS experimental area after the 2008 beam time, recording signals from cosmics. In addition I presented the status of the project in several meetings of the COMPASS Technical Board, and discussed there the further developments.

I supervised several technical and diploma students working on the silicon project. I was responsible for the annual commissioning of the silicon detectors in the COMPASS experimental area in 2007, 2008, and partly still in 2009, when this duty was step by step taken over by Karl Bicker, and I also took part in the commissioning for the 2006 and 2012 beam times. I participated in the COMPASS spectrometer shift duties and took over several weeks of expert-on-call responsibility for the COMPASS silicon and GEM detectors during the physics data taking in the years 2006 - 2010 and 2012.

The basic event selection for the analysis was based on my diploma thesis, where I pioneered the field for COMPASS. Quirin Weitzel continued this in his PhD work on the 3π-high-t' sector, from which the present analysis could profit. I carried out and optimized all Monte Carlo simulations presented in this thesis. The partial-wave analyses and the determination of the presented absolute cross-section were performed by me under the supervision of Jan Friedrich and in close collaboration with Dmitri Ryabchikov, who develops and maintains the employed PWA programme.

I presented my work to the COMPASS collaboration, who agreed to have the results released for public presentation, and talked about them at several international conferences. In addition I participated in the drafting of the COMPASS paper about the first measurement of chiral dynamics in $\pi^-\gamma \to \pi^-\pi^-\pi^+$, which now has been already published [COM12a].

Acknowledgments

Thanks to Stephan Paul for providing a unique working environment with great experts around at his chair, and for giving me the opportunity to work on two completely different, but equally fascinating projects in the COMPASS collaboration.

Thanks to Jan Friedrich for his continuous supervision characterized by extraordinary engagement, and providing remarkable ideas related to really everything concerning silicon detectors and physics analysis.

Thanks to Dmitri Ryabchikov for the close and fruitful collaboration on the PWA, and for always being willing to explain the secrets behind the PWA to me.

Thanks to Norbert Kaiser and Suh-Urk Chung for sharing their scientific expertise in their respective fields with us, which was of major importance for the analysis result.

Thanks to Igor Konorov and Heinz Angerer for their support provided for all the aspects of the silicon electronics.

Merci beaucoup à Alain Magnon and Nicole d'Hose for their interest in the cold silicon project, organizing the necessary infrastructure, and providing moral support.

Merci beaucoup à Jean-Yves Roussé, Dominique Epelle, Thierry Pedrol, and their colleagues from Saclay, for their invaluable work on the silicon cooling system and the help with the assembly of the cryostats.

Thanks to Christian Höppner, for having proactively been the only volunteer to help with the silicon installation in the most critial time before the 2008 beam time.

Thanks to all the silicon diploma students, on whose work I partly relied for this PhD: Charly Bicker, Philipp Zimmerer, Michael Leeb, and Bernd Holzgartner.

Thanks to all the technical students, who supported me with the work on the silicon detectors. Particularly to Gregor Bracher, who greatly supported the work in the lab with his work on a non-commercial monitoring and control system, Martin Elmer, who tested the second bench of silicon sensors, and carried out the analysis of the leakage currents presented in this thesis, Alexandra Rüger, Philipp Weigell, and Talayeh Aledavood.

Thanks to my fellow PhD collegues: Annemarie Dinkelbach, Quirin Weitzel, Sebastian Neubert, Christian Höppner, Florian Haas, Thiemo Nagel, Alex Austregesilo, Markus Krämer, Felix Böhmer, Stefan Huber, and Sverre Dorheim for plenty of interesting discussions on physics and other more or less weird topics. Additional thanks to Sebastian Uhl for great help with all kind of problems related to the COMPASS analysis software. Charly Bicker deserves extra thanks for having taken over responsibilities for the silicon commissioning already during his time as a technical student, and such having relieved me significantly from this work load.

Thanks to Jan and Sebastian for proof-reading most parts of the manuscript and giving

valuable hints for improvements.

Thanks to the admins: Roland Kuhn, Thiemo Nagel, Markus Krämer and Felix Böhmer for keeping the E18 computing infrastructure running.

Thanks to all my office mates, who I had a great time with during all these years. Several years I enjoyed to be in company with Alexander Mann and Boris Grube, and for shorter times also Dima Ryabchikov, Annemarie Dinkelbach, Philipp Tunka, Christian Höppner, Lisa Wörner, Talayeh Aledavood, Alex Austregesilo, Philipp Zimmerer, Stefan Huber, and Charly Bicker.

Thanks to Karin Frank, the administrative backbone of the chair, for always being able to find a way out of the jungle if possible at all.

Thanks to Martin Aigner, Thomas Deuschle, and their colleagues at the workshops, for their excellent work on the custom mechanical parts of the silicon cryostats.

Thanks to the people sharing my life outside the university, especially my family, for their moral support that kept me motivated to continue the work also in hard times. Special thanks to Sebastian for his invaluable support during the last months, with practical and technical issues and great motivation, which allowed me to concentrate on the writing of this thesis.